

**MOLECULAR DESIGN STRATEGIES AND IMAGING OF ELECTRONIC PEPTIDE  
NANOMATERIAL SCAFFOLDS**

by  
Jessie Perrin Dibble

A dissertation submitted to Johns Hopkins University in conformity with the requirements for  
the degree of Doctor of Philosophy

Baltimore, Maryland

August 2021

© 2021 Jessie Dibble  
All Rights Reserved

## Abstract

Peptide- $\pi$  conjugated materials represent a powerful class of supramolecular materials with the unique ability to bridge the traditionally disparate realms of electronics and biological settings. The modular nature of peptide synthesis has facilitated systematic investigations into the impacts of amino acid composition for material properties. This dissertation presents design strategies to achieve new conformations and electronic outcomes within these peptide materials, efforts to characterize mixed peptide assemblies on the nanoscale and attempts to employ them in biological settings. In chapter 1 the state of organic electronics and its extensions to bioelectronics is introduced. Previous efforts from our lab to control peptide- $\pi$ -peptide scaffolds through monomer design and assembly trigger are discussed. Then, the fundamentals of electron microscopy are reviewed along with electron specimen interactions and their use in characterizing nanomaterials.

In chapter 2, constitutional isomerism brought about by swapping regimes of unique hydrophobicity and the influence on physical properties, morphology, and electronic communication among  $\pi$ -cores is examined. The addition of a purely hydrophobic alkyl tail is also discussed wherein access to a range of nanoarchitectures without diluting the impacts of constitutional isomerism is demonstrated. Chapter 3 details efforts to use bromine and sulfur as elemental indicators of co-assembly or self-sorting and examine the nanoscopic details of mixed assemblies by way of STEM-EDS mapping. This characterization method is applied to statistically mixed co-assemblies, self-sorted structures based on exploiting subtle pK<sub>a</sub> differences as previously reported by our lab, and a novel self-sorting paradigm brought about by tailoring specific monomer-monomer interactions. In chapter 4, the field of diphenylalanine research and extensive efforts to effectuate control over the assembly of this unique dipeptide are discussed.

Efforts to control the assembly of diphenylalanine by single fluorine substitution at the beta-carbon are explored wherein preliminary studies suggest that this relatively small change in structure can have dramatic impacts on assembly. Chapter 5 is concerned with biologically relevant nanomaterials and the promise of peptide- $\pi$  conjugates in 3D cell culture applications. Both failed and successful attempts to prepare a hydrogel scaffold containing attributes known to guide neuronal stem cells toward neuronal lineages are presented. Finally, promising efforts to translate peptide- $\pi$ -peptide nanomaterials to *in vivo* stroke recovery models are detailed.

**Thesis Advisor:**

Professor John D. Tovar

**Thesis Readers:**

Dr. Rebekka Klausen, Dr. Thomas Kempa

## Acknowledgements

I would like to express my deepest appreciation for everyone who has supported me before and during this process. The list of people I owe my gratitude to is long and in writing this I feel extremely fortunate. The path I followed to this point started as an undergraduate researcher and the first times I imagined myself as a scientist. Dr. Alex McDonald was my graduate student mentor in the Millhauser group and was the first person to encourage me to continue to graduate school. He taught me so much about thoughtful research and how to communicate it with nuance (as well as a lot about brewing beer and life in general). I do not know if I would be here now if it was not for his continued guidance and encouragement. I also want to express my sincere gratitude to Dr. William Hewitt who was my graduate student mentor in the Lokey group. He guided me into the world of synthetic organic chemistry and was such an inspiring and knowledgeable mentor.

No one has been more impactful on my scientific development than my advisor, Prof. J.D. Tovar. My first several years in graduate school were as difficult emotionally and mentally as they were intellectually. J.D. provided guidance but did not direct. This balance allowed me to learn independence as a scientist and build my confidence over time. It also taught me that successes and failures both have immense value. I am also grateful to Prof. Rebekka Klausen and Prof. Thomas Kempa for being on my graduate board orals. I have learned much from them and am grateful for their guidance and mentorship.

I have met some of my dearest friends in graduate school and in Baltimore and I could not have made it through endless hours of lab work, studying for orals or writing this dissertation



without them. They have become like family to me, and I look forward to years of their friendship. My partner, John, has been my biggest supporter and has certainly carried me over the finish line. I want to thank him endlessly for his encouragement and calming presence during the end of my graduate studies, it has been such a joy to have him as a part of my life.

I would also like to thank my family and their friends who have always showered me in love and supported my dreams. My father has worked hard and selflessly to provide opportunities for his children and without that determination and kindness I would not be where I am. My mother has instilled in me good communication and a pushed me to explore both my creative and analytical sides. She is my closest friend and has guided me through some of my darkest times. My sister is forever my role model, she lights up every room and has been the biggest source of encouragement and laughter during this process.

Dedicated to my loving parents who are also dear friends,

Ava Mckenzie and David Dibble

## Table of Contents

	Abstract.....	ii
	Acknowledgements.....	iv
	List of Tables.....	ix
	List of Figures.....	x
<b>Chapter 1</b>	<b>Introduction – Peptide-<math>\pi</math> Electronics, Molecular Design and Characterization Strategies</b>	
	Organic Electronic Materials.....	2
	Supramolecular Assembly of $\pi$ -conjugated Materials.....	3
	Peptide Templated $\pi$ -Conjugated Supramolecular Assemblies.....	6
	Control of Self-Assembly – Energy Landscapes.....	11
	Fundamentals of Electron Microscopy.....	16
	Conclusion.....	23
	References.....	24
<b>Chapter 2</b>	<b>Constitutional Isomerism to Dictate Morphology and Electronic Communication in <math>\pi</math>-Conjugated Peptides</b>	
	Introduction.....	36
	Results and Discussion.....	41
	Conclusion.....	59
	Experimental Section.....	60
	References.....	63
<b>Chapter 3</b>	<b>Methods in Molecular Engineering Toward Nanoscopic Control and Visualization in Peptide-<math>\pi</math> Conjugates</b>	
	Introduction.....	73
	Results and Discussion.....	77
	Conclusion.....	93
	Experimental Section.....	94
	References.....	97
<b>Chapter 4</b>	<b>Fluorination Strategies for Molecular Engineering of Diphenylalanine Peptides</b>	
	Introduction.....	105
	Results and Discussion.....	111
	Conclusion.....	118
	Experimental Section.....	119
	References.....	119
<b>Chapter 5</b>	<b>Design of Peptide-<math>\pi</math> Hydrogels for Biology</b>	

Introduction.....	125
Results and Discussion.....	129
Conclusion.....	144
Experimental Section.....	144
References.....	148
<b>Appendix      Characterization and Supporting Information</b>	
Chapter 2.....	154
Chapter 3.....	177
Chapter 4.....	189
Chapter 5.....	194
<b>Curriculum Vitae.....</b>	<b>204</b>

## List of Tables

<b>Table 3.1.</b> Summary of peptide samples prepared by different assembly conditions.....	82
<b>Table 4.1.</b> Assemblies of phenylalanine containing peptides can access a myriad of morphologies.....	106
<b>Table A4.1.</b> Experimental details of x-ray diffraction.....	191

## List of Figures

<b>Figure 1.1.</b> Monomeric units and the range of structures they form upon supramolecular assembly.....	5
<b>Figure 1.2.</b> Illustration of the step-wise formation of fibres from rod-like monomers as detailed in peptide aggregation models.....	6
<b>Figure 1.3.</b> Peptides assembly can be leveraged to organize precise geometries of $\pi$ -units. Monomer structure dictates (A) supramolecular outcome in NDI appended di-lysine peptides and can direct the construction of 1D objects in (B) oligothiophenes and (C) diketopyrrolopyrrole.....	8
<b>Figure 1.4.</b> Synthetic strategy to form peptide- $\pi$ -peptide monomers with a diversity of cores on resin.....	9
<b>Figure 1.5.</b> A) General molecular structure of the “triblock” peptide- $\pi$ -peptide monomers that self-assemble under acidic conditions into B) discrete nanostructures. Photophysical changes (C,D) occur upon assembly from molecular dissolved monomers at high pH to aggregates at low pH. Nanostructures can be observed as extended networks (E) and as discrete structures (F) using TEM imaging.....	10
<b>Figure 1.6.</b> Two energy landscapes accessible to peptide amphiphiles that depend on assembly conditions at A) low ionic strength and B) high ionic strength. ....	11
<b>Figure 1.7.</b> A) Variation in the identity of amino acid flanking $\pi$ -conjugated core can greatly impact B) UV and C) photoluminescence spectra of triblock peptide nanomaterials.....	13
<b>Figure 1.8.</b> A) Symmetric peptide monomers form “parallel” $\beta$ -sheets corresponding to excimeric emission while B) asymmetric peptides form “anti-parallel” $\beta$ -sheets that result in excitonic emission.....	14
<b>Figure 1.9.</b> A) Incorporation of subtle pH trigger led to the formation of B) self-sorted or C) co-assembled nanostructures depending on the nature of assembly trigger. D) Emission profiles of GdL-triggered assemblies show evidence of self-sorting with residual electronic coupling and E) HCl-triggered assemblies demonstrated co-assembly, energy migration and charge separation.....	15
<b>Figure 1.10.</b> Light passing through an opaque screen with circular aperture (a) illuminates a display screen and creates a diffraction pattern (b) where two diffraction patterns are just resolved when the maximum of the first overlaps the first minimum of the second (c). If the two points are closer in space, they appear as a single object (d).....	18
<b>Figure 1.11.</b> The interaction of an electron beam generates radiation and changes to electron path and/or energy.....	19

**Figure 1.12.** (a) String of thorium and uranium atoms visualized by STEM-HAADF and the first photo taken of a single atom. (b and c) The grains and grain boundaries can be discerned in a graphene sheet.....20

**Figure 1.13.** Electron-specimen interactions that occur to produce (a) EDS and EELS signals and (b) and Auger electrons.....21

**Figure 1.14.** (a) STEM-HAADF image of Phenylalanine nanowire-platinum nanoparticle composites where HAADF line scan shows higher density in the walls of the nanowire where (b) EDS spectra show distinct presence of Pt signal.....23

**Figure 2.1.** Structure of previously studied systems including (a) synthetic peptide amphiphile with charged,  $\beta$ -sheet forming, head group appended to a lipophilic tail, (b) perylene diimide substituted with a beta-sheet forming peptide and a branched alkyl tail and (c) a peptide linked to a benzothienobenzothiophene unit with an alkyl tail. The charged hydrophilic (red), hydrophobic  $\beta$ -sheet forming peptide (blue),  $\pi$ -conjugated (yellow), and alkyl tail (green) segments are highlighted on each system.....37

**Figure 2.2.** The construction of peptide- $\pi$  conjugates can be achieved through the (a) synthesis of aromatic “amino acids” to produce macrocycles or by conjugation to dipeptides (b,c) to achieve fibrils, spicules and nanotubes among other nanomorphologies.....39

**Figure 2.3.** The  $\pi$ -conjugated peptide library presented in this work (a) that encompasses a range of intermolecular interactions to (b) guide assembly from monomers to a range of nanoarchitectures.....40

**Figure 2.4.** Representative transmission electron micrographs of **2** (a,c) and **3** (b,d) assembled from basic media (a,b) and neutral media (c,d).....45

**Figure 2.5.** Representative transmission electron micrograph of **4-C8** (a,c) and **5-C8** (b,d) following rapid acidification and incubation at room temperature for 30 min (a,c) and after sonication, thermal annealing and equilibration for 16 hours at pH 7 (b,d).....47

**Figure 2.6.** Transmission electron micrograph of **4-C16** dissolved at pH 8.6 and equilibrated at room temperature for (a) 16 hours (b) 2 weeks. **5-C16** dissolved at (a) pH 7.0 and (b) pH 8.6 and equilibrated at room temperature for 16 hours.....49

**Figure 2.7.** Representative transmission electron micrographs of (a) **6** (b) **7-C8** and (c) **7-C16** at pH 9 and (d) **7-C16** at pH 1.....51

**Figure 2.8.** UV-Vis (left panels, solid lines) and photoluminescence (left panels, dashed lines), CD (middle panels), and DLS (right panels) spectra for **1** (a,b,c), **2** (d,e,f) and **3** (g,h,i) in basic (grey traces) and neutral (orange traces) media and in basic-to-acidic (black traces) and neutral-to-acidic (green) assemblies.....53

**Figure 2.9.** UV-Vis (left panels, solid lines) and photoluminescence (left panels, dashed lines), and CD (right panels) spectra for **4-C8** (a,b) **5-C8** (c,d) at pH 10 (grey traces) and pH 1 following rapid acidification (black traces).....55

**Figure 2.10.** UV-Vis (left panels, solid lines), photoluminescence (left panels, dashed lines), and CD (right panels) spectra for **4-C16** (a,b) and **5-C16** (c,d) at basic (grey) and acidic (black) pH.....56

**Figure 2.11.** (Left panel) UV-Vis, solid, and photoluminescence, dashed, and (Right panel) CD traces for (a,b) **6** (c,d) **7-C8** and (e,f) **7-C16** at basic (grey) and acidic (black) pH.....58

**Figure 3.1.** The controlled assembly of supramolecular materials from mixed solutions of monomers has been achieved through (a) assembly trigger to create self-sorted nanostructures. Block co-polymer structures have also been prepared through (b) crystallite seed formation and (c) monomer design.....75

**Figure 3.2.** UV-vis absorbance (dashed) and PL (solid) spectra for **1** (black), **2** (blue traces), and **3** (yellow traces) under acidic conditions.....80

**Figure 3.3.** UV-vis signatures for 1:1 mixtures of (a) **1** and **2** and (b) **1** and **3** following rapid HCl acidification (black traces), separately assembled and then mixed (orange traces), and GdL assembled (purple traces) conditions. PL traces (c-h) following excitation at 350 (green traces) and 480 nm (black traces) following (c,f) rapid HCl acidification, (d,g) under separately assembled and then mixed, and GdL assembled (purple traces) conditions for samples A-C (c-e) and D-F (f-g).....83

**Figure 3.4.** PL traces following excitation at 310 (a,c) and 450 nm (b,d) following rapid HCl acidification (black traces), under separately assembled and then mixed (orange traces), and GdL assembled (purple traces) conditions for samples H-J (a,b) and K-M (c,d). PL traces for homo assembles of peptides **2**, **3**, and **4** are plotted for comparison in blue, yellow and grey respectively.....85

**Figure 3.5.** (a) Large area EDS spectrum of sample G showing strong presence of bromine K $\alpha$  line. (b) The peptide nanomaterials could be imaged wherein that demonstrates (c) bromine occurrence in areas of peptide density.....86

**Figure 3.6.** (a) Spectrum image and line scan path for sample B where (b) the normalized sulfur and bromine signals are detected and quantified.....87

**Figure 3.7.** (a,c,e) Spectrum image and line scan paths for samples A, C and D where (b,d,f) sulfur and bromine signals are detected and quantified.....89

**Figure 3.8.** Spectrum image and elemental mapping for sulfur (green) and bromine (red) for samples (a) b, (b) a, (c) c and (d) d.....90



<b>Figure 3.9.</b> Spectrum images for (a-c) sample I and (d-f) sample H showing the spectrum images (a,d) and elemental mapping for oxygen (yellow, b,e) and sulfur (purple c,f) within the sample.....	91
<b>Figure 3.10</b> Spectrum images for (a-c) sample J and (d-f) sample K showing the spectrum images (a,d) and elemental mapping for oxygen (yellow, b,e) and sulfur (purple c,f) within the sample.....	93
<b>Figure 4.1.</b> Model of the A) crystal structure of diphenylalanine demonstrating a B) porous laminated structure composed of C) individual nanotubes formed by head-to-head hydrogen bonding of diphenylalanine peptide backbone.....	105
<b>Figure 4.2.</b> Simple molecular modifications of diphenylalanine induce morphological changes wherein a) para-fluoro induces tubular formation, b) per-fluorination results in wider tubular structures, c) para-iodo substitution results in a mixture of spheres and fibrillar structures, and d) Fmoc-protection of the N-terminus dictates a nanotubular structure.....	108
<b>Figure 4.3.</b> Effect of fluorination on alkyl spacers in liquid crystal cores. A) Structure of a model liquid crystal core B) stabilization of conformer through negative hyperconjugation.....	109
<b>Figure 4.4.</b> Heatmap demonstrating the changes in electronic distribution upon perfluorination of stilbene as calculated by PC Spartan.....	110
<b>Figure 4.5.</b> a) Relative energies of <b>1-4</b> as obtained by DFT calculations with representative structures of the b) S,R and c) R,R diastereomers.....	113
<b>Figure 4.6.</b> A) HPLC traces of separation of using <b>5</b> and <b>6</b> column and MeOH isocratic method (green trace), gradient from 100:0- 50:50 MeOH:Hex (red trace), gradient from 100:0-98:2 MeOH:IPA (blue trace). <sup>19</sup> F-NMR spectra of B) mixture of diastereomers of <b>5</b> and <b>6</b> and C) following chiral column purification.....	114
<b>Figure 4.7.</b> Chiral screening demonstrates conditions for excellent separation of fluorinated Phth-F-Phe diastereomers.....	116
<b>Figure 4.8.</b> Crystals obtained from a mixture of <b>5</b> and <b>6</b> contained <b>5</b> as the majority component.....	117
<b>Figure 4.9.</b> Close contacts formed in (a) Phth-F-Phe and (b) Phth-Phe crystals.....	118
<b>Figure 5.1.</b> Young's moduli characteristic of various tissues.....	126
<b>Figure 5.2.</b> Schematic of peptide containing donor-acceptor system.....	127
<b>Figure 5.3.</b> Epifluorescence images of differentiated hNSCs stained with A) neuronal markers B) glial and neuronal markers C) color overlay of stained nuclei (blue) cells with neuronal markers (green) and glial markers (red).....	130

<b>Figure 5.4.</b> Absorbance (solid lines) and emission (dashed lines) of peptides a) <b>6</b> and b) <b>5</b> crude under dissolved (basic, black lines) and assembled (acidic, grey lines) conditions.....	135
<b>Figure 5.5.</b> TEM images of peptide <b>5</b> stained with 2% Uranyl acetate. Both scale bars represent 200 nm.....	136
<b>Figure 5.6.</b> Absorbance at 260 nm, absorbance of peptide backbone during A) Preparatory purification, peak isolated at 26.55 min corresponding to peptide <b>5</b> B) Semipreparative purification of <b>5</b> showed large number of new impurities.....	137
<b>Figure 5.7.</b> Emission of peptide <b>8</b> diluted to 50% and 10% in a solution of peptide <b>7</b> under (a) basic and (b) acidic conditions.....	139
<b>Figure 5.8.</b> The a) UV and b) PL traces for <b>10</b> under basic (dashed) and acidic (solid) conditions.....	140
<b>Figure 5.9.</b> Representative electron micrograph following injection of <b>10</b> into stroke cavity.....	141
<b>Figure 5.10.</b> auto fluorescence convolutes hydrogel imaging in stroke and non-stroke brains.....	142
<b>Figure 5.11.</b> Fluorescence images of a) brain slice with saline and hydrogel injections and b) several slices of two brains with hydrogel visualized at the stroke site by monitoring the cy-5 channel.....	143
<b>Figure A.2.1.</b> Peptide library was synthesized by standard solid-phase peptide synthesis adapted with an on-resin carboxylic acid activation procedure.....	154
<b>Figure A.2.2.</b> Transmission electron micrographs of basic-to-acidic processing of peptides (a) <b>4-C8</b> (b) <b>5-C8</b> (c) <b>4-C16</b> (d) <b>5-C16</b> (e) <b>7-C8</b> and (f) <b>7-C16</b> show random aggregates.....	155
<b>Figure A.2.3.</b> Transmission electron micrograph of (a) <b>1</b> and (b) <b>3</b> in basic-to-acidic assemblies and (c) <b>2</b> and (d) <b>3</b> in neutral-to-acidic assemblies.....	156
<b>Figure A.2.4.</b> Representative transmission electron micrograph of (a) <b>4-C16</b> dissolved in buffer pH 7 after sonication, thermal annealing, and equilibration at room temperature for two weeks and <b>5-C16</b> dissolved in (b) pH 7.0 and (c) 8.6 buffers, sonicated, thermally annealed for 24 hours and equilibrated at room temperature for two weeks.....	157
<b>Figure A2.5.</b> UV-Vis (left panels, solid) and photoluminescence (left panels, dashed), and CD (right panels) spectra for (a,b) <b>4-C8</b> (c,d) <b>5-C8</b> (e,f) in basic (grey), acidic (black), 30 minutes after acidification (red) and in thermally annealed samples pH 7 (green).....	158

**Figure A2.6.** UV-Vis (left panels, solid lines), photoluminescence (left panels, dashed lines), and CD (right panels) spectra for 4-C16 (a,b) and 5-C16 in pH 8.6 buffer 16 hours (green traces), 24 hours (orange traces) and two weeks (purple traces) after thermal annealing.....159

**Figure A2.7.** ESI spectrum of HO-DDVA-OT4-AVDD-OH peptide (1). MS (ESI)  $m/z$  1217.0 (M-1H) (calc. 1217.3),  $m/z$  608.3 (M-2H)/2 (calc. 608.7).....164

**Figure A2.8.** ESI spectrum of HO-DDDD-OT4-AVAV-OH peptide (2). MS (ESI)  $m/z$  1217.4 (M-1H) (calc. 1217.3),  $m/z$  608.5 (M-2H)/2 (calc. 608.0),  $m/z$  405.1 (M- 3H)/3 (calc. 405.0).....165

**Figure A2.9.** ESI spectrum of HO-DDDD-VAVA-OT4-OH peptide (3). MS (ESI)  $m/z$  1217.1 (M-1H) (calc. 1217.3),  $m/z$  608.5 (M-2H)/2 (calc. 608.0).....166

**Figure A2.10.** ESI spectrum of HO-DDDD-OT4-AVAV-C8 peptide (4-C8). MS (ESI)  $m/z$  1328.3 (M-1H) (calc. 1328.4),  $m/z$  664.3 (M-2H)/2 (calc. 663.7),  $m/z$  442.9 (M-3H)/3 (calc. 442.1).....167

**Figure A2.11.** ESI spectrum of HO-DDDD-OT4-AVAV-C16 peptide (4-C16). MS (ESI)  $m/z$  1440.5 (M-1H) (calc. 1440.5),  $m/z$  720.6 (M-2H)/2 (calc. 719.7),  $m/z$  480.3 (M-3H)/3 (calc. 479.5).....168

**Figure A2.12.** ESI spectrum of HO-DDDD-VAVA-OT4-C8 peptide (5-C8). MS (ESI)  $m/z$  1328.2 (M-1H) (calc. 1238.4),  $m/z$  663.7 (M-2H)/2 (calc. 663.7).....169

**Figure A2.13.** ESI spectrum of HO-DDDD-VAVA-OT4-C16 peptide (5-C16). MS (ESI)  $m/z$  1440.31 (M-1H) (calc. 1440.5),  $m/z$  720.45 (M-2H)/2 (calc. 719.7).....170

**Figure A2.14:** Analytical HPLC trace of purified HO-DDVA-OT4-AVDD-OH peptide (1). Traces monitoring 260 nm (top) and 420 nm (bottom). Method: Linear gradient of 10%-50% acetonitrile/buffer over 25 minutes, then linear gradient of 50%-10% over 5 minutes.....171

**Figure A2.15.** Analytical HPLC trace of purified HO-DDDD-OT4-AVAV-OH peptide (2). Traces monitoring 260 nm (top) and 420 nm (bottom). Method: Linear gradient of 10%-50% acetonitrile/buffer over 25 minutes, then linear gradient of 50%-10% over 5 minutes.....172

**Figure A2.16.** Analytical HPLC trace of purified HO-DDDD-VAVA-OT4-OH peptide (3). Traces monitoring 260 nm (top) and 420 nm (bottom). Method: Linear gradient of 10%-50% acetonitrile/buffer over 25 minutes, then linear gradient of 50%-10% over 5 minutes.....172

**Figure A2.17.** Analytical HPLC trace of purified HO-DDDD-OT4-AVAV-C8 peptide (4-C8). Traces monitoring 260 nm (top) and 420 nm (bottom). Method: Linear gradient of 20%-60%

acetonitrile/buffer over 25 minutes, then linear gradient of 60%-20% over 5 minutes.....173

**Figure A2.18.** Analytical HPLC trace of purified HO-DDDD-OT4-AVAV-C16 peptide (4-C16). Traces monitoring 260 nm (top) and 420 nm (bottom). Method: Linear gradient of 30%-70% acetonitrile/buffer over 25 minutes, then linear gradient of 70%-30% over 5 minutes.....174

**Figure A2.19.** Analytical HPLC trace of purified HO-DDDD-VAVA-OT4-C8 peptide (5-C8). Traces monitoring 260 nm (top) and 420 nm (bottom). Method: Linear gradient of 20%-60% acetonitrile/buffer over 25 minutes, then linear gradient of 60%-20% over 5 minutes.....174

**Figure A2.20.** Analytical HPLC trace of purified HO-DDDD-VAVA-OT4-C16 peptide (5-C16). Traces monitoring 260 nm (top) and 420 nm (bottom). Method: Linear gradient of 30%-70% acetonitrile/buffer over 25 minutes, then linear gradient of 70%-30% over 5 minutes.....175

**Figure A2.21:** Distinct regimes of chemical character guide the assembly process and morphological outcomes in the current peptide library.....176

**Figure A2.22:** Assembly conditions and morphological outcomes for the 4-C16 and 5-C16 peptides.....177

**Figure A3.1.** UV-vis absorbance (left) and PL (right) spectra for 1 (black), 2 (blue traces), and 3 (yellow traces) under basic conditions.....178

**Figure A3.2.** Emission spectra from a) 1 b) 2 and c) 3 when excited 350 nm (green traces) and 480 nm (black traces).....178

**Figure A3.3.** UV-vis absorbance (a,b) and PL (c,d) spectra for 2 (blue traces), 3 (yellow traces), and 4 (grey traces) under basic(a,c) and acidic (b,d) conditions.....179

**Figure A3.4.** UV-vis absorbance profiles for 1:1 co-assemblies of a) 4 and 2 and b) 4 and 3 when assembled by HCl addition (black traces), when separately assembled and then mixed (yellow traces) and GdL hydrolysis (blue traces).....179

**Figure A3.5.** ESI spectrum of EAA-OT4Br4 peptide (1). MS (ESI)  $m/z$  1275.17 (M-1H) (calc. 1275.82),  $m/z$  637.15 (M-2H)/2 (calc. 637.41),  $m/z$  1912.44 (3\*M-2)/2 (calc. 1912.75).....183

**Figure A3.6.** ESI spectrum of AAA-OT4 peptide (2). MS (ESI)  $m/z$  843.21 (M-1H) (calc. 843.99),  $m/z$  421.29 (M-2H)/2 (calc. 421.50),  $m/z$  1266.30 (3\*M-2)/2 (calc. 1266.49), 1688.21 (4\*M-2)/2 (calc. 1688.98).....184

**Figure A3.7.** ESI spectrum of AAA-OT4 peptide (3). MS (ESI)  $m/z$  1360.31 (M-1H) (calc. 1360.45),  $m/z$  679.70 (M-2H)/2 (calc. 679.23).....185

**Figure A3.8.** ESI spectrum of EAA-OPV3 peptide (4). MS (ESI) m/z 911.24 (M-1H) (calc. 911.35), m/z 455.39 (M-2H)/2 (calc. 455.18).....186

**Figure A3.9.** Analytical HPLC trace of purified EAA-OT4Br<sub>4</sub> peptide (1). Traces monitoring at 420 nm. Method: Linear gradient of 10%-50% acetonitrile/buffer over 25 minutes, then linear gradient of 50%-10% over 5 minutes.....187

**Figure A3.10.** Analytical HPLC trace of purified AAA-OT4 peptide (2). Traces monitoring 420 nm. Method: Linear gradient of 10%-50% acetonitrile/buffer over 25 minutes, then linear gradient of 50%-10% over 5 minutes.....187

**Figure A3.11.** Analytical HPLC trace of purified EAEAA-OT4 peptide (3). Traces monitoring 420 nm. Method: Linear gradient of 10%-50% acetonitrile/buffer over 25 minutes, then linear gradient of 50%-10% over 5 minutes.....188

**Figure A3.12.** Analytical HPLC trace of purified EAA-OPV3 peptide (4). Traces monitoring 350 nm. Method: Linear gradient of 10%-50% acetonitrile/buffer over 25 minutes, then linear gradient of 50%-10% over 5 minutes.....188

**Figure A5.3.** ESI spectrum of DK(NDI-n-Bu)VV-OT4 peptide (7). MS (ESI) m/z 1883.15 (M-1H) (calc. 1883.10), m/z 941.60 (M-2H)/2 (calc. 941.05).....197

**Figure A5.4.** ESI spectrum of DGRDK(Ac)VV-OT4 peptide (8). MS (ESI) m/z 1020.47 (M-2H)/2 (calc. 1020.15), m/z 1360.70 (M\*2-3H)/3 (calc 1360.53).....198

**Figure A5.5.** ESI spectrum of DVV-OT4 peptide (10). MS (ESI) m/z 1043.50 (M-H) (calc. 1043.27), m/z 521.80 (M-2H)/2 (calc 521.14).....199

**Figure A5.6.** ESI spectrum of DK(Cy5)VV-OT4 peptide (11). MS (ESI) m/z 1116.77 (M-2H)/2 (calc. 1116.02).....200

**Figure A5.9.** Analytical HPLC trace of purified DK(NDI-n-Bu)VV-OT4 peptide (7). Traces monitoring at 260 nm (top) and 430 nm (bottom). Method: Linear gradient of 10%-50% acetonitrile/buffer over 25 minutes, then linear gradient of 50%-10% over 5 minutes.....201

**Figure A5.10.** Analytical HPLC trace of purified DGRDK(Ac)VV-OT4 peptide (9). Traces monitoring at 260 nm (top) and 420 nm (bottom). Method: Linear gradient of 10%-50% acetonitrile/buffer over 25 minutes, then linear gradient of 50%-10% over 5 minutes.....202

**Figure A5.11.** Analytical HPLC trace of purified DVV-OT4 peptide (10). Traces monitoring at 260 nm (top) and 420 nm (bottom). Method: Linear gradient of 10%-50% acetonitrile/buffer over 25 minutes, then linear gradient of 50%-10% over 5 minutes.....202

**Figure A5.11.** Analytical HPLC trace of purified DK(Cy5)VV-OT4 peptide (**11**). Traces monitoring at 426 nm (top) and 624 nm (bottom). Method: Linear gradient of 10%-50% acetonitrile/buffer over 25 minutes, then linear gradient of 50%-10% over 5 minutes.....204

## **Chapter 1**

# **Introduction – Peptide- $\pi$ Electronics, Molecular Design and Characterization Strategies**

## Organic Electronic Materials

The origins of organic electronics materials trace back to the mid-20<sup>th</sup> century where a series of advancements lead to the collaboration of MacDiarmid, Heeger, and Shirakawa that culminated in a Nobel prize for their work on iodine-doped polyacetylenes.<sup>1,2</sup> This among other progress in  $\pi$ -conjugated organic materials prompted interest in a shift from conventional “hard” silicon-based to “soft” organic electronic materials with the prospect of low-cost components for wearable devices, sensing, and biomedical applications.<sup>3,4</sup> The “hard” electronics of the 20<sup>th</sup> century were designed on a platform of stability, rigidity, high reliability, high temperature processing and “top-down” preparation through lithographic techniques. Organic electronic materials have distinct advantages of low temperature and solution processing, low energy consumption, and are based on a “bottom-up” fabrication process.<sup>4</sup> That said, mobility values, charge transfer characteristics, and device performance are inherently linked to precise geometric organization of units where bridging the meso-scale to “device”-scale size regimes have presented an opportunity for continued investigation in the 21<sup>st</sup> century.<sup>4-6</sup> While most organic electronic platforms are associated with either small-molecule or polymeric materials, for our purposes herein we will focus on the former, however, it should be noted that a rich body of research can be found on the latter.

While theoretically the optical absorption (i.e. excitation energy of the lowest excited state) of a pristine  $\pi$ -conjugated polymer without defects should present an unlimited conjugation pathway that is defined by the length of the polymer. In practice the “effective conjugation length” is determined by a balance of order and disorder in the system that often limits conjugation to oligomer-length units.<sup>7,8</sup> Oligomers can be uniformly synthesized with tunable physical and



electronic properties; however, thin film fabrication methods available such as vapor-phase deposition are expensive and impractical when compared to the more accessible spin coating procedures conditions for their polymeric counterparts.<sup>9</sup> As such, control of processing and ultimately the three-dimensional (3D) geometric organization of these materials over multiple length scales through supramolecular engineering has come to the forefront of research interest.<sup>5</sup>

### **Supramolecular Assembly of $\pi$ -conjugated Materials**

Self-assembly of two or more molecular building blocks by means of molecular recognition to yield structurally ordered nano-assemblies is the basis of supramolecular chemistry.<sup>10,11</sup> Early investigations in this field explored the properties of weak intermolecular interactions such as hydrophobic and Van der Waals forces, and hydrogen bonding, and these foundations later guided studies of enzyme-substrate binding, and detailed organizational studies of coordinatively saturated species such as the acetic acid dimer.<sup>12,13</sup> In 1961 Charles J. Pedersen's serendipitous discovery of dibenzo-18-crown-6 and his observation of selective metal cation binding was a breakthrough in the field where fundamental concepts were applied to synthetic systems.<sup>14</sup> The term supramolecular chemistry was first described by Jean-Marie Lehn as "the chemistry beyond the molecule" as he examined of the size selective binding of metal cations by polycyclic multidentate ligands called cryptates.<sup>10,15</sup> Systems of increasing sophistication have since been explored, for example, the interlocking "molecular machines" termed rotaxanes and catenanes developed by Stoddart and coworkers.<sup>16-19</sup>

Among weak interactions, hydrogen bonds are an important motif in the design and organization of supramolecular assemblies due to their high selectivity and directionality.<sup>10,20</sup> For

example, the monomers depicted in Figure 1.1 A are composed of two ureidopyrimidinone termini, separated by an alkyl spacer, and form quadruple hydrogen bonds to assemble into the random coiled polymers shown in Figure 1.1 B. These polymers demonstrate remarkable mechanical properties and, like their covalent counterparts, adhere to classical models of polymer physics in solution and in bulk but show a temperature dependent viscosity due to a decrease in hydrogen-bond lifetime as temperature increases.<sup>10</sup> Schenning, Meijer, and co-workers demonstrated the temperature dependent aggregation of mono-functionalized oligo(p-phenylenevinylene)s (MOPV)s in organic solvent. These structures were found to be composed of helical stacks of hydrogen-bonded dimers (Figure 1.1 C,D) and illustrate the utility of supramolecular interactions to assemble  $\pi$ -conjugated subunits into uniform, discrete structures that exhibit well-defined electron transport properties within the assembly.<sup>21–23</sup> Other groups have prepared nanoribbons<sup>24</sup>, fibrils<sup>25</sup> and helical nanotubes<sup>26</sup> by engineering a delicate balance of intermolecular interactions to achieve electrical conduits within the supramolecular aggregate attained under thermodynamically favorable conditions in organic solvents.<sup>27,28</sup> However, unfunctionalized  $\pi$ -conjugated organic semiconductors have limited aqueous solubility and are therefore difficult to process for biologically relevant applications.<sup>29 10,30–32</sup>

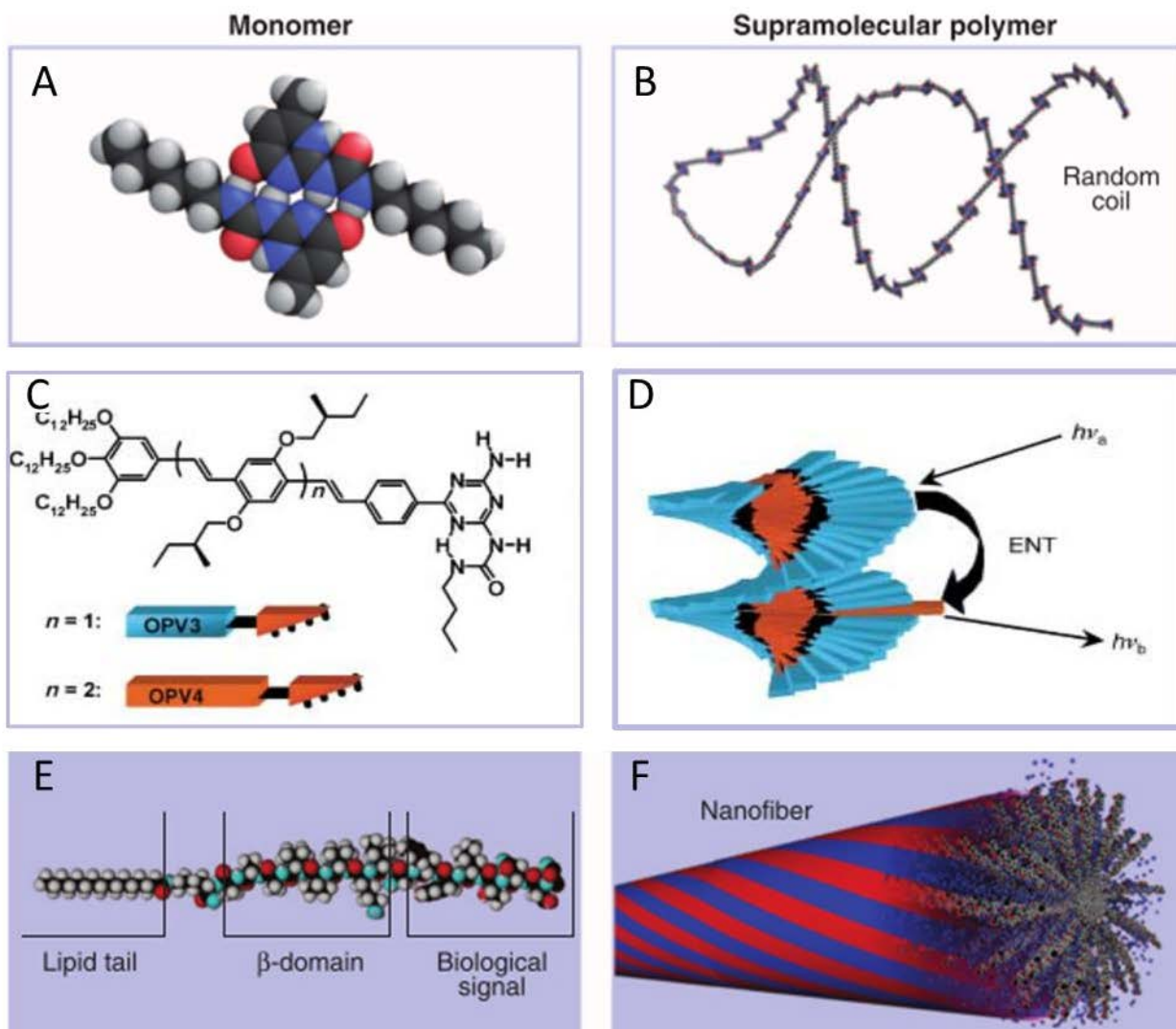


**Figure 1.1.** Monomeric units and the rang of structures they form upon supramolecular assembly. Adapted from Reference 10. Copyright Science, 2012. Reprinted from reference 21. Copyright Wiley-VCH Verlag GmbH & Co. KGaA, Weinheim, 2004.

## Peptide Templated $\pi$ -Conjugated Supramolecular Assemblies

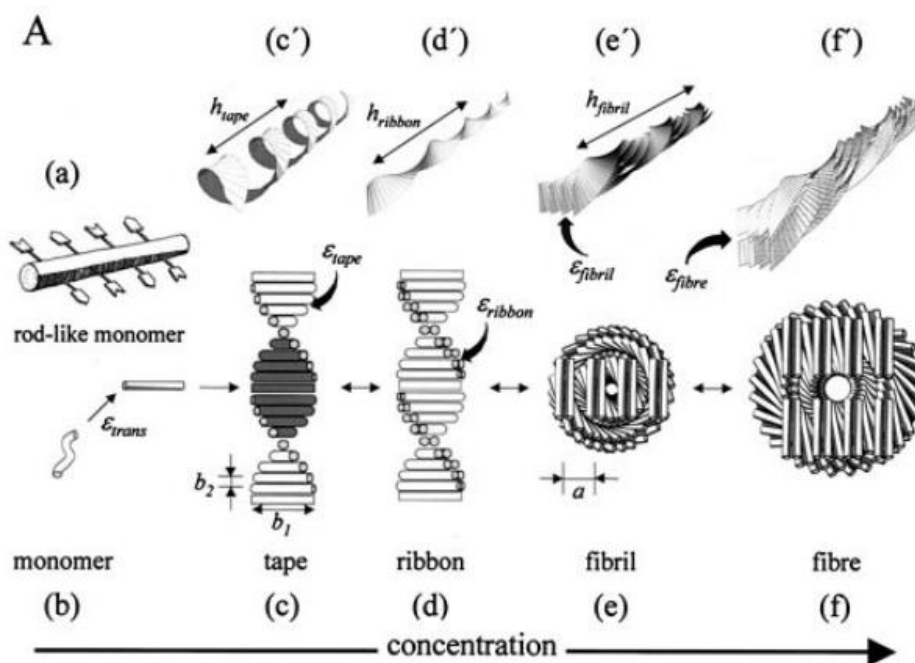


**Figure 1.2.** Illustration of the step-wise formation of fibres from rod-like monomers as detailed in peptide aggregation models. Reprinted from reference 33. Copyright PNAS, 2001.

A significant area of research in supramolecular chemistry has focused on developing biologically relevant nanomaterials, such as proteins and peptides, due to the significant source of hydrogen bond donors and acceptors they present.<sup>13</sup> The hierarchical assembly of peptide units, particularly those forming  $\beta$ -sheets, can be understood through the context of models for amyloid formation as shown in Figure 1.2. The assembly process proceeds in a step-wise fashion through the initial formation of rod-like monomers as the primary chain takes on a  $\beta$ -strand conformation and assembles, due to molecular recognition, into tapes with left-handed helical twist. Tapes associate laterally to form fibrils that ultimately associate into a fibers with finite thickness imposed by steric constraints.<sup>33</sup> An example of this assembly is peptide amphiphiles

composed of a peptide head group and a fatty acid tail that assemble into high aspect-ratio cylindrical nanofibers (Figure 1.1 E,F). Stupp and co-workers have studied these materials extensively from molecular design to function feeding applications in 3D cell culture, templating and biomineralization.<sup>34-40</sup>

The unique organizational power of peptides can be leveraged for  $\pi$ -conjugated units to enact precise geometries and facilitate electronic delocalization.<sup>41-45</sup> Parquette and co-workers examined di-lysine peptides functionalized with NDI in varied substitution and acetylation pattern to form n-type 1D constructs. They found that morphological outcome was intimately linked to the placement of the NDI moiety generating either helical tapes or nanoribbons and demonstrating the subtle changes to monomer structure that influence the eventual assembly and the 3D organization of electronic units (Figure 1.3a).<sup>41</sup> Bäuerle and co-workers reported the conjugation of a regioregular tetra(3-hexylthiophene) with a silk-inspired pentapeptide that formed linear nanoobjects which were in stark contrast to the lamellar structures formed by the tetrathiophene carboxylic acid demonstrating the ability of the hydrogen n peptide unit to overhaul the assembly paradigm (Figure 1.3b).<sup>42</sup> More recently, Brimble and co-workers demonstrated the functionalization of thiophene-diketopyrrolopyrrole with an octapeptide to prepare a fibrous network hydrogel as well as thin film of a co-facially stacked aggregate capable of charge transport (Figure 1.3c).<sup>45</sup>

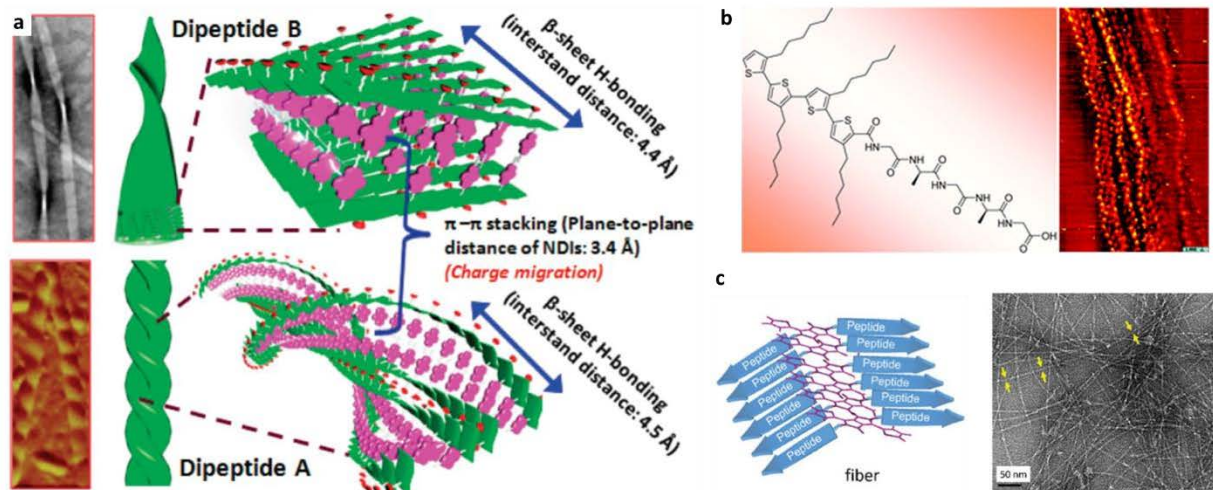


**Figure 1.3.** Peptides assembly can be leveraged to organize precise geometries of  $\pi$ -units. Monomer structure dictates (A) supramolecular outcome in NDI appended di-lysine peptides and can direct the construction of 1D objects in (B) oligothiophenes and (C) diketopyrrolopyrrole. Adapted from references 42, 42 and 45. Copyright the American Chemical Society, 2009, the Royal Society of Chemistry, 2004, and 2020.

Work by our lab incorporated  $\pi$ -conjugated organic semiconductors into short oligopeptide sequences by exploiting routine Fmoc-based solid phase peptide synthesis (SPPS) techniques whereby peptide sequences are assembled on solid supports and functionalized with the  $\pi$ -core through two synthetic strategies. In the first (Figure 1.4, left panel) the aromatic unit with di-carboxylic acid functionality is constructed by solution phase synthesis. The acids are then activated and used to cap the ends of two finished peptide segments on resin. In the second method (Figure 1.4, right panel) the N-terminus of the peptide is capped with  $\text{Ar}^1$  that presents a halogen for reaction with a suitable bi-functionalized coupling partner in Pd-catalyzed cross couplings.<sup>29,46–48</sup> In both cases, cleavage of the peptide from resin reveals two carboxy-termini and the general structure of the “triblock” peptide- $\pi$ -peptide monomers is exemplified in Figure 1.4.

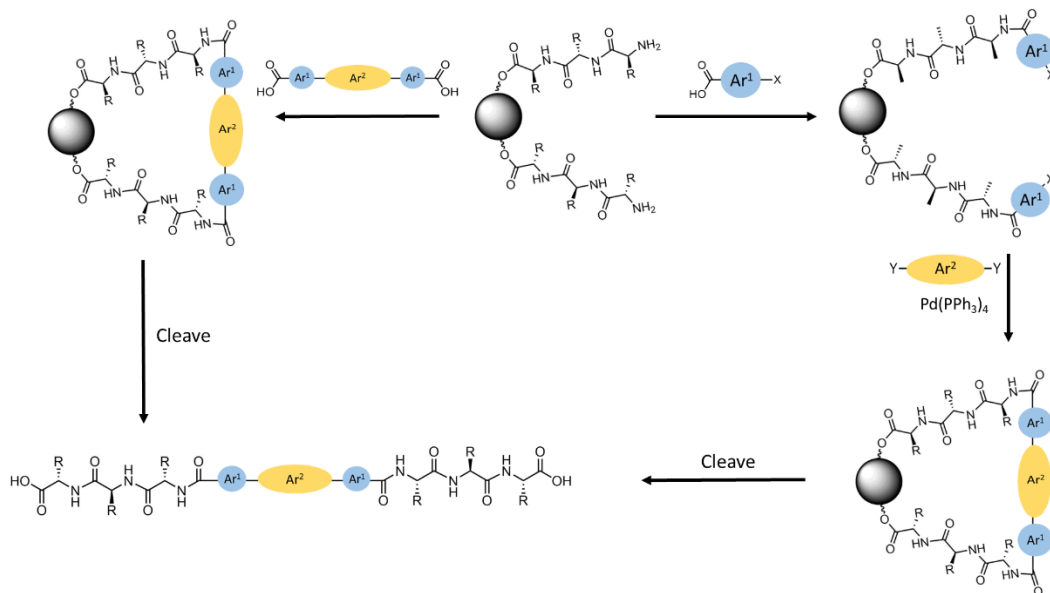


**Figure 1.4:** Synthetic strategy to form peptide- $\pi$ -peptide monomers with a diversity of cores on resin.

Our peptide- $\pi$ -peptide materials are generally designed as follows: acidic residues are deprotonated at high pH ( $\sim 10$ ) and considered molecularly dissolved due to repulsion between like charges that frustrates and disfavors assembly.<sup>49</sup> Lowering the pH or otherwise shielding negative charges triggers assembly into 1-dimensional nanostructures, guided largely by intermolecular hydrogen bonds (Figure 1.5A). The peptide assembly directs the stacking of the  $\pi$ -conjugated cores to form an electronic conduit within the nanostructures as idealized in Figure 1.5B. The photophysical characteristics of the system undergo distinct changes as monomers assemble into supramolecular structures. A hypsochromic-shift in absorption and quenched fluorescence emission intensity upon acidification signify “H-aggregation” or co-facial stacking of the embedded chromophores (Figure 1.5C).<sup>50</sup> Furthermore, the CD spectra exhibit Cotton effects in

the assembly, indicating excitonic coupling of the embedded chromophores in a chiral environment. Finally, nanomaterial morphologies can be characterized by transmission electron microscopy (TEM) and shown to form extended networks as well as discrete structures.<sup>47</sup>

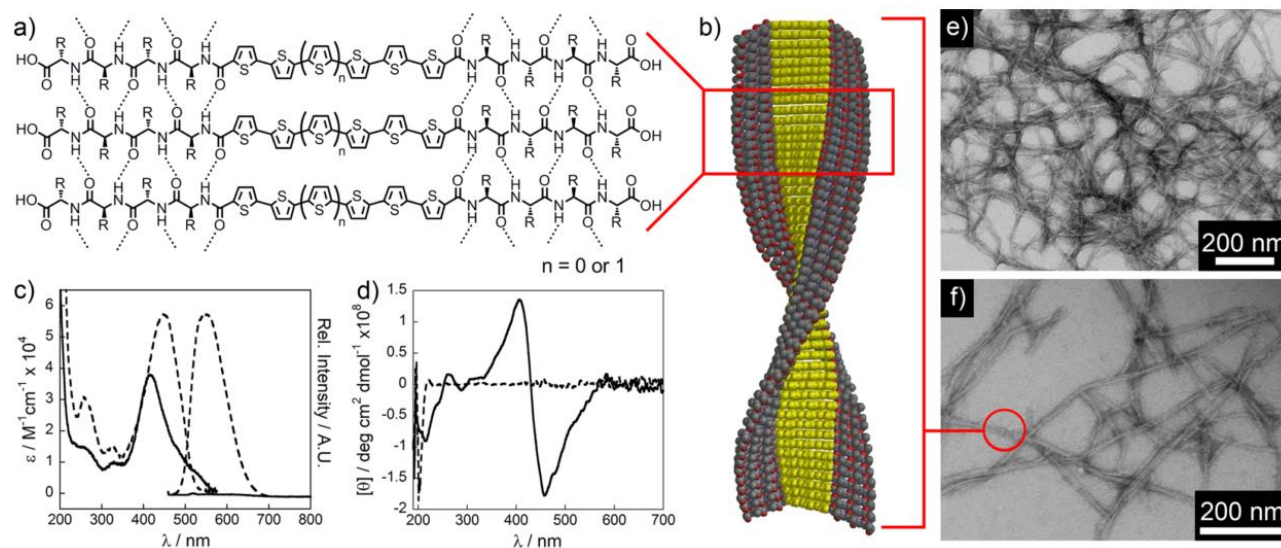


**Figure 1.5.** A) General molecular structure of the “triblock” peptide- $\pi$ -peptide monomers that self-assemble under acidic conditions into B) discrete nanostructures. Photophysical changes (C,D) occur upon assembly from molecular dissolved monomers at high pH to aggregates at low pH. Nanostructures can be observed as extended networks (E) and as discrete structures (F) using TEM imaging. Reprinted from reference 48. Copyright American Chemical Society, 2012.



## Control of Self-Assembly – Energy Landscapes

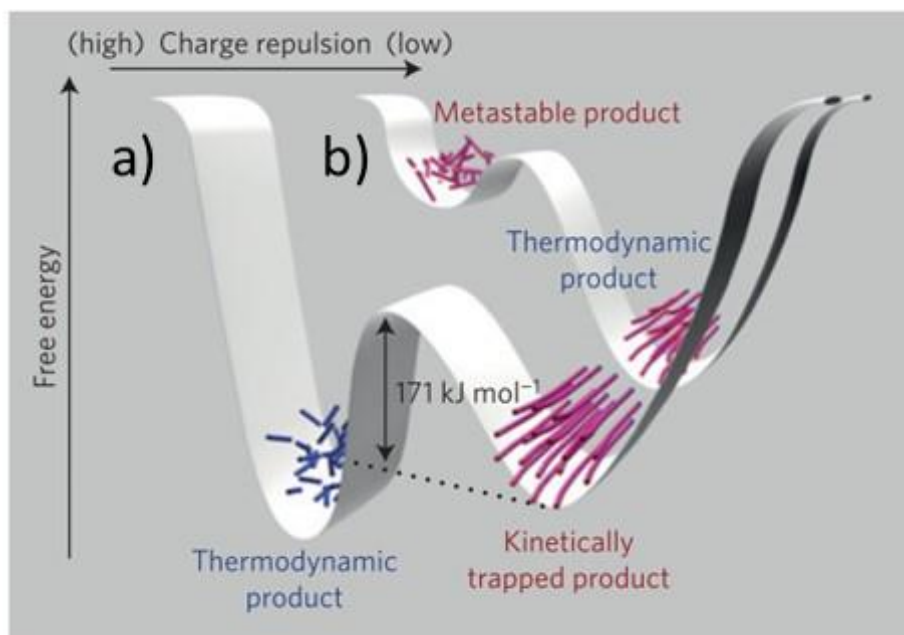


**Figure 1.6.** Two energy landscapes accessible to peptide amphiphiles that depend on assembly conditions at A) low ionic strength and B) high ionic strength. Adapted from reference 53.

Copyright Macmillan Publishers Limited, 2016.

Precise supramolecular construction requires careful navigation of the energy landscapes that dictate the assembly process. Kinetic and thermodynamic influences, while difficult to uncouple, can ultimately dictate order/disorder, co-assembly/self-segregation, and assembly/disassembly characteristics in an emerging polymer.<sup>51</sup> Access to different thermodynamic wells can produce materials with varied function and properties; however, prohibitively high kinetic barriers can trap assemblies in metastable potential wells that prevent structural reorganization to the targeted thermodynamic minimum.<sup>52,53</sup> Recent reports have examined how monomer design can be coupled with controlled assembly conditions to navigate

challenging energy surfaces. Stupp and coworkers demonstrated energy landscapes in peptide amphiphiles with the sequence V<sub>3</sub>A<sub>3</sub>K<sub>3</sub> N-terminally conjugated to 16-carbon aliphatic tails where  $\beta$ -sheet interactions among valine and alanine residues compete with electrostatic repulsion between consecutive lysine residues to respectively promote or frustrate assembly. Two energy surfaces are revealed at low and high ionic strength as illustrated in Figure 1.6. At low ionic strength, limited charge screening produces polydisperse and randomly coiled fibers. These fibers retain their random coil secondary structure after thermal annealing, demonstrating stabilization at a deep thermodynamic minimum on this surface (Figure 1.6A). The low ionic strength surface contains a second minimum corresponding to long, stable, monodisperse  $\beta$ -sheet fibers that can only be obtained by triggering their assembly under high ionic strength conditions, where they are thermodynamically favored (Figure 1.6B), followed by dilution to low ionic strength, thus directing the system between the two energy surfaces. Monomer design can illuminate competing attractive and repulsive interactions, while strategic application of assembly conditions can be used to navigate or link energy landscapes and arrive at desired thermodynamic minima. The field of supramolecular chemistry promises dynamic and stimuli responsive materials whose development will require a nuanced experimental and computational understanding in navigating energy surfaces.<sup>52</sup> We will discuss examples of modular changes in monomer design that, by changing the energy landscape (thermodynamic minima and kinetic barriers) result in varied material properties that emerge at points along these potentials and examine efforts to control either thermodynamically or kinetically the formation of mixed chromophore systems as well as offer a review of efforts from our group to guide the assembly of our peptide- $\pi$ -peptide conjugates.

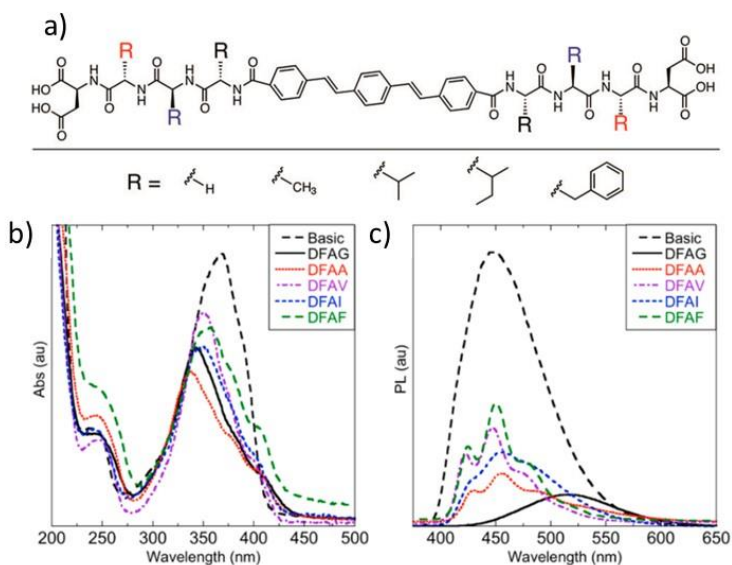


**Figure 1.7.** A) Variation in the identity of amino acid flanking  $\pi$ -conjugated core can greatly impact B) UV and C) photoluminescence spectra of triblock peptide nanomaterials. Adapted from reference 55. Copyright American Chemical Society, 2014.

Modest chemical diversity in monomer design can greatly impact nanostructure morphology and thus electronic behavior in  $\pi$ -conjugated peptide materials. Our lab examined small modifications to amino acid sequences in tri-block conjugated tetrapeptides flanking an oligophenylenevinylene (OPV3)  $\pi$ -conjugated core (Figure 1.7). Changes in photophysical properties were observed, most notably linked to the amino acid identity neighboring the conjugated core. The smallest residue (G) showed dramatic quenching and broadening in photoluminescence indicating excimer-like emission. More sterically demanding side chains (V, I, F) demonstrated structured emission spectra, typically observed upon H-like aggregation of OPV chromophores, indicating geometric differences within the assembly and thus different electronic couplings among the  $\pi$ -conjugated units.<sup>54</sup> Furthermore, the impact of amino acid chemistry was observed in changes to the mechanical properties of hydrogels formed from these peptides, where

amino acids with higher  $\beta$ -sheet forming propensities (V, I) correlated with more rigid hydrogel formation.<sup>55</sup> In another study, the directionality of intermolecular hydrogen bonds in OPV3 peptides were modulated by controlling the monomer symmetry. Preparation of symmetric monomers biased “parallel” (Figure 1.8A) whereas asymmetric monomers biased “anti-parallel”  $\beta$ -sheet motifs (Figure 1.8B) that accompanied a switch from excimeric to excitonic like emission.<sup>56</sup> These structure-function relationships will be critical in extending molecular design principles beyond the empirical methods for developing conjugated peptides with desired electronic, mechanical, and morphological properties.

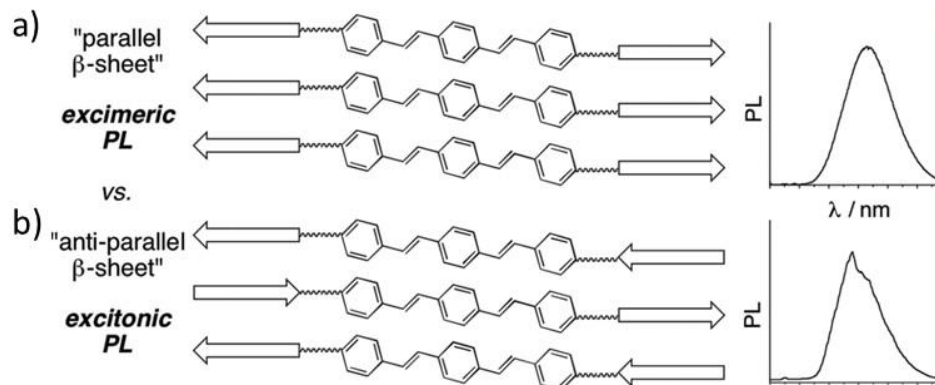


**Figure 1.8.** A) Symmetric peptide monomers form “parallel”  $\beta$ -sheets corresponding to excimeric emission while B) asymmetric peptides form “anti-parallel”  $\beta$ -sheets that result in excitonic emission. Adapted from Reference 57. Copyright American Chemical Society, 2014.

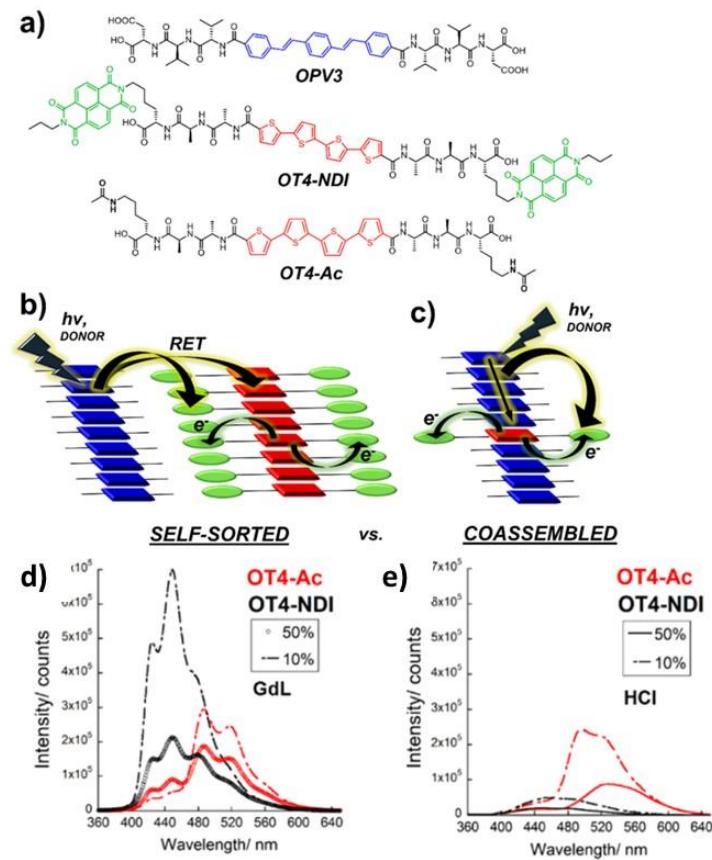


**Figure 1.9.** A) Incorporation of subtle pH trigger led to the formation of B) self-sorted or C) co-assembled nanostructures depending on the nature of assembly trigger. D) Emission profiles of GdL-triggered assemblies show evidence of self-sorting with residual electronic coupling and E) HCl-triggered assemblies demonstrated co-assembly, energy migration and charge separation. Adapted from reference 60. Copyright American Chemical Society, 2017.

The incorporation of a pH triggered assembly paradigm into triblock peptides (Figure 1.9) can facilitate co-assembly or self-segregation of peptides bearing distinct electronic functionalities. This has been demonstrated in triblock peptides wherein a C-terminal aspartic acid residue was incorporated into monomers containing the oligo(phenylenevinylene) (OPV3) core. Substitution at this C-terminal position with a lysine residue imidated with naphthalenediimide (NDI) in peptide

monomers containing a quaterthiophene (OT4) core lead to a difference in apparent pKa of 6.2 and 6.5 for OPV3 and OT4-NDI respectively (Figure 1.9A). Rapid acidification with HCl produced co-assemblies of OPV3 and OT4-NDI (Figure 1.9C) wherein excitation of OPV3 resulted in energy transfer to OT4 and then photoinduced electron transfer to NDI resulting in a quenched emission profile.<sup>57-59</sup> A gradual reduction in pH, through hydrolysis of glucono- $\delta$ -lactone, initiated the preferential assembly of OT4-NDI as the solution pH reached its respective pKa. The remaining molecularly dissolved OPV3 subsequently assembled as the pH further decreased yielding self-sorted structures as evidenced by NMR and XRD analysis (Figure 1.9B). However, despite indications of self-sorting with gradual acidification triggered peptide assembly, evidence of residual energy transfer in sorted peptides was observed, particularly with the OT4-Ac control peptide, showing emission spectra resembling that of OT4 upon excitation of the OPV3 core (Figure 1.9D,E). Insight into the true nature of these self-sorted structure, for example the formation of block co-polymers or intimately intertwined but separate heterostructures would be invaluable for their informed application, for example in p/n heterojunctions.<sup>59</sup>

## Fundamentals of Electron Microscopy

$$d = \frac{\lambda}{2 \cdot NA} = \frac{\lambda}{2n \sin \alpha} \quad (\text{Equation 1})$$

$$\lambda = \frac{h}{m \cdot v} \quad (\text{Equation 2})$$

An examination of the local character of the mixed assemblies described above would be invaluable for the further development of  $\pi$ -peptide conjugates, and we look to microscopy to examine these details. The impetus to many breakthroughs in microscopy is the demand to increase spatial resolution which can be defined as the shortest lateral distance between two objects where they remain observable as distinct entities.<sup>60</sup> In practice, resolution is limited by both lens aberrations, physical defects that prevent the lens from perfectly focusing, and the wave property of light that results in diffraction.<sup>60,61</sup> Diffraction is conceptualized in Figure 1.10a where light from an object enters a circular aperture of radius  $a$  in an opaque diaphragm and is viewed on a blank screen. In place of a single point on the screen, we observe a diffraction pattern that contains a central spot encircled by an oscillating and highly dampened Airy disk (Figure 1.10b). If light from a second object enters the aperture at angle  $\theta$ , the two are resolved when the global Airy maximum from object two overlaps the first minimum of object one as visualized in Figure 1.10c.<sup>60,62</sup> If the sources are closer in space they appear as a single object (Figure 1.10d).<sup>62</sup> Ernst Abbe first recognized this phenomena in the late 19<sup>th</sup> century where he characterized it as the “diffraction barrier” and formulated Equation 1, known as the Abbe criterion. In Equation 1,  $NA$  is the numerical aperture of the objective lens and  $n$  is the refractive index of the medium between the objective and the sample.<sup>61</sup> Assuming aberration correction, the minimum feature size that can be resolved with visible light is approximately 200 nm.<sup>60,61</sup> However, the wealth of knowledge that lies beyond this limit is extensive and the ability to exceed it is critical to understand the operation of systems at smaller size regimes.

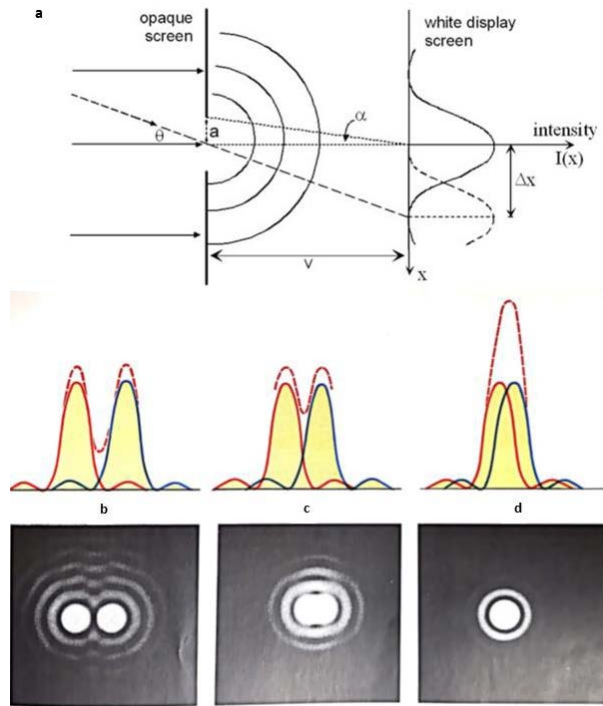


**Figure 1.10.** Light passing through an opaque screen with circular aperture (a) illuminates a display screen and creates a diffraction pattern (b) where two diffraction patterns are just resolved when the maximum of the first overlaps the first minimum of the second (c). If the two points are closer in space, they appear as a single object (d). Adapted from reference 61.

Copyright Springer International Publishing Switzerland, 2006. Adapted from reference 63.

Copyright Saunders College Publishing, 1995.

Spatial resolution can be increased by illumination with ultraviolet wavelengths, and techniques in super resolution such as stimulated emission depletion (STED) which require expensive optics and fluorescent tagging respectively.<sup>60,61,63,64</sup> An important advancement in microscopy and came with the development of the electron microscope in 1932 following theories posited by Louis DeBroglie that matter, with its particle-like behavior, might also behave wave-like as photons do.<sup>65</sup> The DeBroglie wavelength, Equation 2, dictates that particle wavelengths are



equal to the Planck constant ( $h$ ), divided by particle mass ( $m$ ) and velocity ( $v$ ).<sup>66</sup> Electrons can be generated and accelerated to low picometer wavelengths using thermionic, Schottky or field emission guns allowing for spatial resolution down to approximately 0.1 nm and a vast improvement with respect to optical microscopy.<sup>60</sup>

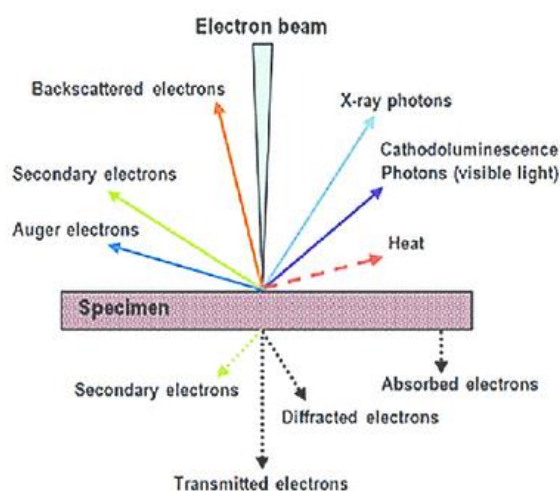


**Figure 1.11.** The interaction of an electron beam generates radiation and changes to electron path and/or energy. Reprinted from reference 69. Copyright InTech, 2016.

In transmission electron microscopy (TEM) transmitted electrons pass through thin samples where an image is formed in a manner like light microscopy -- areas where the sample absorbs, diffracts or scatters the incoming electron beam appear dark and form the image. The electrons that are not transmitted, collide with atoms in the specimen in an elastic or inelastic fashion generating radiation or distinct changes to electron path or energy as shown in Figure 1.11.<sup>67,68</sup> Secondary and backscattered electrons can be analyzed in thick specimens by focusing the electron beam to analyze in a raster scan pattern in what is called scanning electron microscopy (SEM). Similarly, this fine probe scanning technique can be used to detect transmitted or scattered electrons in scanning transmission electron microscopy (STEM). In 1970, using a high-angle

annular dark field (HAADF) detector, the STEM technique produced the first images of single atoms in a string of uranium and thorium deposited on a thin carbon substrate (Figure 1.12a).<sup>60,69</sup> Atoms and columns of atoms can now be routinely imaged using TEM and STEM operating modes as can be seen in Figure 1.12b and c where grain boundaries in the honey-comb hexagonal lattice of graphene are directly observed.<sup>70</sup>

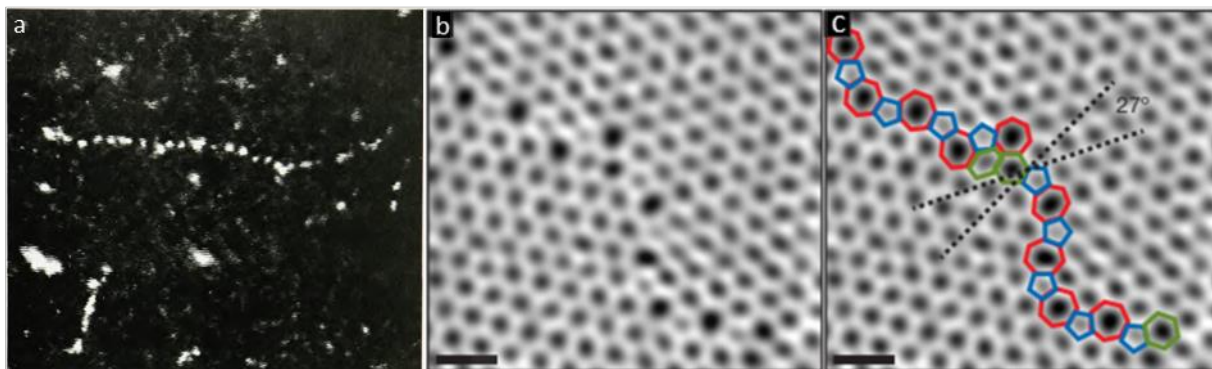


**Figure 1.12.** (a) String of thorium and uranium atoms visualized by STEM-HAADF and the first photo taken of a single atom. (b and c) The grains and grain boundaries can be discerned in a graphene sheet. Adapted from reference 70. Copyright Physics Today, 1970. Adapted from reference 71. Copyright Nature, 2011.

Electron beam-specimen interactions (Figure 1.13) provide an abundance of information in addition to image formation, for example, elemental composition, surface topography characterization and the nature of crystalline phases.<sup>71</sup> Two particularly important interactions are illustrated in Figure 1.13a. High energy electrons can penetrate beyond the valence shell and eject an inner K shell electron, ionizing the atom. This vacancy is filled through a cascade of electronic relaxations originating from an outer shell,  $L_{1-3}$ , accompanied by the emission of X-ray photons. The emitted X-rays have energies unique to the ionized element and can be detected in energy dispersive x-ray spectroscopy (EDS). The inner shell K vacancy can also be filled as shown in

Figure 1.13b by an electron from the  $L_1$  shell. The X-ray photon released can be re-absorbed by an outer  $L_{2,3}$  electron providing it energy to escape its nuclear orbit and be ejected from the sample and detected as an Auger electron. It is useful to note that while the detection of x-rays in TEM has been employed for years, in practice, Auger electron spectroscopy (AES) requires specialized instrumentation and is less commonly used for elemental analysis.<sup>72</sup> Elements with atomic mass ( $Z$ ) less than that of carbon, are more likely to produce Auger electrons than to emit X-rays and have low fluorescence yields ( $\omega$ ) as can be understood from Equation 3. These lighter elements as a result cannot be characterized by EDS.<sup>72,73</sup> However, when a K shell electron is ejected from an element, the beam electron loses energy and can be detected in what is called electron energy loss spectroscopy (EELS). The EELS signal is not limited by fluorescence yield and can be used as a complement to EDS even in lighter elements.<sup>72</sup> Furthermore, detailed structural and chemical bonding information can be extracted from EELS spectra, for example, information about bonding, valence state, nearest neighbor atomic structure and the existence and details for bandgap in a solid, among others.<sup>72,74</sup>

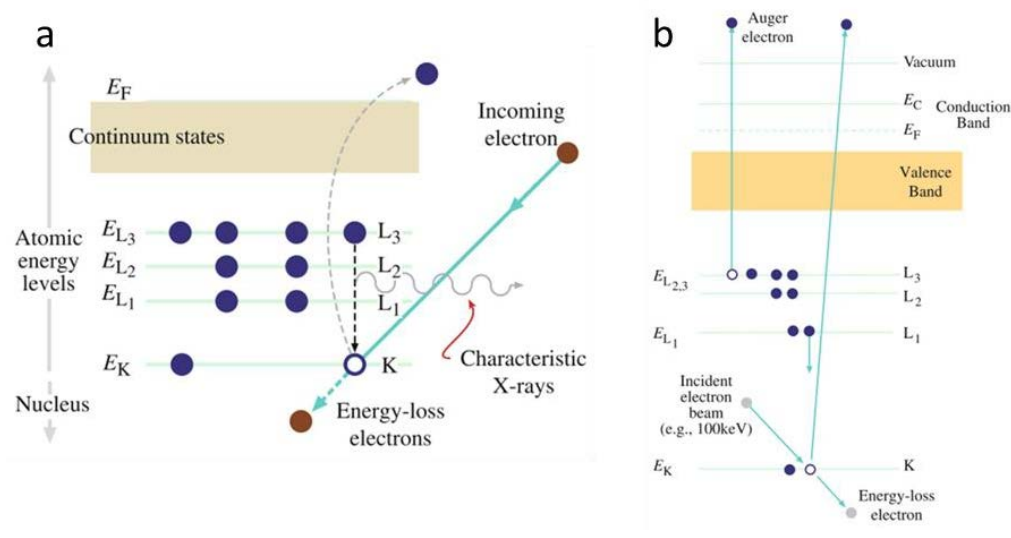


**Figure 1.13.** Electron-specimen interactions that occur to produce (a) EDS and EELS signals and (b) and Auger electrons. Reprinted from reference 73. Copyright Springer Science and Business Media, 2009.

$$\omega = \frac{Z^4}{a+Z^4} \quad (\text{Equation 3})$$

Nanotechnology refers to the manipulation of matter at the atomic and molecular level with dimensions in the range of 1-100 nm. This size regime is just beyond the resolution limits of light microscopies. Electron microscopy has become a pivotal characterization technique in the development of nanotechnologies and exploring the intimate characteristics of nanomaterials.<sup>75</sup> For example, Shelnutt and coworkers examined the formation of diphenylalanine nanotube-nanoparticle composites where a STEM-HAADF line scan demonstrated changes in density profile showing the platinum nanoparticles embedded within the walls of the peptide nanotubes (Figure 1.14a). Further EDS Spectra shows a clear and distinct platinum signal within the nanostructures (Figure 1.14b) and selected area diffraction shows diffraction rings consistent with the presence of platinum.<sup>76</sup> Several examples of peptide nanomaterials being used to template inorganic nanowires, or biomineralization, and even organic polymeric materials. Electron microscopy and elemental mapping were used to examine structure and phase separations where the presence of these inorganic components offer distinct signals for EELS or EDS detection.<sup>76-79</sup> However, the ability to visually map peptide nanomaterials and examine their assembly behavior would prove invaluable for future peptide nanomaterials design and control.

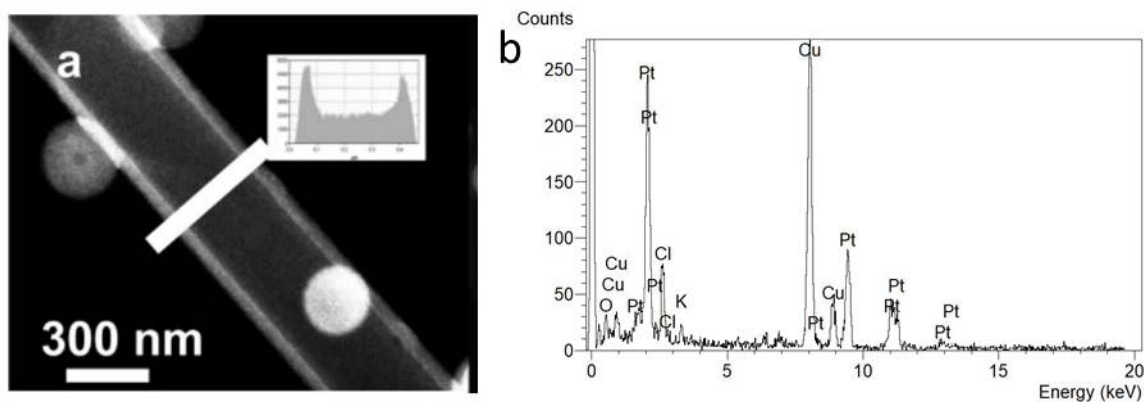


**Figure 1.14.** (a) STEM-HAADF image of Phenylalanine nanowire-platinum nanoparticle composites where HAADF line scan shows higher density in the walls of the nanowire where (b) EDS spectra show distinct presence of Pt signal. Adapted from reference 7. Copyright the Royal Society of Chemistry, 2004.

## Conclusion

Supramolecular chemistry offers emerging avenues for the control of organic semiconducting materials. A large body of research in this area has been devoted to the development of biologically relevant, conducting nanomaterials with capabilities of transmitting charge carriers in aqueous media. Our lab has developed peptide- $\pi$ -peptide architectures wherein the peptidic units reliably guide the assembly of the core into H-type aggregate assemblies. We have demonstrated that changes to peptide composition and presentation can dictate new energy landscapes wherein different minima reveal the subtleties of interchromophore electronic communication accessible. External parameters, such as assembly condition, govern how the energy landscapes are traversed and can be exploited to produce multicomponent assemblies. Within these important foundations is room to further expand the toolkit of molecular

modifications that achieve novel electronic and morphological outcomes. Furthermore, advancements in electron microscopy would be an invaluable tool to understand these materials on the nanoscale. With a more complete understanding of their structure on different hierarchical levels, coupled with their unique ability to bridge the electronic and biotic environments, these materials could be well suited to reach to a vast area of bioelectronics applications from tissue engineering to sensing.

## References

- (1) Brunetti, F. G.; Kumar, R.; Wudl, F. Organic Electronics from Perylene to Organic Photovoltaics: Painting a Brief History with a Broad Brush. *Journal of Materials Chemistry* **2010**, *20* (15), 2934–2948. <https://doi.org/10.1039/b921677d>.
- (2) MacDiarmid, A. G. “Synthetic Metals”: A Novel Role for Organic Polymers. In *Nobel Lecture*; 2000.
- (3) Kelley, T. W.; Baude, P. F.; Gerlach, C.; Ender, D. E.; Muyres, D.; Haase, M. A.; Vogel, D. E.; Theiss, S. D. Recent Progress in Organic Electronics: Materials, Devices, and Processes. *Chemistry of Materials* **2004**, *16* (23), 4413–4422. <https://doi.org/10.1021/cm049614j>.
- (4) Tsutsui, B. T.; Fujita, K. The Shift from “Hard” to “Soft” Electronics. *Advanced Materials* **2002**, No. 13, 949–952.
- (5) Hoebe, F. J. M.; Jonkhøj, P.; Meijer, E. W.; Schenning, A. P. H. J. About Supramolecular Assemblies of  $\pi$ -Conjugated Systems. *Chem. Rev.* **2005**, *105*, 1491–1546. <https://doi.org/10.1021/cr030070z>.
- (6) Koch, N. Organic Electronic Devices and Their Functional Interfaces. *ChemPhysChem* **2007**, *8* (10), 1438–1455. <https://doi.org/10.1002/cphc.200700177>.

- (7) Meier, H.; Stalmach, U.; Kolshorn, H. Effective Conjugation Length and UV/Vis Spectra of Oligomers. *Acta Polymerica* **1997**, *48* (9), 379–384.  
<https://doi.org/10.1002/actp.1997.010480905>.
- (8) Rissler, J. Effective Conjugation Length of  $\pi$ -Conjugated Systems. *Chemical Physics Letters* **2004**, *395* (1–3), 92–96. <https://doi.org/10.1016/j.cplett.2004.07.058>.
- (9) Hong, T. R.; Shin, J.; Um, H. A.; Lee, T. W.; Cho, M. J.; Kim, G. W.; Kwon, J. H.; Choi, D. H. New  $\pi$ -Extended Diketopyrrolopyrrole-Based Conjugated Molecules for Solution-Processed Solar Cells: Influence of Effective Conjugation Length on Power Conversion Efficiency. *Dyes and Pigments* **2014**, *108*, 7–14. <https://doi.org/10.1016/j.dyepig.2014.04.015>.
- (10) Aida, T.; Meijer, E. W.; Stupp, S. I. Functional Supramolecular Polymers. *Science* **2012**, *335*, 813–817.
- (11) Gazit, E. Bioinspired Chemistry: Diversity for Self-Assembly. *Nature Publishing Group* **2010**, *2*, 1010–1011. <https://doi.org/10.1038/nchem.912>.
- (12) Fischer, E. Emil Fischer: Einfluss Der Configuration Auf Die Wirkung Der Enzyme. *Berichte der Deutschen Chemischen Gesellschaft* **1894**, *27*, 2985–2993.
- (13) Lehn, J. -M. Supramolecular Chemistry—Scope and Perspectives Molecules, Supermolecules, and Molecular Devices (Nobel Lecture). *Angewandte Chemie International Edition in English* **1988**, *27*, 89–112. <https://doi.org/10.1002/anie.198800891>.
- (14) Izatt, R. M. Charles J. Pedersen's Legacy to Chemistry. *Chemical Society Reviews* **2017**, *46* (9), 2380–2384. <https://doi.org/10.1039/c7cs00128b>.
- (15) Pastor, A.; Martínez-Viviente, E. NMR Spectroscopy in Coordination Supramolecular Chemistry: A Unique and Powerful Methodology. *Coordination Chemistry Reviews* **2008**, *252*, 2314–2345. <https://doi.org/10.1016/j.ccr.2008.01.025>.

- (16) Tovar, J. D. Supramolecular Construction of Optoelectronic Biomaterials. *Accounts of Chemical Research* **2013**, *46* (7), 1527–1537. <https://doi.org/10.1021/ar3002969>.
- (17) Li, Y.; Liu, T.; Liu, H.; Tian, M. Z.; Li, Y. Self-Assembly of Intramolecular Charge-Transfer Compounds into Functional Molecular Systems. *Accounts of Chemical Research* **2014**, *47* (4), 1186–1198. <https://doi.org/10.1021/ar400264e>.
- (18) Gazit, E. Self-Assembled Peptide Nanostructures: The Design of Molecular Building Blocks and Their Technological Utilization. *Chemical Society Reviews* **2007**, *36* (8), 1263. <https://doi.org/10.1039/b605536m>.
- (19) Erbas-Cakmak, S.; Leigh, D. A.; McTernan, C. T.; Nussbaumer, A. L. Artificial Molecular Machines. *Angewandte Chemie - International Edition* **2000**, *115* (18), 10081–10206. <https://doi.org/10.1021/acs.chemrev.5b00146>.
- (20) Beijer, F. H.; Sijbesma, R. P.; Kooijman, H.; Spek, A. L.; Meijer, E. W. Strong Dimerization of Ureidopyrimidones via Quadruple Hydrogen Bonding. *Journal of the American Chemical Society* **1998**, *120* (27), 6761–6769. <https://doi.org/10.1021/ja974112a>.
- (21) Hoeben, F. J. M.; Herz, L. M.; Daniel, C.; Jonkheijm, P.; Schenning, A. P. H. J.; Silva, C.; Meskers, S. C. J.; Beljonne, D.; Phillips, R. T.; Friend, R. H.; Meijer, E. W. Efficient Energy Transfer in Mixed Columnar Stacks of Hydrogen-Bonded Oligo(p-Phenylene Vinylene)s in Solution. *Angewandte Chemie - International Edition* **2004**, *43* (15), 1976–1979. <https://doi.org/10.1002/anie.200353451>.
- (22) Schenning, A. P. H. J.; Jonkheijm, P.; Peeters, E.; Meijer, E. W. Hierarchical Order in Supramolecular Assemblies of Hydrogen-Bonded Oligo(p-Phenylene Vinylene)s. *Journal of the American Chemical Society* **2001**, *123*, 409–416. <https://doi.org/10.1021/ja0033180>.



- (23) Jonkheijm, P.; Hoebe, F. J. M.; Kleppinger, R.; van Herikhuyzen, J.; Schenning, A. P. H. J.; Meijer, E. W. Transfer of  $\pi$ -Conjugated Columnar Stacks from Solution to Surfaces. *Journal of the American Chemical Society* **2003**, *125* (51), 15941–15949.  
<https://doi.org/10.1021/ja0383118>.
- (24) Messmore, B. W.; Hulvat, J. F.; Sone, E. D.; Stupp, S. I. Synthesis, Self-Assembly, and Characterization of Supramolecular Polymers from Electroactive Dendron Rodcoil Molecules. *Journal of the American Chemical Society* **2004**, *126* (44), 14452–14458.  
<https://doi.org/10.1021/ja049325w>.
- (25) Tian, L.; Szilluweit, R.; Marty, R.; Bertschi, L.; Zerson, M.; Spitzner, E. C.; Magerle, R.; Frauenrath, H. Development of a Robust Supramolecular Method to Prepare Well-Defined Nanofibrils from Conjugated Molecules. *Chemical Science* **2012**, *3* (5), 1512–1521.  
<https://doi.org/10.1039/c2sc00977c>.
- (26) Jin, W.; Fukushima, T.; Niki, M.; Kosaka, A.; Ishii, N.; Aida, T. Self-Assembled Graphitic Nanotubes with One-Handed Helical Arrays of a Chiral Amphiphilic Molecular Graphene. *Proceedings of the National Academy of Sciences of the United States of America* **2005**, *102* (31), 10801–10806. <https://doi.org/10.1073/pnas.0500852102>.
- (27) Rieth, S.; Baddeley, C.; Badjić, J. D. Prospects in Controlling Morphology, Dynamics and Responsiveness of Supramolecular Polymers. *Soft Matter* **2007**, *3* (2), 137–154.  
<https://doi.org/10.1039/b615009h>.
- (28) Jain, A.; George, S. J. New Directions in Supramolecular Electronics. *Materials Today* **2015**, *18* (4), 206–214. <https://doi.org/10.1016/j.mattod.2015.01.015>.
- (29) Vadehra, G. S.; Wall, B. D.; Diegelmann, S. R.; Tovar, J. D. On-Resin Dimerization Incorporates a Diverse Array of  $p$ -Conjugated Functionality within Aqueous Self-Assembling

Peptide Backbonesw. *Chemical Communications* **2010**, 46, 3947–3949.

<https://doi.org/10.1039/c0cc00301h>.

- (30) Ardonna, H. A. M.; Tovar, J. D. Peptide  $\pi$ -Electron Conjugates: Organic Electronics for Biology? *Bioconjugate Chemistry* **2015**, 26, 2290–2302.

<https://doi.org/10.1021/acs.bioconjchem.5b00497>.

- (31) Zelzer, M.; Ulijn, R. v. Next-Generation Peptide Nanomaterials: Molecular Networks, Interfaces and Supramolecular Functionality. *Chem Soc Rev* **2010**, 39 (9), 3351–3357.

<https://doi.org/10.1039/c0cs00035c>.

- (32) González-Rodríguez, D.; Schenning, A. P. H. J. Hydrogen-Bonded Supramolecular  $\pi$ -Functional Materials. *Chemistry of Materials* **2011**, 23 (3), 310–325. <https://doi.org/10.1021/cm101817h>.

- (33) Aggeli, A.; Nyrkova, I. A.; Bell, M.; Harding, R.; Carrick, L.; McLeish, T. C. B.; Semenov, A. N.; Boden, N. Hierarchical Self-Assembly of Chiral Rod-like Molecules as a Model for Peptide Beta-Sheet Tapes, Ribbons, Fibrils and Fibers. *PNAS* **2001**, 99 (21), 11857–11862.

<https://doi.org/10.1021/acsami.7b09505>.

- (34) Jiang, H.; Stupp, S. I. Dip-Pen Patterning and Surface Assembly of Peptide Amphiphiles. *Langmuir* **2005**, 21 (12), 5242–5246. <https://doi.org/10.1021/la0501785>.

- (35) Pashuck, E. T.; Stupp, S. I. Direct Observation of Morphological Transformation from Twisted Ribbons into Helical Ribbons. *Journal of the American Chemical Society* **2010**, 132 (26), 8819–8821. <https://doi.org/10.1021/ja100613w>.

- (36) Sone, E. D.; Stupp, S. I. Semiconductor-Encapsulated Peptide-Amphiphile Nanofibers. *Journal of the American Chemical Society* **2004**, 126 (40), 12756–12757.

<https://doi.org/10.1021/ja0499344>.

- (37) Hsu, L.; Cvetanovich, G. L.; Stupp, S. I. Peptide Amphiphile Nanofibers with Conjugated Polydiacetylene Backbones in Their Core. *Journal of the American Chemical Society* **2008**, *130* (12), 3892–3899. <https://doi.org/10.1021/ja076553s>.
- (38) Jiang, H.; Guler, M. O.; Stupp, S. I. The Internal Structure of Self-Assembled Peptide Amphiphiles Nanofibers. *Soft Matter* **2007**, *3* (4), 454–462. <https://doi.org/10.1039/b614426h>.
- (39) Niece, K. L.; Hartgerink, J. D.; Donners, J. J. J. M.; Stupp, S. I. Self-Assembly Combining Two Bioactive Peptide-Amphiphile Molecules into Nanofibers by Electrostatic Attraction. *Journal of the American Chemical Society* **2003**, *125* (24), 7146–7147. <https://doi.org/10.1021/ja028215r>.
- (40) Hartgerink, J. D.; Beniash, E.; Stupp, S. I. Self-Assembly and Mineralization of Peptide-Amphiphile Nanofibers. *Science (New York, N.Y.)* **2001**, *294*, 1684–1688. <https://doi.org/10.1126/science.1063187>.
- (41) Shao, H.; Nguyen, T.; Romano, N. C.; Modarelli, D. A.; Parquette, J. R. Self-Assembly of 1-D n-Type Nanostructures Based on Naphthalene Diimide-Appended Dipeptides. *Journal of the American Chemical Society* **2009**, *131* (45), 16374–16376. <https://doi.org/10.1021/ja906377q>.
- (42) Peter, B. Synthesis of a Silk-Inspired Peptide–Oligothiophene Conjugate†. *Org. Biol. Chem.* **2004**, *2*, 3541–3544.
- (43) Kumar, R. J.; MacDonald, J. M.; Singh, T. B.; Waddington, L. J.; Holmes, A. B. Hierarchical Self-Assembly of Semiconductor Functionalized Peptide  $\alpha$ -Helices and Optoelectronic Properties. *Journal of the American Chemical Society* **2011**, *133* (22), 8564–8573. <https://doi.org/10.1021/ja110858k>.
- (44) Kas, O. Y.; Charati, M. B.; Rothberg, L. J.; Galvin, M. E.; Kiick, K. L. Regulation of Electronic Behavior via Confinement of PPV-Based Oligomers on Peptide Scaffolds. *Journal of Materials Chemistry* **2008**, *18* (32), 3847–3854. <https://doi.org/10.1039/b800860d>.

- (45) Rani, A.; Kavianinia, I.; Hume, P.; de Leon-Rodriguez, L. M.; Kihara, S.; Williams, D. E.; McGillivray, D. J.; Plank, N. O. V.; Gerrard, J.; Hodgkiss, J. M.; Brimble, M. A. Directed Self-Assembly of Peptide-Diketopyrrolopyrrole Conjugates-a Platform for Bio-Organic Thin Film Preparation. *Soft Matter* **2020**, *16* (28), 6563–6571. <https://doi.org/10.1039/d0sm01071e>.
- (46) Diegelmann, S. R.; Hartman, N.; Markovic, N.; Tovar, J. D. Synthesis and Alignment of Discrete Polydiacetylene-Peptide Nanostructures. *J. Am. Chem. Soc.* **2012**, *134*, 2028–2031. <https://doi.org/10.1021/ja211539j>.
- (47) Sanders, A. M.; Dawidczyk, T. J.; Katz, H. E.; Tovar, J. D. Peptide-Based Supramolecular Semiconductor Nanomaterials via Pd- Catalyzed Solid-Phase. *ACS Macro Letters* **2012**, *1*, 1326–1329. <https://doi.org/10.1021/mz3004665>.
- (48) Sanders, A. M.; Tovar, J. D. Solid-Phase Pd-Catalysed Cross-Coupling Methods for the Construction of p-Conjugated Peptide Nanomaterials. *Supramolecular chemistry* **2014**, *26*, 259–266. <https://doi.org/10.1080/10610278.2013.852675>.
- (49) Tovar, J. D.; Diegelmann, S. R.; Peart, P. A. Non-Traditional Aromatic Topologies and Biomimetic Assembly Motifs as Components of Functional Pi-Conjugated Oligomers. *Materials* **2010**, *3* (2), 1269–1280. <https://doi.org/10.3390/ma3021269>.
- (50) Kasha, M.; Rawls, H. R.; Ashraf El-Bayoumi, M. The Exciton Model in Molecular Spectroscopy. *Pure Appl. Chem* **1965**, *11*, 371–392.
- (51) Panettieri, S.; Ulijn, R. V. Energy Landscaping in Supramolecular Materials. *Current Opinion in Structural Biology* **2018**, *51* (February), 9–18. <https://doi.org/10.1016/j.sbi.2018.02.001>.
- (52) Tantakitti, F.; Boekhoven, J.; Wang, X.; Kazantsev, R. v; Yu, T.; Li, J.; Zhuang, E.; Zandi, R.; Ortony, J. H.; Newcomb, C. J.; Palmer, L. C.; Shekhawat, G. S.; Olvera, M.; Cruz, D.; Schatz, G.

- C.; Stupp, S. I. Energy Landscapes and Functions of Supramolecular Systems. *Nature materials* **2016**, *15*, 469–477. <https://doi.org/10.1038/NMAT4538>.
- (53) Korevaar, P. A.; George, S. J.; Markvoort, A. J.; Smulders, M. M. J.; Hilbers, P. A. J.; Schenning, A. P. H. J.; De Greef, T. F. A.; Meijer, E. W. Pathway Complexity in Supramolecular Polymerization. *Nature* **2012**, *481* (7382), 492–496. <https://doi.org/10.1038/nature10720>.
- (54) Wall, B. D.; Zacca, A. E.; Sanders, A. M.; Wilson, W. L.; Ferguson, A. L.; Tovar, J. D.; Seitz, F. Supramolecular Polymorphism: Tunable Electronic Interactions within  $\Pi$ -Conjugated Peptide Nanostructures Dictated by Primary Amino Acid Sequence. <https://doi.org/10.1021/la500222y>.
- (55) Ardoña, H. A. M.; Besar, K.; Togninalli, M.; Katz, H. E.; Tovar, J. D. Sequence-Dependent Mechanical, Photophysical and Electrical Properties of  $\Pi$ -Conjugated Peptide Hydrogelators. *J. Mater. Chem. C* **2015**, *3* (3), 6505–6514. <https://doi.org/10.1039/c5tc00100e>.
- (56) Wall, B. D.; Zhou, Y.; Mei, S.; Herdeline, J.; Ardoña, H. A. M.; Ferguson, A. L.; Tovar, J. D. Variation of Formal Hydrogen-Bonding Networks within Electronically Delocalized  $\Pi$ -Conjugated Oligopeptide Nanostructures. *Langmuir* **2014**, *30*, 11375–11385. <https://doi.org/10.1021/la501999g>.
- (57) Sanders, A. M.; Magnanelli, T. J.; Bragg, A. E.; Tovar, J. D. Photoinduced Electron Transfer within Supramolecular Donor-Acceptor Peptide Nanostructures under Aqueous Conditions. *Journal of the American Chemical Society* **2016**, *138* (10), 3362–3370. <https://doi.org/10.1021/jacs.5b12001>.
- (58) Ardoña, H. A. M.; Tovar, J. D. Energy Transfer within Responsive  $\Pi$ -Conjugated Coassembled Peptide-Based Nanostructures in Aqueous Environments. *Chem. Sci.* **2015**, *6* (2), 1474–1484. <https://doi.org/10.1039/C4SC03122A>.

- (59) Ardon, H. A. M.; Draper, E. R.; Citossi, F.; Wallace, M.; Serpell, L. C.; Adams, D. J.; Tovar, J. D. Kinetically Controlled Coassembly of Multichromophoric Peptide Hydrogelators and the Impacts on Energy Transport. *Journal of the American Chemical Society* **2017**, *139* (25), 8685–8692. <https://doi.org/10.1021/jacs.7b04006>.
- (60) Egerton, R. F. *Physical Principles of Electron Microscopy*, 2nd ed.; Springer, 2006. <https://doi.org/10.1007/b136495>.
- (61) Hell, S. W. Nanoscopy with Focused Light (Nobel Lecture). *Nobel Lecture* **2014**. <https://doi.org/10.1002/anie.201504181>.
- (62) Kirkpatrick, L. D.; Wheeler, G. F. *Physics: A World View*, 2nd ed.; Saunders College Publ: Philadelphia, 1995.
- (63) Marx, V. Is Super-Resolution Microscopy Right for You? *Nature Methods* **2013**, *10* (12), 1157–1163. <https://doi.org/10.1038/nmeth.2756>.
- (64) Ross, R. J. *Microelectronics Failure Analysis: Desk Reference*, 6th ed.; ASM International: Materials Park, OH, 2011.
- (65) Max Knoll und Ernst Ruska. Das Elektronenmikroskop. *Deutsche Medizinische Wochenschrift* **1932**, *87* (5–6), 318–339. <https://doi.org/10.1007/BF01342199>.
- (66) McQuarrie, D. A. *Quantum Chemistry*, 2nd ed.; University Science Books: Sausalito, CA, 2008.
- (67) Reimer, L.; Kohl, H. *Transmission Electron Microscopy: Physics of Image Formation*, 5th ed.; Springer, 2008.
- (68) Hilal, A. A. Microstructure of Concrete. *High Performance Concrete Technology and Applications* **2016**, 3–24. <https://doi.org/10.5772/64574>.
- (69) Lubkin, G. B. Photo of Single Atoms by Electron Microscope. *Physics Today*. 1970, pp 41–42. <https://doi.org/10.1063/1.3022283>.

- (70) Huang, P. Y.; Ruiz-Vargas, C. S.; van der Zande, A. M.; Whitney, W. S.; Levendorf, M. P.; Kevek, J. W.; Garg, S.; Alden, J. S.; Hustedt, C. J.; Zhu, Y.; Park, J.; McEuen, P. L.; Muller, D. A. Grains and Grain Boundaries in Single-Layer Graphene Atomic Patchwork Quilts. *Nature* **2011**, *469* (7330), 389–392. <https://doi.org/10.1038/nature09718>.
- (71) Mendis, B. G. *Electron Beam-Specimen Interactions and Simulation Methods in Microscopy*; 2018. <https://doi.org/10.1002/9781118696545>.
- (72) Williams, D. B.; Carter, C. B. *Transmission Electron Microscopy: A Textbook for Materials Science*; 2009; Vol. 1914. [https://doi.org/10.1007/978-1-4939-8997-3\\_32](https://doi.org/10.1007/978-1-4939-8997-3_32).
- (73) Kikongi, P.; Salvas, J.; Gosselin, R. Curve-Fitting Regression: Improving Light Element Quantification with XRF. *X-Ray Spectrometry* **2017**, *46* (5), 347–355. <https://doi.org/10.1002/xrs.2760>.
- (74) Kimoto, K.; Asaka, T.; Nagai, T.; Saito, M.; Matsui, Y.; Ishizuka, K. Element-Selective Imaging of Atomic Columns in a Crystal Using STEM and EELS. *Nature* **2007**, *450* (7170), 702–704. <https://doi.org/10.1038/nature06352>.
- (75) *Springer Handbook of Nanotechnology*; Bhushan, B., Ed.; Springer-Verlag: GmbH, 2017.
- (76) Song, Y.; Challa, S. R.; Medforth, C. J.; Qiu, Y.; Watt, R. K.; Miller, J. E.; Swol, V.; Shelnutt, J. A.; Lafayette, W.; March, A. Synthesis of Peptide-Nanotube Platinum-Nanoparticle Composites †. **2004**, 1044–1045.
- (77) Janairo, J. I. B.; Sakaguchi, T.; Hara, K.; Fukuoka, A.; Sakaguchi, K. Effects of Biom mineralization Peptide Topology on the Structure and Catalytic Activity of Pd Nanomaterials. *Chemical Communications* **2014**, *50* (66), 9259–9262. <https://doi.org/10.1039/c4cc04350b>.

- (78) Min, K. I.; Kim, D. H.; Lee, H. J.; Lin, L.; Kim, D. P. Direct Synthesis of a Covalently Self-Assembled Peptide Nanogel from a Tyrosine-Rich Peptide Monomer and Its Biomineralized Hybrids. *Angewandte Chemie - International Edition* **2018**, 57 (20), 5630–5634.  
<https://doi.org/10.1002/anie.201713261>.
- (79) Tovar, J. D.; Rabatic, B. M.; Stupp, S. I. Conducting Polymers Confined within Bioactive Peptide Amphiphile Nanostructures. *Small* **2007**, 3 (12), 2024–2028.  
<https://doi.org/10.1002/sml.200600645>.



## **Chapter 2**

# **Constitutional Isomerism to Dictate Morphology and Electronic Communication in $\pi$ -Conjugated Peptides**

## Introduction

Achieving spatial control of  $\pi$ -electron overlap in organic electronic materials over multiple length scales is a challenge that has frustrated the continued development of organic optoelectronic applications involving light harvesting, light emission and field transmission.<sup>1-4</sup> The bottom-up nature of self-assembly and supramolecular chemistry has emerged to meet this challenge using the additive contributions of weak, non-covalent enthalpic interactions (hydrogen bonding,  $\pi$ - $\pi$  stacking, van der Waals forces etc.) coupled with entropic solvation considerations. These design elements guide the assembly of  $\pi$ -conjugated subunits into complex hierarchical structures and in turn foster specific intermolecular electronic interactions.<sup>2,5</sup> A large body of this research has been influenced by the powerful preorganization exemplified in natural systems where, for example, precise tertiary protein structures construct three-dimensional enzymatic active sites and establish substrate recognition and specificity.<sup>6,7</sup> For example, proteins and oligopeptides have been used to scaffold the assembly of extended  $\pi$ -conjugated units into well-defined geometries that generate interesting electronic materials capable of interfacing the classically disparate environments of nanoelectronics and biological systems.<sup>8-17</sup>

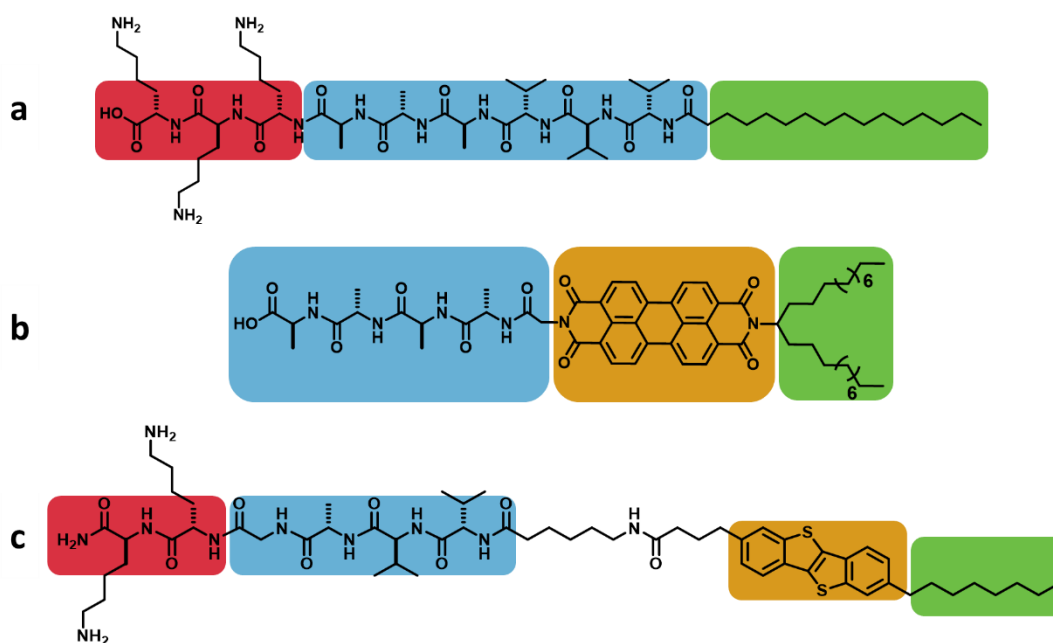


**Figure 2.1:** Structure of previously studied systems including (a) synthetic peptide amphiphile with charged,  $\beta$ -sheet forming, head group appended to a lipophilic tail, (b) perylene diimide substituted with a beta-sheet forming peptide and a branched alkyl tail and (c) a peptide linked to a benzothienobenzothiophene unit with an alkyl tail. The charged hydrophilic (red), hydrophobic  $\beta$ -sheet forming peptide (blue),  $\pi$ -conjugated (yellow), and alkyl tail (green) segments are highlighted on each system.

Lipopeptides are prevalent in natural systems wherein the hydrophobic components of lipids are joined covalently to solubilizing peptides. Synthetic variants such as peptide amphiphiles were first described by Tirrell and co-workers as a series of collagen derived alpha-helical peptides bearing two N-alkyl tails whose length could switch the morphological outcome to form triple helical bundles, monolayers as well as spheroidal and cylindrical micellar structures.<sup>18–21</sup> Stupp and co-workers prepared amphiphiles with an oligo-peptide head group containing residues that promote  $\beta$ -sheet secondary structure and a cone-shaped molecular design that produced cylindrical micelles with very high aspect ratios (Figure 2.1a).<sup>22,23</sup> Stupp's peptide amphiphile platform has

since been extensively studied for a range of applications including regenerative medicine and as a template for inorganic nanostructures.<sup>24</sup> These “bottom-up” peptide assemblies are advantaged in the modular nature of peptide synthesis wherein chemistry of the head group and morphological outcome is intimately dictated by amino acid composition.<sup>25</sup>

Work from several groups examined the covalent addition of  $\pi$ -conjugated oligomers to peptide assemblies wherein the  $\pi$ -system not only introduces quadrupolar interactions, but also an element of hydrophobic character distinct from alkyl chains and peptide segments. Nowick and co-workers prepared synthetic “amino acids” from 4'-amino-(1,1'-biphenyl)-4-carboxylic acid to construct rigid rod-like oligomers that were compatible with solid-phase peptide synthesis and could be readily appended with peptide segments (Figure 2.2a).<sup>26,27</sup> Extensive studies of diphenylalanine and a number of other dipeptides, capped with aromatic groups such as naphthalene, N-(fluorenyl-9-methoxycarbonyl) (Fmoc), or pyrene, reveal the formation of a variety of fibers, tapes and belts where  $\pi$ -stacking,  $\beta$ -sheet formation, molecular shape and extent of charge repulsion dictate supramolecular morphologies and the resulting physical properties (Figure 2.2b).<sup>28–34</sup> Stupp and co-workers examined the effect of amino acid side chain volume, hydrophobicity and  $\beta$ -branching in a terthiophene di-peptide conjugate wherein substitution from glycine to valine, isoleucine and leucine produced flat spicules, spiral sheets, nanotubes and giant flat sheets, respectively (Figure 2.2c).<sup>35</sup> More recently, Tovar and co-workers found that variation in the amino acid composition of two tetrapeptide units flanking an oligo(p-phenylenevinylene) directed a switch from excitonic-like to excimeric-like emission based on the steric and hydrophobic demand of the amino acid side chain.<sup>36</sup>

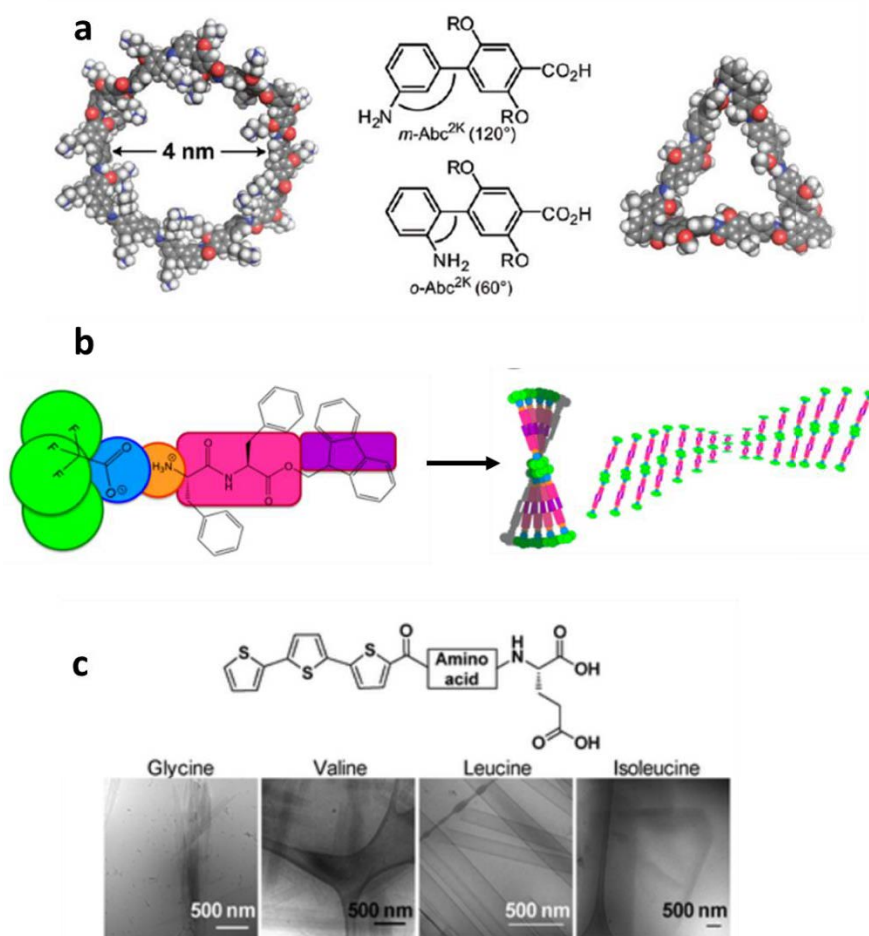


**Figure 2.2.** The construction of peptide- $\pi$  conjugates can be achieved through the (a) synthesis of aromatic "amino acids" to produce macrocycles or by conjugation to dipeptides (b,c) to achieve fibrils, spicules and nanotubes among other nanomorphologies. Adapted from references 27, 30, and 35. Copyright the American Chemical Society 2009 and 2018 and the Royal Society of Chemistry, 2012.

The addition of purely hydrophobic character in the form of *n*-alkyl tails to peptide  $\pi$ -conjugates has been examined by several groups. Schenning and Meijer demonstrated the synthesis of a  $\beta$ -sheet promoting peptide joined on both sides to a tri-alkyl substituted oligo(*p*-phenylenevinylene) wherein geometric organization of the  $\pi$ -conjugated segments is dictated by

the amino acid composition of the peptide.<sup>37</sup> Guo and co-workers reported the assembly of amphiphilic naphthalene diimides into helical nanofibers in organic solvent via direct attachment of a hydrogen bonding peptide on one side and an alkyl tail on the other (Figure 2.1b).<sup>38</sup> Guler and co-workers reported the aqueous assembly of benzothienobenzothiophene into uniform cylindrical nanofibers through conjugation on one side, via a short alkyl spacer, to a  $\beta$ -sheet forming peptide segment with a charged dilysine terminus and to a short hydrophobic tail on the other (Figure 2.1c).<sup>39</sup>

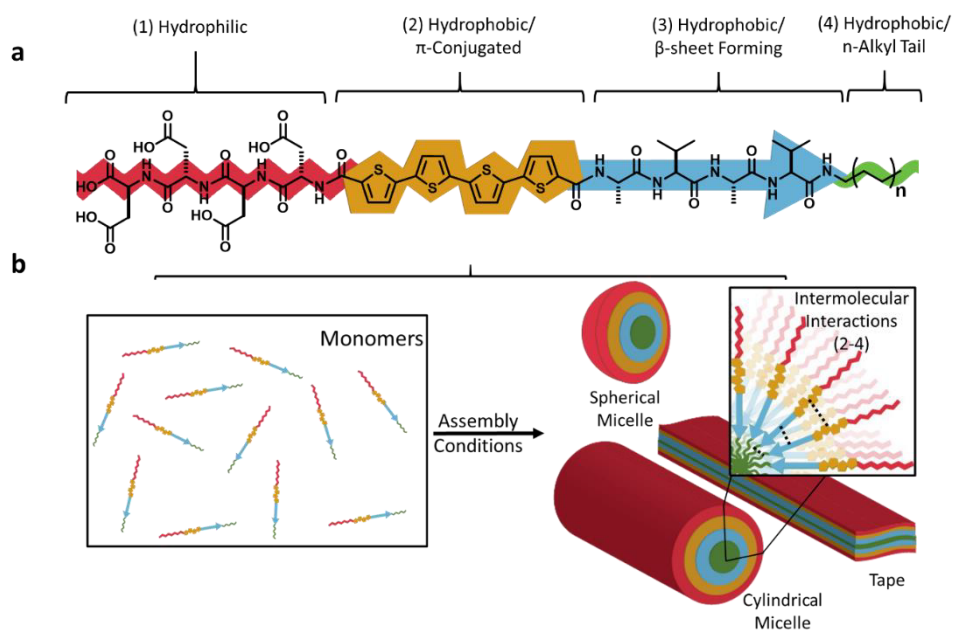


**Figure 2.3.** The  $\pi$ -conjugated peptide library presented in this work (a) that encompasses a range of intermolecular interactions to (b) guide assembly from monomers to a range of nanoarchitectures.

Previous work from our lab and others explored the self-assembly of a wide variety of  $\pi$ -conjugated oligomers flanked by different peptide units whose amino acid side chain composition dictates the nature of the interchromophore  $\pi$ -overlap.<sup>40–42</sup> In this work, we present a versatile on-resin synthetic procedure to prepare  $\pi$ -conjugated oligomers with differential presentation of

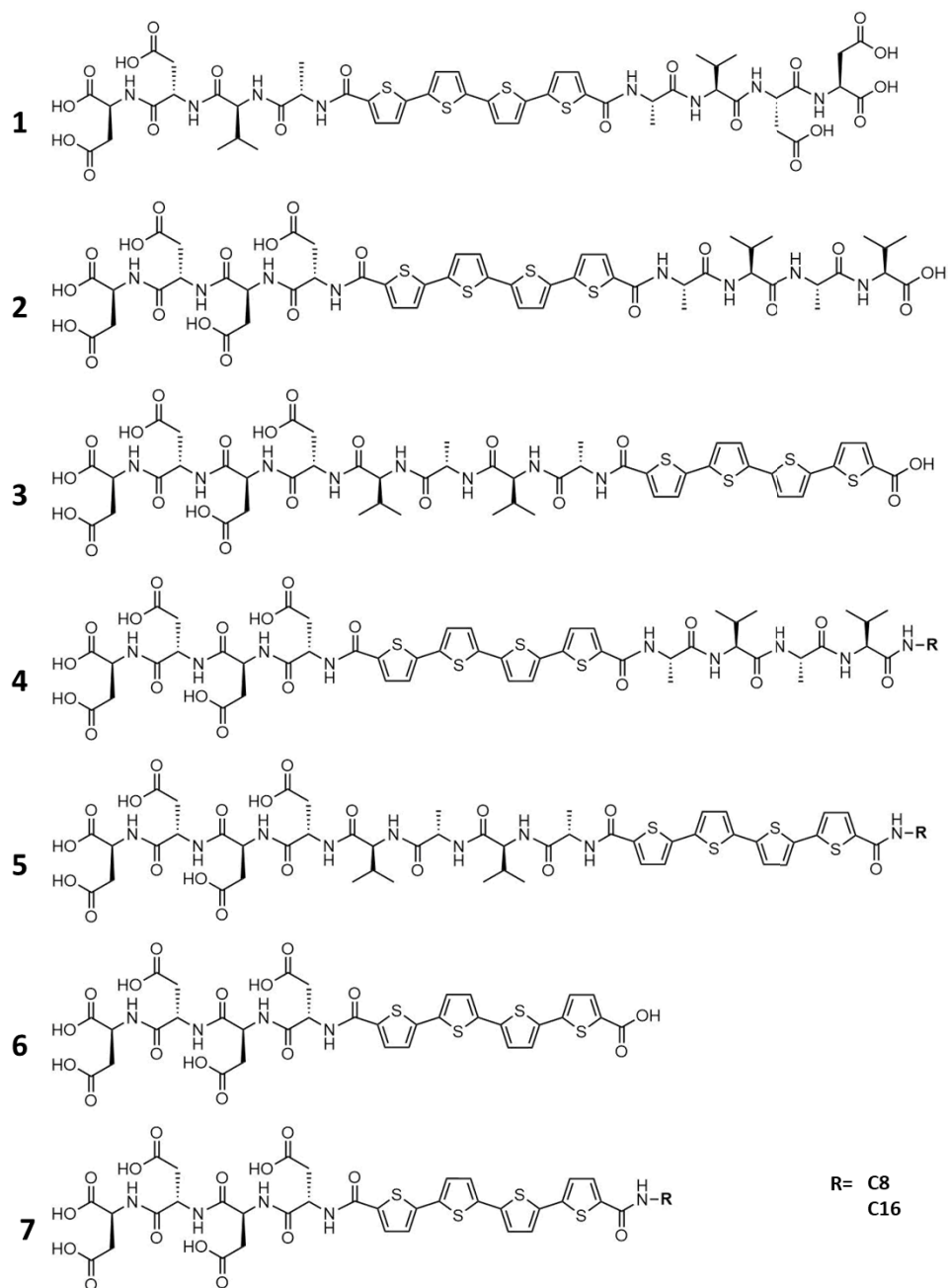
peptide blocks on either side of the  $\pi$ -conjugated core. We start with peptide- $\pi$ -core tri-block molecules and then extend to the more classical peptide amphiphile structure bearing n-alkylated carbon chains. Four distinct structural regimes within this library promote specific intermolecular interactions that dictate nanostructure processing and assembly: (1) an ionizable peptide sequence that encourages water solubility, (2) a relatively hydrophobic  $\beta$ -sheet promoter sequence that engages in hydrogen bonding, (3) a  $\pi$ -conjugated core that introduces  $\pi$ -stacking (e.g. quadrupolar influences) and (4) a hydrophobic alkyl chain that undergoes hydrophobic collapse predominately due to van der Waals forces (Figure 2.3, A2.21).<sup>43</sup> We examine how the diversity and positions of these different hydrophobic blocks govern the self-assembly process and permit access to new nanostructure morphologies. The stark differences in physical properties and related consequences for supramolecular morphologies exhibited by constitutional isomers of oligopeptide sequences in peptide amphiphiles is well documented.<sup>44,45</sup> In the present case, constitutional isomerism is achieved by swapping different regimes of hydrophobic character. These alterations impact the hierarchical assembly, the morphology, and the subsequent electronic communication between the embedded  $\pi$ -conjugated cores.

## Results and Discussion:

**Peptide Design and Synthesis.** *Design.* Considering the triblock peptide architectures previously reported from our lab that displayed symmetric amino acid sequences flanking a  $\pi$ -conjugated core, we prepared **1** based on the widely studied, hole-transporting semiconductor, quaterthiophene (OT4). Peptide **2** presents the same global amino acid composition as **1**, however, the hydrophilic aspartic acids and the hydrophobic  $\beta$ -sheet forming valine and alanine residues are

sequestered on opposite sides of the OT4 core. Peptide **3** is another constitutional isomer wherein the  $\beta$ -sheet forming peptide and the OT4 positions are exchanged with respect to the acidic C-terminus. We envisioned that variation in the presentation of these distinct hydrophobic regimes along the length of the peptide would bias new morphologies and interchromophore electronic communications through a subtle interplay of intermolecular interactions. We also sought to explore these effects in peptides **4** and **5** with the addition of a third hydrophobic segment and the impact of increasing hydrophobic demand in a series of saturated 8 and 16-carbon tails. The nature of our synthetic procedure to prepare peptides **2-5**, as detailed in the next section, produced **6**, **7-C8**, and **7-C16** as side products. In these three peptides we examined the absence of  $\beta$ -sheet promoters on assembly of the  $\pi$ -conjugated core and the morphological and photophysical changes that accompany the addition of a saturated hydrophobic tail to a  $\pi$ -conjugated peptide.





*Synthesis.* This peptide library was prepared employing standard Fmoc-based solid phase peptide synthesis (SPPS) techniques. Peptide **1** was prepared according to our prior on-resin dimerization approach, whereby the Asp-Asp-Val-Ala tetrapeptide was expressed on resin and was used to doubly acylate a core [2,2':5',2'':5'',2''':5''':quaterthiophene]-5,5'''-dicarboxylic acid. The hydrophobic  $\beta$ -sheet forming Val-Ala-Val-Ala tetrapeptide found in peptides **2-5** was synthesized using

standard SPPS, Fmoc deprotected and cleaved from the resin to be used for additional couplings. The hydrophilic Asp-Asp-Asp-Asp tetrapeptide segment found in peptides **2-5** was also synthesized on resin, and the terminal Fmoc group was removed. This resin was capped with [2,2':5',2'':5'',2'''-quaterthiophene]-5,5'''-dicarboxylic acid in the synthesis of peptides **2** and **4** leaving a terminal carboxylic acid functionality which was activated on resin with a solution of benzotriazol-1-yl-oxytripyrrolidinophosphonium hexafluorophosphate (PyBOP) and N,N-diisopropylethylamine (DIPEA). This activated resin was washed with coupling solvent, and then a solution of the hydrophobic Val-Ala-Val-Ala tetrapeptide was added (Figure A2.1). At this point, the peptide was cleaved from the resin to provide peptide **2** while the resin bound material was again activated as described above prior to treatment with the needed alkyl amine leading to peptide **4** after cleavage. This synthesis was modified to prepare peptides **3** and **5** wherein the hydrophilic Asp-Asp-Asp-Asp tetrapeptide segment was prepared on resin and Fmoc deprotected. The Fmoc-protected, hydrophobic Val-Ala-Val-Ala tetrapeptide segment was coupled to the hydrophilic segment, then Fmoc deprotected and capped with [2,2':5',2'':5'',2'''-quaterthiophene]-5,5'''-dicarboxylic acid. This resin bound material was cleaved leading to peptide **3** while the resin bound material was again activated as described above prior to treatment with the needed alkyl amine leading to peptide **5** after cleavage. Attempts to build the amphiphilic octapeptide on one resin resulted in low synthesis yields.

**Morphological Characterization of the Peptide Assemblies.** All peptides were designed with four repeating aspartic acid residues to promote solubility at high pH as a result of ionization, where acidification and screening of these charges ultimately triggered nanostructure assembly. Given the range of hydrophobic character in these peptides, particularly those with n-alkyl tails, we explored different assembly conditions to optimize dissolution and access representative

nanostructure morphologies. A rapid acidification procedure often led to random aggregates, as visualized by transmission electron microscopy (TEM) (Figure A2.2).

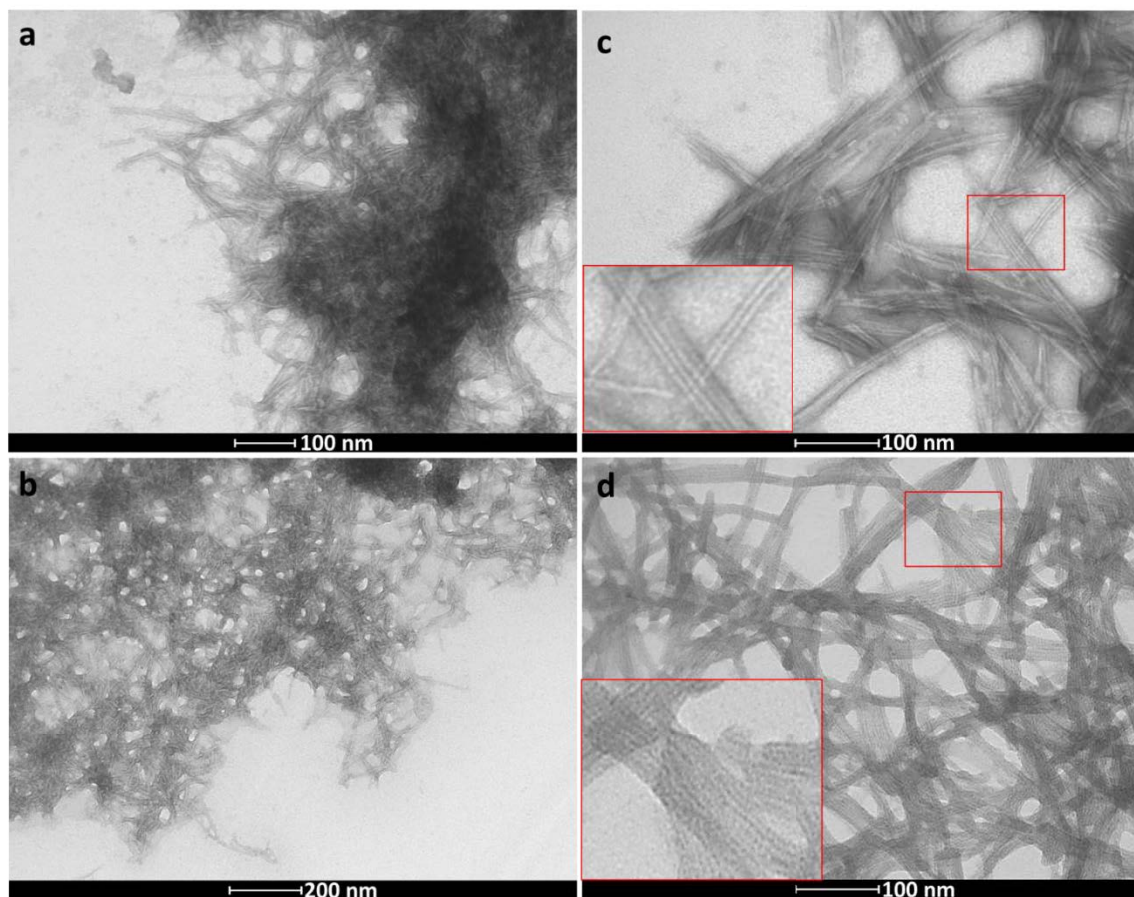


**Figure 2.4.** Representative transmission electron micrographs of **2** (a,c) and **3** (b,d) assembled from basic media (a,b) and neutral media (c,d).

Rapid assembly via acidification of basic solutions of peptides **1**, **2**, and **3** led to nanostructures with widths of  $4.1 \pm 0.8$  nm,  $5.4 \pm 0.8$  nm and  $6.6 \pm 0.3$  nm respectively. Given the 2.9 nm extended molecular length of these peptides, the rapid basic-to-acidic assemblies display varying degrees of lateral association between peptide fibrils. Peptide **1** formed nanostructures with lengths on the order of hundreds of nanometers, like other symmetric peptides previously reported (Figure A2.3a).<sup>12</sup> Peptide **2** formed nanostructures with lengths on the order of hundreds of nanometers

(Figure 2.4a), while the swapped hydrophobe **3** presented a mixture of random aggregates and tightly bundled structures (Figure 2.4b) with lengths significantly shorter than both analogues **1** and **2** (Figure 2.4b).<sup>46,47</sup> This suggests that the balance of enthalpic gains relative to entropic losses among peptides within the assemblies varies with hydrophobe placement. Although peptides **2** and **3** were soluble at high pH, the range of hydrophobic character in this library presented challenging aqueous solubility, thereby prompting an exploration of a variety of dissolution and assembly conditions that were applied to these more soluble peptides. Peptides **2** and **3**, when assembled from neutral media, yielded bundled tape-like structures where peptide **3** displayed what appear as more uniform and well-defined nanostructures (Figure 2.4c,d) than **2**. Higher magnification images show striations coincident with the long axis of the tapes revealing internal order with periodicities of  $3.2 \pm 0.4$  nm and  $3.0 \pm 0.5$  nm in **2** and **3** respectively, comparable to the extended molecular length of these peptides. The order of hydrophobic presentation in these constitutional isomers impacts the mode of packing and dictates lateral interactions. This is apparent through the dispersity observed in **2**, which forms tapes composed of two to six strands, where **3** uniformly forms tapes of around four repeating strands. The differences in morphological outcome based on the dissolution conditions suggest pre-association at neutral pH that is lost upon complete dissolution of the peptide in basic media. The constitutional isomerism between **1**, **2**, and **3** clearly influences molecular packing geometries and dictates lateral interaction and nanostructure length, an effect that is even more pronounced in more organized neutral-to-acidic assemblies.

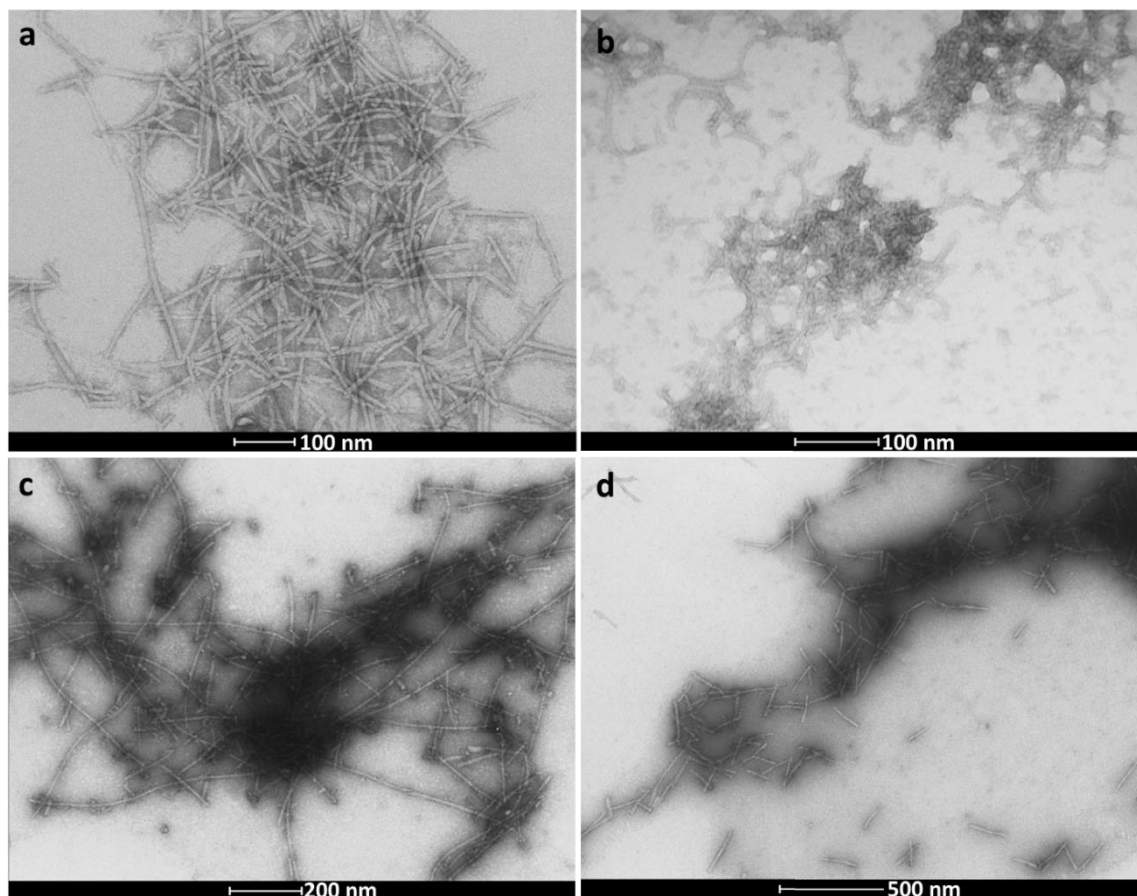


**Figure 2.5.** Representative transmission electron micrograph of **4-C8** (a,c) and **5-C8** (b,d) following rapid acidification and incubation at room temperature for 30 min (a,c) and after sonication, thermal annealing and equilibration for 16 hours at pH 7 (b,d).

We then examined the influence of the addition of a third hydrophobe block on the nanostructure morphological outcomes. The rapid acidification of basic solutions of n-alkyl terminated **4-C8** and **5-C8** resulted uniformly in random aggregates (Figure A2.2). The **4-C8** peptide formed well defined nanostructures only after incubation at room temperature for at least 30 minutes following rapid acidification (Figure 2.5a), suggesting the relaxation of a metastable aggregate to a thermodynamic minimum. The structures measured  $8.3 \pm 0.9$  nm in diameter, approximately double the extended molecular length of approximately 3.5 nm, suggesting an

elongated micellar or cylindrical construction consistent with other alkyl-based peptide amphiphiles. When the hydrophobic peptide segments are swapped in **5-C8**, the nanostructures formed after at least 30 minutes of incubation at room temperature are shorter structures in a dense mat with widths of  $7.2 \pm 1.7$  nm (Figure 2.5b). Several groups established conditions for processing peptide amphiphiles with 16+-carbon tails including incubation at 80°C to effect complete dissolution followed by equilibration at room temperature over an extended period at neutral pH.<sup>44,48–50</sup> After 16 hours under these conditions and at room temperature, the **4-C8** peptide formed elongated nanostructures with widths of  $7.7 \pm 1.8$  nm and lengths of hundreds of nanometers (Figure 2.5c). The swapped peptide- $\pi$  hydrophobe **5-C8** formed rods with widths of  $11.8 \pm 1.1$  nm that were markedly shorter and more uniform in length (Figure 2.5d). As with peptides **1**, **2**, and **3**, the position of the hydrophobic peptide and  $\pi$ -conjugated segments with respect to the charged terminus dictate characteristics of the resulting nanostructure, in these cases, limiting nanofiber length and augmenting the degree of lateral bundling. Furthermore, this effect does not seem to be impacted by a purely hydrophobic terminal alkyl tail.

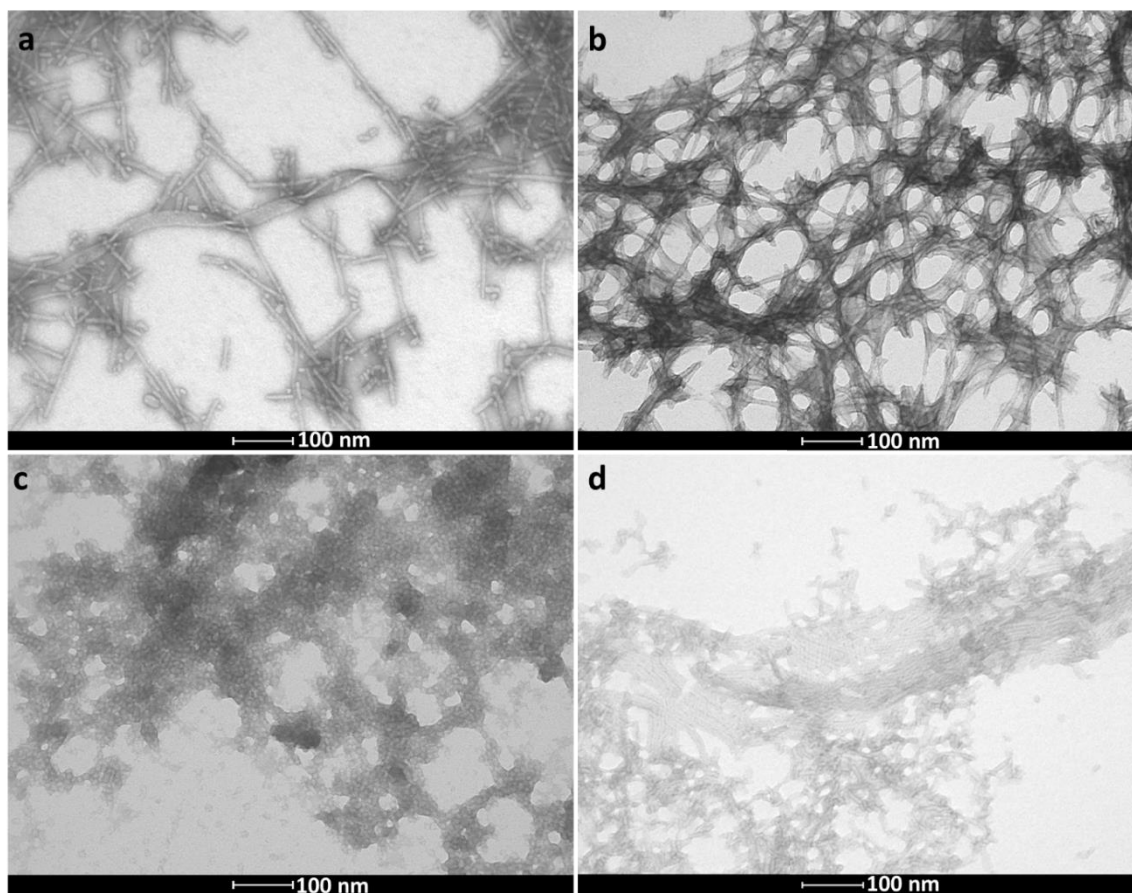


**Figure 2.6.** Transmission electron micrograph of **4-C16** dissolved at pH 8.6 and equilibrated at room temperature for (a) 16 hours (b) 2 weeks. **5-C16** dissolved at (a) pH 7.0 and (b) pH 8.6 and equilibrated at room temperature for 16 hours.

We also examined the influence of increasing hydrophobic demand of a terminal n-alkyl tail by doubling its length. Initial TEM imaging of peptides **4-C16** and **5-C16** under rapid acidification assembly also showed random aggregates (Figure A2.2). Given this additional hydrophobic demand imparted by the extended 16-carbon alkyl tail, these peptides were subjected to sonication for 3 minutes, thermal annealing for 5 minutes at 80°C and equilibration at room temperature for 16 hours under several high pH conditions. In an aqueous 0.05 M glycine-NaOH buffered solution (pH 8.6), **4-C16** formed mixed populations of nanostructures that resemble small spherical

particles, short rod-like fibers with widths of  $7.9\pm1.6$  and nanoribbon-like bundles (Figure 2.6a). Previous studies of similar molecules indicate that equilibration to populations comprised only of ribbons and belts occurs over time.<sup>44,49</sup> Examination of these **4-C16** assemblies after two weeks showed equilibration to networks of highly bundled nanofibers with widths of  $7.7\pm0.5$  nm after two weeks (Figure 2.6b, A2.22). At this pH, **4-C16** may become kinetically trapped in this range of nanoarchitectures where thermal equilibration over an extended period results in relaxation to a more favorable fibrous structure that minimizes electrostatic repulsion among head groups. **4-C16** was also examined in a 0.09 M phosphate-citrate buffer (pH 7.0) and consistently formed short nanorods and spherical particles (Figure A2.4a) suggesting that an intermediate pH, between 7.0 and 8.6, might balance enthalpic intermolecular interactions with charge density, and therefore allow for the persistence of nanoribbons. The **5-C16** showed further diminished aqueous solubility and required sonication and extended 24 hour thermal annealing at 80°C to produce spherical particles of  $9.1\pm1.1$  nm diameters at pH 7.0 and a mixture of elongated nanostructures with  $6.1\pm0.9$  nm widths that were highly aligned in some areas (Figure 2.6 c,d) at pH 8.6. These morphological outcomes were not significantly changed after a two-week incubation at room temperature (Figure A2.4b,c, A2.22). The constitutional isomerism in these peptides may dictate contrasting energy landscapes wherein the **4-C16** landscape contains a shallow barrier that allows equilibration at room temperature to a thermodynamic minimum. However, the **5-C16** peptide required extensive thermal annealing to form any well-defined nanostructures. These constructs persisted over extended periods, suggesting a landscape composed of high thermal barriers between thermodynamic minima.



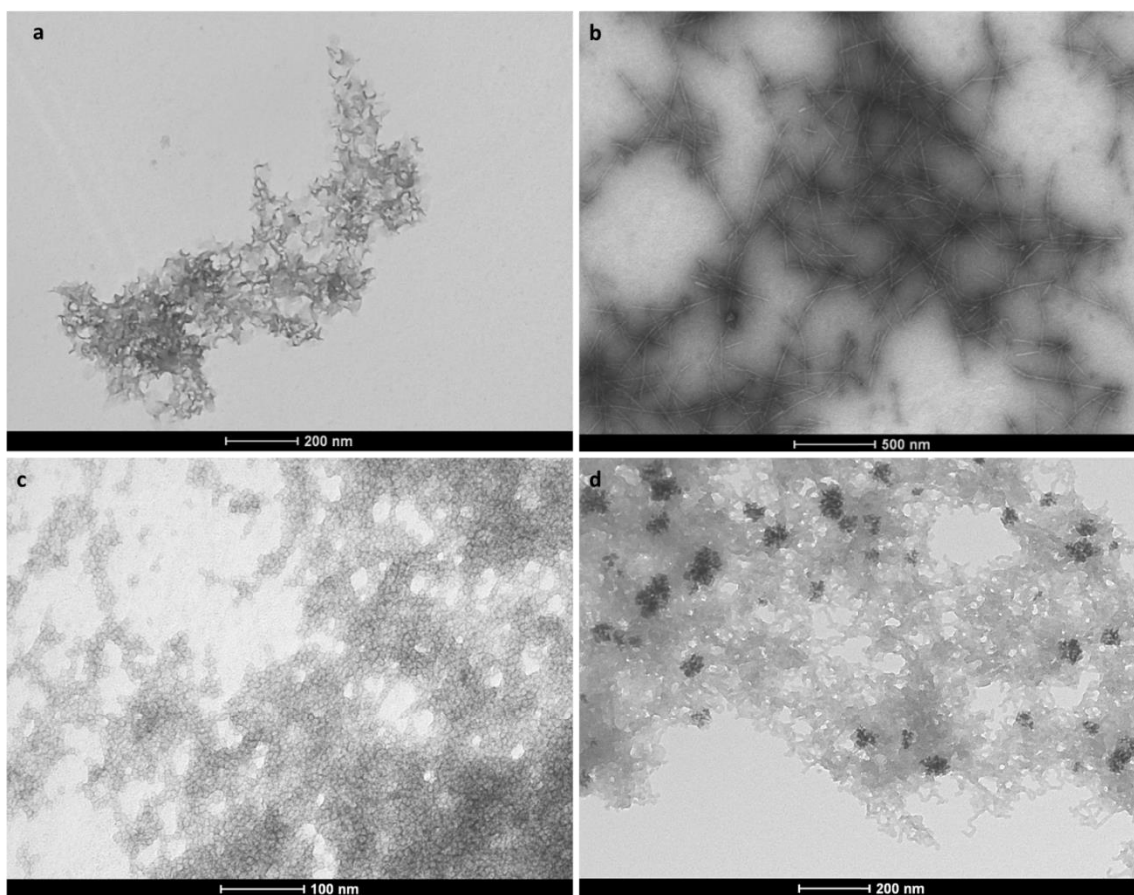


**Figure 2.7:** Representative transmission electron micrographs of (a) **6** (b) **7-C8** and (c) **7-C16** at pH 9 and (d) **7-C16** at pH 1.

TEM examination of peptide **6** consistently showed curled sheet-like morphologies (Figure 2.7a). The addition of an alkyl tail in **7-C8** under basic-to-acidic triggered assembly resulted in random aggregates (Figure A2.2). Dissolution at pH 7 following sonication, annealing, and equilibration at room temperature for 16 hours, as previously described, resulted in fibers with widths of  $12.7 \pm 1.5$  nm and lengths of hundreds of nanometers (Figure 2.7b). At pH 9, **7-C16** formed sole populations of spherical structures with diameters of  $14.4 \pm 1.3$  nm (Figure 2.7c). When the pH of this solution is lowered, elongated, worm-like micelles are observed (Figure 2.7d). Nguyen and coworkers previously explored the kinetics of peptide amphiphile assembly through

molecular dynamics computational methods indicating that upon dissolution in aqueous media, hydrophobic alkyl tails quickly drive micelle formation at high pH where the spherical particles maximize charge separation.<sup>51</sup> When this charge repulsion is minimized at low pH conditions, the spherical particles merge forming nanofibers as observed in the **7-C16** peptide.

**Photophysical Characterization of the Peptide Assemblies:** Previous work from our lab detailed the photophysical consequences that accompany supramolecular assembly of these types of peptides. Upon assembly, the  $\pi$ -conjugated cores are guided into proximity where interaction of the transition dipoles on neighboring molecules brings about distinct photophysical changes with respect to the dissolved monomers. Typically, a hypsochromic-shift in absorption as well as a quenched photoluminescence signature are observed upon acidification and are hallmarks of H-type aggregation, signifying co-facial stacking and near-parallel alignment of transition dipoles in the exciton-coupled  $\pi$ -conjugated system.<sup>52</sup> Circular dichroism spectra also show the evolution of bisignate Cotton effects upon assembly, which further indicate exciton coupling in a twisted chiral environment. In this light, we documented the photophysical character of the present peptide library in order to examine how the presentation of hydrophobic units impacted the local  $\pi$ -core interactions within the observed nanomaterials.

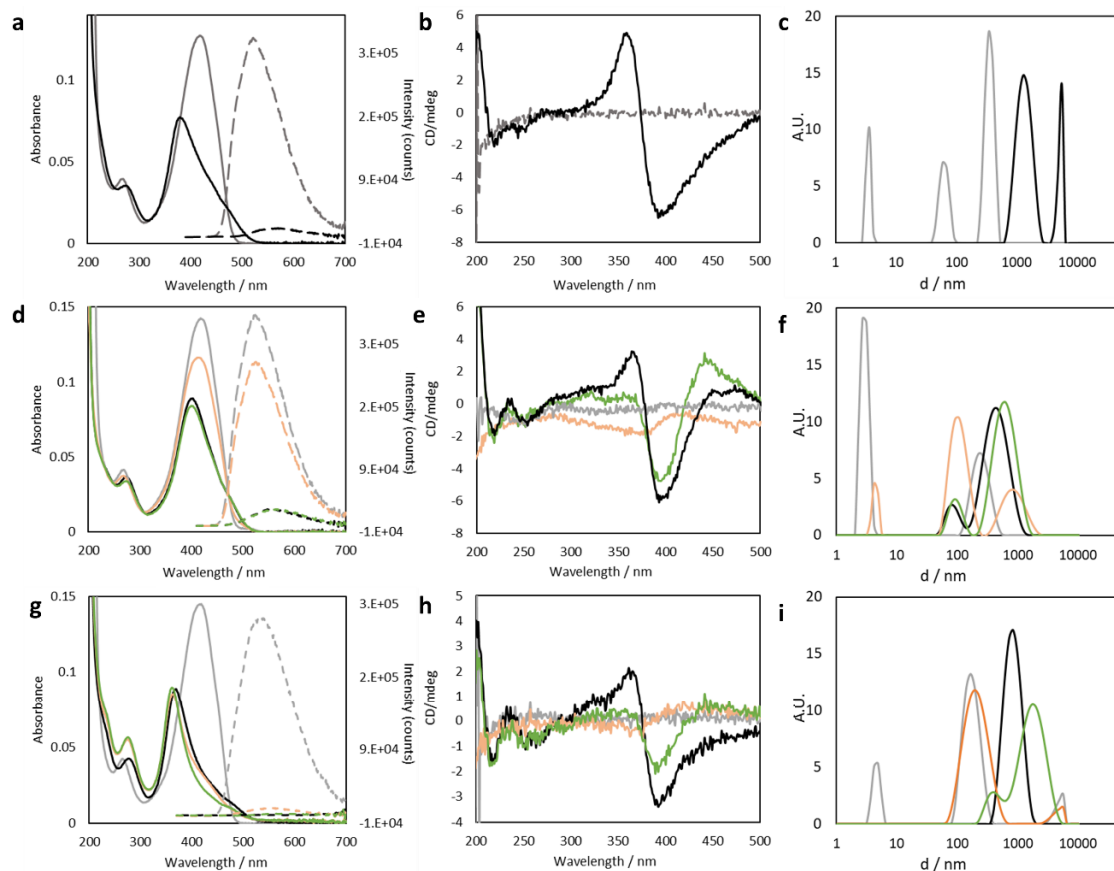


**Figure 2.8.** UV-Vis (left panels, solid lines) and photoluminescence (left panels, dashed lines), CD (middle panels), and DLS (right panels) spectra for **1** (a,b,c), **2** (d,e,f) and **3** (g,h,i) in basic (grey traces) and neutral (orange traces) media and in basic-to-acidic (black traces) and neutral-to-acidic (green) assemblies.

Unless otherwise noted, the peptides in this library exhibited an absorbance maximum of around 420 nm under high pH, molecularly dissolved conditions. Upon assembly by rapid pH decrease, peptides **1**, **2**, and **3** experienced 40, 20 and 50 nm blue-shifts in absorbance  $\lambda_{\text{max}}$  respectively, quenched photoluminescence and strong Cotton effects upon assembly (Figure 2.8, black traces). When dissolved in neutral aqueous media, peptide **2** showed UV-Vis and PL spectral profiles matching those in basic pH solution but a weak bisignate CD feature suggesting a slight

degree of pre-association in the neutral sample (Figure 2.8 d,e, orange traces). Absorbance and photoluminescence traces of neutral-to-acidic assemblies of **2** mirror those of the basic-to-acidic aggregates (Figure 2.8d, green traces). These assemblies show an inverted CD signal with a red-shifted crossover point, possibly due to changes in chromophore geometry that impose local chiral order and dominate the CD signals. (Figure 2.8e, green traces). At neutral pH, Peptide **3** showed a significantly more attenuated absorbance (further blue shifted to 358 nm) and a quenched emission trace that is even further diminished upon acidification (Figure 2.8g). Cotton effects for **3** are negligible at neutral pH or in neutral-to-acidic assemblies indicating that, while intermolecular electronic interactions are present at neutral pH, at low pH they lack any global chiral bias (Figure 2.8h).

Dynamic light scattering experiments (DLS) of **1**, **2**, and **3** show an increase in particle size upon rapid acidification and assembly from basic media (Figure 2.8 c,f,i). Neutral solutions of peptides **2** and **3** consisted of a majority of particles with hydrodynamic volume greater than 100 nm, confirming the presence of pre-assemblies in these solutions that increase in size upon rapid acidification assembly. The hydrophobic peptide localization in this constitutionally isomeric series clearly impacts physical properties (solubility etc.) and assembly conditions that allow access to different nanostructure morphologies and photophysical properties of the assemblies.

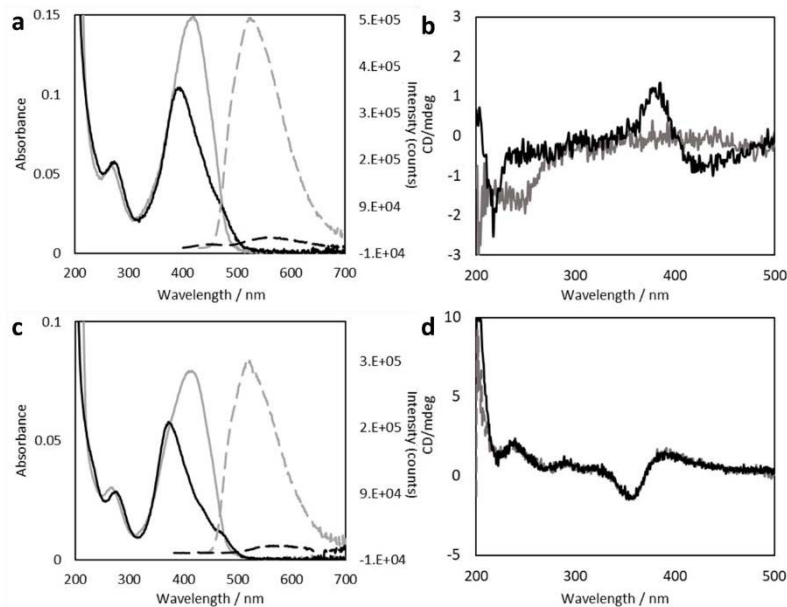


**Figure 2.9.** UV-Vis (left panels, solid lines) and photoluminescence (left panels, dashed lines), and CD (right panels) spectra for **4-C8** (a,b) **5-C8** (c,d) at pH 10 (grey traces) and pH 1 following rapid acidification (black traces).

The **4-C8** peptide experienced a 25 nm UV-Vis blue-shift and weak Cotton effects upon rapid acidification assembly (Figure 2.9 a,b). The **5-C8** peptide had a UV-Vis  $\lambda_{\text{max}}$  of 410 nm at high pH, blue shifted by about 10 nm from typical dissolved OT4-peptides. This feature further blue shifted to 368 nm upon acidification (Figure 2.9 c,d). This peptide showed Cotton effects in both basic and acidic media, again indicating pre-existing electronic interactions in basic unassembled conditions. The opposite handedness observed in the CD spectra for these peptides shows how the constitutional isomerism affects the local nature of the exciton coupling, leading to assemblies with different global chiralities. The **4-C8** and **5-C8** peptides formed cylindrical micellar structures under two different processing conditions (as observed with TEM): after equilibration for at least 30 minutes following acidification from basic solution, and when dissolved in 0.09 M phosphate-citrate buffer (pH 7) and subjected to sonication, thermal annealing

and incubation at room temperature for 16 hours. The **4-C8** peptide showed only subtle shifts in absorbance maxima and emission intensity after incubation at room temperature for 30 minutes and virtually no change in CD response. After thermal annealing at pH 7, absorbance mirrored the response under basic, dissolved conditions, and a featureless CD signal was observed, suggesting dissolution at these high dilution conditions (Figure A2.5 a,b). The **5-C8** peptide, when thermally annealed at pH 7, had augmented absorbance that was red-shifted by several nanometers from the basic solution along with increased emission intensity and a CD response that mirrored basic-to-acidic assembly (Figure A2.5 c,d).

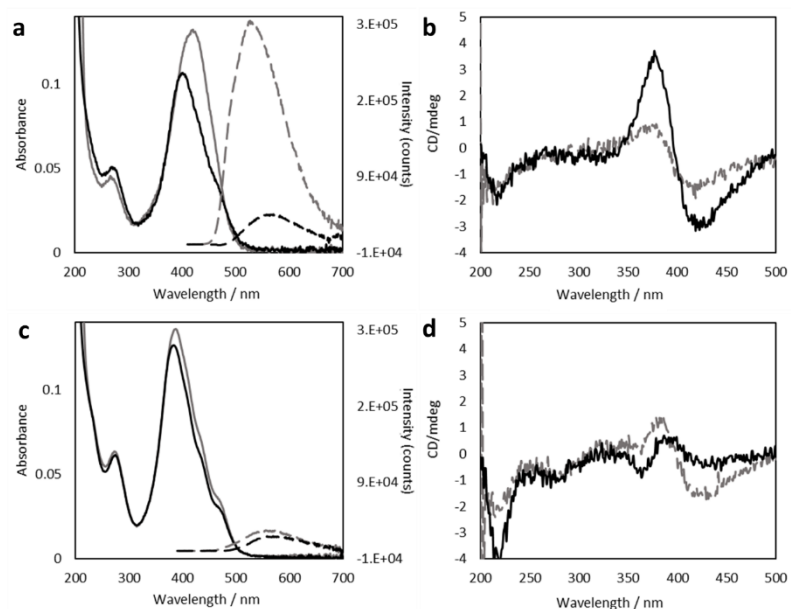


**Figure 2.10.** UV-Vis (left panels, solid lines), photoluminescence (left panels, dashed lines), and CD (right panels) spectra for **4-C16** (a,b) and **5-C16** (c,d) at basic (grey) and acidic (black) pH.

The **4-C16** peptide exhibited a 19 nm blue shift in absorbance (from 425 nm to 406 nm) and a quenched emission upon assembly. Cotton effects for this peptide were observed under basic and

acidic conditions (Figure 2.10a,b). The **5-C16** peptide demonstrated a significantly diminished solubility at high pH as indicated by the blue-shifted absorbance of 390 nm and the quenched emission with respect to typically dissolved OT4 peptides at basic pH. Further, only small perturbations to this peptide's absorbance and photoluminescence were observed upon acidification (Figure 2.10c). This peptide showed Cotton effects at high pH that inverted in sign and attenuated upon acidification, indicating an inversion in helical character and a less pronounced global chiral bias at lower pH conditions, albeit both signals were of very weak intensity (Figure 2.10d). Given the previously described changes in morphological outcome over time in the **4-C16** peptide dissolved at pH 8.6, we monitored this progression spectroscopically. After two weeks of equilibration at room temperature the absorbance is minimally perturbed; however, a decrease in photoluminescence and enhanced CD signature are observed (Figure A2.6 a,b). These changes indicate that equilibration from mixed nanoarchitectures to 1-D structures induces changes to interchromophore geometry that results in stronger excitonic coupling. The **5-C16** peptide was examined following thermal annealing at 80°C for 24 hours and equilibration at room temperature after 24 hours and two weeks. This peptide showed attenuated absorbance and emission but unperturbed CD profiles suggesting stronger interchromophore electronic interaction not accompanied by a global change in chiral bias (Figure A2.6 c,d).

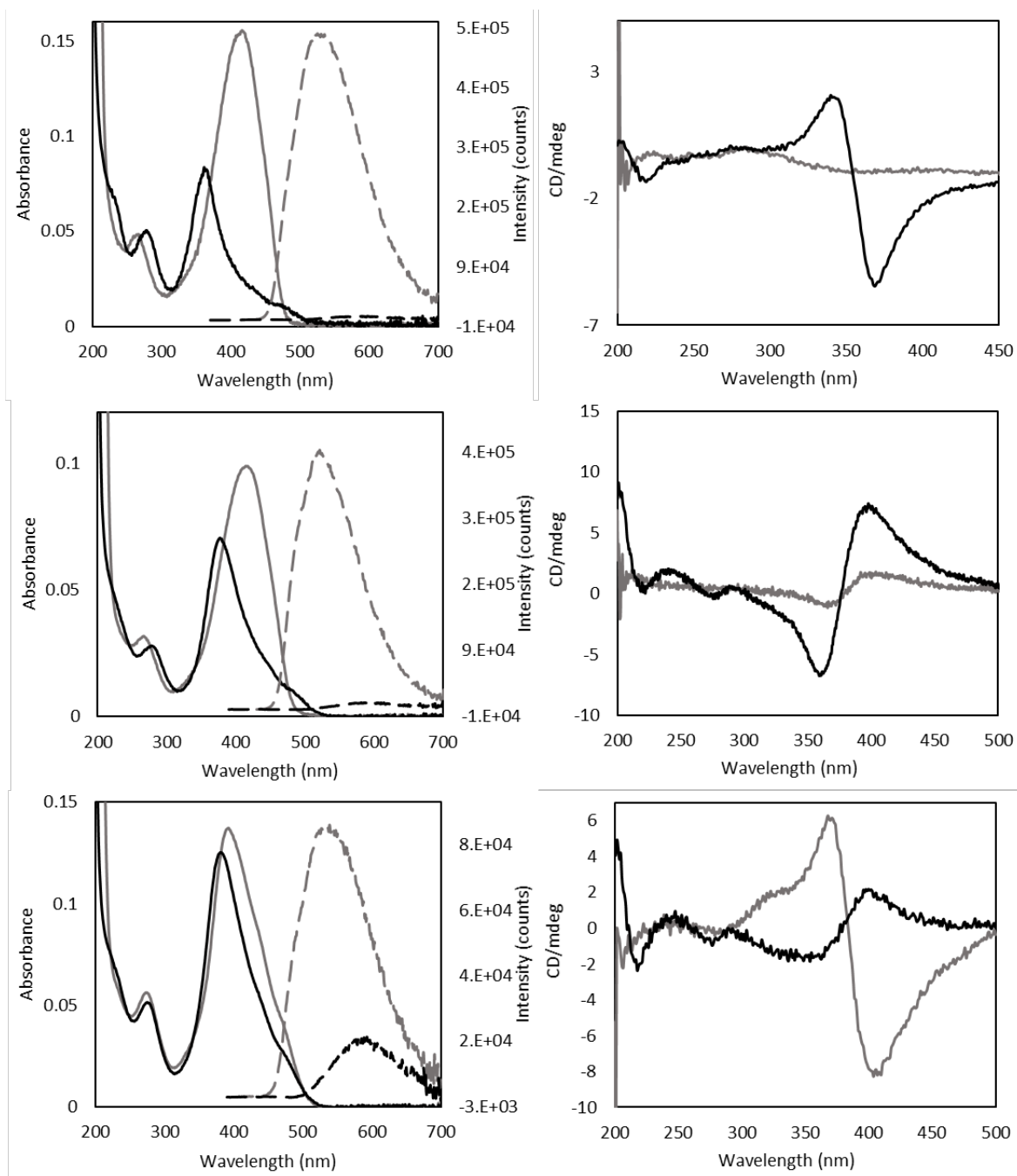


**Figure 2.11:** (Left panel) UV-Vis, solid, and photoluminescence, dashed, and (Right panel) CD traces for (a,b) **6** (c,d) **7-C8** and (e,f) **7-C16** at basic (grey) and acidic (black) pH.

Peptides **6** and **7-C8** showed 50 and 30 nm blue-shifts in absorbance respectively from 415 nm and quenched emission (Figure 2.11 a,c). Interestingly, the negative Cotton effects



observed in **6** become inverted in polarity upon addition of the eight-carbon alkyl tail in the **7-C8** peptide (Figure 2.11 b,d). The **7-C8** peptide was also annealed at pH 7 where the photophysical properties, particularly an increase in emission counts and an attenuated CD signal indicate that the observed cylindrical nanofibers decrease the degree of  $\pi$ -overlap among the embedded chromophores (Figure A2.5). Given the greater hydrophobic demand of the **7-C16**, it follows that it would have decreased aqueous solubility as evidenced by its quenched emission and maximum absorbance of 395 nm which blue-shifted by only 10 nm upon acidification (Figure 2.11 e). Strong negative Cotton effects are observed at high pH that invert in polarity and become attenuated upon acidification (Figure 2.11 f). These observations are interesting given the micellar structures observed via TEM and the chiral environment evidenced by the CD signature.

## Conclusion

We prepared an amphiphilic peptide library bearing an array of different hydrophobic segments that can access a range of nanoarchitectures in aqueous media. The peptides in this library offer four distinct regimes that engage in specific intermolecular interactions: electrostatic interactions of a charged peptide head group, a  $\beta$ -sheet promoting oligopeptide, a  $\pi$ -conjugated core and a saturated alkyl chain. We found that physical properties such as solubility, dispersity in nanostructure bundling and, ultimately, the degree of electronic communication within the  $\pi$ -conjugated core can be dictated by swapping regions of hydrophobicity in these molecules. This effect was not diluted by the addition of extended saturated alkyl tails, where hydrophobic collapse is typically a dominant feature in assembly thermodynamics. We found that peptides composed of two oligopeptide segments and the  $\pi$ -conjugated core are pre-associated in neutral media in a

manner that dictates highly ordered tape-like architectures with dispersity dependent on constitutional isomerism. Furthermore, we found that a high pH environment typically minimizes these pre-associated assemblies and results in one-dimensional structures with disperse degrees of lateral assembly upon acidification. A range of nano-architectures were observed upon addition of saturated hydrocarbon tails ranging among short and elongated micellar structures, spheres and what appear as ribbons. tails. Furthermore, in a peptide composed of a hydrophilic peptide and the OT4 core, curled sheet-like structures are observed. The addition of an 8-carbon alkyl tail allows for the formation of one-dimensional cylindrical nanofibers and extension of this tail to 16-carbons decreases solubility and yields spherical micelles at high pH. This report provides new synthetic techniques to install diverse regions of hydrophobicity in  $\pi$ -conjugated peptide nanomaterials whose nature dictate inter-chromophore communication, which will be useful for the design and development of new supramolecular bioelectronic materials.

## Experimental Section:

**General Considerations.** Reactions were carried out in flame-dried glassware under nitrogen atmosphere. Non-aqueous solvents were dried over molecular sieves and degassed by sparging with nitrogen for a minimum of 15 minutes. *N*-Bromosuccinimide (NBS) was obtained from Sigma-Aldrich and recrystallized before use. Tetrakis(triphenylphosphine)palladium ( $\text{Pd}(\text{PPh}_3)_4$ ) was obtained from Strem Chemicals. Chemicals used in solid phase peptide synthesis (Wang resin, 9-fluorenylmethyloxycarbonyl (Fmoc) protected amino acids, 2-(1H-benzotriazol-1-yl)-1,1,3,3-tetramethyluronium hexafluorophosphate (HBTU), benzotriazol-1-yl-oxytripyrrolidinophosphonium hexafluorophosphate (PyBOP) and *N*-methylpyrrolidone (NMP)) were acquired from Advanced Chem. Tech. *N,N*-Diisopropylethylamine (DIPEA) was purchased from Fisher, and dried over 4Å molecular sieves before use. 2,2':5',2'':5'',2''':5'''-quaterthiophene was

prepared and di-carboxylated to [2,2':5',2'':5'',2'''-quaterthiophene]-5,5'''-dicarboxylic acid following literature precedent.<sup>47,53,54</sup> All other chemicals were provided by Sigma-Aldrich or Fisher and used as they were received unless otherwise noted.

**General Fmoc-Based Peptide Synthesis:** Oligopeptide segments were synthesized via standard Fmoc-based solid phase peptide synthesis starting with the first Fmoc-amino acid preloaded onto Wang resin solid supports. The resin was swelled in dichloromethane (DCM) followed by deprotection of the Fmoc protecting group carried out in a solution of 20% v/v piperidine in *N,N*-dimethylformamide (DMF) for 2×10 min. The resin was washed with 3×NMP, 1×methanol (MeOH) followed by 3×DCM and swelled in DCM for 10 min. For all standard amino acid couplings, a solution of 3 equivalents of the succeeding Fmoc protected amino acid, 2.9 equivalents of HBTU was prepared in 10 mL of NMP and sonicated to dissolve, followed by 10 equivalents of DIPEA and mixed for one min. The resin was drained of DCM, the activated amino acid was added to the chamber, and mixed for a minimum of 1 hour. The resin was then drained and rinsed with 3×NMP, 1×MeOH followed by 3×DCM, swelled in DCM for 10 minutes and the process repeated starting with Fmoc deprotection for each sequential amino acid in the sequence. The success of each coupling step was monitored by performing a Kaiser test.

***N*-terminus-acylation, and on-resin Stille coupling procedure:** Peptides were acylated with 5-bromothiophene-2-carboxylic acid and subjected to Stille cross-coupling conditions in the presence of 5,5'-bis-tributylstannyl-[2,2']-bithiophene as previously described.<sup>55</sup>

**General on resin activation:** The unprotected hydrophilic peptide was capped with a solution of 3 equivalents of [2,2':5',2'':5'',2'''-quaterthiophene]-5,5'''-dicarboxylic acid, 3 equivalents of benzotriazol-1-yl-oxytripyrrolidinophosphonium hexafluorophosphate (PyBOP) and 10 equivalents of DIPEA in NMP through an over-night reaction leaving a terminal carboxylic acid

functionality. The terminal carboxylic acid was activated on resin with a solution of 0.95 equivalents of PyBOP and 10 equivalents DIPEA in NMP for 1 hour. The resin was washed twice with NMP.

**General peptide cleavage and work-up:** Following solid-phase synthesis the peptide was cleaved by mixing the resin in a 2.5:2.5:95 Water:Triisopropylsilane (TIPS):Trifluoroacetic acid (TFA) cocktail for three hours. The solution was collected from the chamber, concentrated under vacuum, and triturated in cold diethylether. The suspended product was centrifuged to isolate and lyophilized. The lyophilized product was HPLC purified. Specific experimental procedures and molecular characterization data for each molecule synthesized can be found in the supporting information.

**Electrospray Ionization Mass Spectrometry (ESI-MS):** ESI signatures were samples using a Thermo Finnigan LCQ Deca Ion Trap Mass Spectrometer operating in negative mode. Samples were prepared in a 1:1 MeOH:water solution with 0.1% ammonium hydroxide.

**UV-Vis and Photoluminescence:** UV-Vis spectra were acquired using a Varian Cary 50 Bio UV-Vis spectrophotometer. Photoluminescence spectra were taken on a PTi Photon Technology International Fluorometer equipped with a Ushio Xenon short arc lamp. Spectroscopic samples were prepared at ca. 3  $\mu$ M in Millipore water. The pH was adjusted by adding either 1M KOH or 1M HCl.

**Circular Dichroism (CD):** CD spectra were obtained with a Jasco J-810 spectropolarimeter. Spectroscopic samples were prepared at ca. 3  $\mu$ M in Millipore water. The pH was adjusted by adding either 1M KOH or 1M HCl.

**Dynamic Light Scattering (DLS):** DLS experiments were conducted using a Zetasizer Nano-ZS90 (Malvern Instruments). DLS samples were prepared at ca. 9  $\mu$ M in Millipore water. The pH was adjusted by adding either 1M KOH or 1M HCl.

**Reverse-Phase HPLC:** Peptides were purified by reverse-phase HPLC on a Varian PrepStar SD-1 system equipped with a Phenomenex, Luna, 5  $\mu$ m particle diameter silica support functionalized with TMS terminated C8. An aqueous 0.1% ammonium formate buffer (pH 8):acetonitrile gradient was used as mobile phase.

**Transmission Electron Microscopy (TEM):** Imaging was performed on a FEI TECNAI 12 TWIN transmission electron microscope equipped with an SIS Megaview III CCD digital camera. The samples were prepared in two ways. The first was by pipetting a drop of 1 mg/mL solution of assembled peptide in water onto ionized 200 mesh Formvar coated copper grids and incubated for 5 minutes at 25°C. Excess solution was removed by floating the grid in a drop of water. The sample was then stained with a 2% uranyl acetate solution, washed by dipping in water, and excess moisture was wicked off by dabbing the grid on filter paper. For peptides 4-7, superior imaging contrast was observed through another sample preparation method where 10  $\mu$ L of a 1 mg/mL solution of assembled peptide was allowed to sit on the grid for one minute. Excess solution was wicked away by dabbing the grid on filter paper. 10  $\mu$ L of 2% uranyl acetate solution was allowed to sit on the grid for 30 seconds and then wicked away on filter paper. In both methods, the grids were allowed to dry completely in air before imaging.

## References

- (1) Hoeben, F. J. M.; Jonkheijm, P.; Meijer, E. W.; Schenning, A. P. H. J. About Supramolecular Assemblies of  $\pi$ -Conjugated Systems. *Chem. Rev.* **2005**, *105*, 1491–1546.  
<https://doi.org/10.1021/cr030070z>.
- (2) Ardon, H. A. M.; Tovar, J. D. Peptide  $\pi$ -Electron Conjugates: Organic Electronics for Biology? *Bioconjugate Chemistry* **2015**, *26*, 2290–2302.  
<https://doi.org/10.1021/acs.bioconjchem.5b00497>.
- (3) Aida, T.; Meijer, E. W.; Stupp, S. I. Functional Supramolecular Polymers. *Science* **2012**, *335*, 813–817.
- (4) Schenning, A. P. H. J.; Meijer, E. W. Supramolecular Electronics; Nanowires from Self-Assembled  $\pi$ -Conjugated Systems. *Chemical Communications* **2005**, 3245–3258.  
<https://doi.org/10.1039/b501804h>.
- (5) Tovar, J. D. Supramolecular Construction of Optoelectronic Biomaterials. *Acc. Chem. Res* **2013**, *46*, 1527–1537.
- (6) Lehn, J. -M. Supramolecular Chemistry—Scope and Perspectives Molecules, Supermolecules, and Molecular Devices (Nobel Lecture). *Angewandte Chemie International Edition in English* **1988**, *27*, 89–112. <https://doi.org/10.1002/anie.198800891>.
- (7) Desiraju, G. R. Chemistry beyond the Molecule. *Nature* **2001**, *412*, 397–400.  
<https://doi.org/10.1038/35086640>.
- (8) Sanders, A. M.; Tovar, J. D. Solid-Phase Pd-Catalysed Cross-Coupling Methods for the Construction of  $\pi$ -Conjugated Peptide Nanomaterials. *Supramolecular chemistry* **2014**, *26*, 259–266. <https://doi.org/10.1080/10610278.2013.852675>.
- (9) Reches, M.; Gazit, E. Casting Metal Nanowires within Discrete Self-Assembled Peptide Nanotubes. *Science* **2003**, *300*, 625–627. <https://doi.org/10.1126/science.1082387>.

- (10) Berdugo, C.; Nalluri, S. K. M.; Javid, N.; Escuder, B.; Miravet, J. F.; Ulijn, R. V. Dynamic Peptide Library for the Discovery of Charge Transfer Hydrogels. *ACS Applied Materials and Interfaces* **2015**, *7*, 25946–25954. <https://doi.org/10.1021/acsami.5b08968>.
- (11) Ashkenasy, N.; Horne, W. S.; Ghadiri, M. R. Design of Self-Assembling Peptide Nanotubes with Delocalized Electronic States. *Small* **2006**, *2* (1), 99–102. <https://doi.org/10.1002/sml.200500252>.
- (12) Diegelmann, S. R.; Gorham, J. M.; Tovar, J. D. One-Dimensional Optoelectronic Nanostructures Derived from the Aqueous Self-Assembly of  $\pi$ -Conjugated Oligopeptides. *J. Am. Chem. Soc.* **2008**, *130*, 13840–13841. <https://doi.org/10.1021/ja805491d>.
- (13) Shao, H.; Parquette, J. R. A  $\pi$ -Conjugated Hydrogel Based on an Fmoc-Dipeptide Naphthalene Diimide Semiconductor. *Chemical Communications* **2010**, *46*, 4285–4287. <https://doi.org/10.1039/c0cc00701c>.
- (14) Shao, H.; Nguyen, T.; Romano, N. C.; Modarelli, D. A.; Parquette, J. R. Self-Assembly of 1-D n-Type Nanostructures Based on Naphthalene Diimide-Appended Dipeptides. *Journal of the American Chemical Society* **2009**, *131* (45), 16374–16376. <https://doi.org/10.1021/ja906377q>.
- (15) Ing, N. L.; Spencer, R. K.; Luong, S. H.; Nguyen, H. D.; Hochbaum, A. I. Electronic Conductivity in Biomimetic  $\alpha$  - Helical Peptide Nano Fibers and Gels. *ACS Nano* **2018**, *12*, 2652–2661. <https://doi.org/10.1021/acsnano.7b08756>.
- (16) Chen, L.; Revel, S.; Morris, K.; Adams, D. J. Energy Transfer in Self-Assembled Dipeptide Hydrogels. *Chemical Communications* **2010**, *46*, 4267–4269. <https://doi.org/10.1039/c003052j>.
- (17) Smith, C. L.; Mears, L. L. E.; Greeves, B. J.; Draper, E. R.; Douth, J.; Adams, D. J.; Cowan, A. J. Gelation Enabled Charge Separation Following Visible Light Excitation Using Self-

Assembled Perylene Bisimides. *Physical Chemistry Chemical Physics* **2019**, *21*, 26466–26476.

<https://doi.org/10.1039/c9cp05839g>.

- (18) Berndt, P.; Fields, G. B.; Tirrell, M. Synthetic Lipidation of Peptides and Amino Acids : Monolayer Structure and Properties. *J. Am. Chem. Soc.* **1995**, *117*, 9515–9522.  
<https://doi.org/10.1021/ja00142a019>.
- (19) Fields, G. B.; Lauer, J. L.; Dori, Y.; Forns, P.; Yu, Y. C.; Tirrell, M. Proteinlike Molecular Architecture: Biomaterial Applications for Inducing Cellular Receptor Binding and Signal Transduction. *Biopolymers* **1998**, *47*, 143–151. [https://doi.org/10.1002/\(SICI\)1097-0282\(1998\)47:2<143::AID-BIP3>3.0.CO;2-U](https://doi.org/10.1002/(SICI)1097-0282(1998)47:2<143::AID-BIP3>3.0.CO;2-U).
- (20) Yu, Y. C.; Berndt, P.; Tirrell, M.; Fields, G. B. Self-Assembling Amphiphiles for Construction of Protein Molecular Architecture. *Journal of the American Chemical Society* **1996**, *118*, 12515–12520. <https://doi.org/10.1021/ja9627656>.
- (21) Gore, T.; Dori, Y.; Talmon, Y.; Tirrell, M.; Bianco-peled, H. Self-Assembly of Model Collagen Peptide Amphiphiles. *Langmuir* **2001**, *17*, 5352–5360. <https://doi.org/10.1021/la010223i>.
- (22) Hendricks, M. P.; Sato, K.; Palmer, L. C.; Stupp, S. I. Supramolecular Assembly of Peptide Amphiphiles. *Accounts of Chemical Research* **2017**, *50*, 2440–2448.  
<https://doi.org/10.1021/acs.accounts.7b00297>.
- (23) Hartgerink, J. D.; Beniash, E.; Stupp, S. I. Self-Assembly and Mineralization of Peptide-Amphiphile Nanofibers. *Science (New York, N.Y.)* **2001**, *294*, 1684–1688.  
<https://doi.org/10.1126/science.1063187>.
- (24) Dehsorkhi, A.; Castelletto, V.; Hamley, I. W. Self-Assembling Amphiphilic Peptides. *Journal of Peptide Science* **2014**, *20*, 453–467. <https://doi.org/10.1002/psc.2633>.



- (25) Dasgupta, A.; Das, D. Designer Peptide Amphiphiles: Self-Assembly to Applications. *Langmuir* **2019**, *35*, 10704–10724. <https://doi.org/10.1021/acs.langmuir.9b01837>.
- (26) Gothard, C. M.; Rao, N. A.; Nowick, J. S. Nanometer-Sized Amino Acids for the Synthesis of Nanometer-Scale Water-Soluble Molecular Rods of Precise Length. *Journal of the American Chemical Society* **2007**, *129*, 7272–7273. <https://doi.org/10.1021/ja072648i>.
- (27) Gothard, C. M.; Nowick, J. S. Nanometer-Scale Water-Soluble Macrocycles from Nanometer-Sized Amino Acids. *Journal of Organic Chemistry* **2010**, *75*, 1822–1830. <https://doi.org/10.1021/jo902268x>.
- (28) Raeburn, J.; Mendoza-Cuenca, C.; Cattoz, B. N.; Little, M. A.; Terry, A. E.; Zamith Cardoso, A.; Griffiths, P. C.; Adams, D. J. The Effect of Solvent Choice on the Gelation and Final Hydrogel Properties of Fmoc–Diphenylalanine. *Soft Matter* **2015**, *11* (5), 927–935. <https://doi.org/10.1039/C4SM02256D>.
- (29) Martin, A. D.; Wojciechowski, J. P.; Bhadbhade, M. M.; Thordarson, P. A Capped Dipeptide Which Simultaneously Exhibits Gelation and Crystallization Behavior. *Langmuir* **2016**, *32* (9), 2245–2250. <https://doi.org/10.1021/acs.langmuir.5b03963>.
- (30) Martí, D.; Mayans, E.; Gil, A. M.; Díaz, A.; Jiménez, A. I.; Yousef, I.; Keridou, I.; Cativiela, C.; Puiggalí, J.; Alemán, C. Amyloid-like Fibrils from a Diphenylalanine Capped with an Aromatic Fluorenyl. *Langmuir* **2018**, *34*, 15551–15559. <https://doi.org/10.1021/acs.langmuir.8b03378>.
- (31) Smith, A. M.; Williams, R. J.; Tang, C.; Coppo, P.; Collins, R. F.; Turner, M. L.; Saiani, A.; Ulijn, R. V. Fmoc-Diphenylalanine Self Assembles to a Hydrogel via a Novel Architecture Based on Pi-Pi Interlocked Beta-Sheets. *Advanced Materials* **2008**, *20* (1), 37–41. <https://doi.org/10.1002/adma.200701221>.

- (32) Yang, Z.; Liang, G.; Ma, M.; Xu, B. Conjugates of Naphthalene and Dipeptides Produce Molecular Hydrogelators with High Efficiency of Hydrogelation and Superhelical Nanofibers. *Journal of Materials Chemistry* **2007**, *17*, 850–854. <https://doi.org/10.1039/b611255b>.
- (33) Fleming, S.; Frederix, P. W. J. M.; Ramos Sasselli, I.; Hunt, N. T.; Ulijn, R. V.; Tuttle, T. Assessing the Utility of Infrared Spectroscopy as a Structural Diagnostic Tool for  $\beta$ -Sheets in Self-Assembling Aromatic Peptide Amphiphiles. *Langmuir* **2013**, *29*, 9510–9515. <https://doi.org/10.1021/la400994v>.
- (34) Raeburn, J.; Pont, G.; Chen, L.; Cesbron, Y.; Lévy, R.; Adams, D. J. Fmoc-Diphenylalanine Hydrogels: Understanding the Variability in Reported Mechanical Properties. *Soft Matter* **2012**, *8*, 1168–1174. <https://doi.org/10.1039/c1sm06929b>.
- (35) Lehrman, J. A.; Cui, H.; Tsai, W. W.; Moyer, T. J.; Stupp, S. I. Supramolecular Control of Self-Assembling Terthiophene-Peptide Conjugates through the Amino Acid Side Chain. *Chemical Communications* **2012**, *48*, 9711–9713. <https://doi.org/10.1039/c2cc34375d>.
- (36) Wall, B. D.; Zacca, A. E.; Sanders, A. M.; Wilson, W. L.; Ferguson, A. L.; Tovar, J. D.; Seitz, F. Supramolecular Polymorphism: Tunable Electronic Interactions within  $\Pi$ -Conjugated Peptide Nanostructures Dictated by Primary Amino Acid Sequence. <https://doi.org/10.1021/la500222y>.
- (37) Matmour, R.; De Cat, I.; George, S. J.; Adriaens, W.; Leclère, P.; Bomans, P. H. H.; Sommerdijk, N. A. J. M.; Gielen, J. C.; Christianen, P. C. M.; Heldens, J. T.; Van Hest, J. C. M.; Löwik, D. W. P. M.; De Feyter, S.; Meijer, E. W.; Schenning, A. P. H. J. Oligo(p-Phenylenevinylene) Peptide Conjugates: Synthesis and Self-Assembly in Solution and at the Solid-Liquid Interface. *Journal of the American Chemical Society* **2008**, *130*, 14576–14583. <https://doi.org/10.1021/ja803026j>.

- (38) Wei, D.; Ge, L.; Wang, Z.; Wang, Y.; Guo, R. Self-Assembled Dual Helical Nanofibers of Amphiphilic Perylene Diimides with Oligopeptide Substitution. *Langmuir* **2019**, *35*, 11745–11754. <https://doi.org/10.1021/acs.langmuir.9b01745>.
- (39) Khalily, M. A.; Usta, H.; Ozdemir, M.; Bakan, G.; Dikecoglu, F. B.; Edwards-Gayle, C.; Hutchinson, J. A.; Hamley, I. W.; Dana, A.; Guler, M. O. The Design and Fabrication of Supramolecular Semiconductor Nanowires Formed by Benzothienobenzothiophene (BTBT)-Conjugated Peptides. *Nanoscale* **2018**, *10*, 9987–9995. <https://doi.org/10.1039/c8nr01604f>.
- (40) Ardon, H. A. M.; Draper, E. R.; Citossi, F.; Wallace, M.; Serpell, L. C.; Adams, D. J.; Tovar, J. D. Kinetically Controlled Coassembly of Multichromophoric Peptide Hydrogelators and the Impacts on Energy Transport. *Journal of the American Chemical Society* **2017**, *139* (25), 8685–8692. <https://doi.org/10.1021/jacs.7b04006>.
- (41) Ardoña, H. A. M.; Tovar, J. D. Energy Transfer within Responsive Pi-Conjugated Coassembled Peptide-Based Nanostructures in Aqueous Environments. *Chem. Sci.* **2015**, *6* (2), 1474–1484. <https://doi.org/10.1039/C4SC03122A>.
- (42) Ardoña, H. A. M.; Besar, K.; Togninalli, M.; Katz, H. E.; Tovar, J. D. Sequence-Dependent Mechanical, Photophysical and Electrical Properties of Pi-Conjugated Peptide Hydrogelators. *J. Mater. Chem. C* **2015**, *3* (3), 6505–6514. <https://doi.org/10.1039/c5tc00100e>.
- (43) Ortony, J. H.; Newcomb, C. J.; Matson, J. B.; Palmer, L. C.; Doan, P. E.; Hoffman, B. M.; Stupp, S. I. Internal Dynamics of a Supramolecular Nanofibre. *Nature Materials* **2014**, *13*, 812–816. <https://doi.org/10.1038/nmat3979>.
- (44) Cui, H.; Cheetham, A. G.; Pashuck, E. T.; Stupp, S. I. Amino Acid Sequence in Constitutionally Isomeric Tetrapeptide Amphiphiles Dictates Architecture of One-Dimensional Nanostructures. *J. Am. Chem. Soc.* **2014**, *136*, 12461–12468. <https://doi.org/10.1021/ja507051w>.

- (45) Wang, Y.; Yang, X.; Liu, T.; Li, Z.; Leskauskas, D.; Liu, G.; Matson, J. B. Molecular-Level Control over Plasmonic Properties in Silver Nanoparticle/Self-Assembling Peptide Hybrids. *Journal of the American Chemical Society* **2020**, *142*, 9158–9162. <https://doi.org/10.1021/jacs.0c03672>.
- (46) Wall, B. D.; Tovar, J. D. Synthesis and Characterization of Pi-Conjugated Peptide-Based Supramolecular Materials. *Pure Appl. Chem* **2012**, *84*, 1039–1045. <https://doi.org/10.1351/PAC-CON-11-10-24>.
- (47) Vadehra, G. S.; Wall, B. D.; Diegelmann, S. R.; Tovar, J. D. On-Resin Dimerization Incorporates a Diverse Array of p-Conjugated Functionality within Aqueous Self-Assembling Peptide Backbones. *Chemical Communications* **2010**, *46*, 3947–3949. <https://doi.org/10.1039/c0cc00301h>.
- (48) Miravet, J. F.; Escuder, B.; Segarra-Maset, M. D.; Tena-Solsona, M.; Hamley, I. W.; Dehsorkhi, A.; Castelletto, V. Self-Assembly of a Peptide Amphiphile: Transition from Nanotape Fibrils to Micelles. *Soft Matter* **2013**, *9*, 3558–3564. <https://doi.org/10.1039/c3sm27899a>.
- (49) Cui, H.; Muraoka, T.; Cheetham, A. G.; Stupp, S. I. Self-Assembly of Giant Peptide Nanobelts. *Nano Letters* **2009**, *9*, 945–951. <https://doi.org/10.1021/nl802813f>.
- (50) Anderson, C. F.; Chakroun, R. W.; Su, H.; Mitrut, R. E.; Cui, H. Interface-Enrichment-Induced Instability and Drug-Loading-Enhanced Stability in Inhalable Delivery of Supramolecular Filaments. *ACS Nano* **2019**, *13*, 12957–12968. <https://doi.org/10.1021/acsnano.9b05556>.
- (51) Fu, I. W.; Markegard, C. B.; Nguyen, H. D. Solvent Effects on Kinetic Mechanisms of Self-Assembly by Peptide Amphiphiles via Molecular Dynamics Simulations. *Langmuir* **2015**, *31* (1), 315–324. <https://doi.org/10.1021/la503399x>.

- (52) Kasha, M.; Rawls, H. R.; Ashraf El-Bayoumi, M. The Exciton Model in Molecular Spectroscopy. *Pure Appl. Chem* **1965**, *11*, 371–392.
- (53) Jiang, H.; Zhang, L.; Cai, J.; Ren, J.; Cui, Z.; Chen, W. Quinoidal Bithiophene as Disperse Dye: Substituent Effect on Dyeing Performance. *Dyes and Pigments* **2018**, *151*, 363–371. <https://doi.org/10.1016/j.dyepig.2018.01.017>.
- (54) Capozzi, B.; Dell, E. J.; Berkelbach, T. C.; Reichman, D. R.; Venkataraman, L.; Campos, L. M. Length-Dependent Conductance of Oligothiophenes. *Journal of the American Chemical Society* **2014**, *136*, 10486–10492. <https://doi.org/10.1021/ja505277z>.
- (55) Dimerizations, C. S.; Sanders, A. M.; Dawidczyk, T. J.; Katz, H. E.; Tovar, J. D. Peptide-Based Supramolecular Semiconductor Nanomaterials via Pd- Catalyzed Solid-Phase “ Dimerizations .” *ACS Macro Letters* **2012**, *1*, 1326–1329.

## **Chapter 3**

# **Methods in Molecular Engineering Toward Nanoscopic Control and Visualization in Peptide- $\pi$ Conjugates**

## Introduction.

Programmed self-assembly of  $\pi$ -conjugated nanomaterials through elegant assembly triggers or monomer interaction energies can effectuate either narcissistic self-sorting or statistically blended co-assembly of distinct semiconducting units from solution.<sup>1-3</sup> These controlled assembly mechanisms underlie the next generation of functional supramolecular materials and are critical for applications that depend heavily on precise hierarchical ordering and directional energy transfer such as organic heterojunctions or light harvesting systems respectively.<sup>4,5</sup> Given the abundant examples of precise supramolecular construction and specificity achieved by biomacromolecules, these assembly strategies can be translated synthetically to biologic-semiconducting hybrid systems. Peptide nanomaterials have been used to assemble multiple chromophores into distinct domains or mixed structures from solution due to the directional nature of the hydrogen bond, and the modular nature of synthetic peptide procedures that can incorporate a diversity of chemistries through amino acid side chains.<sup>1,2,6</sup> However, new characterization methods and even direct observation of co-polymerization and hierarchical structure in self-sorted structures would be invaluable for implementing these materials in bioelectronics applications.

Precise supramolecular construction requires careful navigation of the energy landscapes governing the assembly process. Kinetic and thermodynamic influences, while difficult to uncouple, can ultimately dictate order/disorder, co-assembly/self-sorting, and assembly/disassembly characteristics in an emerging polymer. While most supramolecular polymerizations occur spontaneously under thermodynamic control, exercising a detailed understanding of energy surfaces could support supramolecular materials in applications that require spatial and temporal precision.<sup>7-9</sup> Recent reports have examined how monomer design,

which dictates a given energy landscape, can be coupled with controlled assembly conditions (solvent composition, cooling rate etc.) to navigate challenging energy surfaces to access different polymerization mechanisms, avoiding the dispersity and “single state” of the thermodynamic product and arrive at desired co-polymeric outcomes in length and structure.<sup>9–12</sup> Adams and co-workers examined the pH triggered assembly of perylene bisimide and stilbene based xerogels achieving self-sorting by slow pH reduction through hydrolysis of glucono- $\delta$ -lactone and co-mixing via HCl rapid assembly under kinetic control (Figure 3.1a).<sup>3,13</sup> A widely sought supramolecular construction is a block co-polymer which have been attained by isolating kinetically trapped species to act as seed crystals on which the polymerization can occur in a manner analogous to methods in covalent polymer chemistry that control length and dispersity (i.e. living polymerization).<sup>11,14–16</sup> In a seminal work from Manners and co-workers, the controlled polymerization of poly(ferrocenylsilane) with poly(dimethylsiloxane) and poly(isoprene) from kinetically stable, uniform crystallite seeds, was achieved through epitaxial growth forming block cylindrical co-polymers (Figure 3.1b).<sup>17,18</sup> This was extended to semi-crystalline pi-conjugated systems through a self-seeding annealing process that minimized defects within a poly(3-hexylthiophene)-block-polystyrene seed on which a polythiophene block co-polymer with a different corona could be grown to produce a tri-block micellar fiber.<sup>19,20</sup> More recently, George and co-workers reported the cooperative block-copolymerization of two naphthalenediimide derivatives under thermodynamic control where the unique emission profiles of the monomer units permit spectroscopic and imaging characterization.<sup>9</sup> The same group, more recently, reported tri-component block co-polymerization of naphthalene appended dipeptides under kinetic control (Figure 3.1c).<sup>21</sup> Kinetically trapped structures often undergo energetic relaxation to a thermodynamic minimum wherein new intermolecular geometries described by those minima can



be associated with corresponding changes in material properties that could also be advantageous for stimuli responsive materials applications.<sup>22–24</sup>

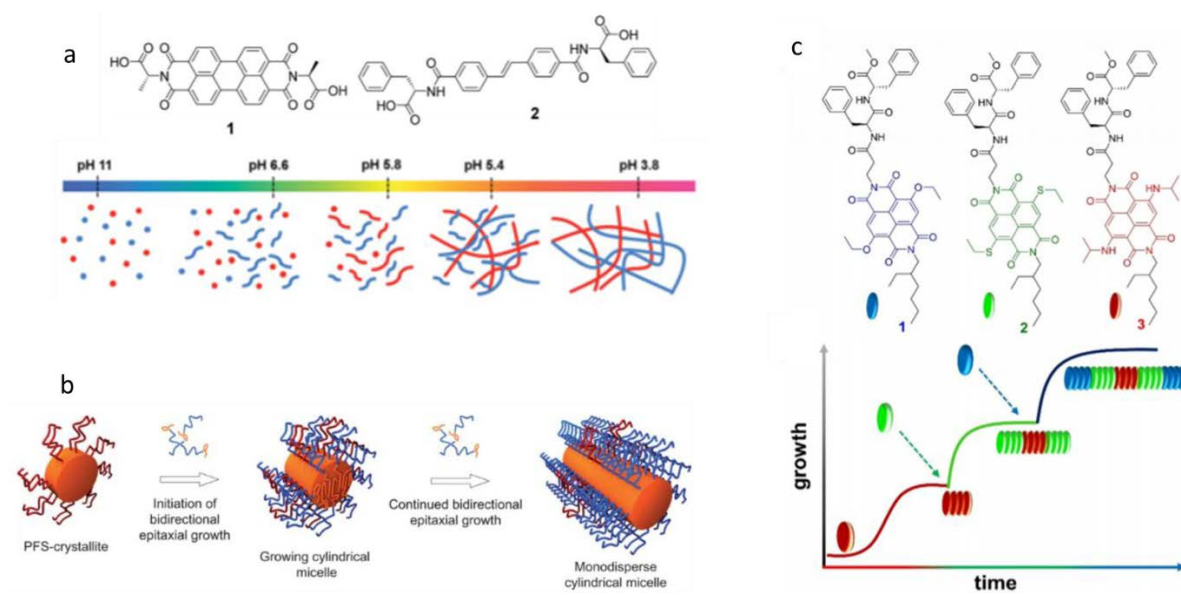


**Figure 3.1.** The controlled assembly of supramolecular materials from mixed solutions of monomers has been achieved through (a) assembly trigger to create self-sorted nanostructures. Block co-polymer structures have also been prepared through (b) crystallite seed formation and (c) monomer design. Adapted from references 13, 17, and 21. Copyright the Royal society of Chemistry, 2016, Macmillan Publishers 2010, and Wiley-VCH GmbH, 2021.

Monomer design illuminates the competing attractive and repulsive intermolecular interactions that ultimately dictate the contours of the energy surface wherein the strategic application of assembly conditions can be used to navigate and arrive at desired thermodynamic minima or kinetically trapped states.<sup>8,25–27</sup> Our lab previously examined single amino acid substitutions in tetrapeptides flanking oligophenylenevinylene (OPV3)  $\pi$ -conjugated cores whose photophysical signatures could be used to report on the nature of the assembly. The emission profiles changed from excimeric-like to excitonic-like by substituting a small glycine for more bulky hydrophobic residues, respectively. Through these subtle changes to intermolecular

interactions of the monomer, different thermodynamic minima are accessed where the resulting geometric and spatial changes within the assembly modify electronic couplings among the  $\pi$ -conjugated units.<sup>28</sup> In a later study we examined a pH triggered assembly paradigm in triblock peptides to guide co-assembly or self-segregation of peptides bearing distinct electronic functionalities. The slow reduction in pH by GdL hydrolysis could preferentially assemble peptides based on their apparent pKa and create self-sorted structures while rapid acidification produced statistically mixed co-assemblies.<sup>6,29,30</sup> However, despite NMR and XRD evidence of self-sorting by GdL assembly, residual energy transfer was observed in photophysical studies. Insight into the true nature of these self-sorted structures, for example the formation of block copolymers or intimately intertwined but separate heterostructures would be invaluable for the informed application of these materials, for example in p/n heterojunctions.<sup>30</sup>

Given the dynamic nature of supramolecular assembly, it follows that a paradigm to directly observe polymeric outcomes would be invaluable. Previous work from Meijer and co-workers examined the exchange pathways of supramolecular assemblies of 1,3,5-benzenetricarboxamides modified with Cy5 and Cy3 fluorescent dyes that could be used as labels in stochastic optical reconstruction microscopy (STORM) to reveal the details of monomer exchange along the polymer length.<sup>31</sup> In a later study, Stupp and co-workers applied this super-resolution technique to peptide amphiphile assemblies revealing that exchange occurs as monomers or small clusters randomly insert into the fiber wherein varying exchange rates along the fiber length suggest regions of stronger and weaker cohesive forces among monomers.<sup>32</sup> More recently, Uljin and co-workers devised a non-covalent approach to stimulated emission-depletion (STED) super resolution microscopy using electrostatics to label a positively charged peptide nanofiber with a negatively charged Alexa-488 fluorescent dye to observe dynamic processes such

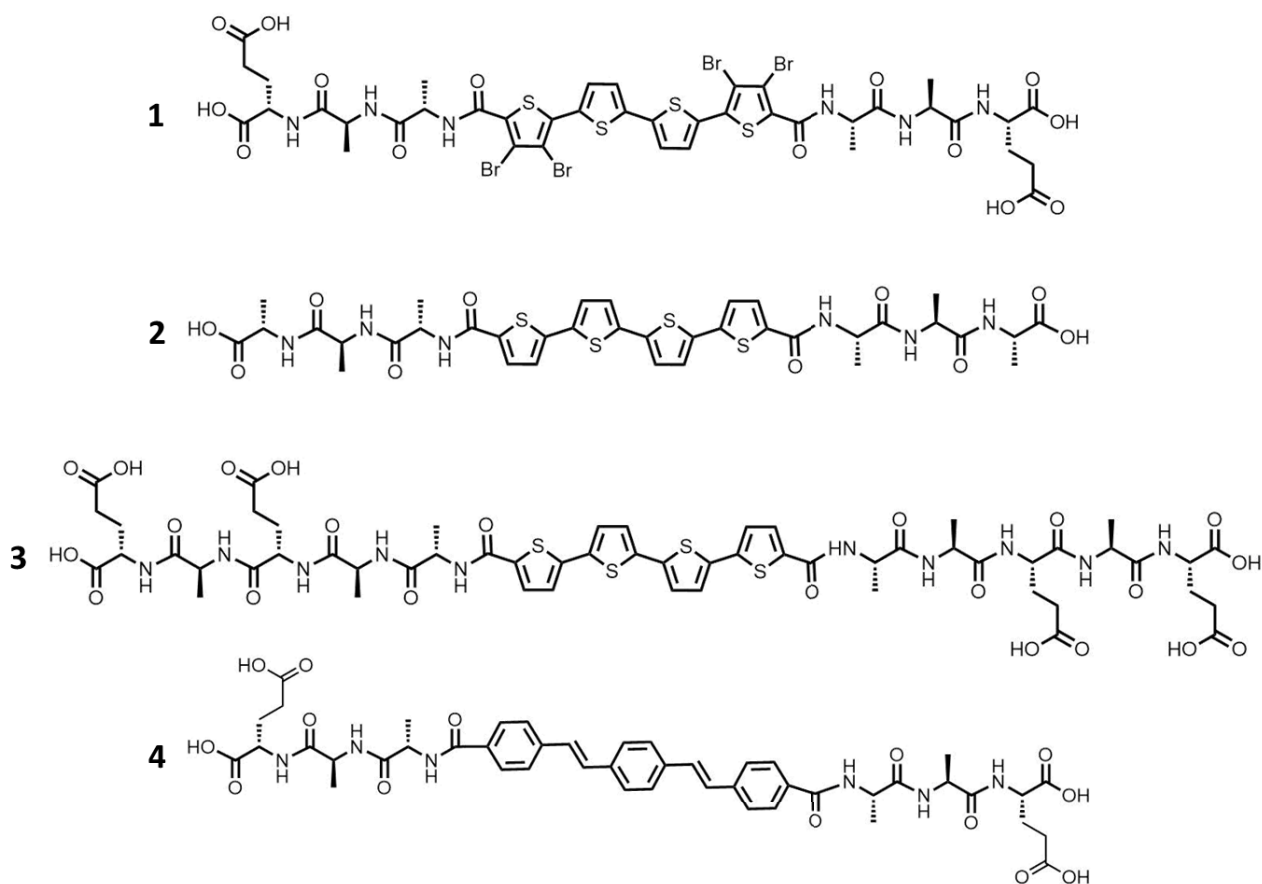
as enzymatic degradation.<sup>33</sup> The necessity of covalent dye labeling in STORM imaging may impact molecular geometry and packing, and the non-covalent and non-specific nature of electrostatic labeling excludes differential imaging in assemblies formed from solutions containing multiple species and limits the versatility of these optical light microscopies for specific applications.

Given our previous report of pH triggered assemblies that demonstrated residual evidence of energy transfer in photophysical measurements of self-sorted materials, we were interested in the hierarchical ordering of peptide heterostructures by different assembly mechanisms. For example, does residual energy transfer arise from interactions among separately sorted structures that are intimately intertwined or, for example, domains of sorted peptides in a single block-like polymeric structure? Herein, we examine the self-sorting or co-mixing of  $\pi$ -conjugated peptides with selective bromine tagging for elemental contrast in scanning TEM (STEM) coupled to energy dispersive x-ray spectroscopy (EDS) elemental analysis. We demonstrate measurable self-sorting and co-mixing in these systems by STEM-EDS by changing the sequence or assembly trigger which will be a helpful advancement to characterize new materials for electronics applications. We confirm this imaging technique with a different peptide system, previously demonstrated to engage in energy transfer in mixed co-assemblies.<sup>6</sup>

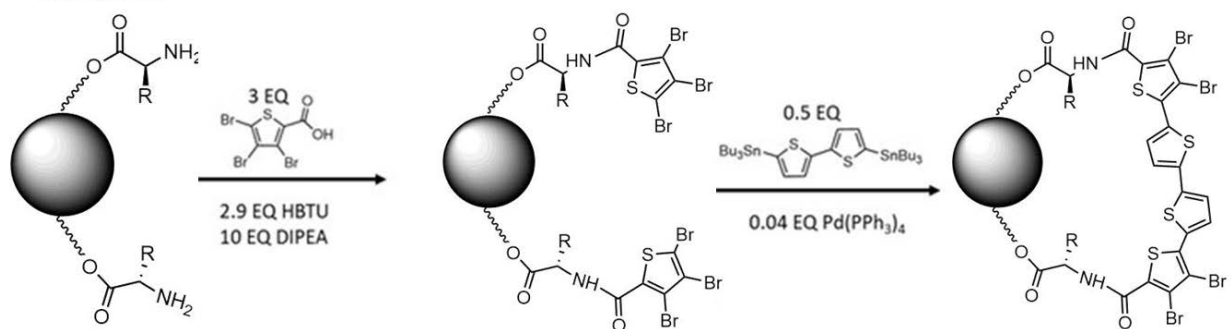
## **Results and Discussion.**

**Peptide Design and Synthesis.** *Design.* We designed two peptide systems, one in which a GdL pH triggered assembly ensures self-sorting of **1** and **2** as in previously reported systems.<sup>1</sup> In peptide **3** we incorporated an elongated peptide hydrogen bonding motif to encourage self-sorting upon rapid HCl acidification with **1** by biasing homo over hetero monomer interaction energetics.

Peptide **1** presents two terminal glutamic acids, and thus four solubilizing acidic functional groups, and two alanine repeats flanking a quaterthiophene (OT4)  $\pi$ -conjugated core, brominated on both outer rings at both  $\beta$ -positions to provide elemental contrast in STEM-EDS when differentially assembled from solution mixtures with **2** and **3** respectively. Peptide **2** contains three repeating alanine residues flanking a bare OT4  $\pi$ -conjugated core but is otherwise size matched with peptide **1**. The lack of acidic side chains in **2** leaves just the two terminal carboxylic acid functionalities, as compared to the four in **1**, culminating in an effective pKa difference between **1** and **2** that should effectuate self-sorting upon slow hydrolysis of GdL. Self-sorting has been demonstrated in coiled-coil peptides where the extension of the coil leads to the increased stability of homo vs. hetero interaction energies.<sup>34</sup> We envisioned that the longer peptide sequence lengths in **3** would allow it to preferentially engage in assemblies with its own extended hydrogen bonding motif rather than co-mix with the shorter sequence of **1**. We also hypothesized that mixtures of **4** with **2** and **3** could be examined under the same sample conditions with STEM-EDS using sulfur as an elemental marker for co-mixture or self-sorting.



Scheme 1



*Synthesis.* Peptides were assembled on solid-supports via standard Fmoc-based solid-phase peptide synthesis (SPPS). The Wang resin was preloaded with the first Fmoc-protected amino acid and the desired peptide segment was extended on resin and terminated with either 5-bromo-2-thiophenecarboxylic acid or 3,4,5-tribromothiophene-2-carboxylic acid. On-resin Stille coupling conditions, as previously reported by our lab, were applied with a 5,5'-bis(tributylstannyl)-2,2'-

bithiophene coupling partner to prepare either the bare or tetrabrominated OT4 (Scheme 1), taking advantage of the known regioselectivity for  $\alpha$ -thienyl bromides to undergo selective cross-coupling in preference to the more sluggish  $\beta$ -thienyl bromides.<sup>35</sup> The peptides were then cleaved from the resin to reveal the dual carboxylic acid termini.

**Spectroscopic Characterization of Peptide Assemblies.** Carboxylic acid functional groups along the peptide backbone render the peptides molecularly dissolved at high pH due to the stronger solvation of the electron-rich carboxylate groups. Upon acidification and protonation of these carboxylates, the assembly process is driven by enthalpic interactions that guide the embedded chromophores into co-facial stacking arrangements that bring about distinct spectroscopic changes. For example, under basic conditions **1**, **2**, and **3** have essentially identical UV-vis absorbance ( $\lambda_{\text{max}}$  of 422, 414, and 418 nm respectively) (Figure A3.1). A hypsochromic shift in absorbance ( $\lambda_{\text{max}}$  to 412, 367, and 370 nm, respectively) is observed for **1**, **2**, and **3** respectively upon acidification as well as a marked quench in emission intensity (Figure 3.2). These spectroscopic changes are typical hallmarks of H-like, co-facial stacking of the embedded  $\pi$ -conjugated cores and have been used to probe the assembly of peptide- $\pi$ -peptide nanomaterials in previous work by us and by others.<sup>36–38</sup>

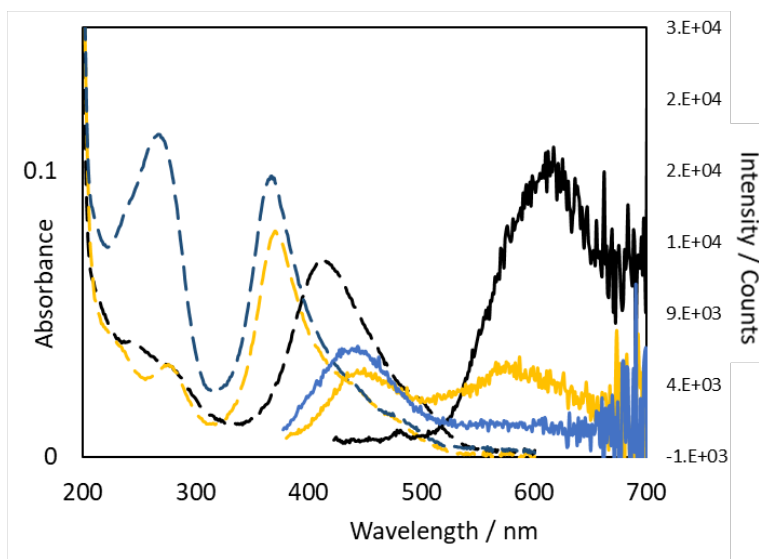


**Figure 3.2.** UV-vis absorbance (dashed) and PL (solid) spectra for **1** (black), **2** (blue traces), and **3** (yellow traces) under acidic conditions.

A consequence of OT4 bromination is the red shift in absorbance and emission profiles with respect to its unbrominated analogues. The strong overlap in absorbance of **1** and the emission of **2**, and **3** under acidic conditions around 440 nm meets the precondition for Förster resonance type energy transfer (ie. overlap of donor emission and acceptor absorbance that is maximized by specific inter-chromophore spacing distances and angles).<sup>39,40</sup> However, the spectroscopic characteristics that typify this type of energy transfer, such as enhanced acceptor emission intensity, can be diminished in these peptide assemblies by other forms of energy transfer or relaxation pathways (e.g. aggregated oligothiophene emission intensities tend to be very weak).<sup>6</sup> Furthermore, the broad and bimodal nature of the emission profiles of **2** and **3** respectively (with a low energy  $\lambda_{\text{max}}$  at ca. 580 nm), could overlap with the similarly broad emission profile of **1** ( $\lambda_{\text{max}}$  at 620 nm) and interfere with the assignment of any amplified acceptor emission. We examined these homo-assemblies by excitation at 350 nm where **1** should minimally absorb and 480 nm

where **2** and **3** should minimally absorb but found residual excitation under these conditions that could further complicate FRET analysis (Figure A3.2).

**Table 3.1.** Summary of peptide samples prepared by different assembly conditions.

Sample Name	Peptide Composition	Assembly Conditions	Expected Outcome
A	1,2	HCl	Statistical Co-assembly
B	1,2	Separately Assembled	Sorted Structures
C	1,2	GdL	Sorted Structures
D	1,3	HCl	Sorted Structures
E	1,3	Separately Assembled	Sorted structures
F	1,3	GdL	Sorted Structures
G	1	HCl	Homo-assemblies
H	4,2	HCl	Statistical Co-assembly
I	4,2	Separately Assembled	Sorted Structures
J	4,2	GdL	Sorted Structures
K	4,3	HCl	Sorted Structures
L	4,3	Separately Assembled	Sorted Structures
M	4,3	GdL	Sorted Structures

We examined the 1:1 co-assemblies of peptides **1-3** under three conditions as specified in Table 1. The UV traces for the solutions A-F are shown in Figure 3.3 a and b. In sample A, **1** and **2** should create statistical co-assemblies while in sample D, **1** and **3** are designed to self-sort. Counterintuitively, the UV trace of sample A has a bimodal absorbance that closely resembles that of the separately assembled samples B and E while D appears as a single broad peak. On the other hand, a bimodal absorbance is not observed in samples C or F, the GdL assemblies that should



theoretically form self-sorted structures. These conflicting data points are not aided by the PL signatures for samples A-F (Figure 3.3 c-h) where no obvious spectral changes are observed regardless of assembly condition or peptide identity. These data suggests that the global and statistical nature of these measurements cannot reliably distinguish the local changes in the presentation of the different monomers within the assembly for this brominated co-assembly system.

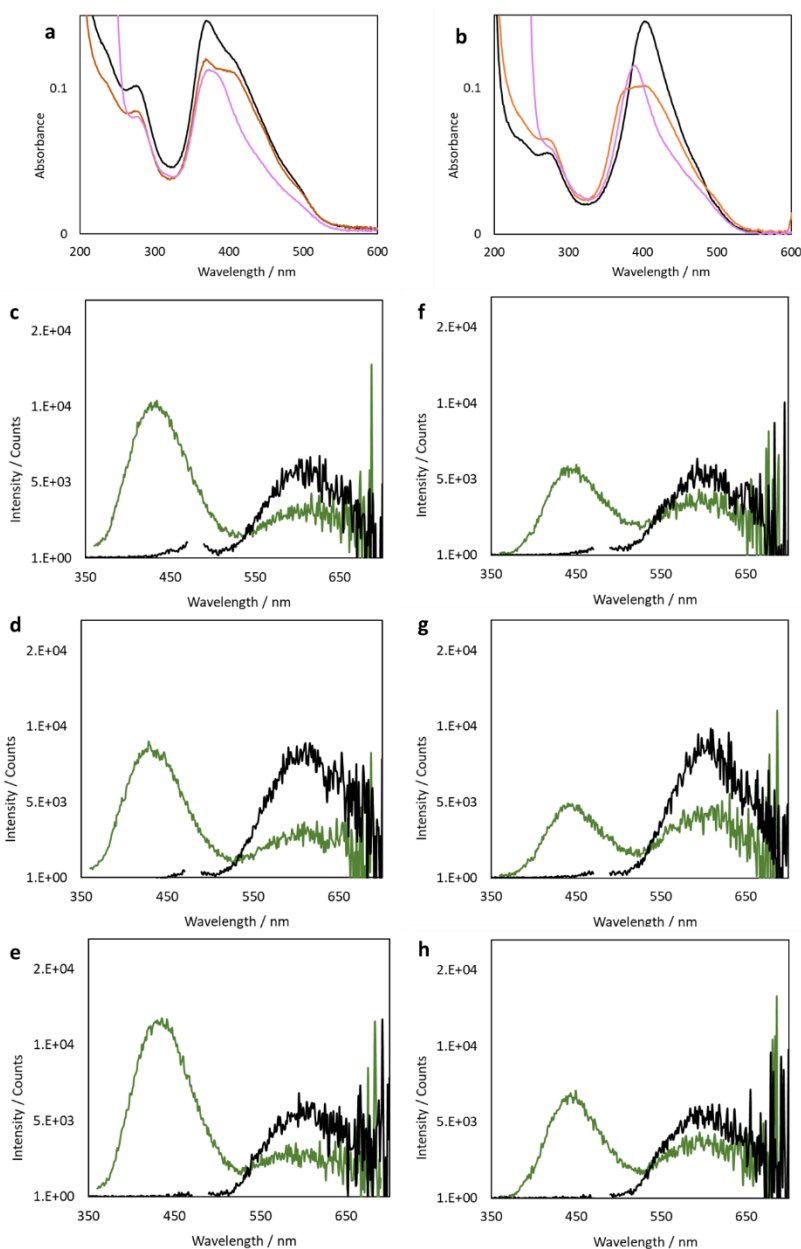


**Figure 3.3.** UV-vis signatures for 1:1 mixtures of (a) **1** and **2** and (b) **1** and **3** following rapid HCl acidification (black traces), separately assembled and then mixed (orange traces), and GdL assembled (purple traces) conditions. PL traces (c-h) following excitation at 350 (green traces) and 480 nm (black traces) following (c,f) rapid HCl acidification, (d,g) under separately assembled and then mixed, and GdL assembled (purple traces) conditions for samples A-C (c-e) and D-F (f-g).

The requisite overlap of donor emission and acceptor absorbance has also been demonstrated by our lab with OT4 and 1,4-distyrylbenzene (OPV3) wherein UV/PL measurements were suggestive of energy transfer from OPV3 to OT4.<sup>6</sup> As such we examined UV-vis absorbance (Figure A3.3, A3.4) and emission (Figure 3.4) of peptide **4** under different assembly conditions with **2** and **3** (samples H-M). Again, we probed these assemblies at 310 nm where OPV3 absorbs but OT4 absorbs minimally and at 450 nm where OT4 absorbs but OPV3 absorbs minimally. The emission of OPV3 (Figure 3.4, grey traces) under acidic conditions (ex. 310 nm) is relatively intense when compared to both OT4 bearing peptides (Figure 3.4, blue and yellow traces). Sample H (ex. 310 nm) shows a quenched emission relative to homo-assemblies of OPV3, however, the same sample when excited at 450 nm demonstrated enhanced emission relative to both OPV3 and OT4 homo assemblies at that same wavelength. Together these changes are suggestive of energy transfer from OPV3 to OT4. On the other hand, sample K (ex. 310 nm) shows an emissive signature similar to the separately assembled and mixed (sample L) and GdL assembled (sample M) possibly suggesting a degree of self-sorting in the HCl assembled sample of **3** and **4**. Similar to sample H, sample K shows an enhanced emission intensity at 450nm again suggesting energy

transfer from OPV3 to OT4. That said, there is also enhanced emission in samples L and M in the 450 nm channel relative to homo assemblies, suggesting energy transfer in these most certainly sorted structures. In this case, while the OPV3-OT4 systems provides evidence of self-sorting the indications of residual energy transfer are contradictory and impel an examination on a more local level to uncover details of nano domains within these materials.

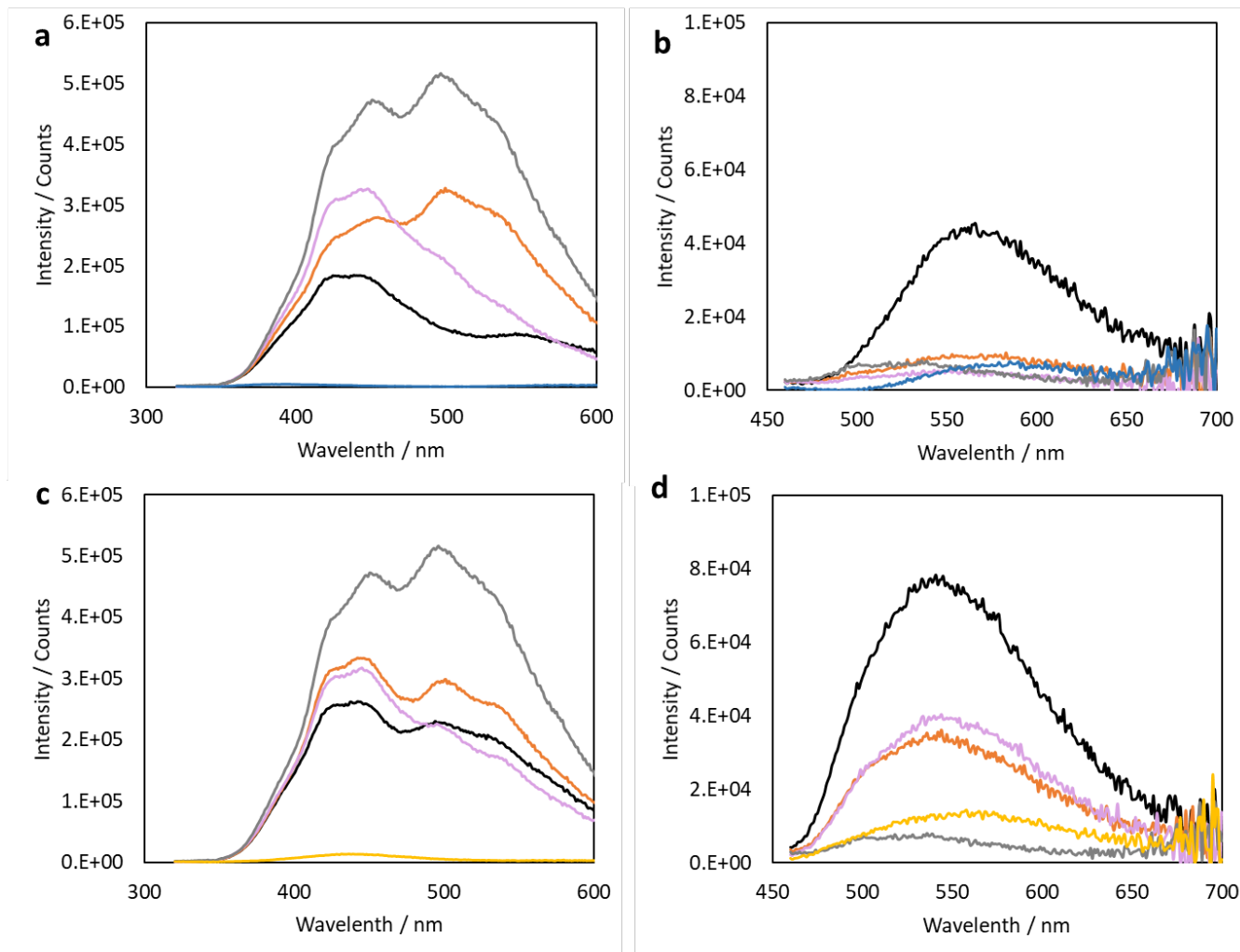


**Figure 3.4.** PL traces following excitation at 310 (a,c) and 450 nm (b,d) following rapid HCl acidification (black traces), under separately assembled and then mixed (orange traces), and GdL assembled (purple traces) conditions for samples H-J (a,b) and K-M (c,d). PL traces for homo assemblies of peptides **2**, **3**, and **4** are plotted for comparison in blue, yellow and grey respectively.

**Transmission Electron Microscopy and Elemental Analysis of Peptide Assemblies.** In principle, STEM-EDS could be used to generate elemental maps of bromine distributions within co-assemblies and illuminate more local indications self-sorting that were undistinguishable or convoluted in photophysical measurements. Samples A-D, G, and H-K were prepared and imaged with STEM-EDS techniques, with the help of Dr. Sz-Chian Liou at the University of Maryland NanoCenter. First, the viability and sensitivity of STEM-EDS to bromine was assessed by collecting an EDS spectrum over a large area of sample G, stained with 2% uranyl acetate, wherein a strong bromine peak at ca. 11.9 keV was observed corresponding to the bromine  $K_{\alpha}$  line. Next an elemental map of sample G was collected to show a coincidence of bromine in the regions where peptide material was present demonstrating that bromine can not only be detected in peptide nanomaterials using this technique but mapped on to regions of peptide nanowires (Figure 3.5).

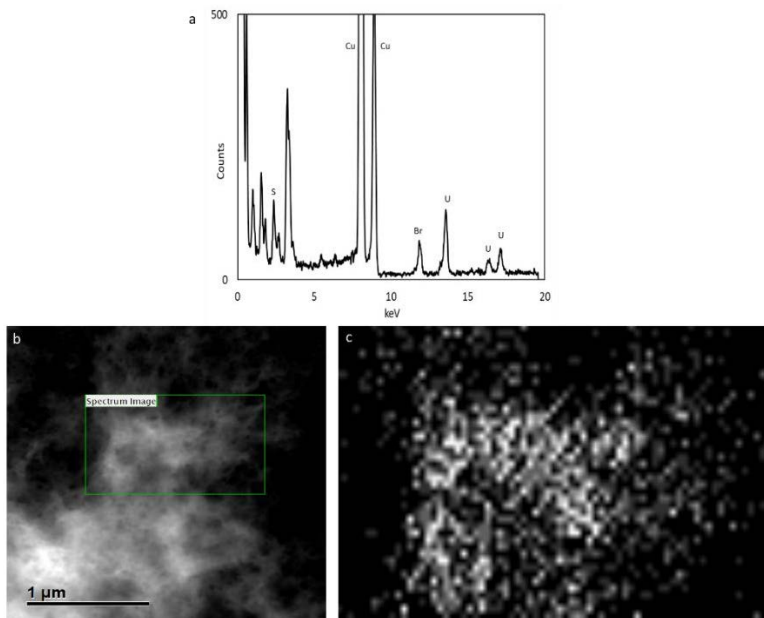


**Figure 3.5.** (a) Large area EDS spectrum of sample G showing strong presence of bromine  $K_{\alpha}$  line. (b) The peptide nanomaterials could be imaged wherein that demonstrates (c) bromine occurrence in areas of peptide density.

In general, minimization of the support film thickness increases image quality and spatial resolution. Furthermore, increased background signal from the 2% uranyl acetate stain typically used in bright field imaging sample preparation can obscure signals from the specimen. Thus, all samples were prepared on lacey carbon film and while nanomaterial is still visible, the distinct outline of each structure is less clearly defined without stain. Furthermore, initial elemental area heat mapping techniques were explored, the samples were delicate and characterized by low bromine EDS signal that limited the insightfulness of this technique. Line scan plots allow for longer dwell times and access higher signal to noise with significantly reduced data collection time due to limitations with instrumentation and were used initially to examine bromine distributions within the samples. Given the presence of sulfur peptides **1-3** we use this as an indicator of peptide presence while the bromine tag was used to signify self-sorting or co-mixing in the assemblies. We first examined Sample B wherein the separately assembled and then mixed sample preparation would ensure self-sorting among **1** and **2** (Figure 3.6). Indeed, areas of bromine enrichment can be observed with a signal emerging in the latter half of the scan while the sulfur signal is clearly detected throughout the entirety of the trace (Figure 3.6 b).

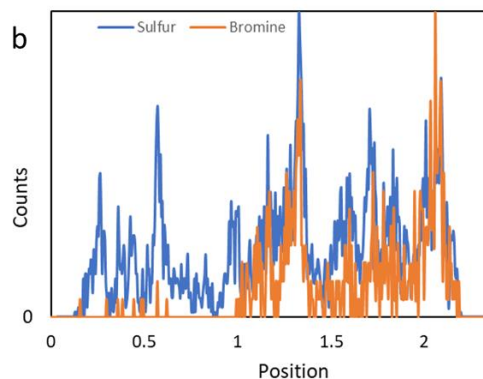
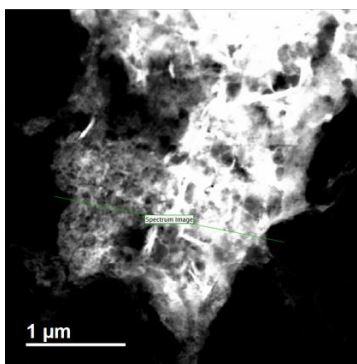


**Figure 3.6.** (a) Spectrum image and line scan path for sample B where (b) the normalized sulfur and bromine signals are detected and quantified.

To report on the influence of different assembly conditions to control supramolecular outcomes in co-assemblies, we examined samples A and C wherein the assembly trigger should control co-mixing or self-sorting, respectively. Figure 3.7a shows the spectrum profile for sample A where a line scan reveals the relative sulfur and bromine distributions to track with each other. More specifically, as the sulfur intensity increases so does the bromine intensity with the same general peak shape and character. When this same sample is assembled with a GdL pH reduction trigger we see the bromine signal does not perfectly mimic the intensity and shape of the sulfur signal, for example a spike in sulfur signal around 0.25 and 0.65 is not mimicked to the expected intensity in the bromine trace (Figure 3.7 c,d). These subtle changes to line scan profiles indicate self-sorting as would be expected under this subtle pH triggered assembly condition. We also examined sample D demonstrating similar outcomes. While the sample appears thinner and the signal to noise is diminished, there are clear areas where bromine and sulfur track together and regions where they do not, for example just before positions 1 and after 3 we see dramatic spikes in the sulfur signal but not in the bromine channel (Figure 3.7e,f).

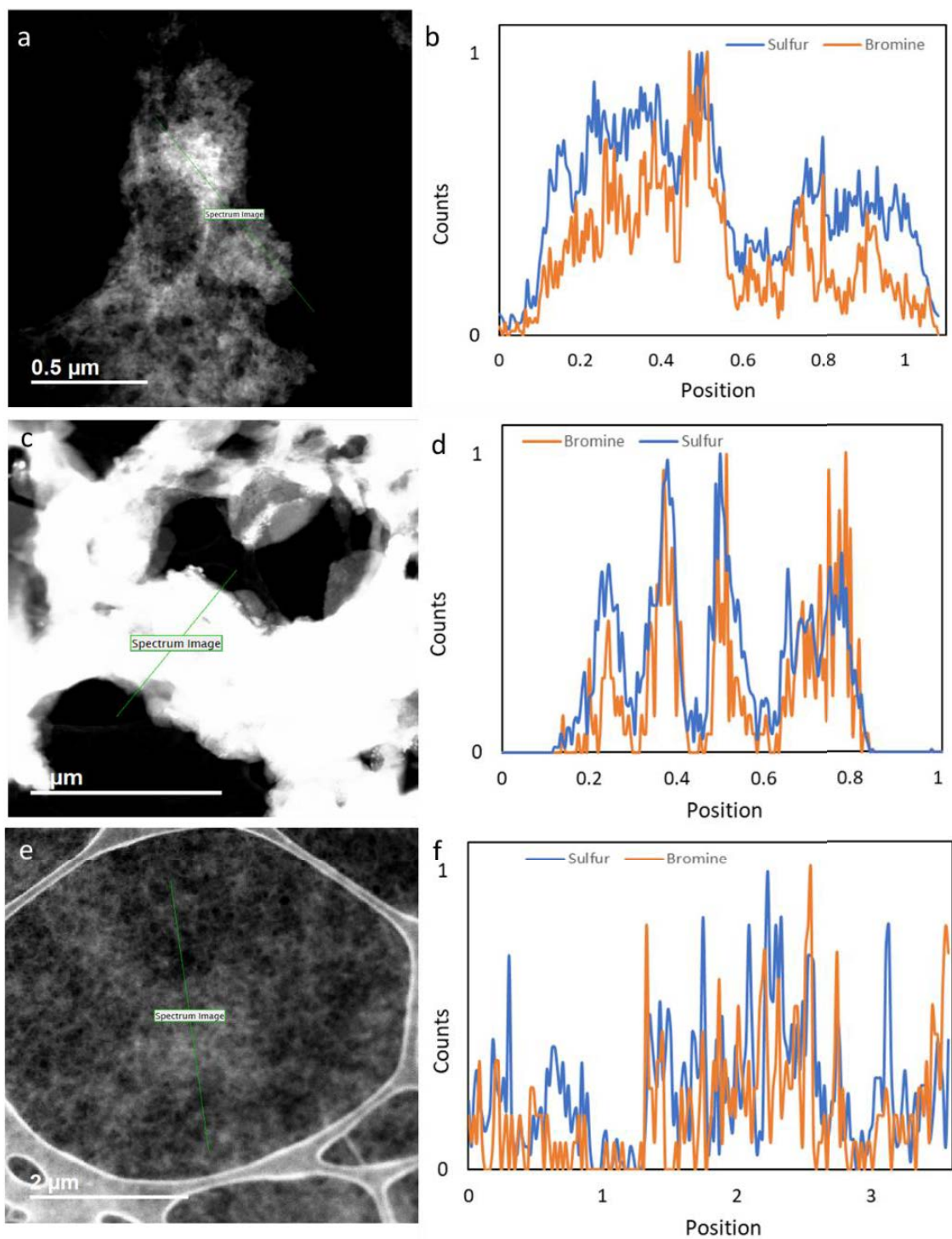


**Figure 3.7.** (a,c,e) Spectrum image and line scan paths for samples A, C and D where (b,d,f) sulfur and bromine signals are detected and quantified.



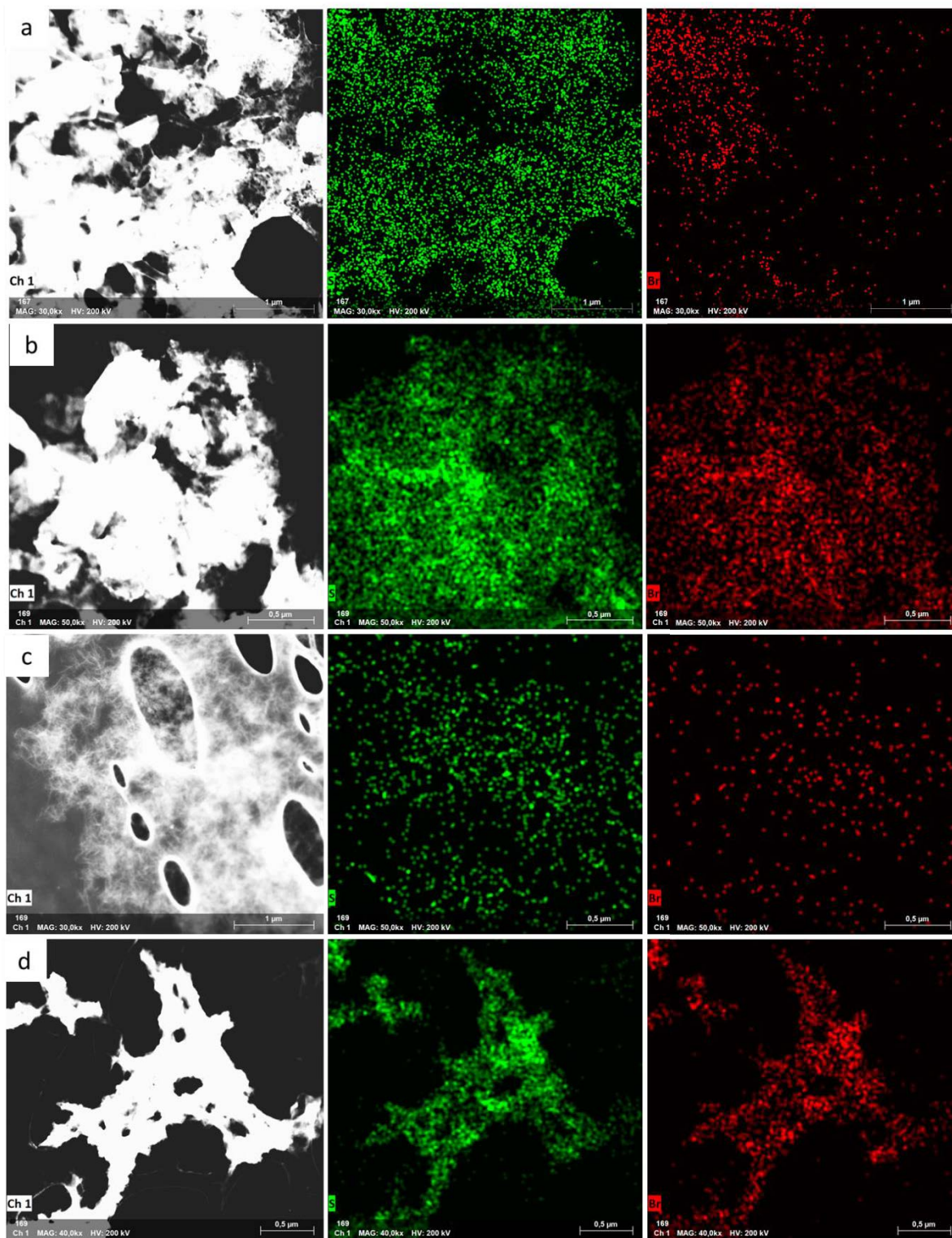


**Figure 3.8.** Spectrum image and elemental mapping for sulfur (green) and bromine (red) for samples (a) b, (b) a, (c) c and (d) d.



The elemental mapping data was collected for samples A-D wherein the localization of peptide was monitored by examination of sulfur presence and the effect of self-sorting or co-mixing was assessed by the enrichment of the bromine signal. As expected, samples A and B showed clear evidence of statistical co-assembly and sorted structures respectively. In the GdL, self-sorted, sample C we see regions of sulfur enrichment that do not have a corresponding signal in the sulfur channel that is suggestive of local regimes of segregation between the peptides. In the HCl triggered assembly of peptides **1** and **3** we see that the effects of self-sorting are more subtle. Regions wherein the signals do not coincide are observed, for example the region at the top right of the image. Given that these assemblies are rapidly assembled from a homogenous solution of peptide, it may be that advancements in technology can elucidate the subtle local orderings in this sample. However, checking this work with another mixed system would allow us to confirm some of these observations of self-sorting.

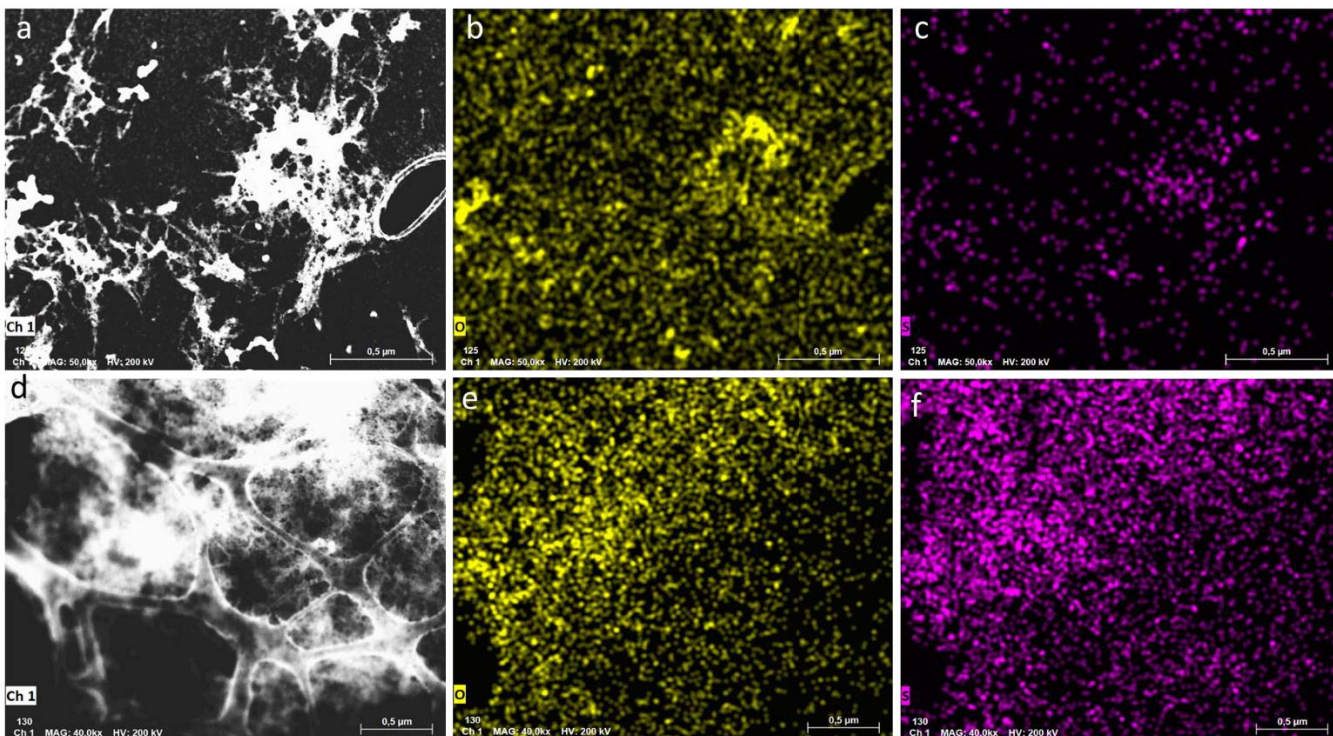


**Figure 3.9.** Spectrum images for (a-c) sample I and (d-f) sample H showing the spectrum images (a,d) and elemental mapping for oxygen (yellow, b,e) and sulfur (purple c,f) within the sample.

As such, I examined co-assemblies of OPV3 and OT4 (samples H-K) wherein we exploited oxygen as a marker of peptide presence and sulfur to indicate self-sorting or co-mixing. The separately assembled and mixed sample I shows subtle differences between oxygen and sulfur distributions as would be expected in this sorted sample (Figure 3.9 a-c). Statistical mixtures (ie. the HCl assembly of **2** and **4** in sample H) clearly show even distribution of both elements across the sample (Figure 3.9 d-f). In the GdL assembly of **2** and **4**, sample J, sulfur enrichment is observed at the top of the image but is minimal elsewhere. Oxygen has a strong signal throughout the image, albeit also enriched near the top (Figure 3.10 a-c). On the other hand, sulfur domains in sample K, the HCl assembly of **3** and **4**, are more subtle but can be distinguished (Figure 3.10 d-f). It could be that the nature of GdL triggered assembly creates clearly defined nanodomains of each peptide by exploiting their different effective pKas. The HCl assembly of **3** and **4** occurs rapidly from homogenous solution and relies on differences in monomer interaction energy that indeed trigger self-sorting but with structures that are more intimately associated which tracks well with the PL data suggesting residual energy transfer in sample K. The results demonstrate that STEM-EDS line scans can be used generally to examine outcomes of assembly paradigms through changes in assembly trigger as well as monomer design by tracking elemental composition on the nanoscale. That said, these studies push the resolution limits of available instrumentation. As technology advances and more resolved images can be attained, even more information could be gleaned from these elemental mapping techniques for informed material design.

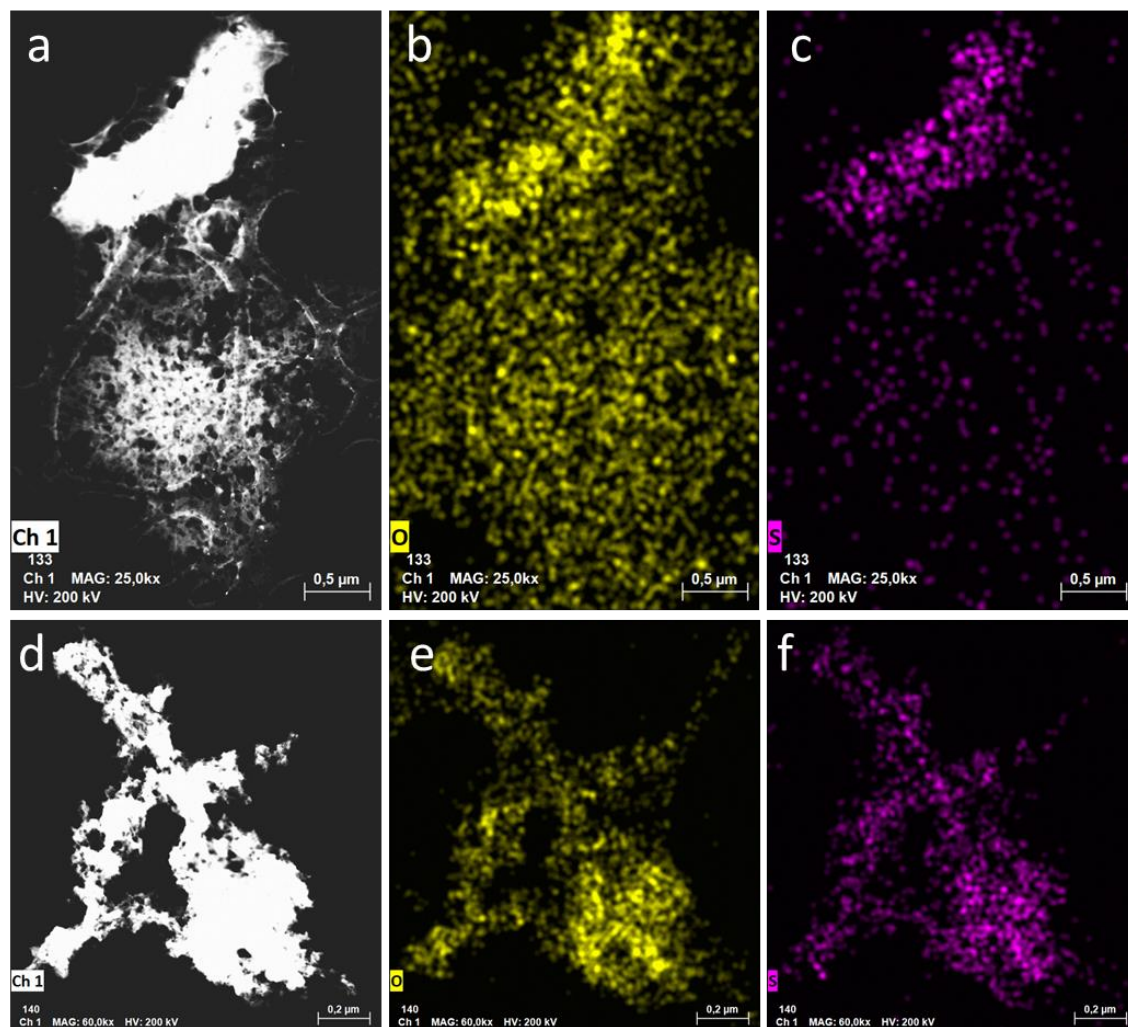


**Figure 3.10.** Spectrum images for (a-c) sample J and (d-f) sample K showing the spectrum images (a,d) and elemental mapping for oxygen (yellow, b,e) and sulfur (purple c,f) within the sample.

### Conclusion.

We have prepared a series of peptides to explore co-assembly of  $\pi$ -conjugated peptide nanomaterials. We developed a simple synthetic scheme that, when paired with on-resin palladium catalyzed Stille coupling procedures previously developed by our lab, allows the incorporation of bromine labels into a OT4 core. The nature of the assembly process can then be carefully selected by tailoring the peptide substituents flanking the brominated core and an unbrominated core to dictate self-sorting or co-mixing. We explore this by exploiting a pKa differential in the

brominated and unbrominated peptides and produce self-sorted structures through a slow decrease in pH upon hydrolysis of GdL. In another system we initiate self-sorting by assembly of a brominated peptide with an unbrominated peptide that has a longer hydrogen bonding motif to stabilize homo over hetero monomer interactions. We examine these assemblies through photophysical measurements wherein their broad excimeric signals and overlapping emission profiles obscure possible energy transfer that would be diagnostic in these systems. Instead we examined these assemblies through STEM-EDS imaging using the bromine labels as an elemental tag to uncover clear differences in line-scan profiles showing controlled self-sorting or co-mixing depending on system and assembly conditions. We also examine co-assemblies of OPV3-OT4 by way of photophysical and STEM-EDS measurements to confirm differences in assembly condition and monomer design on supramolecular outcome. With additional information using, for example, diffraction techniques, we envision that these distinct elemental analyses will be helpful in the implementation of similar materials in applications where spatial and hierarchical control of nanomaterial structure is critical to device function and performance.

## Experimental.

**General Considerations.** Reactions were carried out in flame-dried glassware under nitrogen atmosphere. Non-aqueous solvents were dried over molecular sieves and degassed by sparging with nitrogen for a minimum of 15 minutes. *N*-Bromosuccinimide (NBS) was obtained from Sigma-Aldrich and recrystallized before use. Tetrakis(triphenylphosphine)palladium ( $\text{Pd}(\text{PPh}_3)_4$ ) was obtained from Strem Chemicals. Chemicals used in solid phase peptide synthesis (Wang resin, 9-fluorenylmethyloxycarbonyl (Fmoc) protected amino acids, 2-(1H-benzotriazol-1-yl)-1,1,3,3-tetramethyluronium hexafluorophosphate (HBTU), benzotriazol-1-yl-

oxytripyrrolidinophosphonium hexafluorophosphate (PyBOP) and *N*-methylpyrrolidone (NMP)) were acquired from Advanced Chem. Tech., *N,N*-Diisopropylethylamine (DIPEA) was purchased from Fisher, and dried over 4Å molecular sieves before use. 4,4'-((1*E*,1'*E*)-1,4-phenylenebis(ethene-2,1-diyl))dibenzoic acid (OPV3 diacid) and 3,4,5-tribromothiophene-2-carboxylic acid were synthesized according to literature precedent.<sup>41,42</sup> All other chemicals were provided by Sigma-Aldrich or Fisher and used as they were received unless otherwise noted.

**General Fmoc-Based Peptide Synthesis:** Oligopeptide segments were synthesized via standard Fmoc-based solid phase peptide synthesis starting with the first Fmoc-amino acid preloaded onto Wang resin solid supports. The resin was swelled in dichloromethane (DCM) followed by deprotection of the Fmoc protecting group carried out in a solution of 20% v/v piperidine in *N,N*-dimethylformamide (DMF) for 2×10 min. The resin was washed with 3×NMP, 1×methanol (MeOH) followed by 3×DCM and swelled in DCM for 10 min. For all standard amino acid couplings, a solution of 3 equivalents of the succeeding Fmoc protected amino acid, 2.9 equivalents of HBTU was prepared in 10 mL of NMP and sonicated to dissolve, followed by 10 equivalents of DIPEA and mixed for one min. The resin was drained of DCM, the activated amino acid was added to the chamber, and mixed for a minimum of 1 hour. The resin was then drained and rinsed with 3×NMP, 1×MeOH followed by 3×DCM, swelled in DCM for 10 minutes and the process repeated starting with Fmoc deprotection for each sequential amino acid in the sequence. The success of each coupling step was monitored by performing a Kaiser test.

***N*-terminus-acylation, and on-resin Stille coupling procedure:** Peptides were acylated with 5-bromothiophene-2-carboxylic acid or 3,4,5-tribromothiophene-2-carboxylic acid and subjected to Stille cross-coupling conditions in the presence of 5,5'-bis-tributylstannyl-[2,2']-bithiophene as previously described.<sup>43</sup>

**General peptide cleavage and work-up:** Following solid-phase synthesis the peptide was cleaved by mixing the resin in a 2.5:2.5:95 Water:Triisopropylsilane (TIPS):Trifluoroacetic acid (TFA) cocktail for three hours. The solution was collected from the chamber, concentrated under vacuum, and triturated in cold diethylether. The suspended product was centrifuged to isolate and lyophilized. The lyophilized product was HPLC purified. Specific experimental procedures and molecular characterization data for each molecule synthesized can be found in the supporting information.

**Electrospray Ionization Mass Spectrometry (ESI-MS):** ESI signatures were samples using a Thermo Finnigan LCQ Deca Ion Trap Mass Spectrometer operating in negative mode. Samples were prepared in a 1:1 MeOH:water solution with 0.1% ammonium hydroxide.

**UV-Vis and Photoluminescence:** UV-Vis spectra were acquired using a Varian Cary 50 Bio UV-Vis spectrophotometer. Photoluminescence spectra were taken on a PTi Photon Technology International Fluorometer equipped with a Ushio Xenon short arc lamp. Spectroscopic samples of homo assemblies were prepared at ca. 3  $\mu$ M in Millipore water with a final volume of 3100  $\mu$ L. For co-assemblies, the appropriate volume of stock solutions were both added to 3000  $\mu$ L of Milli-Q water and the remaining volume was added to dilute to 3100  $\mu$ L and final concentration of ca. 3  $\mu$ M for both peptides. The pH was adjusted by adding either 1M KOH, 1M HCl or 10 mg/mL GdL. HCl samples were measured immediately upon addition of acid while GdL samples were measured at approximately 24 hours after GdL addition.

**Reverse-Phase HPLC:** Peptides were purified by reverse-phase HPLC on a Varian PrepStar SD-1 system equipped with a Phenomenex, Luna, 5  $\mu$ m particle diameter silica support functionalized with TMS terminated C8. An aqueous 0.1% ammonium formate buffer (pH 8):acetonitrile gradient was used as mobile phase.



**Transmission Electron Microscopy (TEM):** Conventional transmission electron microscopy (TEM), scanning TEM (STEM) high-angle annular dark-field (HAADF), and STEM energy dispersive x-ray spectroscopy (EDS) line-scans were collected using a JEM 2100 field emission TEM equipped with a Flash 6T/60 Bruker, silicon drift, EDS detector. The accelerating voltage was 200 keV for TEM. STEM-EDS line-scans and maps were acquired at a solid angle of 0.189 sr with 1-2 seconds per pixel dwell time and 1-2 nm step size. The samples were prepared by pipetting a drop of 1 mg/mL solution of assembled peptide in water onto ionized 200 mesh lacy carbon coated copper grids and incubated for 5 minutes at 25°C. Excess solution was removed by floating the grid in a drop of water. Some samples were then stained with a 2% uranyl acetate solution, washed by dipping in water, and excess moisture was wicked off by dabbing the grid on filter paper. The grids were allowed to dry completely in air before imaging.

## References.

- (1) Ardon, H. A. M.; Tovar, J. D.; Draper, E. R.; Adams, D. J.; Citossi, F.; Serpell, L. C.; Wallace, M. Kinetically Controlled Coassembly of Multichromophoric Peptide Hydrogelators and the Impacts on Energy Transport. *Journal of the American Chemical Society* **2017**, *139*, 8685–8692. <https://doi.org/10.1021/jacs.7b04006>.
- (2) Aronsson, C.; Dänmark, S.; Zhou, F.; Öberg, P.; Enander, K. Self-Sorting Heterodimeric Coiled Coil Peptides with Defined and Tuneable Self-Assembly Properties. *Nature Publishing Group* 1–10. <https://doi.org/10.1038/srep14063>.
- (3) Cross, E. R.; Sproules, S.; Schweins, R.; Draper, E. R.; Adams, D. J. Controlled Tuning of the Properties in Optoelectronic Self-Sorted Gels. *Journal of the American Chemical Society* **2018**, 8–11. <https://doi.org/10.1021/jacs.8b05359>.

- (4) Khalily, M. A.; Bakan, G.; Kucukoz, B.; Topal, A. E.; Karatay, A.; Yaglioglu, G.; Dana, A.; Guler, M. O. Fabrication of Supramolecular n/p-Nanowires via Coassembly of Oppositely Charged Peptide-Chromophore Systems in Aqueous Media. *ACS Nano* **2017**, *11*, 6881–6892. <https://doi.org/10.1021/acsnano.7b02025>.
- (5) Channon, K. J.; Devlin, G. L.; Macphee, C. E. Efficient Energy Transfer within Self-Assembling Peptide Fibers : A Route to Light-Harvesting Nanomaterials. *J. Am. Chem. Soc.* **2009**, No. 131, 12520–12521. <https://doi.org/10.1021/ja902825j>.
- (6) Ardoña, H. A. M.; Tovar, J. D. Energy Transfer within Responsive Pi-Conjugated Coassembled Peptide-Based Nanostructures in Aqueous Environments. *Chem. Sci.* **2015**, *6* (2), 1474–1484. <https://doi.org/10.1039/C4SC03122A>.
- (7) Ghosh, G.; Dey, P.; Ghosh, S. Controlled Supramolecular Polymerization of Pi-Systems. *Chem Comm* **2020**, *56*, 6757–6769. <https://doi.org/10.1039/d0cc02787a>.
- (8) Panettieri, S.; Ulijn, R. V. Energy Landscaping in Supramolecular Materials. *Current Opinion in Structural Biology* **2018**, *51* (February), 9–18. <https://doi.org/10.1016/j.sbi.2018.02.001>.
- (9) Sarkar, A.; Behera, T.; Sasmal, R.; Capelli, R.; Empereur-mot, C.; Mahato, J.; Agasti, S. S.; Pavan, G. M.; Chowdhury, A.; George, S. J. Cooperative Supramolecular Block Copolymerization for the Synthesis of Functional Axial Organic Heterostructures. *J. Am. Chem. Soc.* **2020**, *142*, 11528–11539. <https://doi.org/10.1021/jacs.0c04404>.
- (10) Zhang, K.; Yeung, M. C.; Leung, S. Y.; Yam, V. W. Living Supramolecular Polymerization Achieved by Collaborative Assembly of Platinum (II) Complexes and Block Copolymers. *PNAS* **2017**, *114* (45), 11844–11849. <https://doi.org/10.1073/pnas.1712827114>.
- (11) Zhang, W.; Jin, W.; Fukushima, T.; Saeki, A.; Aida, T. Supramolecular Linear Heterojunction Composed of Graphite-Like Semiconducting Nanotubular Segments. *Science* **2011**, *75*.



- (12) Voets, I. K.; Palmans, A. R. A.; Meijer, E. W. Supramolecular Block Copolymers under Thermodynamic Control. *J. Am. Chem. Soc.* **2018**, *140*, 7168–7175.  
<https://doi.org/10.1021/jacs.8b02706>.
- (13) Article, E.; Draper, E. R.; Lee, J. R.; Wallace, M.; Frank, J.; Cowan, A. J.; Adams, D. J. Self-Sorted Photoconductive Xerogels. *Chemical Science* **2016**, *7*, 6499–6505.  
<https://doi.org/10.1039/c6sc02644c>.
- (14) Pal, A.; Malakoutikhah, M.; Leonetti, G.; Tezcan, M.; Colomb-delsuc, M.; Nguyen, V. D.; Gucht, J. van der; Otto, S. Controlling the Structure and Length of Self-Synthesizing Supramolecular Polymers through Nucleated Growth and Disassembly. *Angewandte Chemie* **2015**, *54*, 7852–7856. <https://doi.org/10.1002/anie.201501965>.
- (15) Wang, K.; Guo, Z.; Zhang, L.; Sun, K.; Yu, P.; Zhou, S.; Wang, W.; Li, Z. Co-Assembly of Donor and Acceptor towards Organogels Tuned by Charge Transfer Interaction Strength. *Soft Matter* **2017**, *13* (10), 1948–1955. <https://doi.org/10.1039/C6SM02691E>.
- (16) Sugiyasu, K. A Block Supramolecular Polymer and Its Kinetically Enhanced Stability. *J. Am. Chem. Soc.* **2018**, *140*, 10570–10577. <https://doi.org/10.1021/jacs.8b06016>.
- (17) Whittell, G. R.; Chabanne, L.; Mitchels, J. M.; Gilroy, J. B.; Ga, T.; Richardson, R. M.; Winnik, M. A.; Manners, I. Monodisperse Cylindrical Micelles by Crystallization-Driven Living Self-Assembly. *Nature Chemistry* **2010**, *2* (May), 3–7. <https://doi.org/10.1038/nchem.664>.
- (18) Wang, X.; Guerin, G.; Wang, H.; Wang, Y.; Manners, I.; Winnik, M. A. Cylindrical Block Copolymer Micelles and Co-Micelles of Controlled Length and Architecture. *Science* **2007**, *317* (August), 644–648.
- (19) Self-assembly, P. C. C.; Patra, S. K.; Ahmed, R.; Whittell, G. R.; Lunn, D. J.; Dunphy, E. L.; Winnik, M. A.; Manners, I. Cylindrical Micelles of Controlled Length with a  $\pi$ -Conjugated

Polythiophene Core via Crystallization-Driven Self-Assembly. *J. Am. Chem. Soc.* **2011**, *133*, 8842–8845.

- (20) Qian, J.; Li, X.; Lunn, D. J.; Gwyther, J.; Hudson, Z. M.; Kynaston, E.; Rupar, P. A.; Winnik, M. A.; Manners, I. Uniform, High Aspect Ratio Fiber-like Micelles and Block Co-Micelles with a Crystalline  $\Pi$ -Conjugated Polythiophene Core by Self-Seeding. *J. AM. CHEM. SOC* **2014**, *136*, 4121–4124.
- (21) Sarkar, A.; Sasmal, R.; Das, A.; Venugopal, A.; Agasti, S.; George, S. J. Tricomponent Supramolecular Multiblock Copolymers With Tunable Composition via Sequential Seeded Growth. *Angewandte Chemie* **2021**. <https://doi.org/10.1002/ange.202105342>.
- (22) Yagai, S.; Ishii, M.; Karatsu, T.; Kitamura, A. Gelation-Assisted Control over Excitonic Interaction in Merocyanine Supramolecular Assemblies. *Angewandte Chemie* **2007**, *119*, 8151–8155. <https://doi.org/10.1002/ange.200702263>.
- (23) Das, A.; Molla, R.; Banerjee, A.; Paul, A. Hydrogen-Bonding Directed Assembly and Gelation of Donor – Acceptor Chromophores : Supramolecular Reorganization from a Charge-Transfer State to a Self-Sorted State. *Chem. Eur. J.* **2011**, *4*, 6061–6066. <https://doi.org/10.1002/chem.201100606>.
- (24) Nanorods, M. D.; Lohr, A.; Lysetska, M.; Würthner, F. Supramolecular Stereomutation in Kinetic and Thermodynamic Self-Assembly of Helical Merocyanine Dye Nanorods. *Angewandte Chemie* **2005**, *44*, 5071–5074. <https://doi.org/10.1002/anie.200500640>.
- (25) Dobson, C. M. Protein Folding and Misfolding. *Nature* **2003**, *426*, 884–890.
- (26) Dinner, A. R.; Andrej, S.; Smith, L. J.; Dobson, C. M.; Karplus, M. Understanding Protein Folding via Free-Energy Surfaces from Theory and Experiment. *Cell* **2000**, *4*, 331–339.

- (27) Tantakitti, F.; Boekhoven, J.; Wang, X.; Kazantsev, R. v.; Yu, T.; Li, J.; Zhuang, E.; Zandi, R.; Ortony, J. H.; Newcomb, C. J.; Palmer, L. C.; Shekhawat, G. S.; Olvera, M.; Cruz, D.; Schatz, G. C.; Stupp, S. I. Energy Landscapes and Functions of Supramolecular Systems. *Nature materials* **2016**, *15*, 469–477. <https://doi.org/10.1038/NMAT4538>.
- (28) Wall, B. D.; Zacca, A. E.; Sanders, A. M.; Wilson, W. L.; Ferguson, A. L.; Tovar, J. D.; Seitz, F. Supramolecular Polymorphism: Tunable Electronic Interactions within  $\Pi$ -Conjugated Peptide Nanostructures Dictated by Primary Amino Acid Sequence. *Langmuir* **2014**, *30*, 5946–5956. <https://doi.org/10.1021/la500222y>.
- (29) Sanders, A. M.; Magnanelli, T. J.; Bragg, A. E.; Tovar, J. D. Photoinduced Electron Transfer within Supramolecular Donor-Acceptor Peptide Nanostructures under Aqueous Conditions. *Journal of the American Chemical Society* **2016**, *138* (10), 3362–3370. <https://doi.org/10.1021/jacs.5b12001>.
- (30) Ardon, H. A. M.; Draper, E. R.; Citossi, F.; Wallace, M.; Serpell, L. C.; Adams, D. J.; Tovar, J. D. Kinetically Controlled Coassembly of Multichromophoric Peptide Hydrogelators and the Impacts on Energy Transport. *Journal of the American Chemical Society* **2017**, *139* (25), 8685–8692. <https://doi.org/10.1021/jacs.7b04006>.
- (31) Aggregates, O.; Albertazzi, L.; Zwaag, D. Van Der; Leenders, C. M. A.; Fitzner, R.; Hofstad, R. W. Van Der; Meijer, E. W. Probing Exchange Pathways in One-Dimensional Aggregates with Super-Resolution Microscopy. *Science* **2014**, *344* (May), 491–495.
- (32) Silva, R. M. P.; Zwaag, D. Van Der; Albertazzi, L.; Lee, S. S.; Meijer, E. W.; Stupp, S. I. Super-Resolution Microscopy Reveals Structural Diversity in Molecular Exchange among Peptide Amphiphile Nanofibres. *Nature Communications* **2016**, No. May, 1–10. <https://doi.org/10.1038/ncomms11561>.

- (33) Kumar, M.; Son, J.; Huang, R. H.; Sementa, D.; Lee, M.; Brien, S. O.; Ulijn, R. v. In Situ, Noncovalent Labeling and Stimulated Emission Depletion-Based Super-Resolution Imaging of Supramolecular Peptide Nanostructures. *ACS Nano* **2020**, *14*, 15056–15063. <https://doi.org/10.1021/acsnano.0c05029>.
- (34) Thomas, F.; Boyle, A. L.; Burton, A. J.; Woolfson, D. N. A Set of de Novo Designed Parallel Heterodimeric Coiled Coils with Quantified Dissociation Constants in the Micromolar to Sub - Nanomolar Regime. *J. Am. Chem. Soc* **2013**, *135*, 5161–5166. <https://doi.org/10.1021/ja312310g>.
- (35) Sanders, A. M.; Tovar, J. D. Solid-Phase Pd-Catalysed Cross-Coupling Methods for the Construction of  $\pi$ -Conjugated Peptide Nanomaterials. *Supramolecular chemistry* **2014**, *26*, 259–266. <https://doi.org/10.1080/10610278.2013.852675>.
- (36) Wall, B. D.; Zhou, Y.; Mei, S.; Herdeline, J.; Ardoña, A. M.; Ferguson, A. L.; Tovar, J. D. Variation of Formal Hydrogen-Bonding Networks within Electronically Delocalized  $\Pi$ -Conjugated Oligopeptide Nanostructures. *Langmuir* **2014**, *30*, 11375–11385. <https://doi.org/10.1021/la501999g>.
- (37) Ardoña, H. A. M.; Besar, K.; Togninalli, M.; Katz, H. E.; Tovar, J. D. Sequence-Dependent Mechanical, Photophysical and Electrical Properties of  $\Pi$ -Conjugated Peptide Hydrogelators. *J. Mater. Chem. C* **2015**, *3* (3), 6505–6514. <https://doi.org/10.1039/c5tc00100e>.
- (38) Tovar, J. D.; Claussen, R. C.; Stupp, S. I. Probing the Interior of Peptide Amphiphile Supramolecular Aggregates. *Journal of the American Chemical Society* **2005**, *127* (20), 7337–7345. <https://doi.org/10.1021/ja043764d>.
- (39) Sindbert, S.; Kalinin, S.; Nguyen, H.; Kienzler, A.; Clima, L.; Bannwarth, W.; Appel, B.; Sabine, M.; Seidel, C. A. M. Accurate Distance Determination of Nucleic Acids via FRET Resonance

Energy Transfer : Implications of Dye Linker Length and Rigidity. *J. Am. Chem. Soc* **2011**, *133*, 2463–2480. <https://doi.org/10.1021/ja105725e>.

- (40) Dacres, H.; Wang, J.; Dumancic, M. M.; Trowell, S. C. Experimental Determination of the Förster Distance for Two Commonly Used Bioluminescent Resonance Energy Transfer Pairs. *Analytical Chemistry* **2010**, *82* (1), 432–435. <https://doi.org/10.1021/ac9022956>.
- (41) Wang, J.; Seefeld, M. A.; Luengo, J. Unusual Ligand-Dependent Chemoselective Suzuki – Miyaura Cross-Coupling Reactions of 3-Bromo-4-Trifloyl-Thiophenes. *Tetrahedron Letters* **2011**, *52* (48), 6346–6348. <https://doi.org/10.1016/j.tetlet.2011.09.026>.
- (42) Vadehra, G. S.; Wall, B. D.; Diegelmann, S. R.; Tovar, J. D. On-Resin Dimerization Incorporates a Diverse Array of p-Conjugated Functionality within Aqueous Self-Assembling Peptide Backbones. *Chemical Communications* **2010**, *46*, 3947–3949. <https://doi.org/10.1039/c0cc00301h>.
- (43) Dimerizations, C. S.; Sanders, A. M.; Dawidczyk, T. J.; Katz, H. E.; Tovar, J. D. Peptide-Based Supramolecular Semiconductor Nanomaterials via Pd- Catalyzed Solid-Phase “ Dimerizations .” *ACS Macro Letters* **2012**, *1*, 1326–1329.

## **Chapter 4**

### **Fluorination Strategies for Molecular Engineering of Diphenylalanine Peptides**

## Introduction

Intermolecular interactions among aromatic units, termed  $\pi$ - $\pi$  stacking, are critical for the folding, stabilization and function of proteins, but also constitute a powerful force in misfolding and aggregation.<sup>1</sup> Indeed, phenylalanine dipeptide is considered an important consensus sequence in the assembly of amyloid plaques that manifests in neurological disorders such as Alzheimer's disease.<sup>2,3</sup> The power of aromatic residues to self-associate is supported by the observation that even an unmodified phenylalanine amino acid can self-assemble into distinct fibrillar structures.<sup>4</sup> In the context of nanomaterials, diphenylalanine and its derivatives have found a place as environmentally benign yet powerful low molecular weight gelators in applications such as tissue scaffolding, cell culture, and drug delivery.<sup>5</sup> Efforts to understand the mechanisms of Phe-Phe assembly and their impacts on physical properties will be crucial not only for advancement in these numerous applications but fundamental investigations of these primary units could reflect on our understanding of the field as a whole and the basis of nanotechnology.

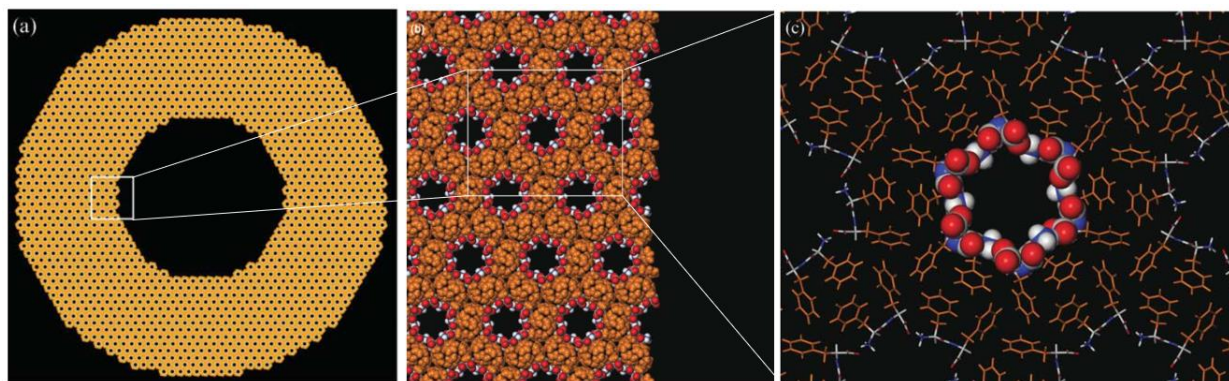


**Figure 4.1.** Model of the A) crystal structure of diphenylalanine demonstrating a B) porous laminated structure composed of C) individual nanotubes formed by head-to-head hydrogen bonding of diphenylalanine peptide backbone. Adapted from reference 2. Copyright Royal Society of Chemistry, 2006.

Studies by Reches and Gazit concluded that crystallized assemblies of nanotubes exhibit a

polymorphic crystal structure from that of isolated tubes.<sup>6</sup> Gorbitz and coworkers later compared the crystal structure of diphenylalanine fibers prepared by fast evaporation of an aqueous solution of the peptide at 80°C to that of an isolated peptide nanotube grown through a solvent switch technique. These structures were self-consistent and identical to x-ray spectra predicted through computational modeling. The crystal structure as demonstrated by Gorbitz is represented in Figure 4.1. Nanotube channels are constructed from the head-to-tail salt bridge formation by six diphenylalanine molecules Figure 4.1c. Nanotubes stack vertically through hydrogen bonding and assembled further into fibers through side chain edge-to-face  $\pi$ -stacking interactions as can be seen in Figure 4.2a,b.<sup>7,8</sup> The hydrophilic inner structure of the pore runs parallel to the long axis of the fiber and has been shown to engage in host-guest chemistries, for example the encapsulation of solvated metal ions.<sup>4,7</sup> More recent molecular dynamics simulations reveal that the aromatic interactions steer the assembly early on in the assembly process and the zwitterionic interactions power organization into a more ordered state that eventually forms higher order assemblies again driven by side chain interactions.<sup>9</sup> Furthermore, investigations into the assembly and crystal structures of other aromatic dipeptide species, most notably the phenylalanine-tryptophan dipeptide, yielded similar porous crystal structures as observed in the diphenylalanine species.<sup>7</sup>

**Table 4.1:** Assemblies of phenylalanine containing peptides can access a myriad of morphologies.

Reprinted from reference 4. Copyright Royal Society of Chemistry, 2014.



Compound name	Assemblies structured	Additional information
H-Phe-Phe-OH (FF)	Tubes, spheres, quantum-dots	Young modulus = 19–30 GPa, $\beta$ -sheet
H-Phe-Phe-NH <sub>2</sub>	Nanotubes	
Ac-Phe-Phe-NH <sub>2</sub>	Nanotubes	Nanospheres
H-Phg-Phg-OH	Nanospheres	
H-Cys-Phe-Phe-OH	Nanospheres	Young modulus = 140–275 GPa
Boc-Phe-Phe-OH (Boc-FF)	Tubes, spheres	
Cbz-Phe-Phe-OH	Amyloid-like structures	$\alpha$ -Helix or $\beta$ -turn $G' = 2 \times 10^4$ Pa, $\beta$ -sheet
Cyclo-Phe-Phe	Tubular structures	
Fmoc-Phe-Phe-OH	Fibrous-hydrogel	$\beta$ -Sheet
Fmoc-Phe-Gly-OH	Fibrous-hydrogel	
Fmoc-2-Nal-OH	Fibrous-hydrogel	$\beta$ -Sheet
Fmoc-Gly-Phe-OH	Microtubes	
Fmoc-Phe-Arg-Gly-Asp-OH	Fibrous-hydrogel	$\beta$ -Sheet
Fmoc-Arg-Gly-Asp-Phe-OH	Fibrous-hydrogel	
Fmoc-Arg-Gly-Asp-OH	Nanotubes	Spheres
Fmoc-Phe-Ser( <i>t</i> Bu)	Spheres	
Fmoc-Phe-Pro-OH	Spheres	Point stiffness $\sim 1.25$ GPa
di-D-1-naphthylalanine	Tubular structures	
di-D-2-naphthylalanine	Tubular structures	9
H-( <i>p</i> -fluoro-Phe)-(p-fluoro-Phe)-OH	Tubular structures	
H-(pentafluoro-Phe)-(pentafluoro-Phe)-OH	Tubular structures	9
H-( <i>p</i> -iodo-Phe)-(p-iodo-Phe)-OH	Fibrillar structures	
H-( <i>p</i> -nitro-Phe)-(p-nitro-Phe)-OH	Fibrillar structures and spheres	$\beta$ -Sheet
H-(4-phenyl-Phe)-(4-phenyl-Phe)-OH	Squared plates	
H-Phe-Phe-Phe-OH	Nanoplates	

N or C-terminal modifications to diphenylalanine have been well documented to influence crystal structure and supramolecular architectures ranging from tubes and spheres to hydrogels (Table 1).<sup>4</sup> For example unprotected Phe-Phe can assemble into mixed populations of tubes and spheres, however, the addition of an N-terminal tert-butyl dicarbonate group (Boc) can form tubes and spheres as the solvent is switched from water to water ethanol mixtures respectively.<sup>10</sup> Another system that has been widely studied is the N-fluorenylmethoxycarbonyl protected diphenylalanine (Fmoc-Phe-Phe) which readily forms a hydrogel under physiological conditions based on nanocylindrical structures formed from anti-parallel  $\beta$ -sheets among the peptides and interlocking pi-pi stacking interactions between the Fmoc and phenyl moieties as is shown in Figure 4.2d. This, again, highlights the power of the  $\pi$ - $\pi$  stacking interactions as the formation of the nanotubular structures within Phe-Phe nanomaterials remains despite the absence of head-to-tail hydrogen bonding observed in the unprotected structure.<sup>11</sup> Adams and co-workers have extensively studied the properties of Fmoc-Phe-Phe and other capped diphenylalanine hydrogels diving deep into their rheological properties, assembly conditions, network characteristics and molecular packing and electronic properties.<sup>12–16</sup>

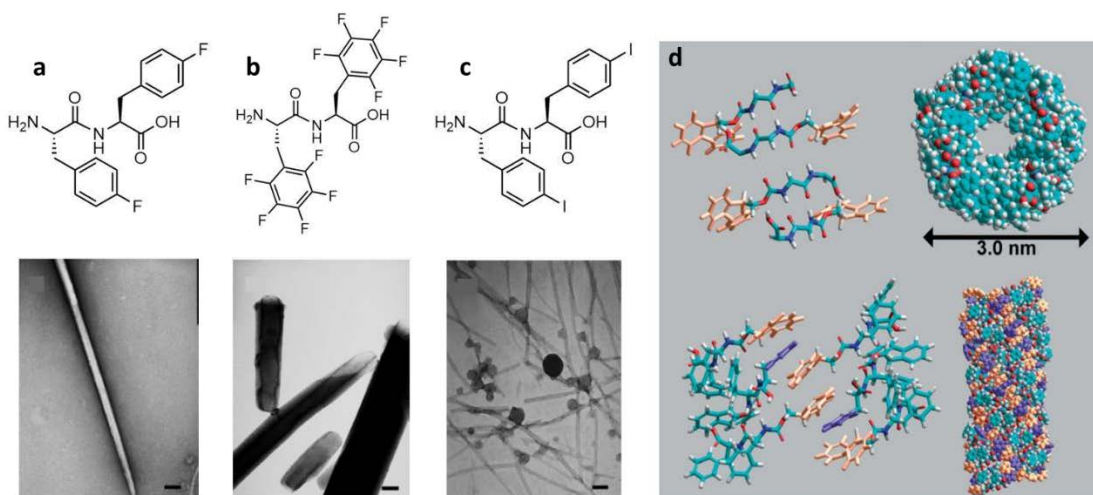


**Figure 4.2:** Simple molecular modifications of diphenylalanine induce morphological changes wherein a) para-fluoro induces tubular formation, b) per-fluorination results in wider tubular structures, c) para-iodo substitution results in a mixture of spheres and fibrillar structures, and d) Fmoc-protection of the N-terminus dictates a nanotubular structure. Reprinted from references 18 and 11. Copyright IOP Publishing Ltd, 2006 and WILEY-VCH Verlag GmbH & Co. KGaA, Weinheim, 2008.

Nanostructure morphology has also been controlled through modulation of electronic distributions.<sup>17</sup> For example, and as shown in Table 1, aromatic substitution of phenylalanine containing peptides with electron withdrawing groups such as a fluorine and other halogens can dictate the formation of tubes, fibers, or plates (Figure 4.2 a-c).<sup>17,18</sup> Fluorine has often been exploited as a conformational tool in organic chemistry and biological chemistry. With its atomic radius between hydrogen and oxygen, and high electronegativity, a single hydrogen-to-fluorine substitution can dramatically alter electronic distributions with minimal change to molecular size.<sup>19</sup> Nilsson and coworkers found that perfluorination and even monofluorination of the Phe-Phe phenyl ring increased gelation rates when compared to unfluorinated reference

compounds.<sup>5,20,21</sup> Another example lies in liquid crystal (LC) technology wherein fluorination of rigid LC cores establishes dielectric anisotropy and facilitates molecular reorientation upon the application of an external electric field.<sup>22,23</sup> Fluorine incorporation into small alkyl bridges between mesogenic LC cores has also proven useful for manipulating material performance by increasing clearing temperatures and the nematic phase ranges. Computational analysis of cores linked by CF<sub>2</sub>-CF<sub>2</sub> spacers (Figure 4.3A) by Kirsch and Bremer demonstrated that molecular conformation is governed by a preference of 2.62 kcal mol<sup>-1</sup> for the gauche conformation as opposed to a preference of 0.66 kcal mol<sup>-1</sup> in the non-fluorinated analog. This preference is attributed to  $\sigma_{\text{CH}}$  to  $\sigma^*_{\text{CF}}$  “negative” hyperconjugation that can only be achieved in the gauche conformation (Figure 4.3B). Finally, this result is consistent with the increased clearing point and nematic phase range observed, properties that are enhanced with “straight” molecular geometry in the gauche-conformation as opposed to the “bent” geometry of the anti-conformation.<sup>22</sup> Due to the focus of previous studies on aromatic fluorination, and the unexploited prospect of perturbations in stereo-electronics such as the gauche, anomeric effect and hyperconjugation, fluorination at the  $\beta$ -carbon is an interesting next step for control over diphenylalanine supramolecular structures.<sup>19</sup>

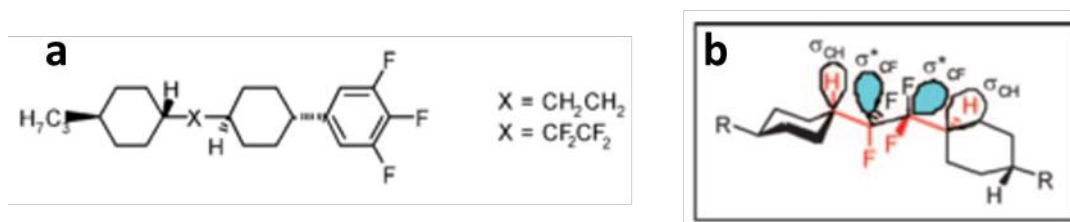


**Figure 4.3:** Effect of fluorination on alkyl spacers in liquid crystal cores. A) Structure of a model liquid crystal core B) stabilization of conformer through negative hyperconjugation. Adapted from reference 22. Copyright Wiley-VCH Verlag GmbH&Co. KGaA, Weinheim, 2010.

The impacts of fluorination are not limited to intramolecular phenomena. Due to its high

electronegativity, fluorine has been well documented to influence intermolecular interactions and crystal structures by changing electronic distributions. For example, the perfluorination of aromatic systems inverts the electronic distribution within the molecule with respect to protonated analogues as is exemplified with stilbene and perfluorostilbene in Figure 4.4. Patrick and Prosser in 1960 reported the crystal geometry of a 1:1 mixture of stilbene and perfluorostilbene as stacked structures of alternating protonated and fluorinated molecules. The packing arrangement reported for the co-crystal was disparate from the edge-to-face stacking observed in pure solutions of these molecules and was attributed to favorable electrostatic interactions from fluorination. Finally, changes in electronic distributions due to fluorination expand the available intermolecular interactions accessible such as  $F\cdots H$  hydrogen bonding,  $C-F\cdots\pi$ , and in rare occasions  $F\cdots F$  interactions.<sup>24</sup>

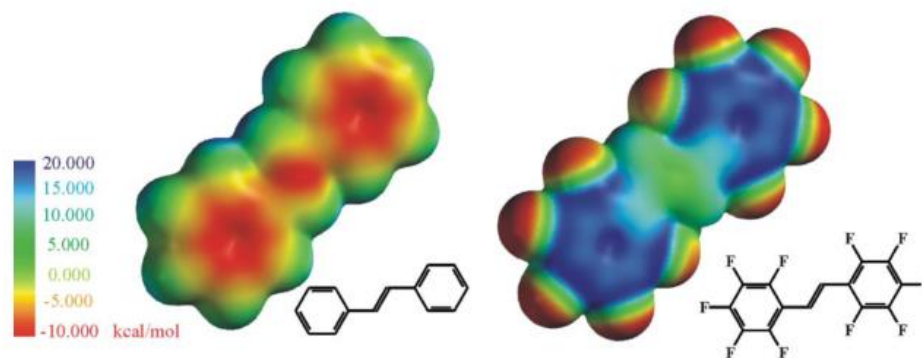
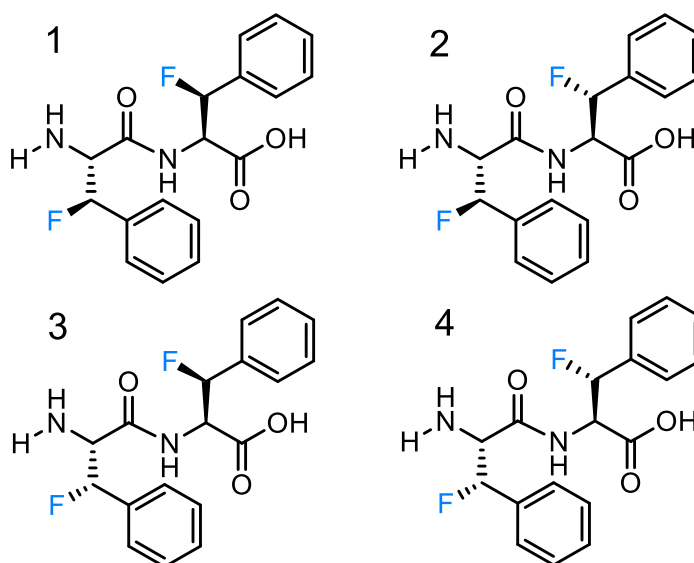


**Figure 4.4.** Heatmap demonstrating the changes in electronic distribution upon perfluorination of stilbene as calculated by PC Spartan. Reprinted from reference 24. Copyright Royal Society of Chemistry, 2005.

Given the unique physical and chemical properties of phenylalanine peptide, the strong dipole moment of the C-F bond and differences in molecular conformation and intermolecular interactions observed upon fluorination, we thought to systematically study of the impacts of

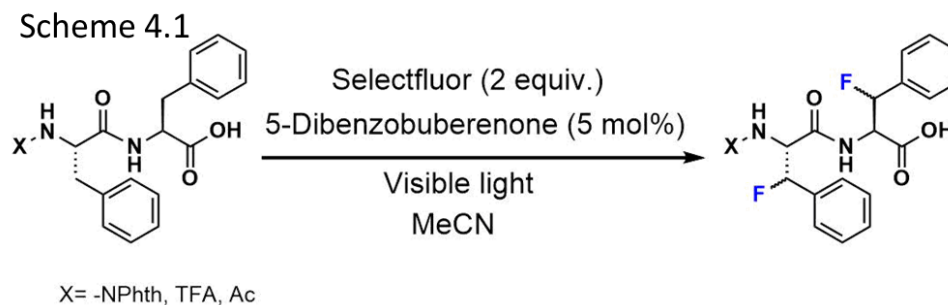
mono-fluorination at diphenylalanine's  $\beta$ -carbons. We suspected that spatial orientation of C-F dipole vectors as presented in the four possible diastereomers (**1-4**) would dramatically impact molecular conformation and assembly properties with respect to nonfluorinated analogs while posing a minimal structural perturbation. With this work, we hope to contribute a new strategy of molecular engineering Phe-Phe by way of this simple fluorine atomic substitution that could inform future applications of this promising dipeptide material.



## Results and Discussion

Advances in fluorination chemistry in recent years have yielded a mild approach to selectively fluorinate amino acids. Leckta and coworkers demonstrated remarkably selective mono-fluorination of phenylalanine and phenylalanine containing peptides at  $\beta$ -positions, using Selectfluor®, catalytic amounts of a dibenzosuberone photosensitizer and visible light (Scheme 4.1). The photochemical nature of the radical reaction requires strategic selection of protecting groups to prevent side reactions and maintain high yields. While C-terminal protection is unnecessary, N-terminal protecting groups such as phthalimido (NPhth), trifluoroacetate (TFA)

and acetate (Ac) were necessary to achieve 80%, 67% and 57% fluorination yields respectively.<sup>25</sup>



As an initial step, I performed preliminary DFT calculations using the crystal structure coordinates of the unprotected unfluorinated dipeptide (CCDC #: 163340). While holding the atomic coordinates of the crystal structure static, we made fluorine substitutions at each alpha carbon to generate all four possible monofluoro diastereomers and calculated the free energy of these new species as compared to the unfluorinated molecule (Figure 4.5a) using the B3LYP functional and 6-31+G(D) basis set. The most striking outcomes of this computational study are that the free energies of the S,R and R,R diastereomers are calculated to be 0.0 and 55.0 kcal/mol higher than the unfluorinated dipeptide (Figure 4.5 b,c). In the S,R case, the unchanged free energy could be due to a F-H hydrogen bond-like interaction, as shown in Figure 4.6c wherein the H(81) and F(85) atoms appear to be in close contact. On the other hand, the high free energy of the R,R diastereomer may be due to the unfavorable proximity of F(85) and F(84) as shown in Figure 4.6d. These preliminary results provide motivation for this study and indicate that simple fluorination of these peptides could control supramolecular assembly, crystal packing and possible physical properties of these materials.

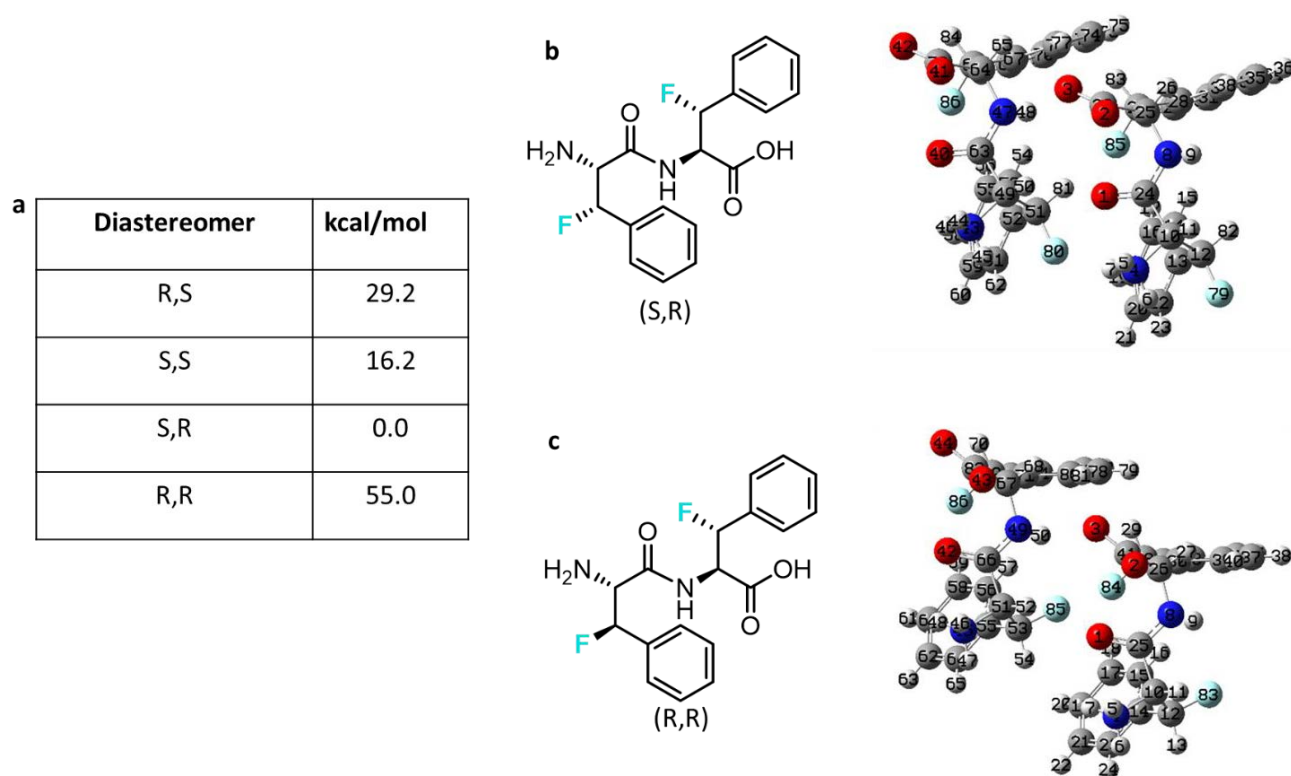


**Figure 4.5.** a) Relative energies of **1-4** as obtained by DFT calculations with representative structures of the b) S,R and c) R,R diastereomers.

Experimentally, I started by obtaining difluorinated NPhth-Phe-Phe-OH prepared by Desta Bume in the Leckta group. The phthalimido protecting group was selected for its optimized yield and compatibility with fluorination and the reaction conditions have been well established to selectively mono-fluorinate the benzylic beta-carbon.<sup>25,26</sup> I started by attempting separation by flash chromatography of all four NPhth-Phe-Phe-OH diastereomeric products but was unsuccessful due to co-elution. Ideally, the summation of differently arranged dipole vectors should offer subtle differences in polarity that would allow for separation, however, in practice this could not be achieved. I then obtained a mixture of fluorinated NPhth-Phe-OH diastereomers from Stefan Harry from the Leckta group (**5**, **6**) with the idea that it could be coupled on resin to prepare monofluorinated diphenylalanines or serve as a test case for the hypothesis that even mono

fluorination would disrupt normal electronic distributions to sufficiently change molecular interactions.

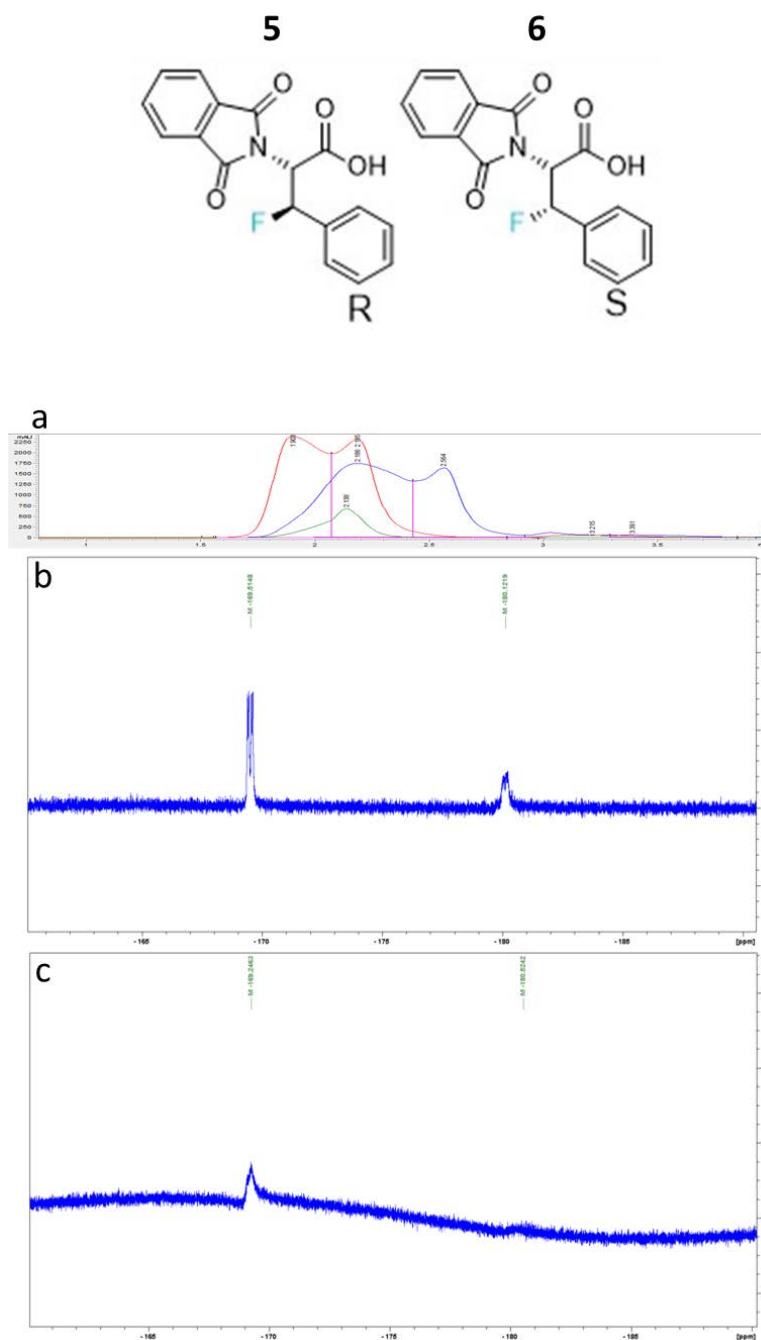


**Figure 4.6.** A) HPLC traces of separation of using **5** and **6** column and MeOH isocratic method (green trace), gradient from 100:0- 50:50 MeOH:Hex (red trace), gradient from 100:0-98:2



MeOH:IPA (blue trace).  $^{19}\text{F}$ -NMR spectra of B) mixture of diastereomers of **5** and **6** and C) following chiral column purification.

I tried a series of normal phase separation methods that were not able resolve the fluorinated diastereomers from each other. I was able to borrow a Pirkle-type column for separations, whose chiral stationary phase can engage in  $\pi$ - $\pi$ , dipole, and hydrogen-bonding interactions, that I screened under isocratic and gradient conditions to separate the diastereomers. An isocratic separation method with methanol as the eluent failed to separate the diastereomers (Figure 4.6a, green trace). A gradient method with methanol and hexanes achieved small resolution (Figure 4.6 a, red trace) that increased with a more gradual change in solvent polarity, where a gradient from pure methanol to 98% isopropanol achieved the best separation (Figure 4.6a, blue trace).  $^{19}\text{F}$ -NMR is diagnostic in assessing the diastereomeric purity of these molecules as the fluorine environments are distinct chemically. The  $^{19}\text{F}$ -NMR of the mixture of diastereomers in Figure 4.6b shows the distinct chemical shifts of the diastereomers at around -169 and -180 ppm. Due to the small injection size dictated by the chiral column used, 10 injections of the diastereomer mixture were cumulatively collected and compiled using a fraction collector timed to collect in 20 second intervals as to consistently collect time-points of the separated peaks. A dilute sample of the first peak was analyzed with  $^{19}\text{F}$ -NMR overnight generating the spectra in Figure 4.6c showing a small peak corresponding to the diastereomer at around -169 ppm, however a disturbance in the baseline at -180 ppm indicates possible incomplete separation of the diastereomers. A column with higher injection load would have been advantageous to assess the viability of this chiral column for separating these diastereomers, however, chiral separations are complex and highly dependent on the specific intermolecular interactions available within the column stationary phase and with limited access to a diversity of chiral phases, it is difficult to assess proper separation conditions.<sup>27</sup>

As such, I sent mixtures of Phth-F-Phe-OH enantiomers to Phenomenex for chiral screening wherein, the use of an amylose-1 stationary phase and Hexane:Ethanol:TFA (70:30:0.1) eluent achieved excellent resolution of diastereomers from each other as well as from other impurities (Figure 4.7). This avenue would be able to afford pure enantiomers to be studied on their own or used in peptide synthesis to prepare peptides with specific fluorine substitutions. However, the preparative column required for a gram scale purification would be in the ~\$10,000 range and this avenue could not be further pursued.

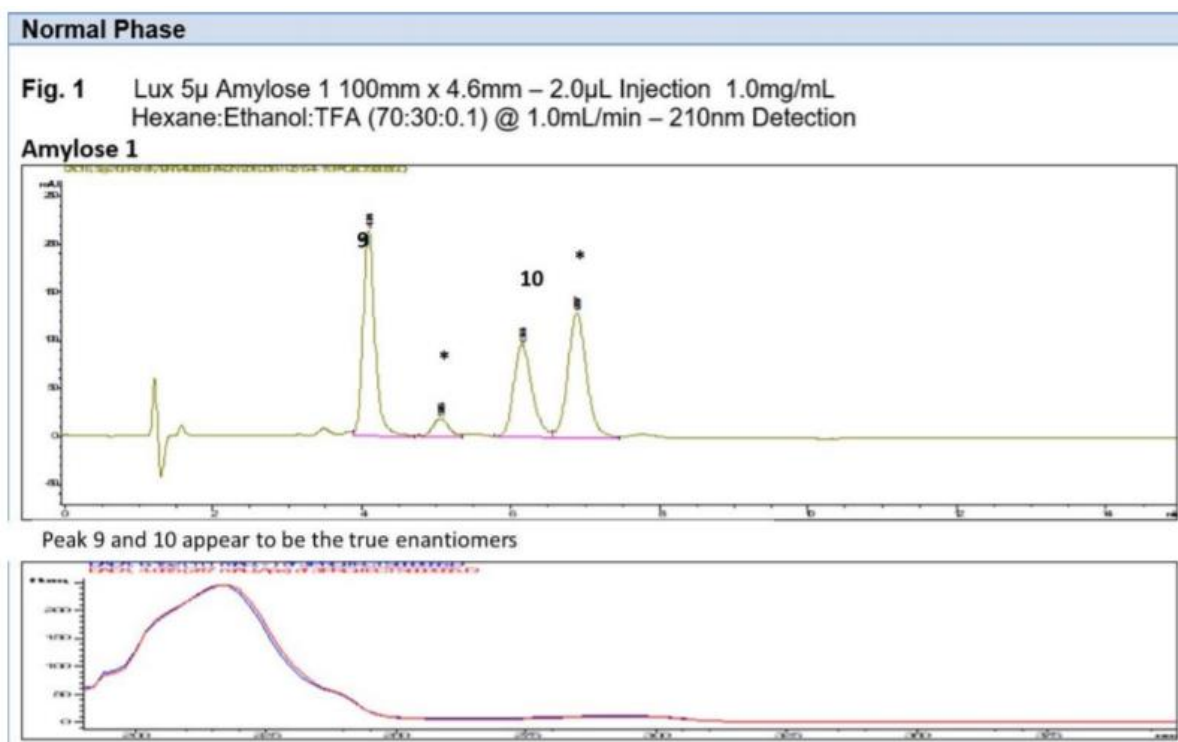


**Figure 4.7.** Chiral screening demonstrates conditions for excellent separation of fluorinated Phth-F-Phe diastereomers.

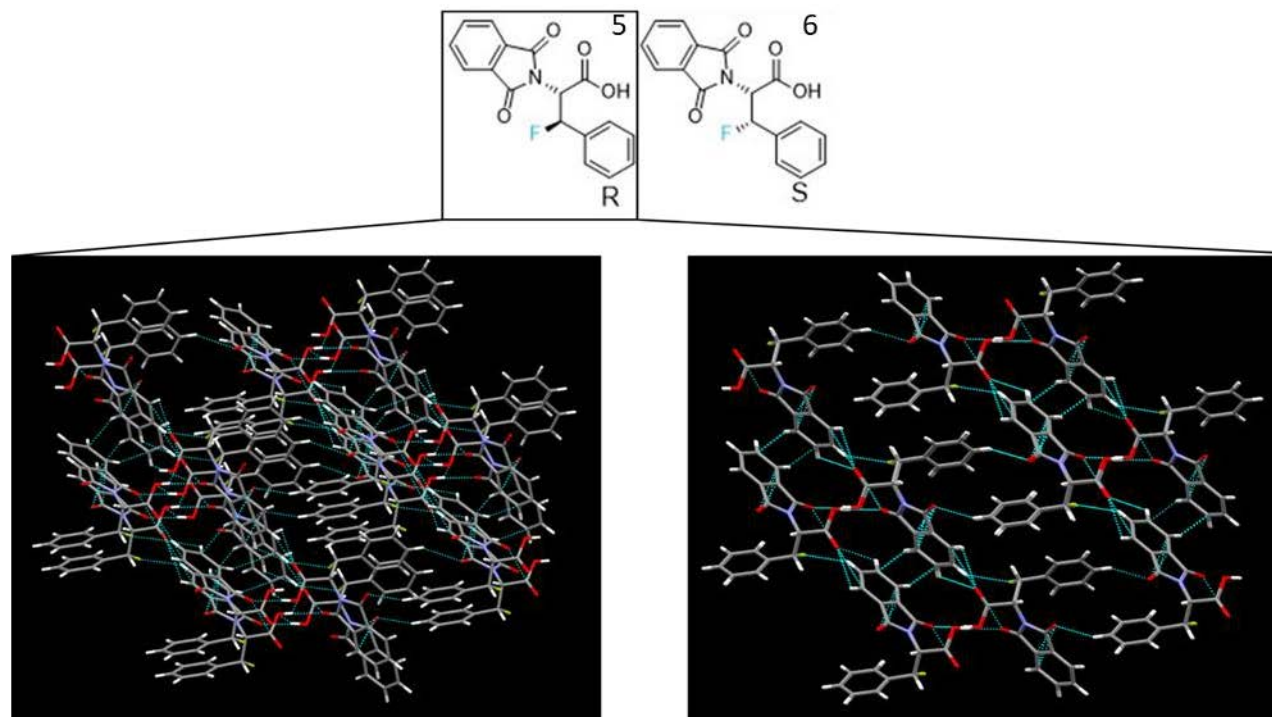


**Figure 4.8.** Crystals obtained from a mixture of **5** and **6** contained **5** as the majority component.

Despite difficulty attaining diastereomeric purity as detailed above, small, slender monoclinic crystals of Phth-F-Phe, were obtained through slow evaporation of **5** in ethyl acetate and analyzed by x-ray diffraction. From the mixture of enantiomers and a some unfluorinated amino acid, **B** with an *R* diastereomeric configuration at the  $\beta$ -carbon, preferentially crystalized with ca. 20% occupancy of the unfluorinated analogue. The crystal structure shows what appears to be  $\pi$ -stacking among phthalimide protecting groups and phenyl side chain rings respectively as shown from two perspectives in Figure 4.8. Interestingly, the fluorine atom is labeled as being close contact, less than the sum of van der Waals radii, with a proton on a neighboring phthalimide protecting group as can be seen by the blue dashed indicator and white arrow in Figure 4.9a. On the other hand, the crystal structure of the unfluorinated amino acid (CCDC: 138514) does not show any close contacts with its hydrogens at the  $\beta$ -position (Figure 4.9b, white arrow). This difference highlights that the presence of the Fluorine indeed influences how these molecules pack

into organized arrays. In the future, being able to separate the fluorinated diastereomers from the unfluorinated amino acid followed by crystallization would be an excellent start to pushing this project further.

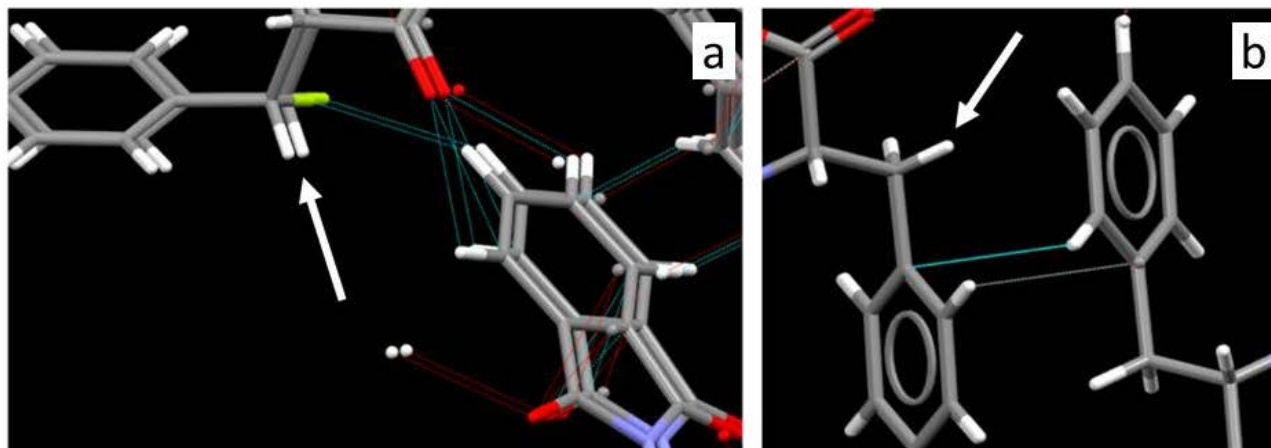


**Figure 4.9:** Close contacts formed in (a) Phth-F-Phe and (b) Phth-Phe crystals.

## Conclusion

Diphenylalanine and its derivatives present an interesting class of powerful small molecule gelators with tunable properties that arise from small modifications to monomer structure. Advances in fluorine chemistry have produced elegant methods of monofluorination at the beta-carbon of phenylalanine and phenylalanine containing peptides. Given its dramatic electronegativity and size, hydrogen-to-fluorine substitutions present the possibility to bring about new inter- and intramolecular interactions among phenylalanine dipeptides without greatly impacting overall molecular size. Preliminary DFT calculations provide impetus to this study suggesting that the energetics of monomer interaction will change depending on spatial orientation of the fluorine bonds in di-fluoro diphenylalanines. As such, chromatographic separations of the four di-fluoro Phth-diphenylalanine diastereomers were attempted without success. Separation methods of the Phth-F-Phe amino acid diastereomers were discovered in chiral screening but present a significant financial investment. That said, crystallization of this amino acid

demonstrates preferential crystallization of the R-diastereomer with some occupancy of the unfluorinated amino acid, demonstrating new close contacts in the structure not observed in the pure starting material. These preliminary crystallographic differences are a promising next step to use this simple fluorine substitution toward molecular engineering strategies for this important dipeptide.

## Experimental

**Electrospray Ionization Mass Spectrometry (ESI-MS):** ESI signatures were samples using a Thermo Finnigan LCQ Deca Ion Trap Mass Spectrometer operating in negative mode. Samples were prepared in a 1:1 MeOH:water solution with 0.1% ammonium hydroxide.

**Reverse-Phase HPLC:** Peptides were purified by reverse-phase HPLC on a Varian PrepStar SD-1 system equipped with a Phenomenex, Luna, 5  $\mu$ m particle diameter silica support functionalized with TMS terminated C8. An aqueous 0.1% ammonium formate buffer (pH 8):acetonitrile gradient was used as mobile phase.

**Computational Information:** Calculations were performed at the DFT level (B3LYP/6-31+G(D)) on crystallographic coordinates using Gaussian 09.

## References

- (1) Burley, S. K.; Petsko, G. A. Aromatic-Aromatic Interaction: A Mechanism of Protein Structure Stabilization. *Science* **1985**, 229 (4708), 23–28.
- (2) Görbitz, C. H. The Structure of Nanotubes Formed by Diphenylalanine, the Core Recognition Motif of Alzheimer's  $\beta$ -Amyloid Polypeptide. *Chem. Commun.* **2006**, No. 22, 2332–2334.  
<https://doi.org/10.1039/B603080G>.

- (3) Adler-Abramovich, L.; Marco, P.; Arnon, Z. A.; Creasey, R. C. G.; Michaels, T. C. T.; Levin, A.; Scurr, D. J.; Roberts, C. J.; Knowles, T. P. J.; Tendler, S. J. B.; Gazit, E. Controlling the Physical Dimensions of Peptide Nanotubes by Supramolecular Polymer Coassembly. *ACS Nano* **2016**, *10*, 7436–7442. <https://doi.org/10.1021/acsnano.6b01587>.
- (4) Adler-Abramovich, L.; Gazit, E. The Physical Properties of Supramolecular Peptide Assemblies: From Building Block Association to Technological Applications. *Chem. Soc. Rev.* **2014**, *43* (20), 6881–6893. <https://doi.org/10.1039/C4CS00164H>.
- (5) Ryan, D. M.; Doran, T. M.; Anderson, S. B.; Nilsson, B. L. Effect of C-Terminal Modification on the Self-Assembly and Hydrogelation of Fluorinated Fmoc-Phe Derivatives. *Langmuir* **2011**, *27* (7), 4029–4039. <https://doi.org/10.1021/la1048375>.
- (6) Reches, M.; Gazit, E. Casting Metal Nanowires within Discrete Self-Assembled Peptide Nanotubes. *Science* **2003**, *300*, 625–627. <https://doi.org/10.1126/science.1082387>.
- (7) Görbitz, C. H. The Structure of Nanotubes Formed by Diphenylalanine, the Core Recognition Motif of Alzheimer's  $\beta$ -Amyloid Polypeptide. *Chem. Commun.* **2006**, No. 22, 2332–2334. <https://doi.org/10.1039/B603080G>.
- (8) Wang, M.; Du, L.; Wu, X.; Xiong, S.; Chu, P. K. Charged Diphenylalanine Nanotubes and Controlled Hierarchical Self-Assembly. *ACS Nano* **2011**, *5* (6), 4448–4454. <https://doi.org/10.1021/nn2016524>.
- (9) Jeon, J. H.; Mills, C. E.; Shell, M. S. Molecular Insights into Diphenylalanine Nanotube Assembly: All-Atom Simulations of Oligomerization. *Engineering Sciences and Fundamentals 2013 - Core Programming Area at the 2013 AIChE Annual Meeting: Global Challenges for Engineering a Sustainable Future* **2013**, *2*, 996.

- (10) Adler-Abramovich, L.; Kol, N.; Yanai, I.; Barlam, D.; Shneck, R. Z.; Gazit, E.; Rousso, I. Self-Assembled Organic Nanostructures with Metallic-like Stiffness. *Angewandte Chemie - International Edition* **2010**, *49* (51), 9939–9942. <https://doi.org/10.1002/anie.201002037>.
- (11) Smith, A. M.; Williams, R. J.; Tang, C.; Coppo, P.; Collins, R. F.; Turner, M. L.; Saiani, A.; Ulijn, R. V. Fmoc-Diphenylalanine Self Assembles to a Hydrogel via a Novel Architecture Based on Pi-Pi Interlocked Beta-Sheets. *Advanced Materials* **2008**, *20* (1), 37–41. <https://doi.org/10.1002/adma.200701221>.
- (12) Draper, E. R.; McDonald, T. O.; Adams, D. J. A Low Molecular Weight Hydrogel with Unusual Gel Aging. *Chemical Communications* **2015**, *51* (30), 6595–6597. <https://doi.org/10.1039/c5cc01334h>.
- (13) Chen, L.; Revel, S.; Morris, K.; Adams, D. J. Energy Transfer in Self-Assembled Dipeptide Hydrogels. *Chemical Communications* **2010**, *46* (24), 4267–4269. <https://doi.org/10.1039/c003052j>.
- (14) Draper, E. R.; Dietrich, B.; McAulay, K.; Brasnett, C.; Abdizadeh, H.; Patmanidis, I.; Marrink, S. J.; Su, H.; Cui, H.; Schweins, R.; Seddon, A.; Adams, D. J. Using Small-Angle Scattering and Contrast Matching to Understand Molecular Packing in Low Molecular Weight Gels. *Matter* **2020**, *2* (3), 764–778. <https://doi.org/10.1016/j.matt.2019.12.028>.
- (15) Raeburn, J.; Mendoza-Cuenca, C.; Cattoz, B. N.; Little, M. A.; Terry, A. E.; Zamith Cardoso, A.; Griffiths, P. C.; Adams, D. J. The Effect of Solvent Choice on the Gelation and Final Hydrogel Properties of Fmoc-Diphenylalanine. *Soft Matter* **2015**, *11* (5), 927–935. <https://doi.org/10.1039/c4sm02256d>.
- (16) Fuentes-Caparras, A. M.; Canales-Galarza, Z.; Barrow, M.; Dietrich, B.; Laüger, J.; Nemeth, M.; Draper, E. R.; Adams, D. J. Mechanical Characterization of Multilayered Hydrogels: A

- Rheological Study for 3D-Printed Systems. *Biomacromolecules* **2021**, 22 (4), 1625–1638.  
<https://doi.org/10.1021/acs.biomac.1c00078>.
- (17) Yan, X.; Li, J. Self-Assembly and Application of Diphenylalanine-Based Nanostructures. *Chemical Society Reviews* **2010**, 39 (6), 1877–1890. <https://doi.org/10.1039/b915765b>.
- (18) Reches, M.; Gazit, E. Designed Aromatic Homo-Dipeptides: Formation of Ordered Nanostructures and Potential Nanotechnological Applications. *Physical Biology* **2006**, 3 (1).  
<https://doi.org/10.1088/1478-3975/3/1/S02>.
- (19) Hunter, L. The C-F Bond as a Conformational Tool in Organic and Biological Chemistry. *Beilstein Journal of Organic Chemistry* **2010**, 6, 1–14. <https://doi.org/10.3762/bjoc.6.38>.
- (20) Ryan, D. M.; Anderson, S. B.; Nilsson, B. L. The Influence of Side-Chain Halogenation on the Self-Assembly and Hydrogelation of Fmoc-Phenylalanine Derivatives. *Soft Matter* **2010**, 6 (14), 3220–3231. <https://doi.org/10.1039/c0sm00018c>.
- (21) Ryan, D. M.; Anderson, S. B.; Senguen, F. T.; Youngman, R. E.; Nilsson, B. L. Self-Assembly and Hydrogelation Promoted by F5-Phenylalanine. *Soft Matter* **2010**, 6 (3), 475–479.  
<https://doi.org/10.1039/b916738b>.
- (22) Kirsch, P.; Bremer, M. Understanding Fluorine Effects in Liquid Crystals. *ChemPhysChem* **2010**, 11 (2), 357–360. <https://doi.org/10.1002/cphc.200900745>.
- (23) Tschierske, C. *Liquid Crystals Materials Design and Self-Assembly*; 1980; Vol. 7.  
[https://doi.org/10.1016/0302-4598\(80\)87026-7](https://doi.org/10.1016/0302-4598(80)87026-7).
- (24) Reichenbacher, K.; Süss, H. I.; Hulliger, J. Fluorine in Crystal Engineering—“the Little Atom That Could.” *Chem. Soc. Rev.* **2005**, 34 (1), 22–30. <https://doi.org/10.1039/B406892K>.



- (25) Bume, D. D.; Pitts, C. R.; Jokhai, R. T.; Lectka, T. Direct, Visible Light-Sensitized Benzylic C[Sbnd]H Fluorination of Peptides Using Dibenzosuberone: Selectivity for Phenylalanine-like Residues. *Tetrahedron* **2016**, 72 (40), 6031–6036. <https://doi.org/10.1016/j.tet.2016.08.018>.
- (26) Bloom, S.; McCann, M.; Lectka, T. Photocatalyzed Benzylic Fluorination: Shedding “Light” on the Involvement of Electron Transfer. *Organic Letters* **2014**, 16 (24), 6338–6341. <https://doi.org/10.1021/ol503094m>.
- (27) Zhao, Y.; Woo, G.; Thomas, S.; Semin, D.; Sandra, P. Rapid Method Development for Chiral Separation in Drug Discovery Using Sample Pooling and Supercritical Fluid Chromatography-Mass Spectrometry. *Journal of Chromatography A* **2003**, 1003 (1–2), 157–166. [https://doi.org/10.1016/S0021-9673\(03\)00725-8](https://doi.org/10.1016/S0021-9673(03)00725-8).

## **Chapter 5**

### **Design of Peptide- $\pi$ Hydrogels for Biology**

## Introduction

Cell culture techniques have played a pivotal role in biomedicine to probe physiology and pathophysiology of cells and tissues outside of the organism. However, the 2D nature of materials used in traditional cell culture platforms limits their ability to mimic the external microenvironment that directly impacts the spatial and temporal cues that dictate complex cellular responses such as cellular morphology, differentiation, migration, and communication. Indeed, studies in the last decade demonstrated that cells display atypical behavior when they are removed from their 3D native environment. Thus, 3D cell culture has become a promising platform by which to model extracellular space for physiologically relevant cell culture studies.<sup>3</sup> Hydrogels prepared from peptide- $\pi$ -peptide nanomaterials are promising candidates for 3D cell culture applications as biocompatible peptide sequences are present on the surface and can “communicate” with the biotic environment. Further, the modular nature of peptide synthesis allows for facile incorporation of bioactive epitopes, such as laminin derived IKVAV and RGD, that have been shown to facilitate adhesion, migration and neurite extension in dendritic root ganglion cells.<sup>4,5</sup>

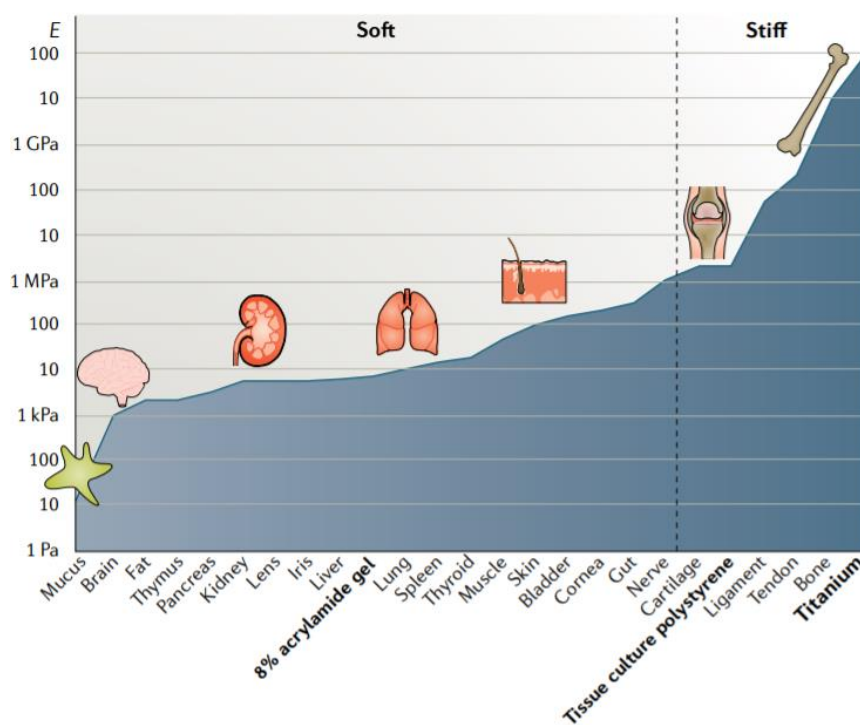


**Figure 5.1:** Young's moduli characteristic of various tissues. Reprinted from reference 8. Copyright Nature, 2020.

The stiffness of cell culture substrates has been demonstrated to direct aspects of cell physiology wherein cells exert mechanical forces on the substrate and draw on the mechanical response from the environment as a deciding factor in cell fate.<sup>6-8</sup> More specifically, this feedback loop has been demonstrated to impact the clustering and occupancy of mechanosensors known as integrin adhesion complexes that modulate cell signaling cascades and thus effect cell proliferation, differentiation and migration.<sup>9,10</sup> Young's modulus, which demonstrates the geometry independent stiffness of a material, ranges from about 0.1kPa to 1MPa in most tissues.<sup>11</sup> Consequently, the mechanical properties of hydrogel scaffolds should mimic tissue from which the cells originate (Figure 5.1).<sup>11,12</sup> For example, progenitor cells have been demonstrated to preferentially differentiate into neurons in the presence of a softer mechanical environment more

closely resembling the brain.<sup>13</sup> Our lab has developed a cross-linking scheme based on several well-known bioconjugation reactions. For example, peptides containing alkene terminated alloxycarbonyl (Alloc) protected lysine residues were crosslinked with a thiol terminated, heterobifunctional, ethylene glycol spacer arm upon treatment with 365 nm light through the radical-initiated thiol-ene reaction.<sup>4</sup> Variations in crosslinker concentrations could be used to tune the rheological properties of our hydrogels to match the stiffness ranges of tissues *in vivo* and in turn increase long term stability of the gels.

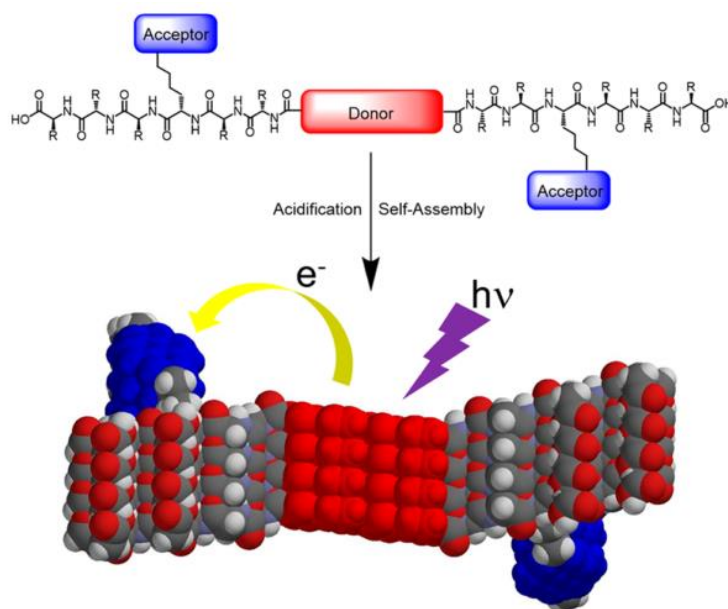


**Figure 5.2.** Schematic of peptide containing donor-acceptor system. Reprinted from Reference 17.

Copyright American Chemical Society 2016

An intriguing aspect of  $\pi$ -conjugated peptide hydrogel materials is the capacity to generate electric fields and charge carriers in aqueous environments. Electric fields are generated *in vivo* through sodium and potassium gradients and charges carried by biomolecules such as transmembrane receptors, growth hormones and signaling molecules. Endogenous electric fields are unique to each cell and tissue type and are used as a guiding cue for cellular processes such as

differentiation during development and regenerating tissues.<sup>14</sup> For example, embryonic development begins with cellular polarization that spreads throughout the embryo and is responsible for delivering the appropriate cues that ultimately define regions of the developing organism, for example, the anterior and posterior domains.<sup>15</sup> The impact of electric fields on cellular physiology has also been demonstrated in cell culture studies. For example, Langer and coworkers demonstrated enhanced neurite outgrowth and neuronal differentiation of PC-12 cells when cultured on conductive, oxidized polypyrrole and subjected to electric stimuli.<sup>16</sup> Work from our lab has demonstrated the synthesis and characterization of peptides containing a quaterthiophene (OT4) core and naphthalenediimide (NDI) appended to peptides via lysine side chains as shown in Figure 5.2. Through transient absorption spectroscopy, these chromophores were shown to take part in a photo-induced electron transfer from the donor (OT4) to the acceptor (NDI) in aqueous media. This donor-acceptor couple is a promising system by which to generate electric fields in a cell culture environment and stimulate cells with electric fields to guide stem cell differentiation.<sup>17</sup>

Peptide based nanomaterial systems have been shown to form self-supporting hydrogels based on entanglement and are compelling materials to mimic the ECM for tissue engineering applications addressing the crucial aspects above as they 1) are equipped with  $\pi$ -conjugated subunits capable of generating charge carriers in aqueous media<sup>17-20</sup> 2) are biocompatible, on the size order of the extracellular matrix, and can be modified with bioactive epitopes<sup>4</sup> 3) have tunable mechanical properties that can be modulated to the requirements for a given cell line.<sup>4</sup> This study aims to exploit and optimize the modular nature of these peptide-based hydrogel systems while incorporating the donor-acceptor

electronic functionalities described above to provide an environment compatible with electrosensitive cell lines for cell culture and neuronal tissue engineering purposes.

## **Results and Discussion**

### **Synthetic Strategy and Design of Multifunctional Hydrogels**

Damage to the adult central nervous system (CNS) can have devastating long term effects on cognitive function and lead to a cascade of neuronal degeneration.<sup>1</sup> Adult neurons in the peripheral nervous system can regenerate axons and dendritic connections upon injury depending on their size and location, however, neurons in the CNS cannot.<sup>21</sup> Cell therapy and nerve tissue engineering is a promising means by which to replace damaged areas of the central nervous system, particularly through the use of stem cells.<sup>1</sup> However, neural stem cells in the CNS generally give rise to three different cell types; oligodendrocytes and astrocytes, collectively referred to as glia, and neurons.<sup>22</sup> Oligodendrocytes are responsible for the myelination process while astrocytes support neurons (with water, ions etc.) and are the main component of glial scarring following injury to the CNS.<sup>23</sup> The recovery of function after injury is contingent upon replacing damaged neuronal connections which requires control over stem cell fate toward neuronal lineages.<sup>2</sup> To demonstrate the demand for a tailored hydrogel system I conducted a differentiation study with human neuronal stem cells (hNSCs) on Matrigel film in the absence of electrical and chemical stimulation. Figure 5.3A shows the epifluorescence images of cells stained for  $\beta$ III-tubulin markers indicating neuronal differentiation. Figure 5.2B shows the epifluorescence image of the same frame stained with markers for both  $\beta$ III-tubulin and GFAP, demonstrating a high preference

for glial lineages. Finally, Figure 5.2C shows a colored overlay with the cell nuclei stained with DAPI highlighting low neuronal yield of this unsophisticated cell culture technique.

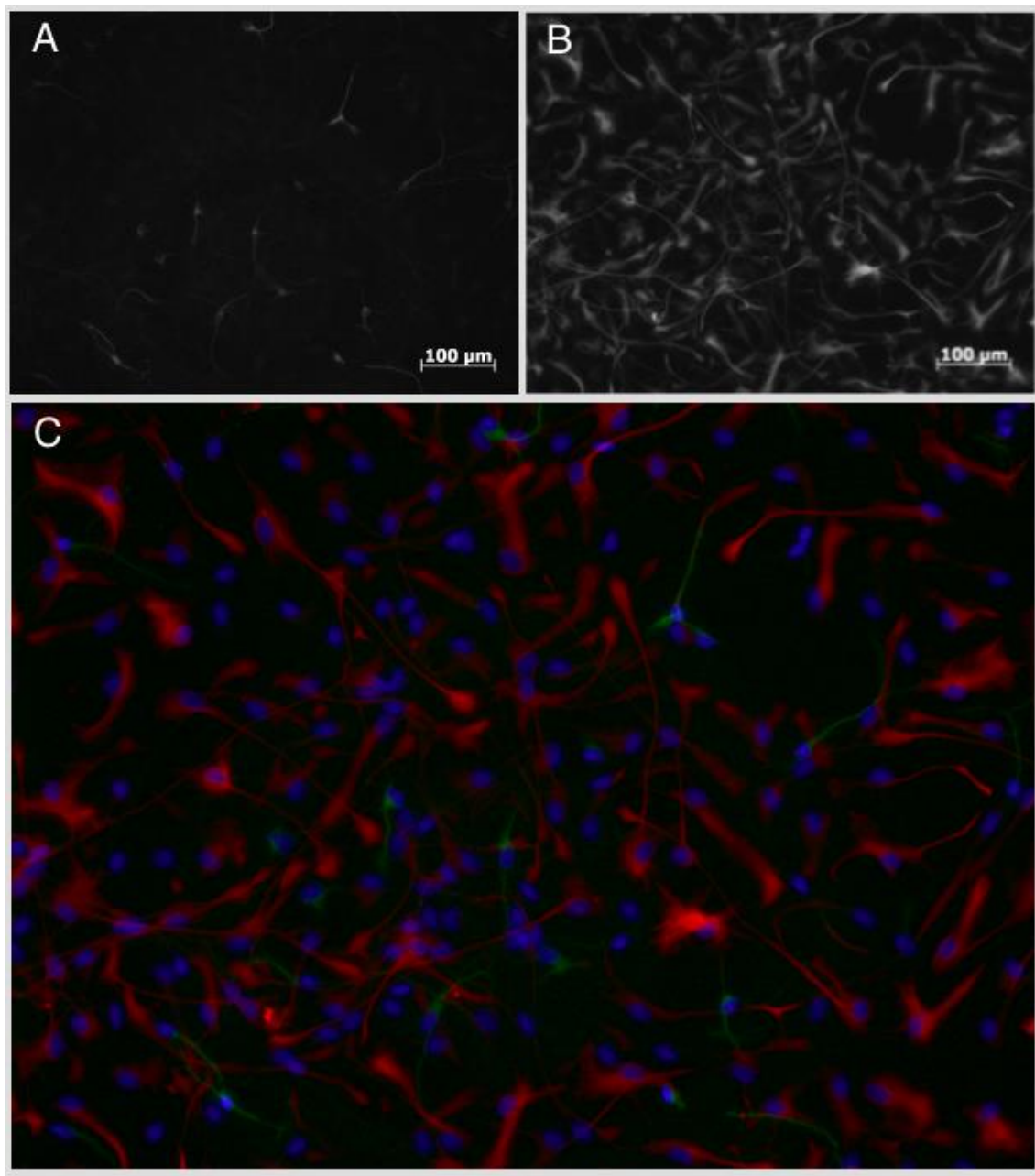
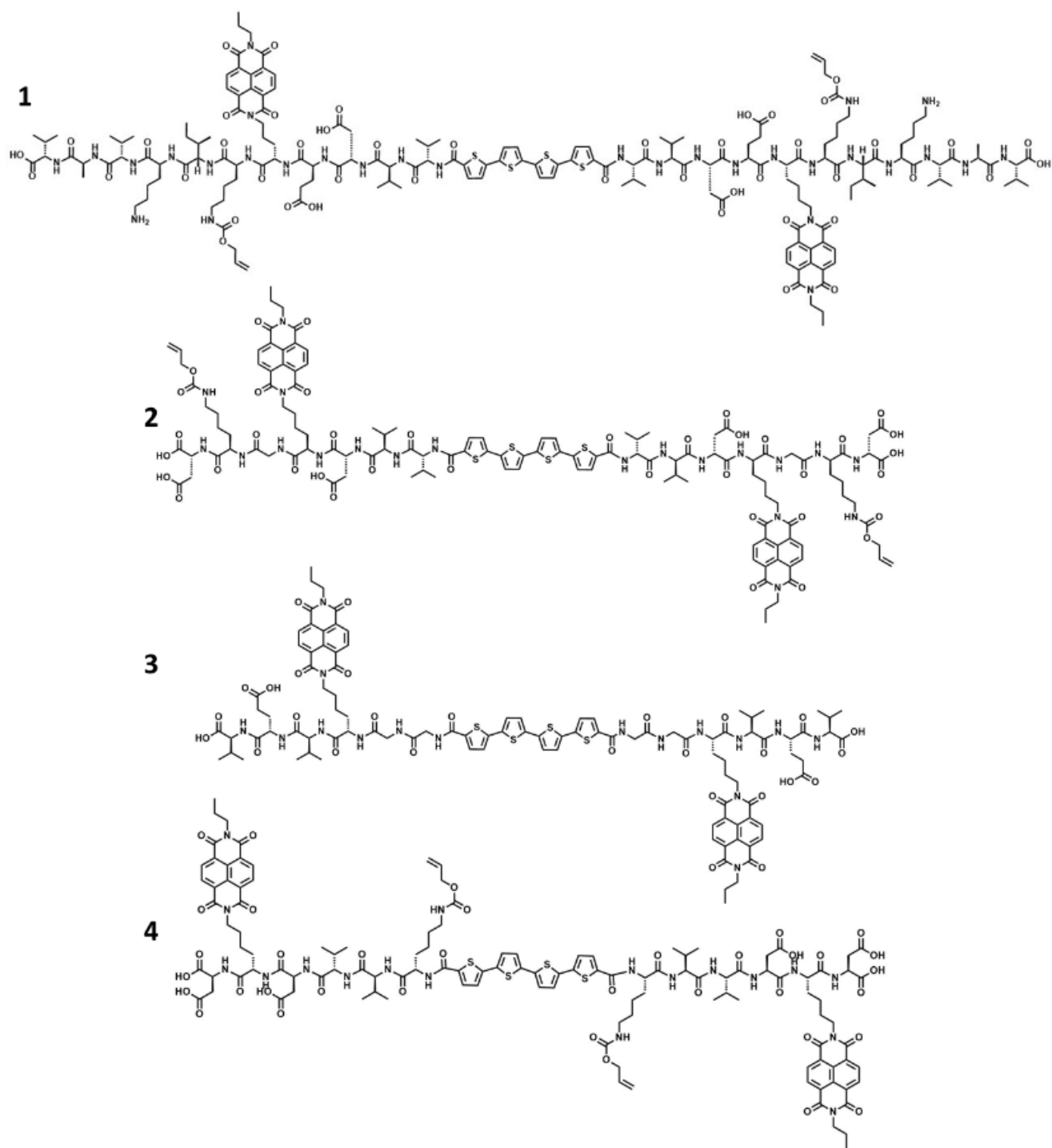


**Figure 5.3:** Epifluorescence images of differentiated hNSCs stained with A) neuronal markers B) glial and neuronal markers C) color overlay of stained nuclei (blue) cells with neuronal markers (green) and glial markers (red).



Thus, I moved to prepare peptide-pi-peptide constructs with the following attributes: 1) a donor-acceptor system based on 4T and NDI to stimulate cells with electric fields in a 3D cell culture environment 2) present bioactive epitopes within the hydrogel scaffold 3) tune the rheological properties of the gel suited to that of neuronal tissues for the purposes of guiding cell differentiation to neuron. Many synthetic challenges were presented in this project from the start and required me to formulate a step-wise investigation procedure that I follow with any challenge in the laboratory. I first assess the purity of all reagents to ensure no issues with chemical feed stocks and then reprepare any on-hand reagent solutions that could be a source of contamination. If step one does not reveal any issues, I conduct a thorough overview of each reaction step as can be uncovered from the literature and consider potential issues with reaction set-up, this can include synthesis of a literature compound to ensure proper technique. If the first two steps do not expose any obvious issues or do not achieve successful synthesis, I focus on small changes to reaction parameters or target design that can often open a successful route. In the next several sections I will detail a chronology of my trials, some of the roadblocks, and creative avenues I devised to prepare a peptide system with the above three stated attributes.

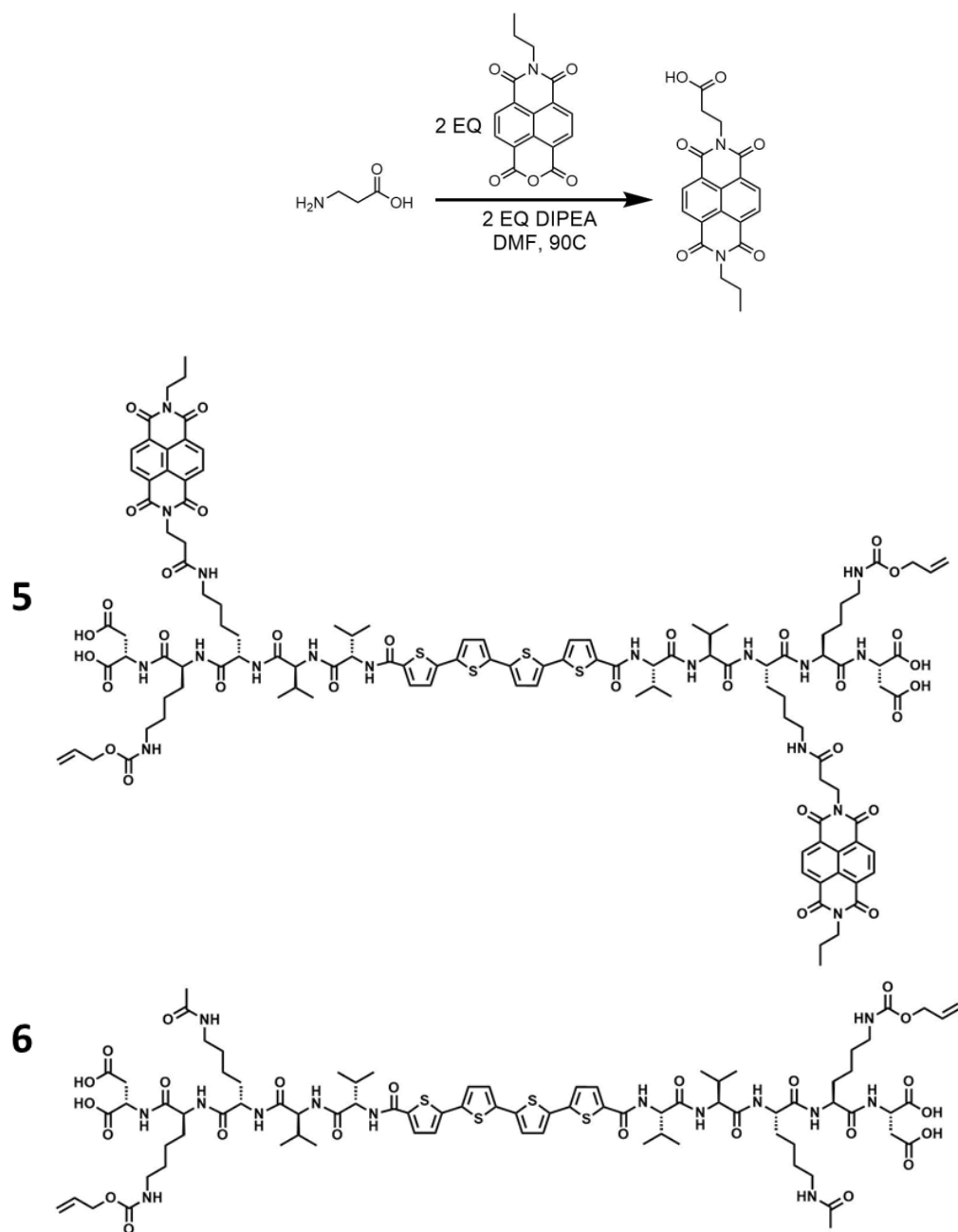


My first target was the undeca-peptide **1** which incorporates the laminin-derived bioactive epitope IKVAV, an OT4 core and NDI appended via lysine residues. Further, an Alloc functionalized lysine is incorporated to facilitate crosslinking through the thiol-ene photoreaction

as previously reported by our lab.<sup>4</sup> The length and complexity of this peptide presented challenges. Solid phase peptide synthesis is generally streamlined through literature precedent and I could not identify issues with my synthetic procedure. There are, however, well documented “difficult sequences” that are usually composed of several hydrophobic residues in a row leading to poor solvation and thus incomplete deprotection and acylation. I made many attempts to prepare this peptide including changes to solvent composition (the “magic mixture”: DCM:DMF:NMP 1:1:1), the addition of chaotropic salts (LiCl) and use of detergents (Triton-X).<sup>24</sup> With the inability to construct the peptide backbone of **1** I moved to a simpler target, **2**, that incorporated the donor-acceptor dyad and Alloc modified lysine residues. My thought was that hydrogelation of compound **2** followed by the addition of 1% cysteine containing peptide sequences, such as CIKVAV or CRGD, under thiol-ene reaction conditions could yield a hydrogel equipped with bioactive epitopes wherein the remaining active sites could be exploited for cross-linking. I again encountered synthetic difficulties, for example, the peptide backbone could be prepared and the OT4 incorporated, but the final step of NDI attachment would fail. To rule out issues with reagent contamination or procedure I prepared peptide **3**, a peptide containing both OT4 and NDI previously made by us and was successful. Apart from variation in peptide sequence, the most obvious functional difference between compounds **2** and **3** is the presence of the Alloc protected lysine residue during NDI incorporation. My thoughts were that the Alloc might be engaging in side-reactions, such as Diels-Alder, with the incoming NDI moiety that would be deleterious for the imidation step. I attempted to switch the order of synthetic operations with an attempted synthesis of **4**, wherein the Lys(NDI) and Lys(Alloc) are switched in position relative to the OT4 core. In this respect, extension of the peptide would proceed with NDI imidation immediately after incorporation of the first lysine. Then, the peptide could be further extended to incorporate the

Lys(Alloc). While this synthetic route was finally successful, it was plagued by significant biproducts and low yields making separation difficult.

**Scheme 1.**



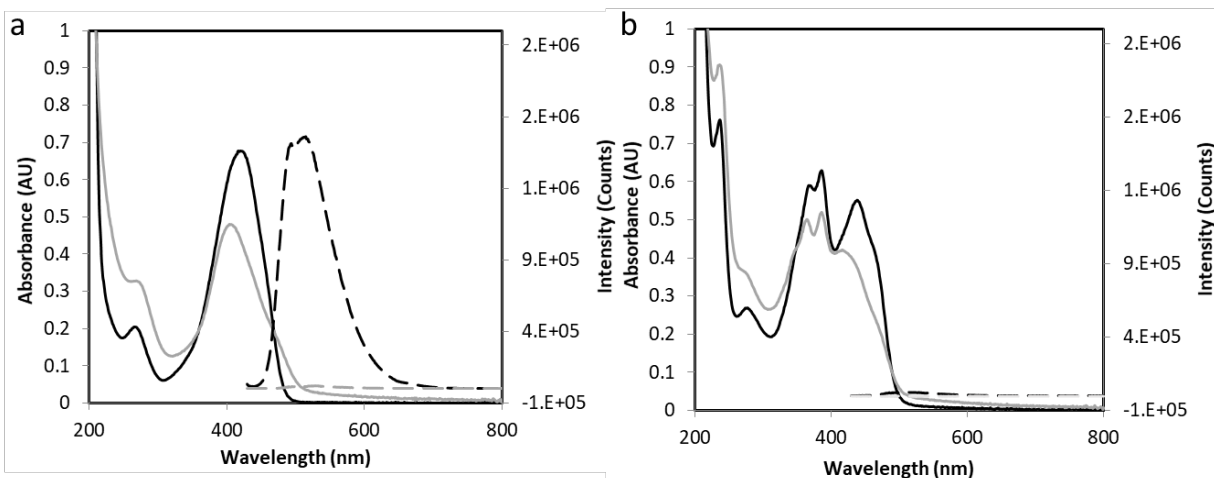


**Figure 5.4:** Absorbance (solid lines) and emission (dashed lines) of peptides a) **6** and b) **5** crude under dissolved (basic, black lines) and assembled (acidic, grey lines) conditions.

My next phase of attempts involved strategies to bypass the on-resin imidation procedure by way of an NDI functionalized amino acid that could be coupled on-resin under typically SPPS acylation conditions.<sup>25</sup> I was initially able to successfully synthesize Fmoc-Lys(NDI) and had some success with incorporating it into peptides, however, I encountered difficulties attaining sufficient Fmoc-Lys(NDI) to scale up the peptide synthesis for characterization. The imidation of N-propyl-1,4,5,8-naphthalenetetracarboxylic acid monoanhydride with  $\beta$ -alanine has been reported and is synthetically facile and can achieve high yield with simple isolation steps (Scheme 1).<sup>26</sup> The addition of  $\beta$ -Ala(NDI) to a free lysine side chain through typical solid phase coupling conditions yielded peptide **5** in good yields. The acetylated control of peptide **6** undergoes a blue shift in absorbance and quench in emission upon assembly (Figure 5.4a). Preliminary characterization of crude peptide **5** on the other hand exhibits a dramatic quench in fluorescence, even in the molecularly dissolved state that is associated with this donor-acceptor system as previously

reported.<sup>17</sup> TEM images of **5** are shown in Figure 5.5 demonstrating the formation of one-dimensional nanostructures.

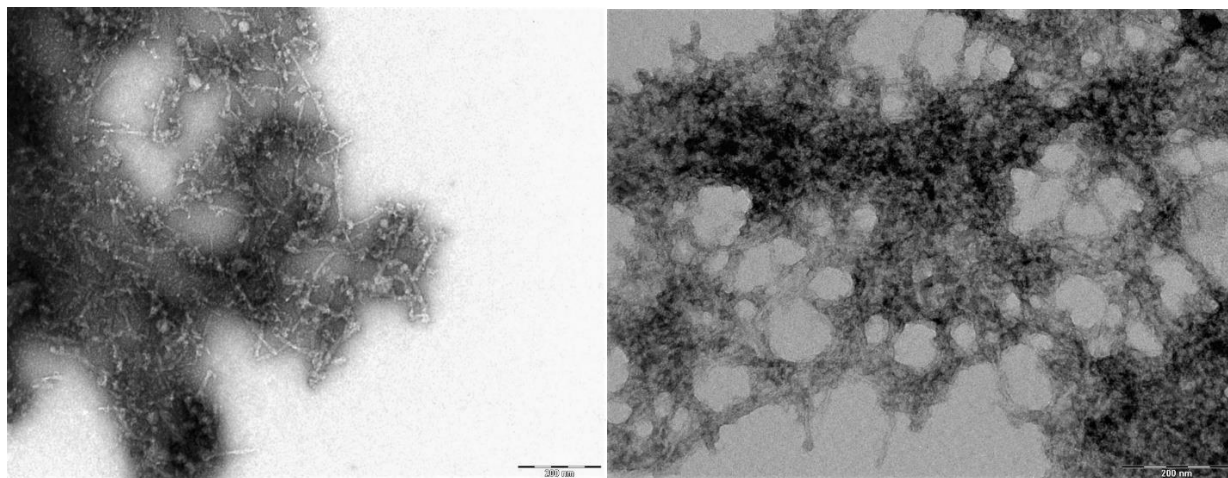


**Figure 5.5.** TEM images of peptide **5** stained with 2% Uranyl acetate. Both scale bars represent 200 nm.

Despite the apparent success in synthesis and characterization with peptide **5**, degradation could be observed between purification steps. For example, Figure 5.6a shows the HPLC trace at 260 nm for an initial preparative purification step following synthesis of peptide **5**. ESI analysis of the fractions collected revealed the elution of peptide **5** in fraction 10 at 25.553 minutes. This fraction was collected, lyophilized and re-injected with a longer gradient to achieve finer separation. Figure 5.6b shows the HPLC trace for this second injection at 260nm revealing many new impurities that should have been removed with the first purification step. Due to the inherent necessity of these materials to be processable and stable in water, this material design was clearly inappropriate for our purposes and the monomer was again redesigned.

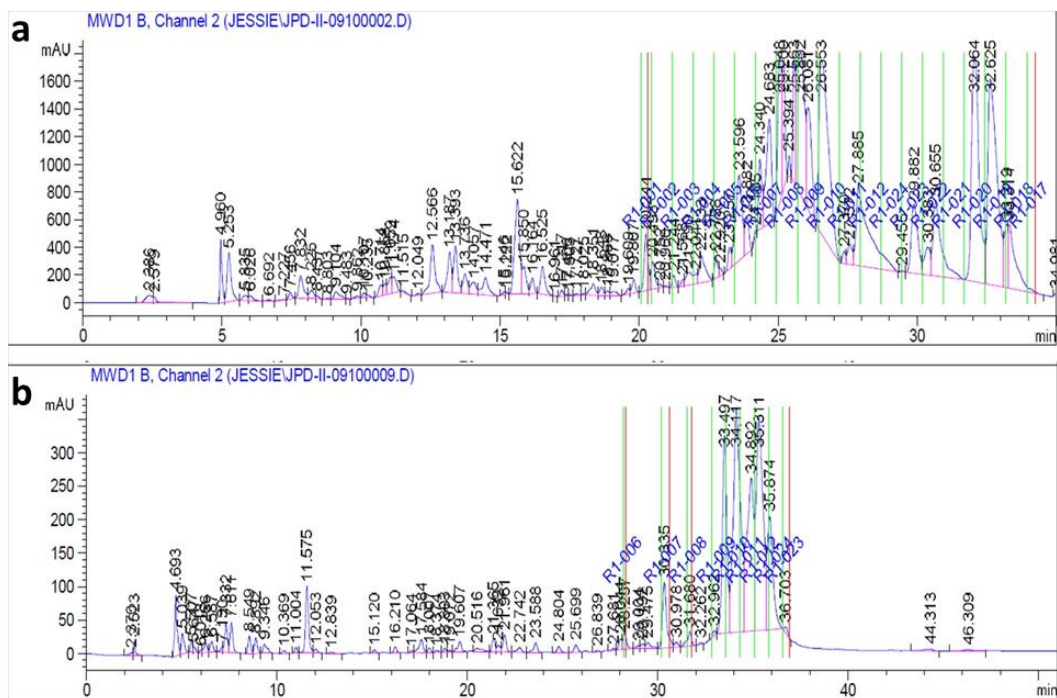
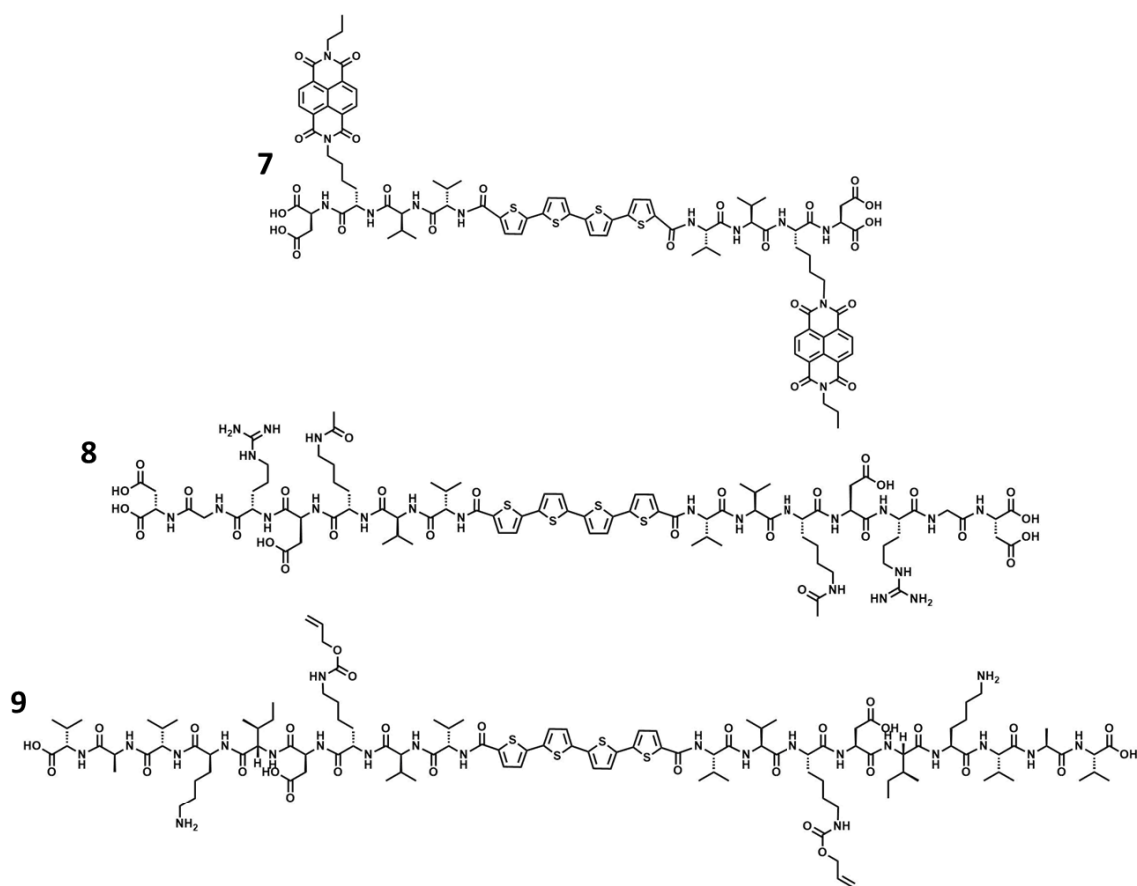


**Figure 5.6.** Absorbance at 260 nm, absorbance of peptide backbone during A) Preparatory purification, peak isolated at 26.55 min corresponding to peptide **5** B) Semipreparative purification of **5** showed large number of new impurities.



A new approach wherein each component – bioactivity, NDI and crosslinking functionalities – are included into separate peptides and then co-assembled into hydrogels was then assessed. These peptides contain the same internal consensus sequence of DK(X)VV-OT4 wherein the lysine side chain amine can be modulated with various functionalities (X). Peptides **7** and **8** have been prepared where peptide **7** is imidated with NDI while **8** contains the fibronectin derived bioactive epitope RGD and an acetylated lysine. Both 50% and 10% dilutions of peptide **8** in a matrix of peptide **7** show quenched emission upon assembly that is characteristic of the photoinduced electron transfer within the NDI-OT4 dyad (Figure 5.7). Furthermore, peptides at both 50% and 10% dilution of **8** in **7** qualitatively exhibit gel-like characteristics at 1 wt%, however quantification of these properties will need to be established with rheological studies before beginning *in vitro* studies. Furthermore, peptide **9**, contains an Alloc protected lysine that could be



assembled and diluted in the same manner and cross-linked to increase stability and tune the modulus to match that of tissues of interest.

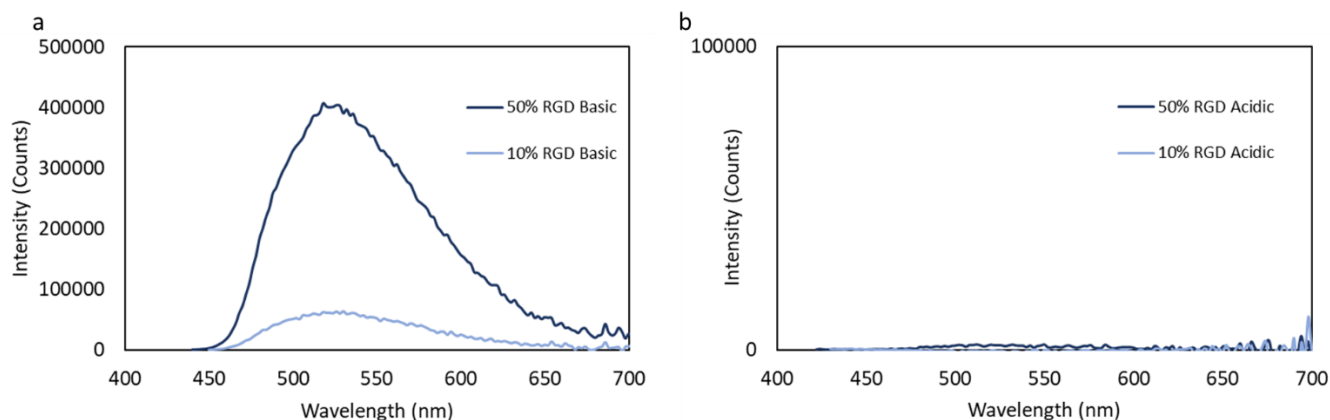
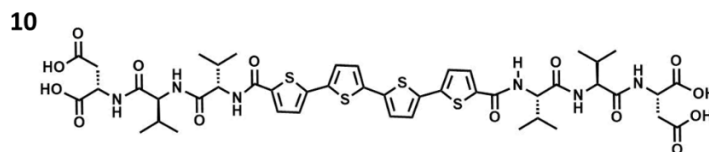


**Figure 5.7:** Emission of peptide **8** diluted to 50% and 10% in a solution of peptide **7** under (a) basic and (b) acidic conditions.

### ***In vivo* Stroke Recovery Work**



Apart from my efforts to construct complex peptides for an *in vitro* cell culture platform, I have engaged in an ongoing collaboration with the labs of Dr. Stephen Zeiler and Dr. Ryan Felling. In this work, we hope to explore our peptide-pi conjugates for the purposes of stroke recovery with *in vivo* mouse models. With these preliminary studies we hoped to confirm that injection of dissolved peptide into the high ionic strength biotic environment will trigger assembly of a hydrogel directly in the tissue. Furthermore, we hypothesize that injection of peptide into the

region of stroke injury will establish the electrical conduits needed and alter the extracellular composition to facilitate better long-term recovery of neuronal activity in the stroke cavity. I synthesized and characterized peptide **10** which undergoes a blue-shift in absorbance and quench in emission upon assembly (Figure 5.8). A 1 mg/mL solution of this material was provided to the Zeiler and Felling labs who conducted all *in vivo* experiments.

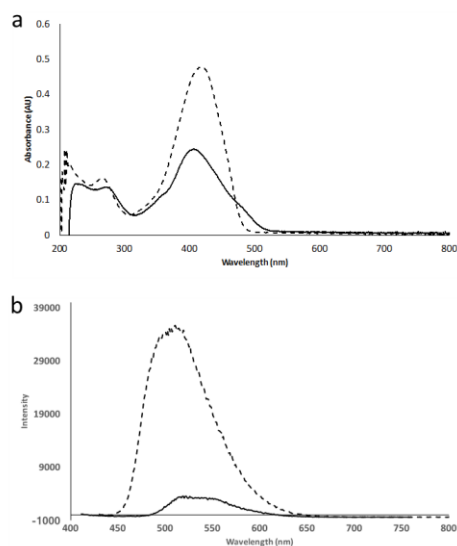


**Figure 5.8.** The a) UV and b) PL traces for **10** under basic (dashed) and acidic (solid) conditions

The solution of peptide **10** was injected into a stroke cavity and imaged following fixation with electron microscopy (Figure 5.9). Linear structures with lengths of around 100 nm can be observed extending from the injection site (Figure 5.9, white void space) indicating assembly and formation of hydrogel in the brain. These structures were not observed elsewhere in the stroke cavity indicating there might be an issue with the process of fixation, aggregation of the material or its diffusion into the surrounding tissue.

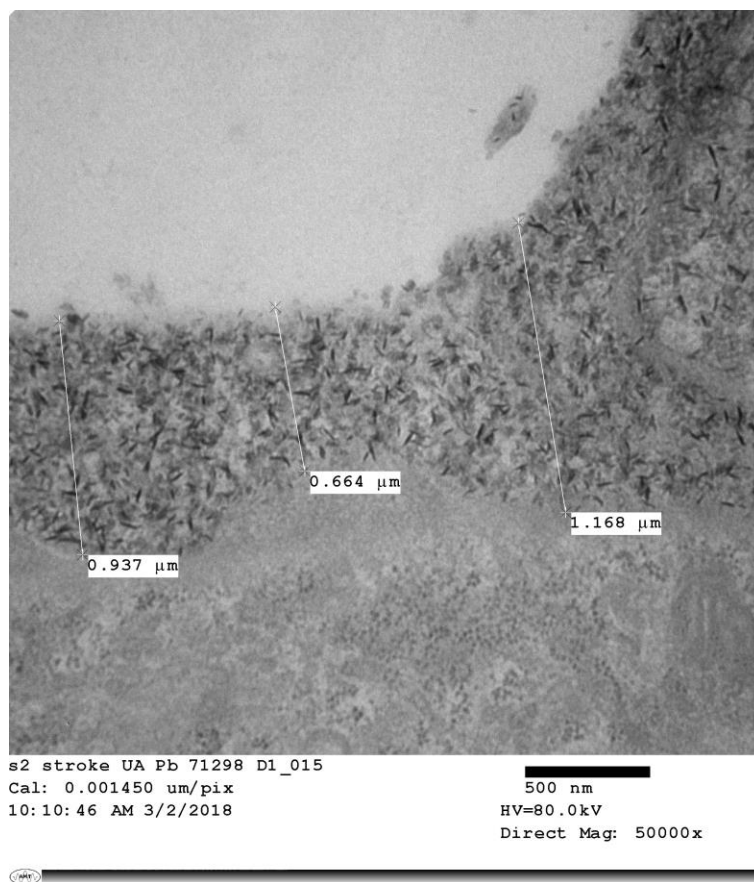


**Figure 5.9.** Representative electron micrograph following injection of **10** into stroke cavity.

The process of preparing samples for electron microscopy is time consuming and presents a challenge as fixation and staining the tissue may create artifacts that interfere with observation. While peptide **10** displays a quench in emission upon assembly, residual emission may be used as a handle to visualize hydrogel formation in brain slices and dramatically decrease processing time with respect to electron microscopy. This process would vastly improve experimental procedure as we advance toward behavioral studies. Figure 5.10 shows side-by-side fluorescence imaging of the injection sites of hydrogen and saline in stroke and non-stroke brains. In general, no discernable difference is observed between the two groups due to convolution from tissue autofluorescence

(which coincides with the GFP emission wavelength) that is often observed in CNS damage even from the needle wound itself.

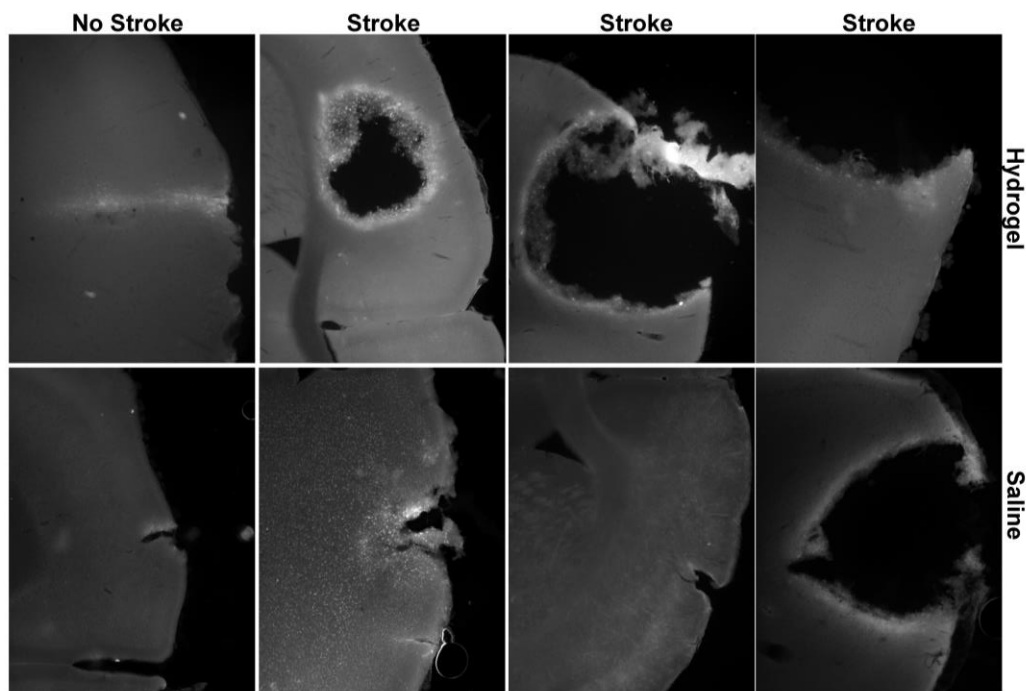


**Figure 5.10.** Tissue auto fluorescence convolutes hydrogel imaging in stroke and non-stroke brains.

As such we worked to prepare a peptide conjugate that could carry a fluorophore with distinct emission from this auto fluorescence. I prepared peptide **11** through acylation of a lysine side chain with Cy5 who's emission falls at 662 nm, well out of the range of the CNS autofluorescence. Figure 5.11a shows fluorescence images of a brain slice containing two injection sites, one of saline and one of hydrogel. As observed with peptide **10** there is little difference between the fluorescence imaging in the GFP channel, however, when imaged in the Cy-5 channel we see a clear fluorescence signal representing hydrogel formation in the tissue. Figure 5.11b shows several slices of two different stroke brains confirming the presence of hydrogel deep within the stroke

tissue. Peptide **11** is therefore a promising platform to begin animal trials to assess the ability of these unique hydrogels to aid in stroke recovery. Furthermore, the hydrogel platform developed with electronic, mechanical, and bioactive compatible properties will be an interesting next step for examining these peptide-pi conjugates in CNS wound healing and stroke recovery.

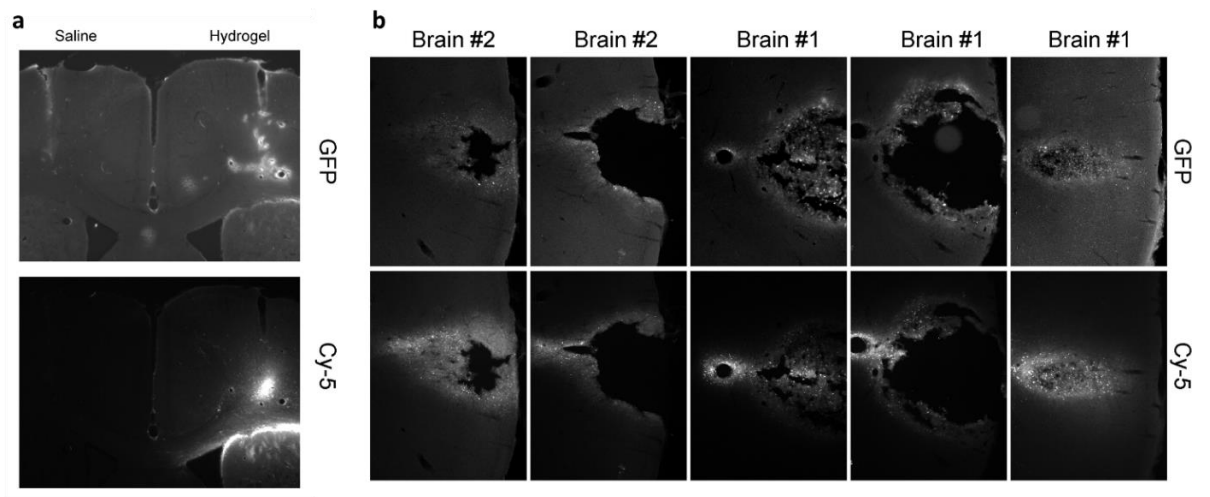
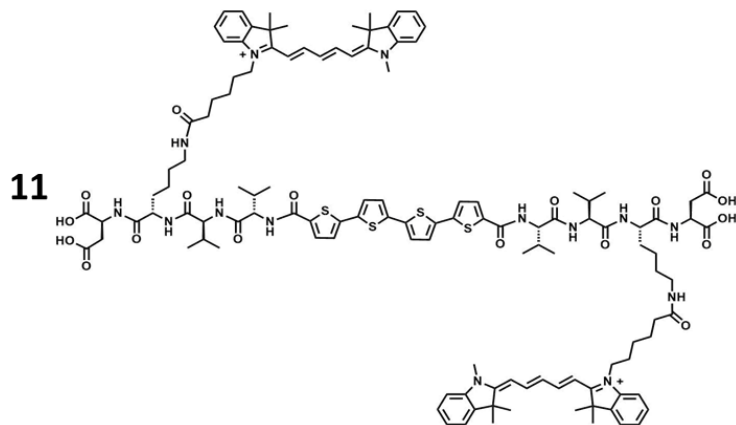


**Figure 5.11.** Fluorescence images of a) brain slice with saline and hydrogel injections and b) several slices of two brains with hydrogel visualized at the stroke site by monitoring the cy-5 channel.

## Conclusion

Peptide nanomaterials appended with pi-conjugated electronic units represent a powerful class of biomaterials well suited for tissue engineering or biosensing applications. The impaired ability of the CNS to recover after nerve injury and its propensity for glial scarring provides motivation for new strategies in cell therapies. External cues that direct stem cells toward neuronal lineages *in vitro* have been well documented, for example, the presence of external electric fields, the mechanical stiffness of the extracellular space and the presence of specific bioactive peptide cues present on the extracellular matrix, all of which should be tailored to match the environment of the native tissue. As such, after a series of successes and failures, a peptide-pi-peptide platform was produced wherein a peptide containing OT4-NDI capable of producing transient electric fields in aqueous media photonicallly and a bioactive epitope bearing peptide can be co-assembled. Likewise, the addition of an Alloc containing peptide could be incorporated to tune the mechanical properties of a tri-component hydrogel. The preliminary results for use of a pi-core bearing peptide in an *in vivo* mouse model were also presented. Electron microscope data demonstrate the formation of hydrogel in the stroke cavity, and addition of a far-red chromophore to the peptide allow for imaging of the gel by way fluorescence microscopy bypassing convolution from endogenous fluorescence. With this multi-component hydrogel platform established and conformation of hydrogel formation *in vivo*, cell culture studies and behavioral studies respectively will be a promising next step to assess these materials towards this needed area of research.

## Experimental

**General Considerations.** Reactions were carried out in flame-dried glassware under nitrogen atmosphere. Non-aqueous solvents were dried over molecular sieves and degassed by sparging

with nitrogen for a minimum of 15 minutes. Tetrakis(triphenylphosphine)palladium ( $\text{Pd(PPh}_3)_4$ ) was obtained from Strem Chemicals. Chemicals used in solid phase peptide synthesis (Wang resin, 9-fluorenylmethyloxycarbonyl (Fmoc) protected amino acids, 2-(1H-benzotriazol-1-yl)-1,1,3,3-tetramethyluronium hexafluorophosphate (HBTU), benzotriazol-1-yl-oxytripyrrolidinophosphonium hexafluorophosphate (PyBOP) and *N*-methylpyrrolidone (NMP)) were acquired from Advanced Chem. Tech., *N,N*-Diisopropylethylamine (DIPEA) was purchased from Fisher, and dried over 4Å molecular sieves before use. The synthesis of *N*-propyl-1,4,5,8-naphthalenetetracarboxylic acid monoanhydride and *n*-Bu-NDI-β-alanine were carried out according to literature precedent.<sup>1726</sup> All other chemicals were provided by Sigma-Aldrich or Fisher and used as they were received unless otherwise noted.

**General Fmoc-Based Peptide Synthesis:** Oligopeptide segments were synthesized via standard Fmoc-based solid phase peptide synthesis starting with the first Fmoc-amino acid preloaded onto Wang resin solid supports. The resin was swelled in dichloromethane (DCM) followed by deprotection of the Fmoc protecting group carried out in a solution of 20% v/v piperidine in *N,N*-dimethylformamide (DMF) for 2×10 min. The resin was washed with 3×NMP, 1×methanol (MeOH) followed by 3×DCM and swelled in DCM for 10 min. For all standard amino acid couplings (and the addition of *n*-Bu-NDI-β-alanine), a solution of 3 equivalents of the succeeding Fmoc protected amino acid, 2.9 equivalents of HBTU was prepared in 10 mL of NMP and sonicated to dissolve, followed by 10 equivalents of DIPEA and mixed for one min. The resin was drained of DCM, the activated amino acid was added to the chamber, and mixed for a minimum of 1 hour. The resin was then drained and rinsed with 3×NMP, 1×MeOH followed by 3×DCM, swelled in DCM for 10 minutes and the process repeated starting with Fmoc deprotection

for each sequential amino acid in the sequence. The success of each coupling step was monitored by performing a Kaiser test.

***N*-terminus-acylation, and on-resin Stille coupling procedure:** Peptides were acylated with 5-bromothiophene-2-carboxylic acid and subjected to Stille cross-coupling conditions in the presence of 5,5'-bis-tributylstannyl-[2,2']-bithiophene as previously described.<sup>27</sup>

**General Lys(Mtt) deprotection and Imidation Procedure:** The resin bound peptide bearing Lys(Mtt) was deprotected in a solution of 93:5:2 DCM:Trifluoroacetic Acid (TFA):Triisopropylsilane (TIPS) for 15 min (x2). The resin was drained and washed with 3×DCM, 3×NMP, 3×DMF, 3×95:5 DMF:DIPEA, 3×DMF, 3×NMP, 3×DCM. The resin was then dried and added to a Schlenk tube with N-propyl-1,4,5,8-naphthalenetetracarboxylic acid monoanhydride, a stir bar, and then fit with a reflux condenser. Following atmosphere exchange, 10 mL of dry, degassed DMF was added and the mixture was heated to 50°C for 1 hr, with continuous bubbling of N<sub>2</sub>. Then suspension was then heated to 110°C for 22 hours. After cooling, the resin was transferred to a peptide chamber and washed (3×NMP, 3×DMF, 2×iPrOH, 2×H<sub>2</sub>O, 2×acetonitrile, 2×diethylether, 2×hexanes).

**General peptide cleavage and work-up:** Following solid-phase synthesis the peptide was cleaved by mixing the resin in a 2.5:2.5:95 Water:TIPS:TFA cocktail for three hours. The solution was collected from the chamber, concentrated under vacuum, and triturated in cold diethylether. The suspended product was centrifuged to isolate and lyophilized. The lyophilized product was



HPLC purified. Specific experimental procedures and molecular characterization data for each molecule synthesized can be found in the supporting information.

**Electrospray Ionization Mass Spectrometry (ESI-MS):** ESI signatures were samples using a Thermo Finnigan LCQ Deca Ion Trap Mass Spectrometer operating in negative mode. Samples were prepared in a 1:1 MeOH:water solution with 0.1% ammonium hydroxide.

**UV-Vis and Photoluminescence:** UV-Vis spectra were acquired using a Varian Cary 50 Bio UV-Vis spectrophotometer. Photoluminescence spectra were taken on a PTi Photon Technology International Fluorometer equipped with a Ushio Xenon short arc lamp. Spectroscopic samples of homo assemblies were prepared at ca. 3  $\mu$ M in Millipore water with a final volume of 3100  $\mu$ L. For co-assemblies, the appropriate volume of stock solutions were both added to 3000  $\mu$ L of Milli-Q water and the remaining volume was added to dilute to 3100  $\mu$ L and final concentration of ca. 3  $\mu$ M for both peptides. The pH was adjusted by adding either 1M KOH, 1M HCl or 10 mg/mL GdL. HCl samples were measured immediately upon addition of acid while GdL samples were measured at approximately 24 hours after GdL addition.

**Reverse-Phase HPLC:** Peptides were purified by reverse-phase HPLC on a Varian PrepStar SD-1 system equipped with a Phenomenex, Luna, 5  $\mu$ m particle diameter silica support functionalized with TMS terminated C8. An aqueous 0.1% ammonium formate buffer (pH 8):acetonitrile gradient was used as mobile phase.

**Transmission Electron Microscopy (TEM):** Imaging was performed on a FEI TECNAI 12 TWIN transmission electron microscope equipped with an SIS Megaview III CCD digital camera. The samples were prepared in two ways. The first was by pipetting a drop of 1 mg/mL solution of assembled peptide in water onto ionized 200 mesh Formvar coated copper grids and incubated for 5 minutes at 25°C. Excess solution was removed by floating the grid in a drop of water. The sample was then stained with a 2% uranyl acetate solution, washed by dipping in water, and excess moisture was wicked off by dabbing the grid on filter paper. For peptides 4-7, superior imaging contrast was observed through another sample preparation method where 10µL of a 1 mg/mL solution of assembled peptide was allowed to sit on the grid for one minute. Excess solution was wicked away by dabbing the grid on filter paper. 10 µL of 2% uranyl acetate solution was allowed to sit on the grid for 30 seconds and then wicked away on filter paper. In both methods, the grids were allowed to dry completely in air before imaging.

## References

- (1) Horner, P. J.; Gage, F. H. Regenerating the Damaged Central Nervous System. *Nature* **2000**, 407, 963–970. <https://doi.org/10.1016/j.bbali.2010.02.007>.
- (2) Prabhakaran, M. P.; Venugopal, J. R.; Ramakrishna, S. Mesenchymal Stem Cell Differentiation to Neuronal Cells on Electrospun Nanofibrous Substrates for Nerve Tissue Engineering. *Biomaterials* **2009**, 30 (28), 4996–5003. <https://doi.org/10.1016/j.biomaterials.2009.05.057>.
- (3) Tibbitt, M. W.; Anseth, K. S. Hydrogels as Extracellular Matrix Mimics for 3D Cell Culture. *Biotechnology and Bioengineering* **2009**, 103 (4), 655–663. <https://doi.org/10.1002/bit.22361>.

- (4) Liyanage, W.; Mao, H.; Tovar, J. D. Cross-Linking Approaches to Tuning the Mechanical Properties of Peptide  $\pi$  - Electron Hydrogels. *Bioconjugate Chemistry* **2017**, *28*, 751–759. <https://doi.org/10.1021/acs.bioconjchem.6b00593>.
- (5) Park, S. Y.; Park, J.; Sim, S. H.; Sung, M. G.; Kim, K. S.; Hong, B. H.; Hong, S. Enhanced Differentiation of Human Neural Stem Cells into Neurons on Graphene. *Advanced Materials* **2011**, *23* (36), 263–267. <https://doi.org/10.1002/adma.201101503>.
- (6) Discher, D. E. Tissue Cells Feel and Respon to the Stiffness of Their Substrate. *Science* **2005**, *310* (5751), 1139–1143. <https://doi.org/10.1126/science.1116995>.
- (7) Trappmann, B.; Gautrot, J. E.; Connelly, J. T.; Strange, D. G. T.; Li, Y.; Oyen, M. L.; Cohen Stuart, M. A.; Boehm, H.; Li, B.; Vogel, V.; Spatz, J. P.; Watt, F. M.; Huck, W. T. S. Extracellular-Matrix Tethering Regulates Stem-Cell Fate. *Nature Materials* **2012**, *11* (7), 642–649. <https://doi.org/10.1038/nmat3339>.
- (8) Guimarães, C. F.; Gasperini, L.; Marques, A. P.; Reis, R. L. The Stiffness of Living Tissues and Its Implications for Tissue Engineering. *Nature Reviews Materials* **2020**, *5* (5), 351–370. <https://doi.org/10.1038/s41578-019-0169-1>.
- (9) Wells, R. G. The Role of Matrix Stiffness in Regulating Cell Behavior. *Hepatology* **2008**, *47* (4), 1394–1400. <https://doi.org/10.1002/hep.22193>.
- (10) Yeh, Y. C.; Ling, J. Y.; Chen, W. C.; Lin, H. H.; Tang, M. J. Mechanotransduction of Matrix Stiffness in Regulation of Focal Adhesion Size and Number: Reciprocal Regulation of Caveolin-1 and B1 Integrin. *Scientific Reports* **2017**, *7* (1), 1–14. <https://doi.org/10.1038/s41598-017-14932-6>.

- (11) Liu, J.; Zheng, H.; Poh, P. S. P.; Machens, H. G.; Schilling, A. F. Hydrogels for Engineering of Perfusable Vascular Networks. *International Journal of Molecular Sciences* **2015**, *16* (7), 15997–16016. <https://doi.org/10.3390/ijms160715997>.
- (12) Tong, Z.; Jia, X. Biomaterials-Based Strategies for the Engineering of Mechanically Active Soft Tissues. *MRS Communications* **2011**, *4* (164), 31–39. <https://doi.org/10.1126/scisignal.2001449.Engineering>.
- (13) Seidlits, S. K.; Khaing, Z. Z.; Petersen, R. R.; Nickels, J. D.; Vanscoy, J. E.; Shear, J. B.; Schmidt, C. E. The Effects of Hyaluronic Acid Hydrogels with Tunable Mechanical Properties on Neural Progenitor Cell Differentiation. *Biomaterials* **2010**, *31* (14), 3930–3940. <https://doi.org/10.1016/j.biomaterials.2010.01.125>.
- (14) Serena, E.; Figallo, E.; Tandon, N.; Cannizzaro, C.; Gerecht, S.; Elvassore, N.; Vunjak-Novakovic, G. Electrical Stimulation of Human Embryonic Stem Cells: Cardiac Differentiation and the Generation of Reactive Oxygen Species. *Experimental Cell Research* **2009**, *315* (20), 3611–3619. <https://doi.org/10.1016/j.yexcr.2009.08.015>.
- (15) Funk, R. H. W. Endogenous Electric Fields as Guiding Cue for Cell Migration. *Frontiers in Physiology* **2015**, *6* (May), 1–8. <https://doi.org/10.3389/fphys.2015.00143>.
- (16) Schmidt, C. E.; Shastri, V. R.; Vacanti, J. P.; Langer, R. Stimulation of Neurite Outgrowth Using an Electrically Conducting Polymer. *Applied Biological Sciences* **1997**, *94*, 8948–8953.
- (17) Sanders, A. M.; Magnanelli, T. J.; Bragg, A. E.; Tovar, J. D. Photoinduced Electron Transfer within Supramolecular Donor-Acceptor Peptide Nanostructures under Aqueous Conditions. *Journal of the American Chemical Society* **2016**, *138* (10), 3362–3370. <https://doi.org/10.1021/jacs.5b12001>.

- (18) Vadehra, G. S.; Wall, B. D.; Diegelmann, S. R.; Tovar, J. D. On-Resin Dimerization Incorporates a Diverse Array of p-Conjugated Functionality within Aqueous Self-Assembling Peptide Backbones. *Chemical Communications* **2010**, *46*, 3947–3949.  
<https://doi.org/10.1039/c0cc00301h>.
- (19) Diegelmann, S. R.; Hartman, N.; Markovic, N.; Tovar, J. D. Synthesis and Alignment of Discrete Polydiacetylene-Peptide Nanostructures. *J. Am. Chem. Soc.* **2012**, *134*, 2028–2031.  
<https://doi.org/10.1021/ja211539j>.
- (20) Ardon, H. A. M.; Tovar, J. D. Peptide  $\pi$ -Electron Conjugates: Organic Electronics for Biology? *Bioconjugate Chemistry* **2015**, *26*, 2290–2302.  
<https://doi.org/10.1021/acs.bioconjchem.5b00497>.
- (21) Pfister, L. A.; Papaloïzos, M.; Merkle, H. P.; Gander, B. Nerve Conduits and Growth Factor Delivery in Peripheral Nerve Repair. *Journal of the peripheral nervous system* **2007**, *12* (2), 65–82. <https://doi.org/10.1111/j.1529-8027.2007.00125.x>.
- (22) Wen, S.; Li, H.; Liu, J. Dynamic Signaling for Neural Stem Cell Fate Determination. *Cell adhesion & migration* **2009**, *3* (1), 107–117. <https://doi.org/10.4161/cam.3.1.7602>.
- (23) Pharmacology, N. *Neuroimmune Pharmacology Textbook*.
- (24) Tickler, A. K.; Wade, J. D. Overview of Solid Phase Synthesis of “Difficult Peptide” Sequences. *Current Protocols in Protein Science* **2007**, No. November, 18.8.1-18.8.6.  
<https://doi.org/10.1002/0471140864.ps1808s50>.
- (25) Lee, K. S.; Parquette, J. R. A Self-Assembled Nanotube for the Direct Aldol Reaction in Water. *Chem. Commun.* **2015**, *51* (86), 15653–15656. <https://doi.org/10.1039/C5CC06142C>.
- (26) Nalluri, S. K. M.; Berdugo, C.; Javid, N.; Frederix, P. W. J. M.; Ulijn, R. v. Biocatalytic Self-Assembly of Supramolecular Charge-Transfer Nanostructures Based on n-Type Semiconductor-

Appended Peptides. *Angewandte Chemie - International Edition* **2014**, 53 (23), 5882–5887.

<https://doi.org/10.1002/anie.201311158>.

- (27) Dimerizations, C. S.; Sanders, A. M.; Dawidczyk, T. J.; Katz, H. E.; Tovar, J. D. Peptide-Based Supramolecular Semiconductor Nanomaterials via Pd- Catalyzed Solid-Phase “ Dimerizations .” *ACS Macro Letters* **2012**, 1, 1326–1329.

## **Appendix**

### **Characterization Data and Supporting Information**

## Chapter 2

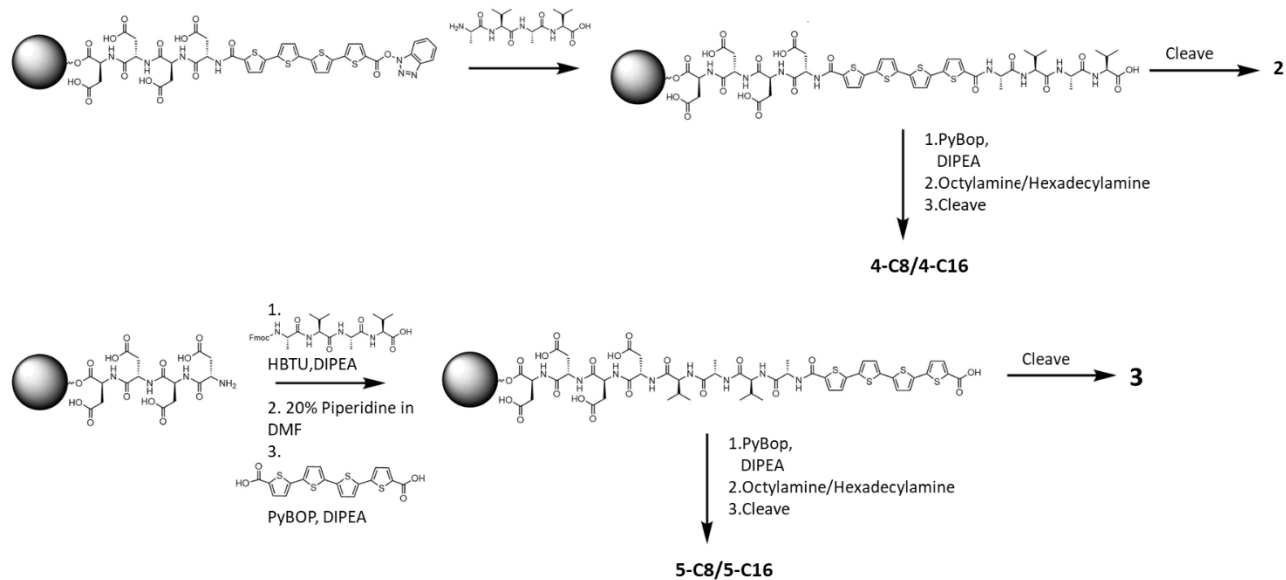


**Figure A2.1.** Peptide library was synthesized by standard solid-phase peptide synthesis adapted with an on-resin carboxylic acid activation procedure.



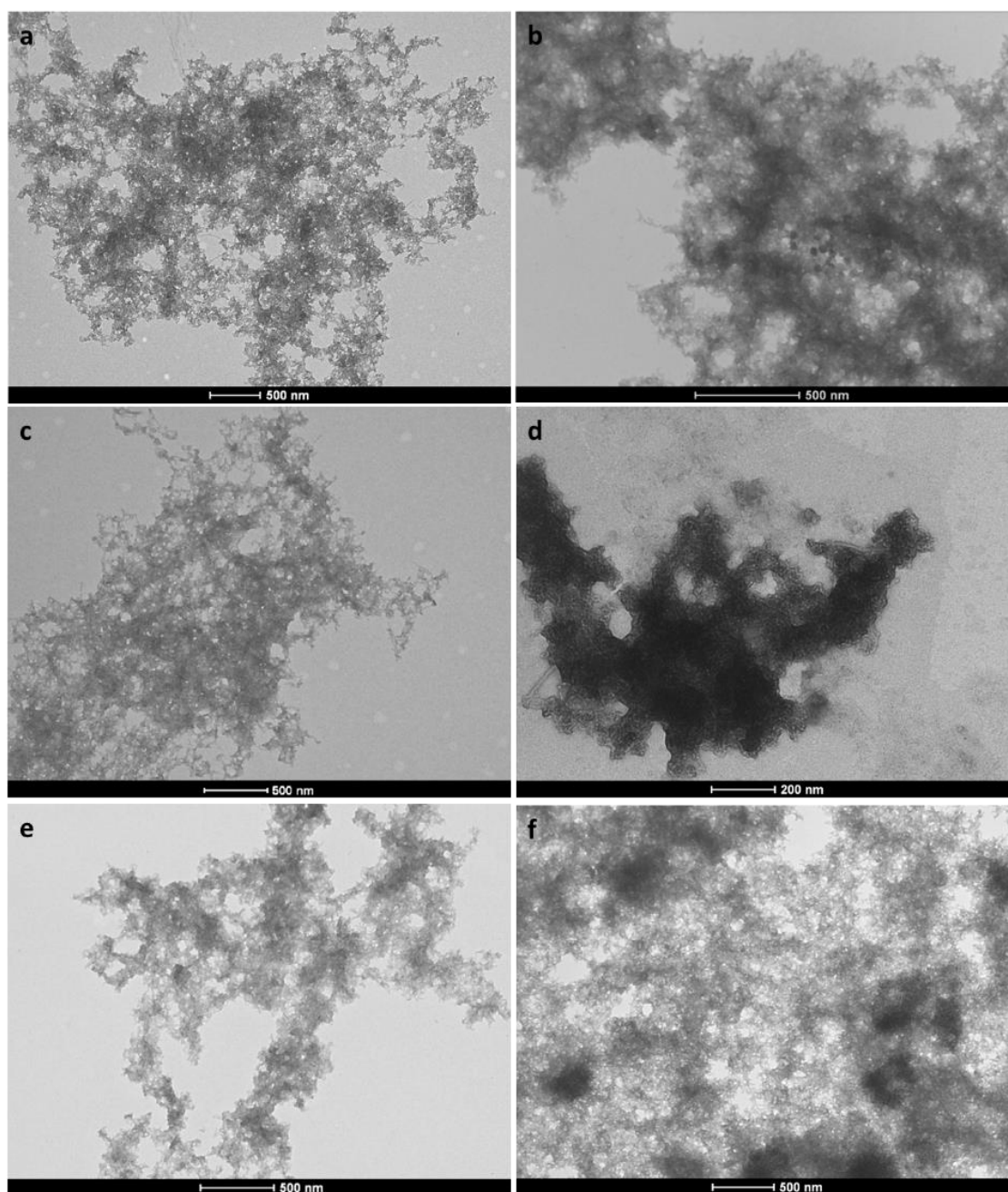


**Figure A2.2:** Transmission electron micrographs of basic-to-acidic processing of peptides (a) 4-C8 (b) 5-C8 (c) 4-C16 (d) 5-C16 (e) 7-C8 and (f) 7-C16 show random aggregates.

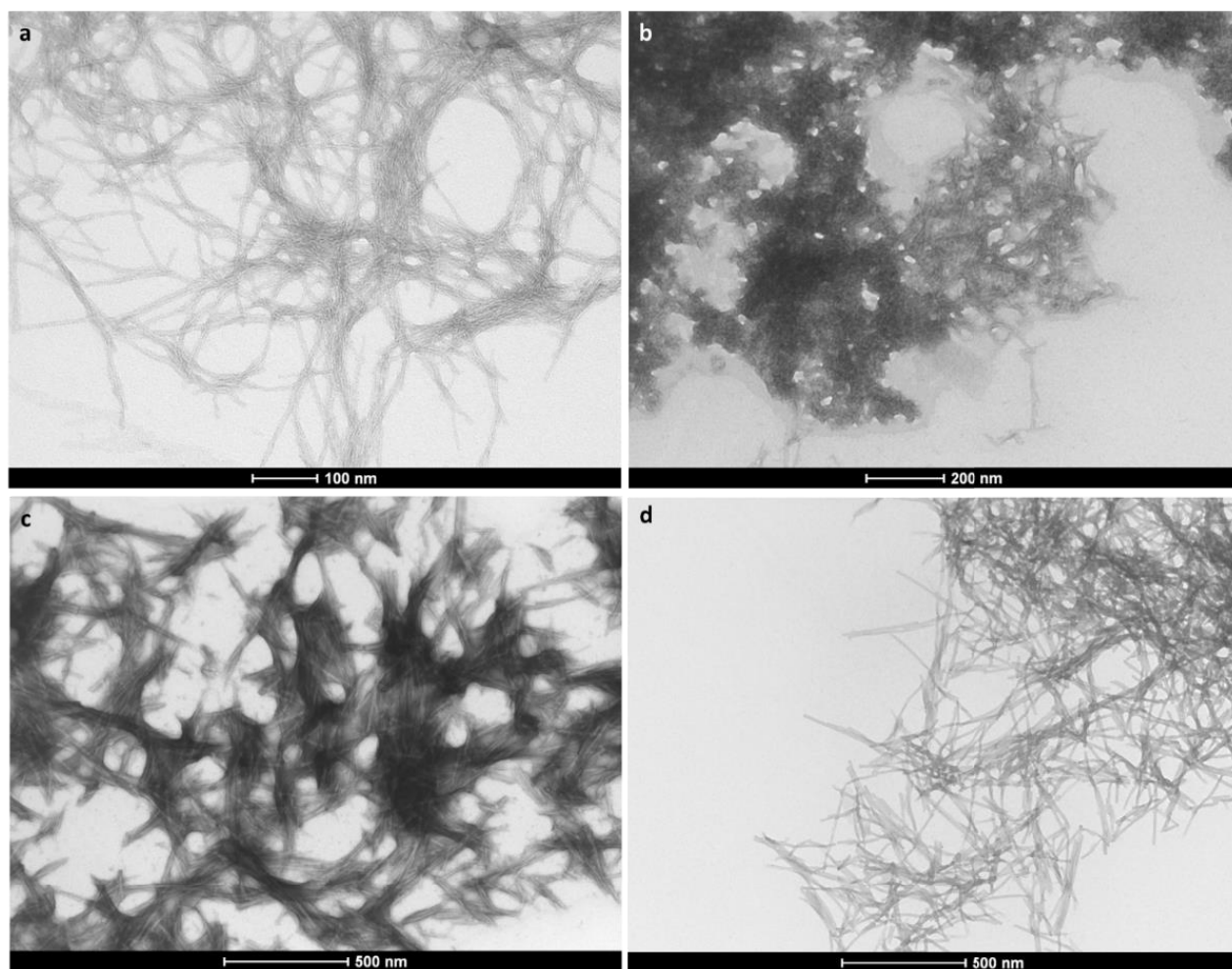


**Figure A2.3.** Transmission electron micrograph of (a) 1 and (b) 3 in basic-to-acidic assemblies and (c) 2 and (d) 3 in neutral-to-acidic assemblies.

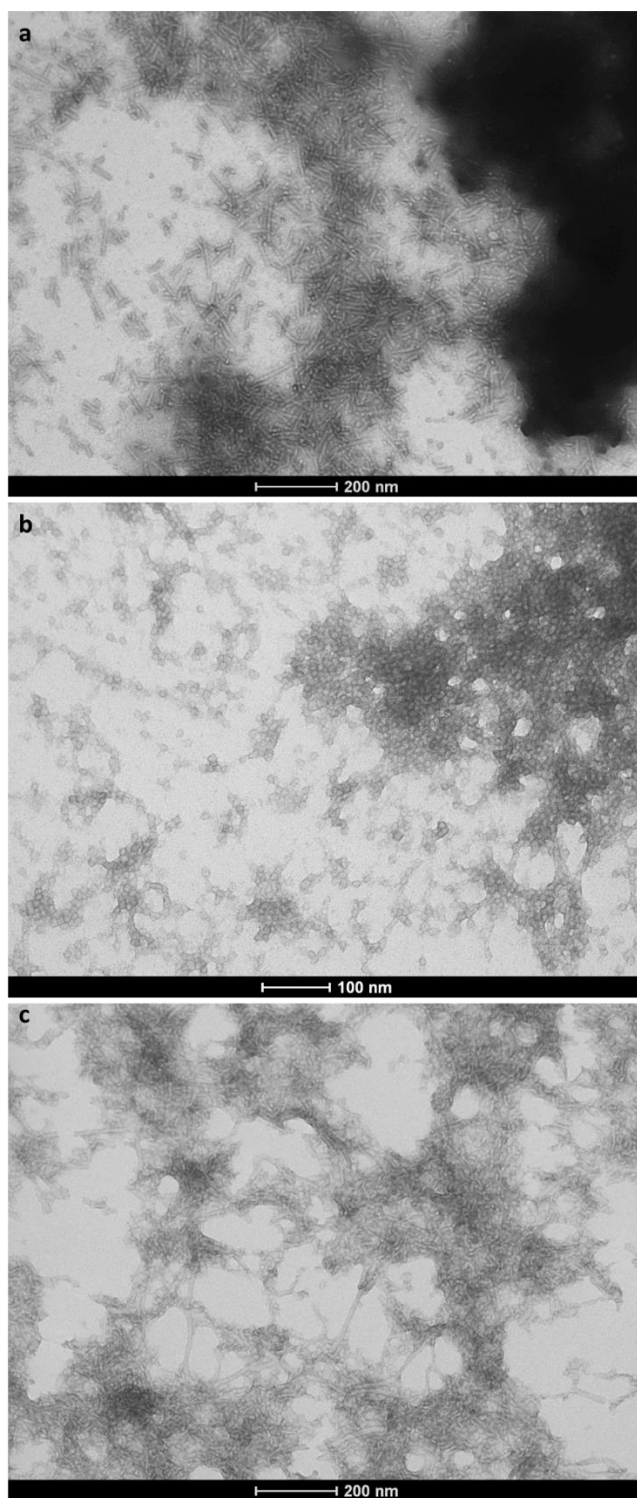


**Figure A2.4.** Representative transmission electron micrograph of (a) 4-C16 dissolved in buffer pH 7 after sonication, thermal annealing, and equilibration at room temperature for two weeks and

5-C16 dissolved in (b) pH 7.0 and (c) 8.6 buffers, sonicated, thermally annealed for 24 hours and equilibrated at room temperature for two weeks.

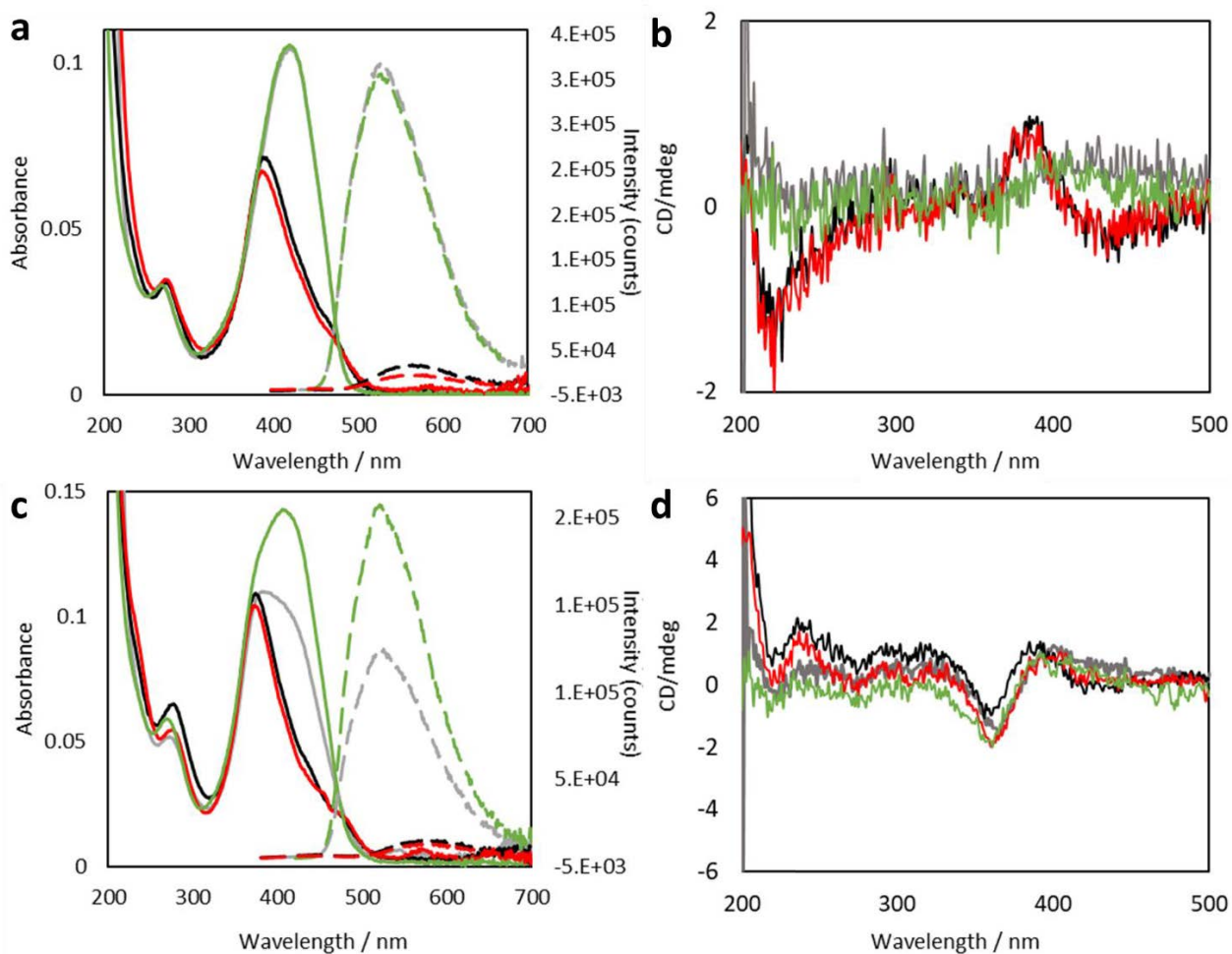


**Figure A2.5.** UV-Vis (left panels, solid) and photoluminescence (left panels, dashed), and CD (right panels) spectra for (a,b) 4-C8 (c,d) 5-C8 (e,f) in basic (grey), acidic (black), 30 minutes after acidification (red) and in thermally annealed samples pH 7 (green).

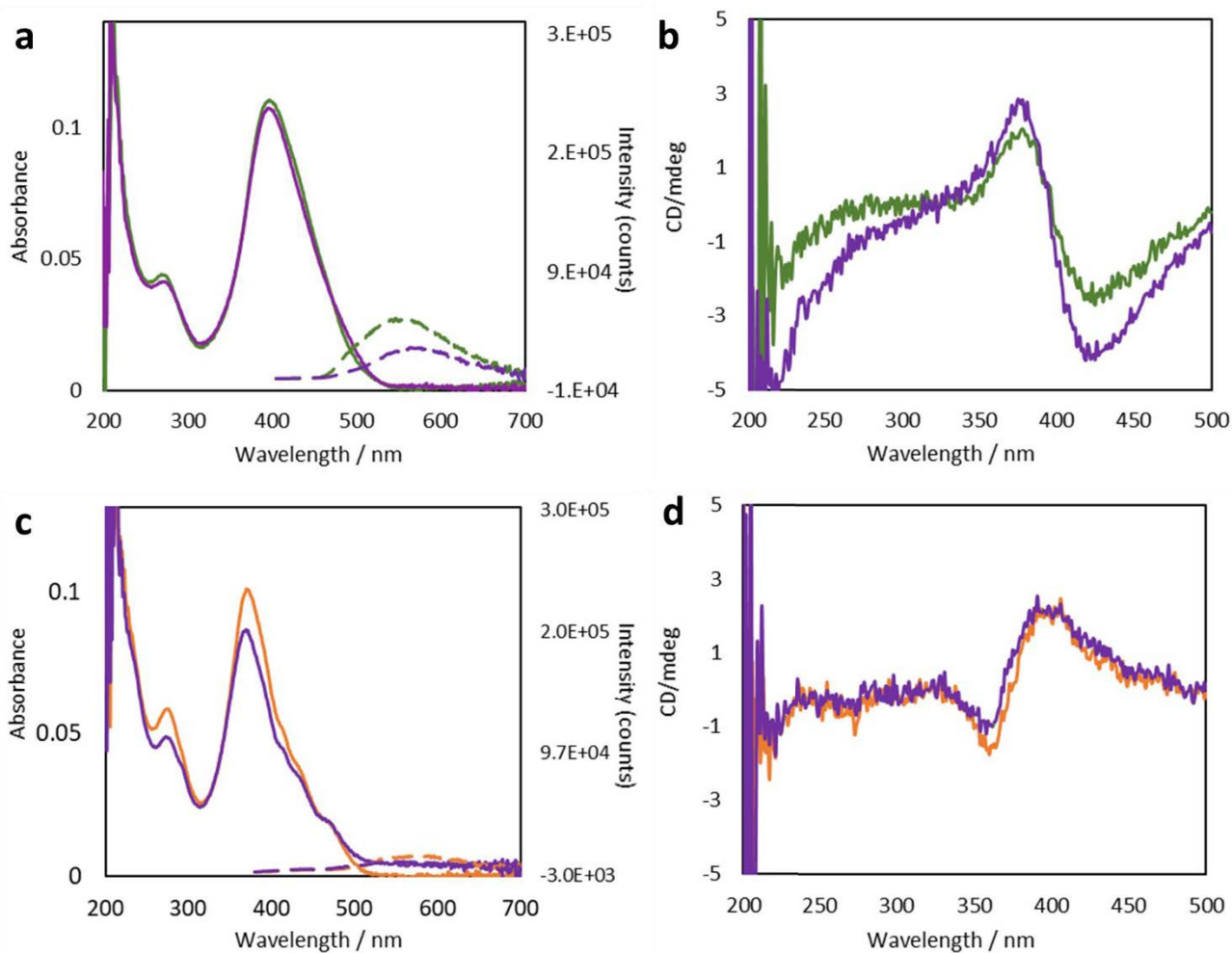
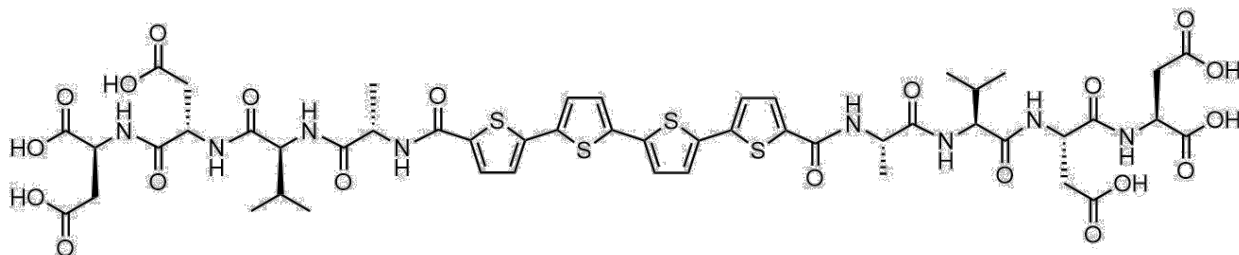
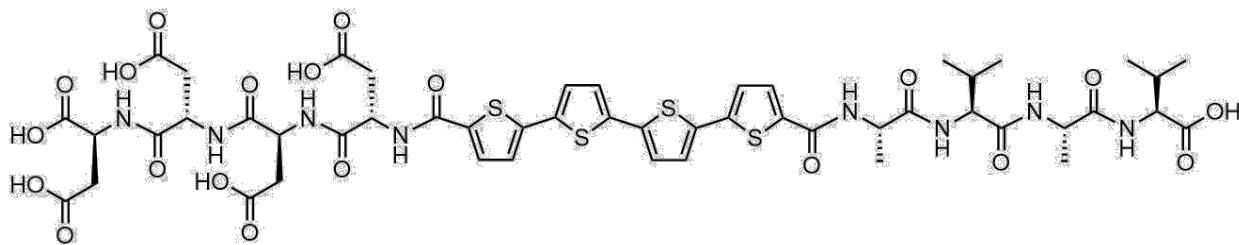


**Figure A2.6.** UV-Vis (left panels, solid lines), photoluminescence (left panels, dashed lines), and CD (right panels) spectra for 4-C16 (a,b) and 5-C16 in pH 8.6 buffer 16 hours (green traces), 24 hours (orange traces) and two weeks (purple traces) after thermal annealing.

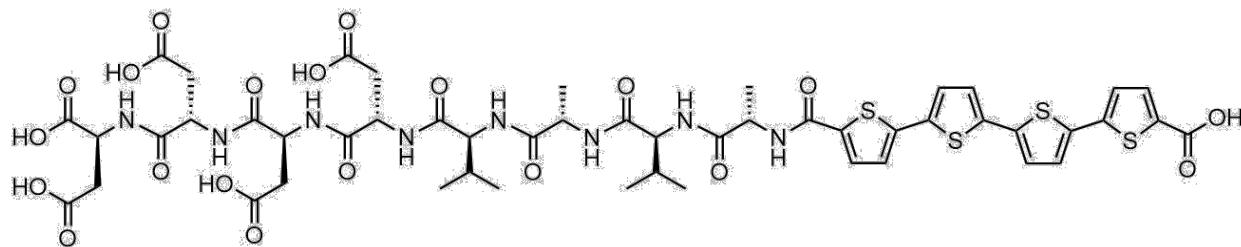
## Synthesis Details and Molecular Characterization Data:



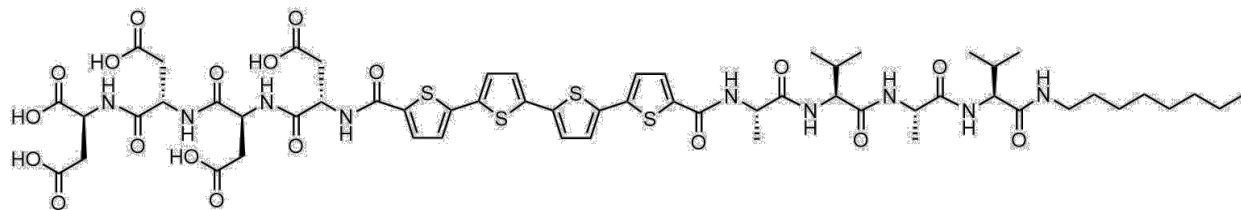
**HO-DDVA-OT4-AVDD-OH (1):** Solid supported Wang-DDVA-NH<sub>2</sub> peptide (0.2 mmol) was *N*-acylated with 5-bromothiophene-2-carboxylic acid and subjected to the standard Stille coupling procedure in the presence of 5,5'-bis-tributylstannyl-[2,2']-bithiophene (0.1 mmol, 0.07 g) and Pd(PPh<sub>3</sub>)<sub>4</sub> (0.008 mmol, 0.009 g). Following general cleavage, work-up, and HPLC purification, the peptide was obtained as a light orange powder (0.017 mmol, 9%). DATA UV-Vis (H<sub>2</sub>O)  $\lambda$ /nm (pH 10): 420. MS (ESI) *m/z* 1217.0 (M-1H) (calc. 1217.3), *m/z* 608.3 (M-2H)/2 (calc. 608.7).



**HO-DDDD-OT4-AVAV-OH (2):** Solid supported Wang-DDDD-NH<sub>2</sub> peptide (0.2 mmol) was *N*-acylated with [2,2':5',2'':5'',2'''-quaterthiophene]-5,5'''-dicarboxylic acid and then subjected to the on-resin activation procedure. A solution of HO-VAVA-NH<sub>2</sub> (0.4 mmol) was prepared and added to the resin and mixed for 16 hours. Following general cleavage, work-up, and HPLC purification, the peptide was obtained as a light orange powder (0.007 mmol, 3%). DATA UV-Vis (H<sub>2</sub>O)  $\lambda$ /nm (pH 10): 420. MS (ESI) *m/z* 1217.4 (M-1H) (calc. 1217.3), *m/z* 608.5 (M-2H)/2 (calc. 608.0), *m/z* 405.1 (M-3H)/3 (calc. 405.0).

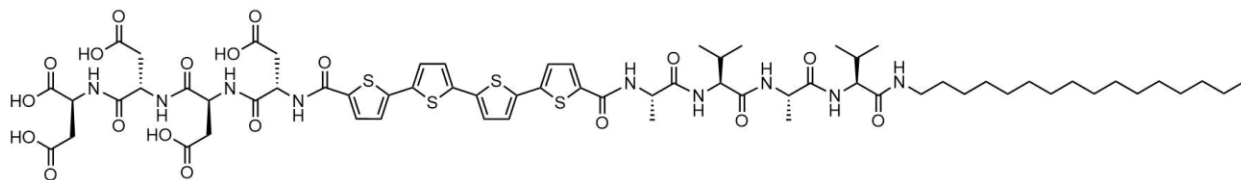


**HO-DDDD-VAVA-OT4-OH (3):** Solid supported Wang-DDDD-NH<sub>2</sub> peptide (0.2 mmol) was *N*-acylated with HO-VAVA-NHFmoc (0.4 mmol). The terminal Fmoc was deprotected and capped with [2,2':5',2'':5'',2'''-quaterthiophene]-5,5'''-dicarboxylic acid. Following general cleavage, work-up, and HPLC purification, the peptide was obtained as a light orange powder (0.016 mmol, 8%). DATA UV-Vis (H<sub>2</sub>O)  $\lambda$ /nm (pH 10): 417. MS (ESI) *m/z* 1217.1 (M-1H) (calc. 1217.3), *m/z* 608.5 (M-2H)/2 (calc. 608.0).

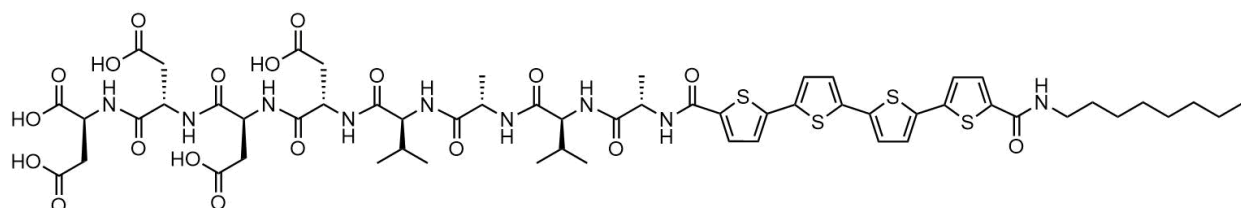


**HO-DDDD-OT4-AVAV-C8 (4-C8):** Solid supported Wang-DDDDD-NH<sub>2</sub> peptide (0.2 mmol) was *N*-acylated with [2,2':5',2'':5'',2'''-quaterthiophene]-5,5'''-dicarboxylic acid and subjected to the on-resin activation procedure. A solution of HO-VAVA-NH<sub>2</sub> (0.4 mmol) was prepared and added to the resin and mixed for 16 hours. The terminal carboxylic acid was again subjected to the on-resin activation procedure. A solution of octylamine (0.6 mmol, 0.10 mL) in NMP was added and stirred for 16 hours. Following general cleavage, work-up, and HPLC purification, the peptide was obtained as a light orange powder (0.002 mmol, 1%). DATA UV-Vis (H<sub>2</sub>O)  $\lambda$ /nm (pH 10): 413. MS (ESI) *m/z* 1328.3 (M-1H) (calc. 1328.4), *m/z* 664.3 (M-2H)/2 (calc. 663.7), *m/z* 442.9 (M-3H)/3 (calc. 442.1).



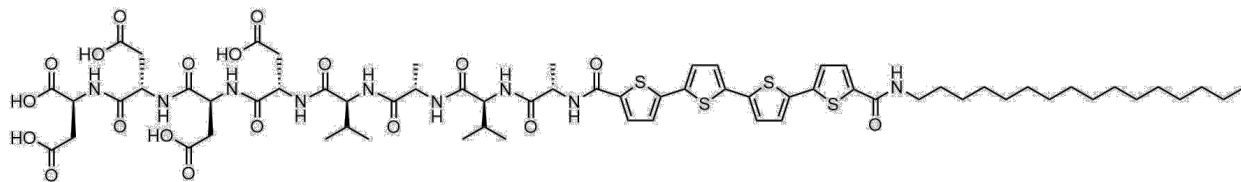


**HO-DDDD-OT4-AVAV-C16 (4-16):** Solid supported Wang-DDDD-NH<sub>2</sub> (0.2 mmol) peptide was *N*-acylated with [2,2':5',2'':5'',2''':5''']-quaterthiophene-5,5'''-dicarboxylic acid and subjected to the on-resin activation procedure. A solution of HO-VAVA-NH<sub>2</sub> (0.4 mmol) was prepared and added to the resin and mixed for 16 hours. The terminal carboxylic acid was again subjected to the on-resin activation procedure. A solution of hexadecylamine (0.6 mmol, 0.14 mL) in NMP was added and stirred for 16 hours. Following general cleavage, work-up, and HPLC purification, the peptide was obtained as a light orange powder (0.002 mmol, 1%). DATA UV-Vis (H<sub>2</sub>O)  $\lambda$ /nm (pH 10): 420. MS (ESI) *m/z* 1440.5 (M-1H) (calc. 1440.5), *m/z* 720.6 (M-2H)/2 (calc. 719.7), *m/z* 480.3 (M-3H)/3 (calc. 479.5).



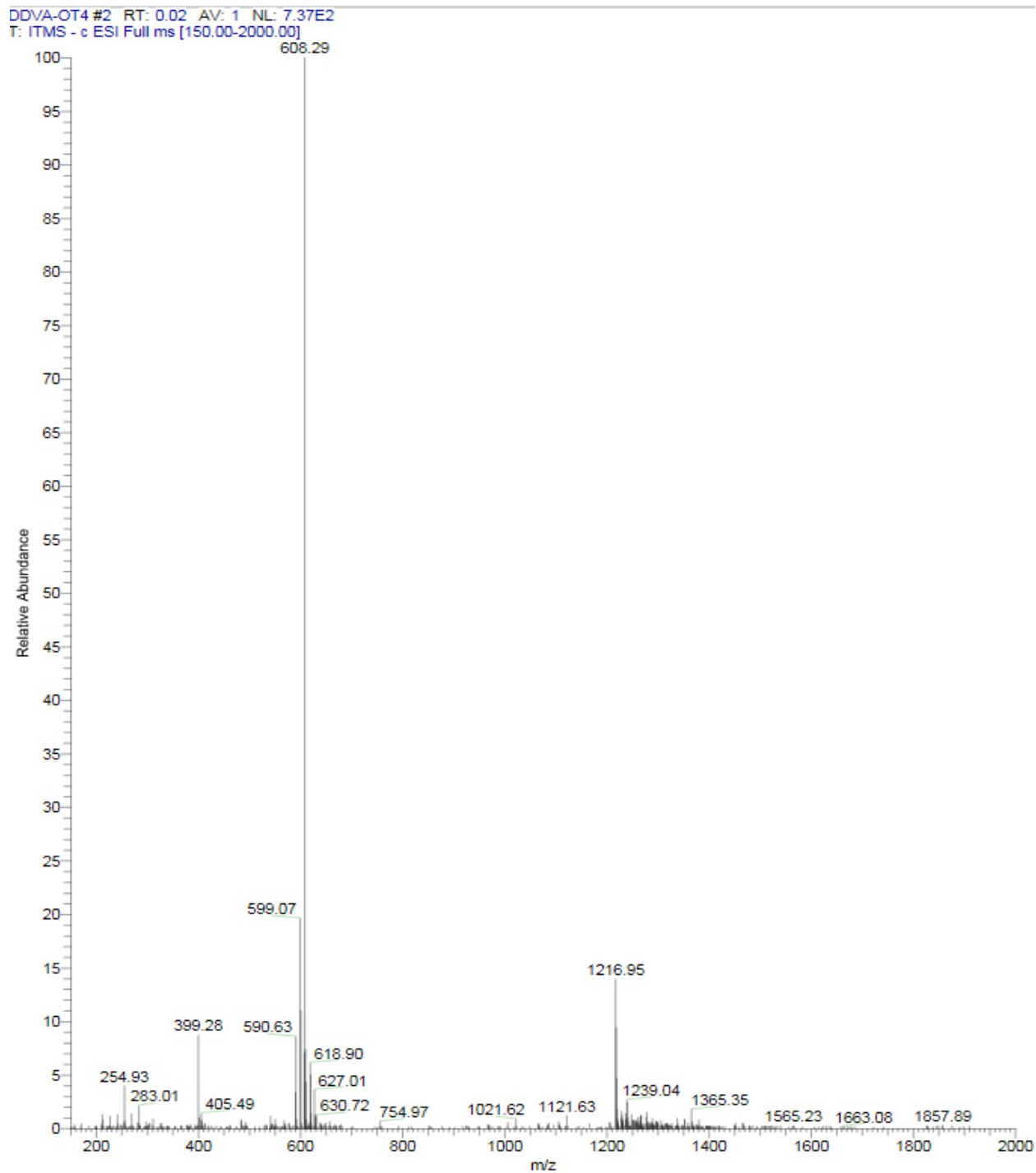
**HO-DDDD-VAVA-OT4-C8 (5-C8):** Solid supported Wang-DDDD-NH<sub>2</sub> (0.2 mmol) peptide was *N*-acylated with HO-VAVA-NHFmoc (0.4 mmol). The terminal Fmoc was deprotected and capped with [2,2':5',2'':5'',2''':5''']-quaterthiophene-5,5'''-dicarboxylic acid and subjected to the on-resin activation procedure. A solution of octylamine (0.6 mmol, 0.10 mL) in NMP was prepared and added to the resin and mixed for 16 hours. Following general cleavage, work-up, and HPLC purification, the peptide was obtained as a light orange powder (0.004 mmol, 2%). DATA UV-Vis (H<sub>2</sub>O)  $\lambda$ /nm (pH 10): 417. MS (ESI) *m/z* 1328.2 (M-1H) (calc. 1238.4), *m/z* 663.7 (M-2H)/2 (calc. 663.7).



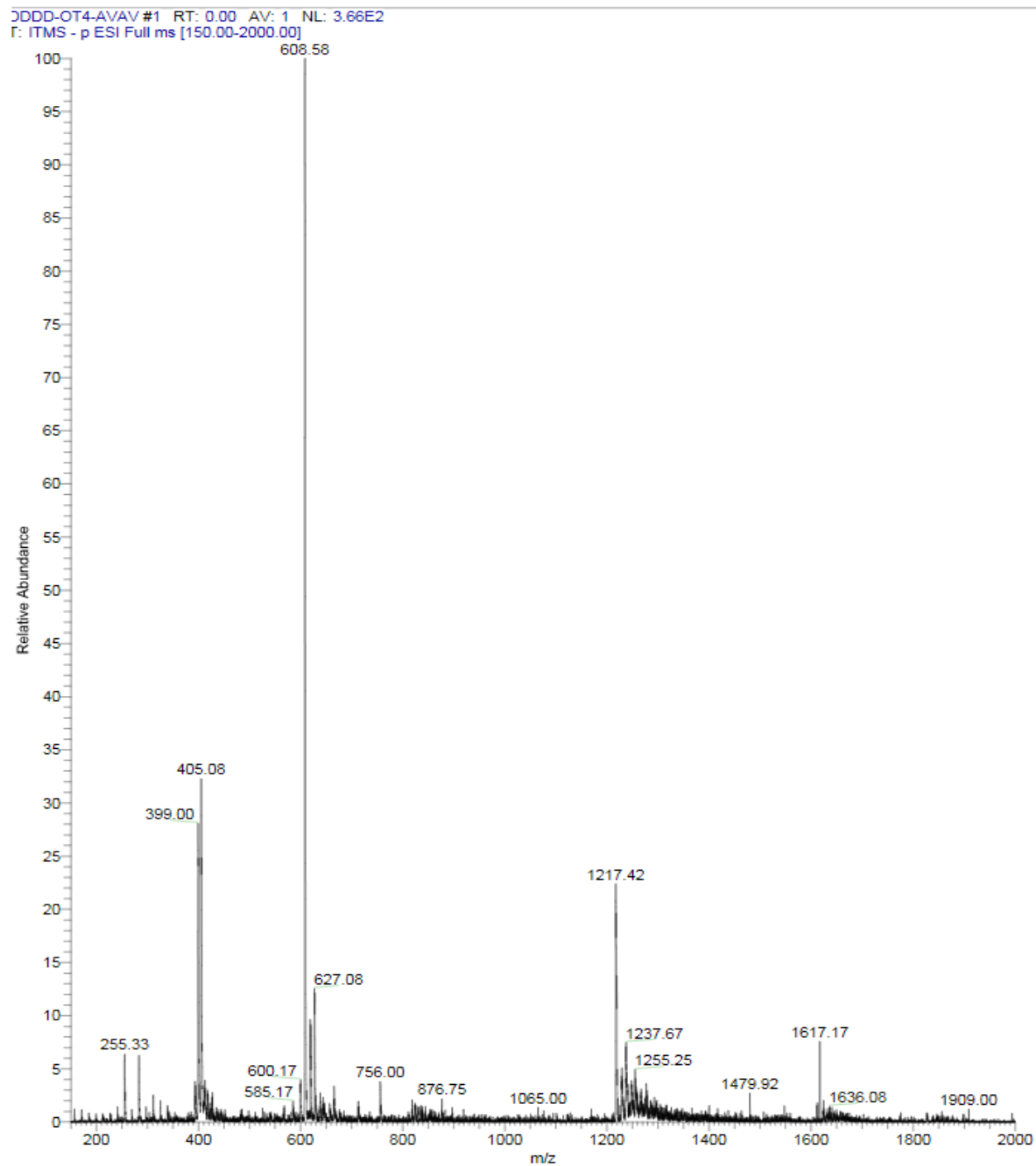


**HO-DDDD-VAVA-OT4-16 (5-C16):** Solid supported Wang-DDDD-NH<sub>2</sub> peptide (0.2 mmol) was *N*-acylated with HO-VAVA-NHFmoc (0.4 mmol). The terminal Fmoc was deprotected and capped with [2,2':5',2'':5'',2''':5''',2''''-quaterthiophene]-5,5''''-dicarboxylic acid and subjected to the on-resin activation procedure. A solution of hexadecylamine (0.6 mmol, 0.14 mL) in NMP was prepared and added to the resin and mixed for 16 hours. Following general cleavage, work-up, and HPLC purification, the peptide was obtained as a light orange powder (0.001 mmol, 1%). UV-Vis (H<sub>2</sub>O)  $\lambda_{\text{nm}}$  (pH 10): 402. MS (ESI)  $m/z$  1440.31 (M-1H) (calc. 1440.5),  $m/z$  720.45 (M-2H)/2 (calc. 719.7).

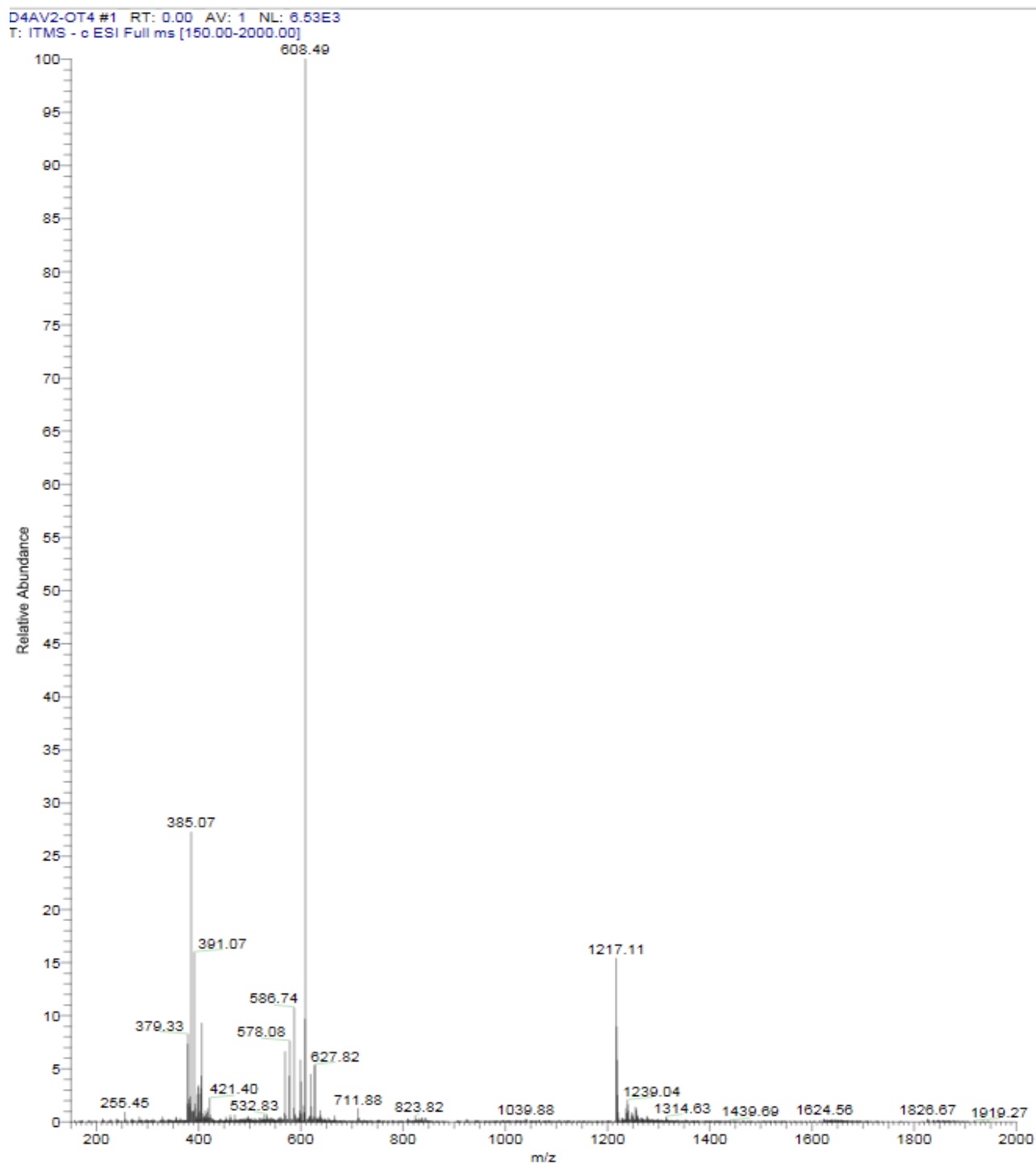
## ESI Mass Spectra:



**Figure A2.7.** ESI spectrum of HO-DDVA-OT4-AVDD-OH peptide (1). MS (ESI)  $m/z$  1217.0 (M-1H) (calc. 1217.3),  $m/z$  608.3 (M-2H)/2 (calc. 608.7).

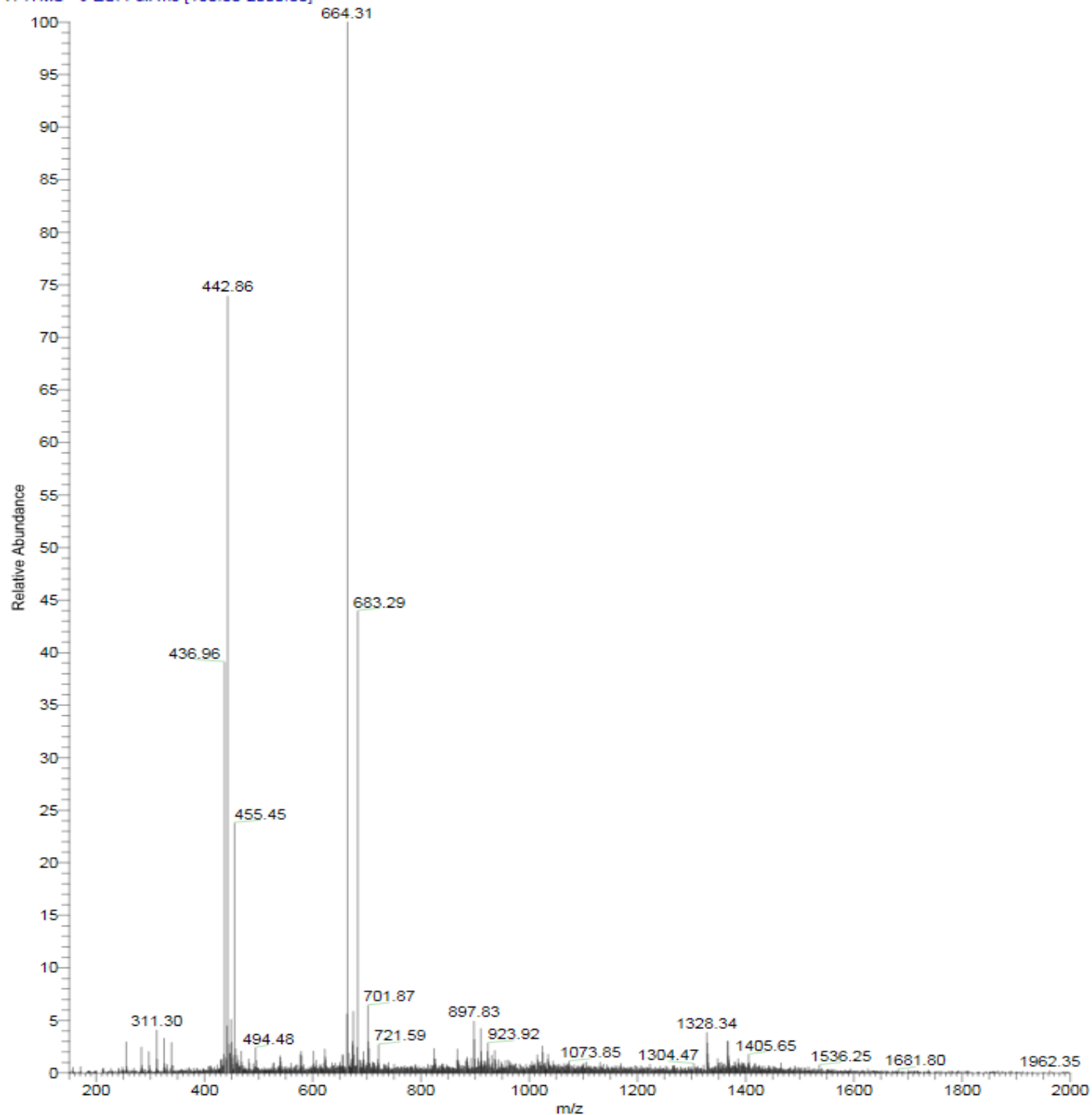


**Figure A2.8.** ESI spectrum of HO-DDDD-OT4-AVAV-OH peptide (2). MS (ESI)  $m/z$  1217.4 (M-1H) (calc. 1217.3),  $m/z$  608.5 (M-2H)/2 (calc. 608.0),  $m/z$  405.1 (M- 3H)/3 (calc. 405.0).

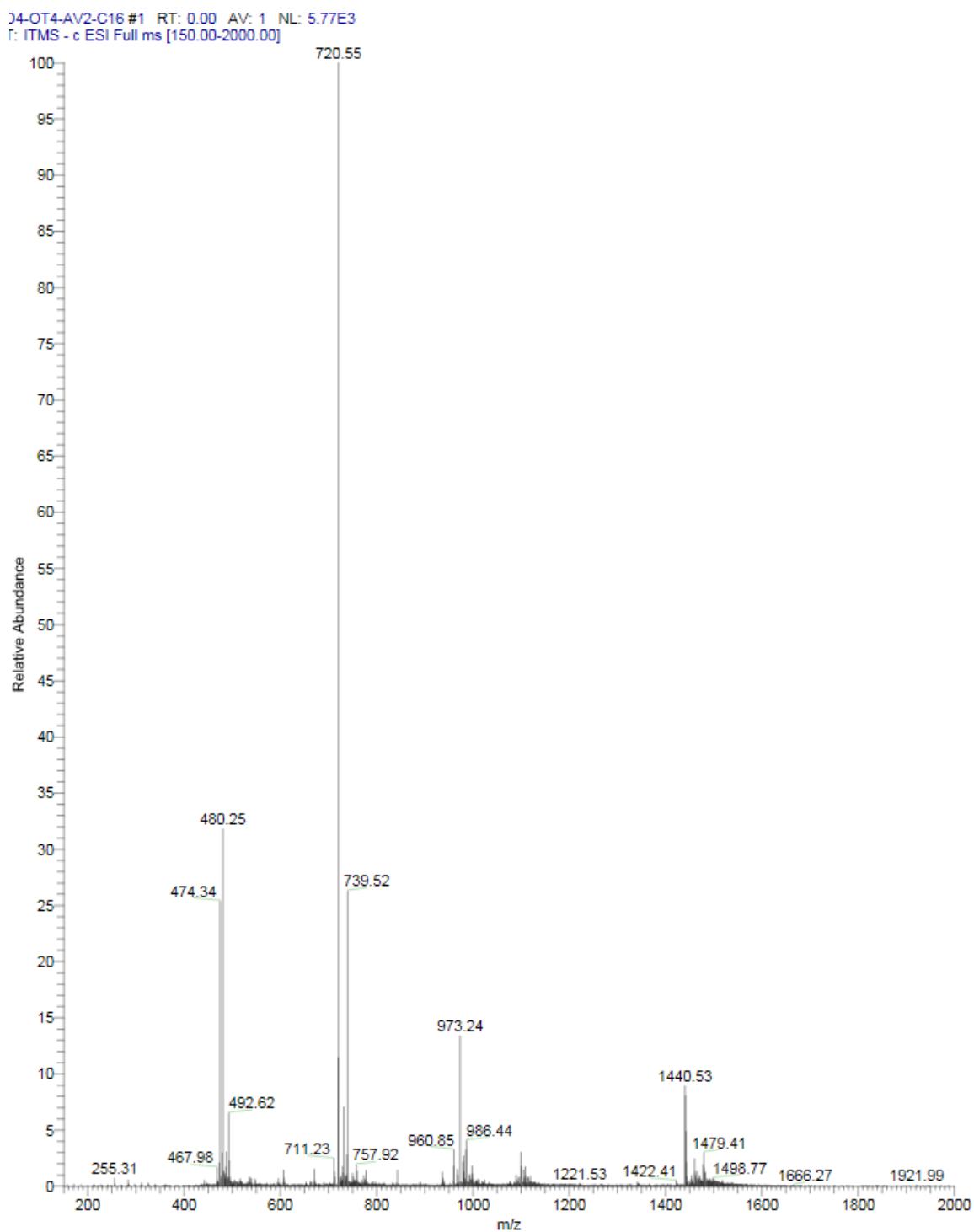


**Figure A2.9.** ESI spectrum of HO-DDDD-VAVA-OT4-OH peptide (3). MS (ESI)  $m/z$  1217.1 (M-1H) (calc. 1217.3),  $m/z$  608.5 (M-2H)/2 (calc. 608.0).

DDDD-OT4-AVAV-C8 #1 RT: 0.00 AV: 1 NL: 2.04E3  
T: ITMS - c ESI Full ms [150.00-2000.00]

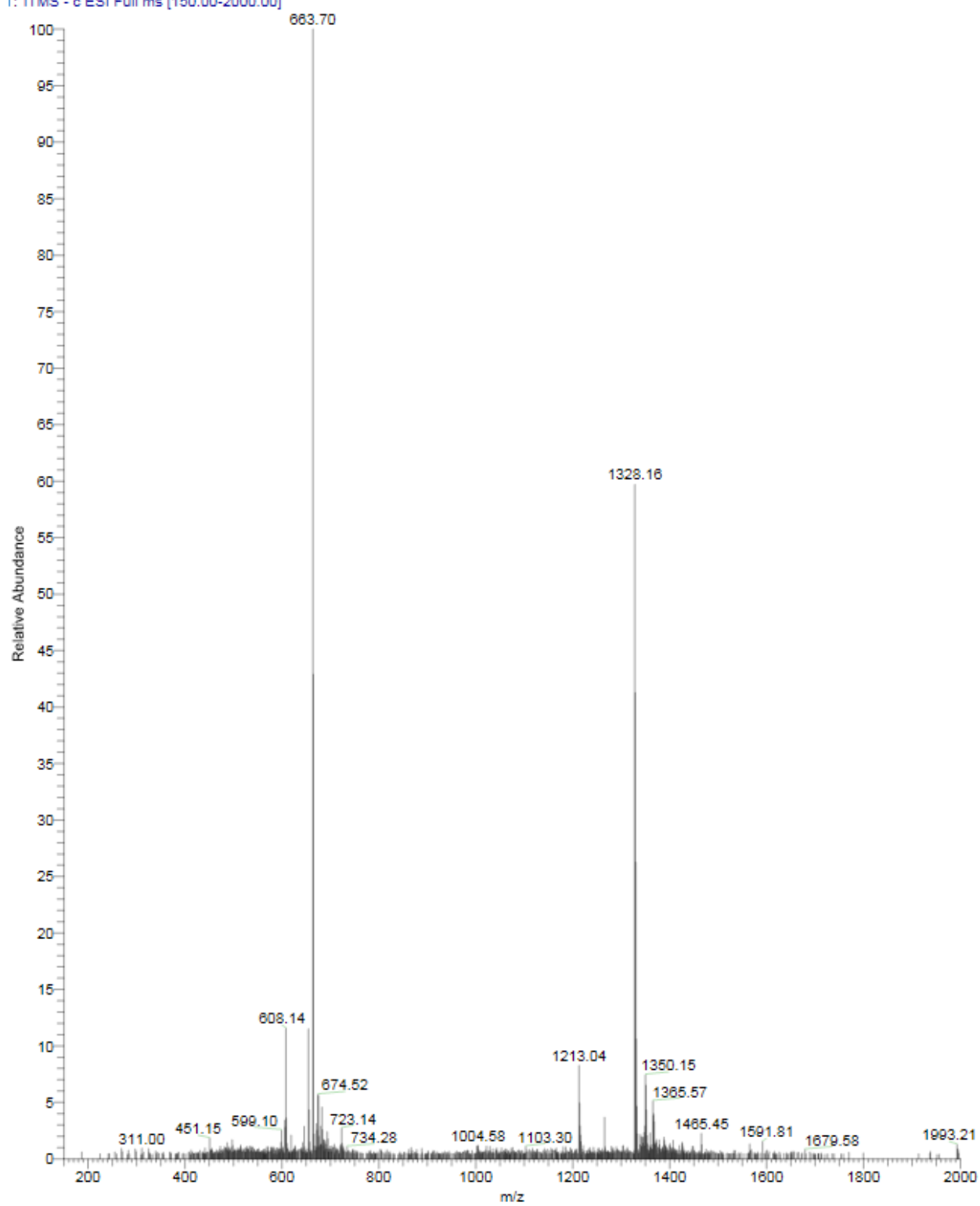


**Figure A2.10.** ESI spectrum of HO-DDDD-OT4-AVAV-C8 peptide (4-C8). MS (ESI)  $m/z$  1328.3 (M-1H) (calc. 1328.4),  $m/z$  664.3 (M-2H)/2 (calc. 663.7),  $m/z$  442.9 (M-3H)/3 (calc. 442.1).

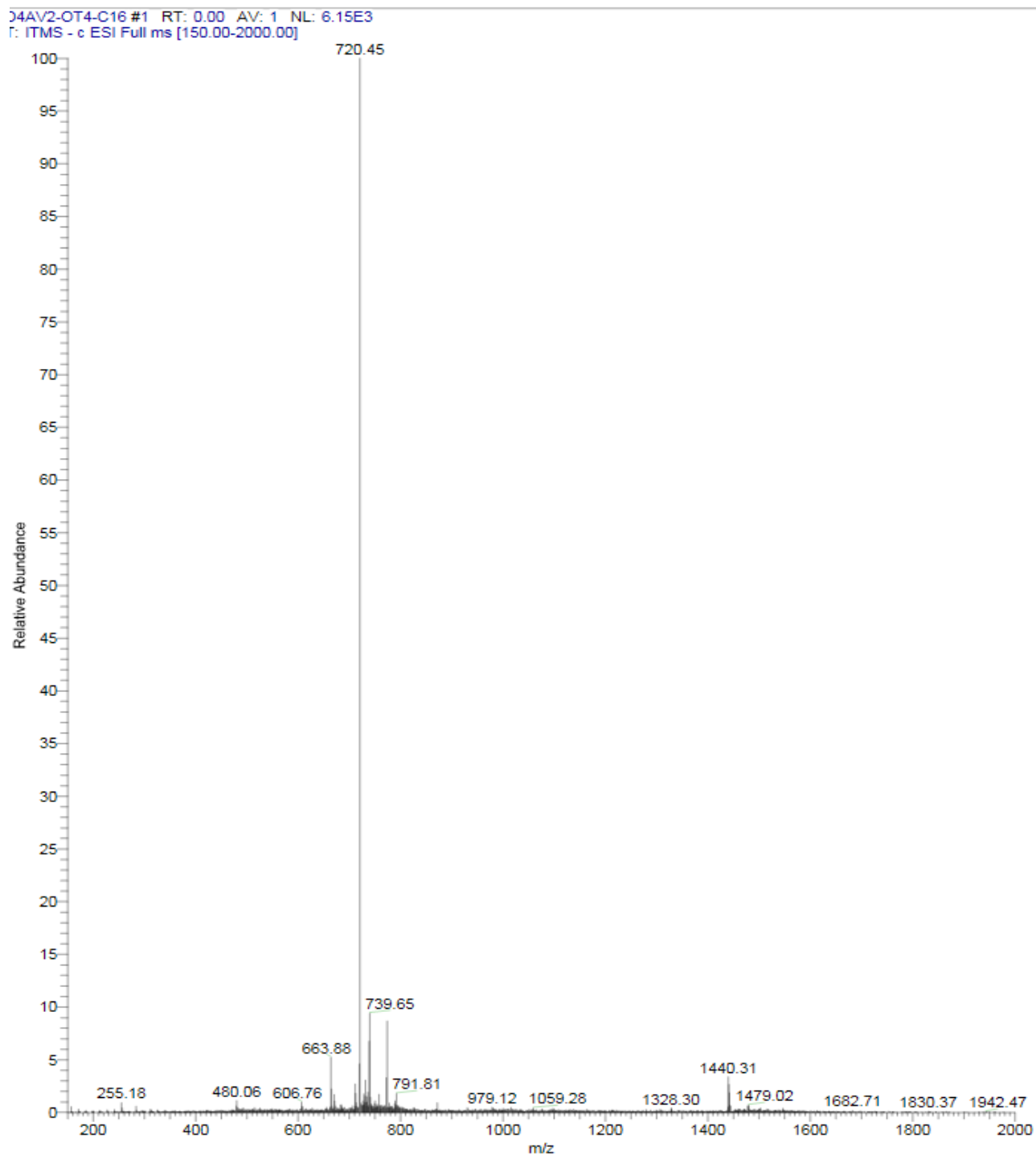


**Figure A2.11.** ESI spectrum of HO-DDDD-OT4-AVAV-C16 peptide (4-C16). MS (ESI)  $m/z$  1440.5 (M-1H) (calc. 1440.5),  $m/z$  720.6 (M-2H)/2 (calc. 719.7),  $m/z$  480.3 (M-3H)/3 (calc. 479.5).

04VA2-OT4-C8 #10 RT: 0.15 AV: 1 NL: 2.70E2  
f: ITMS - c ESI Full ms (150.00-2000.00)



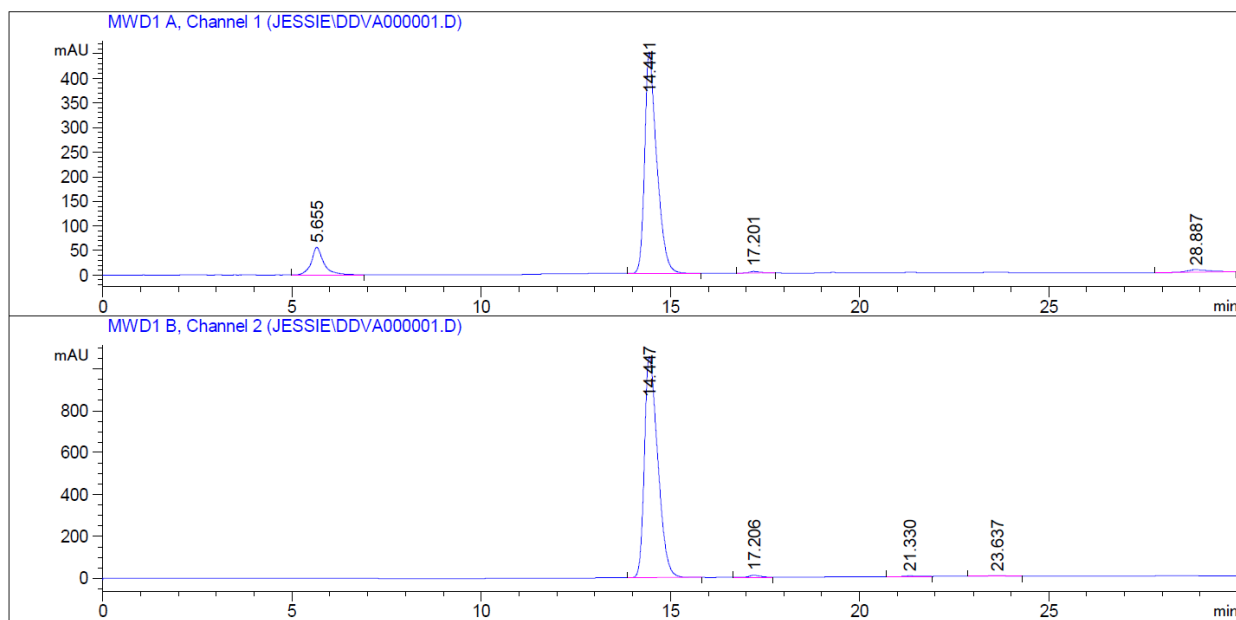
**Figure A2.12.** ESI spectrum of HO-DDDD-VAVA-OT4-C8 peptide (5-C8). MS (ESI)  $m/z$  1328.2 (M-1H) (calc. 1238.4),  $m/z$  663.7 (M-2H)/2 (calc. 663.7).



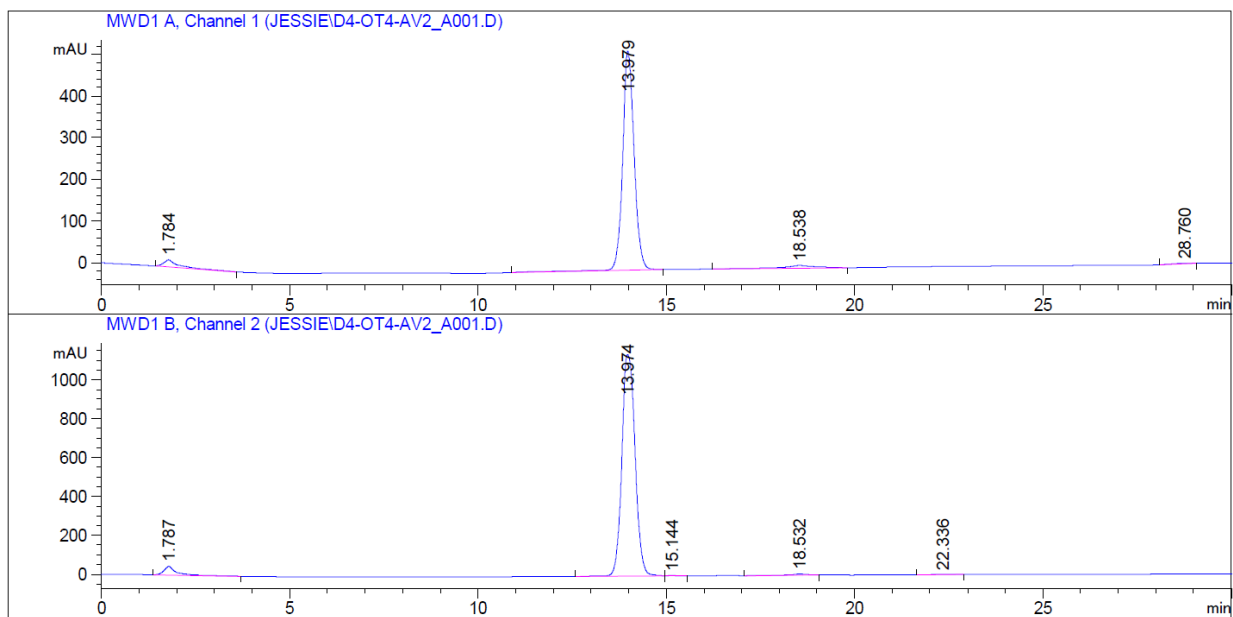


**Figure A2.13.** ESI spectrum of HO-DDDD-VAVA-OT4-C16 peptide (5-C16). MS (ESI)  $m/z$  1440.31 (M-1H) (calc. 1440.5),  $m/z$  720.45 (M-2H)/2 (calc. 719.7).

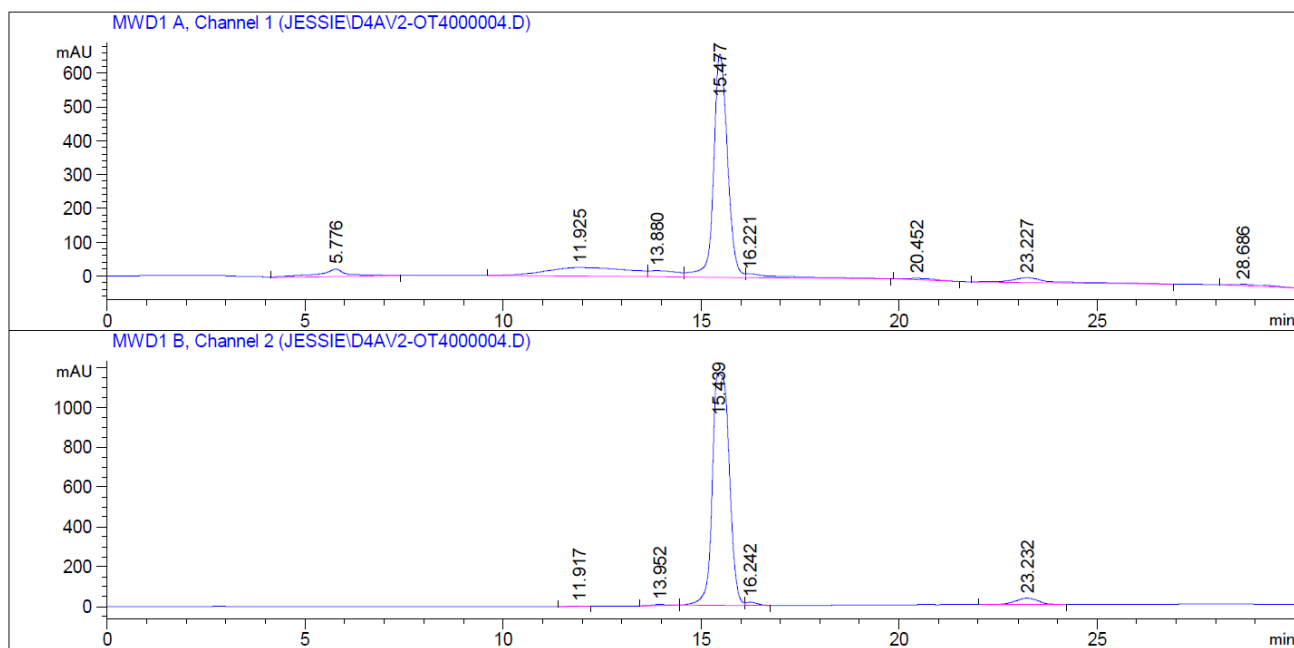
### HPLC Traces of Purified Peptides



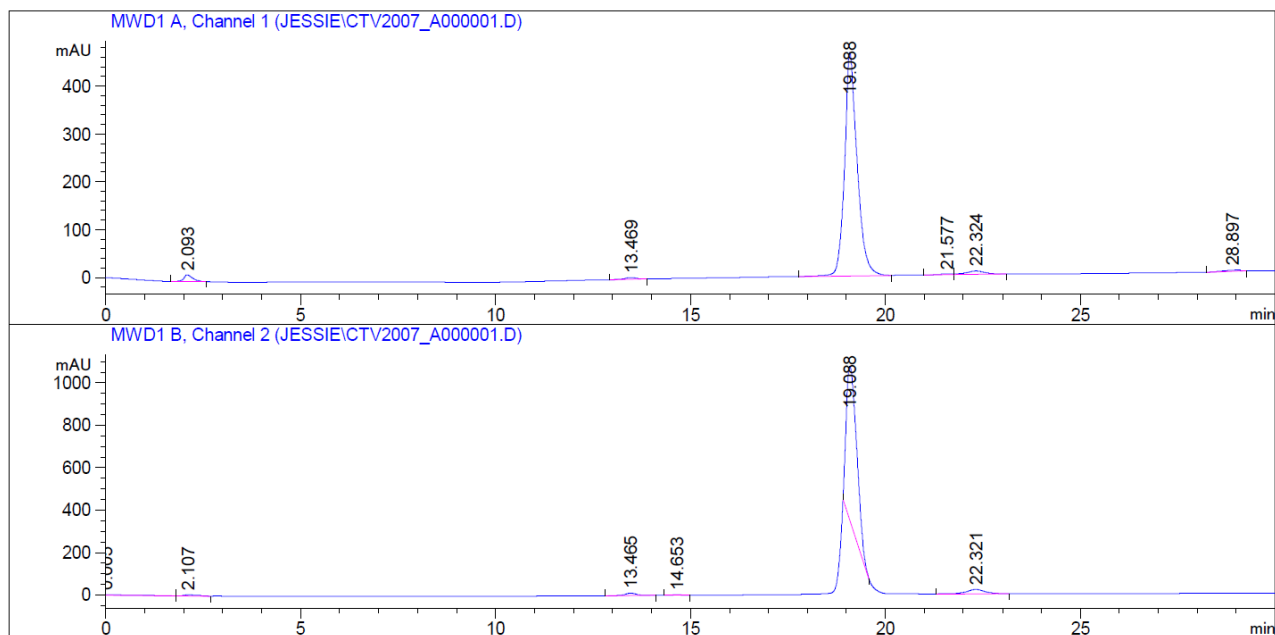
**Figure A2.14:** Analytical HPLC trace of purified HO-DDVA-OT4-AVDD-OH peptide (1). Traces monitoring 260 nm (top) and 420 nm (bottom). Method: Linear gradient of 10%-50% acetonitrile/buffer over 25 minutes, then linear gradient of 50%-10% over 5 minutes.



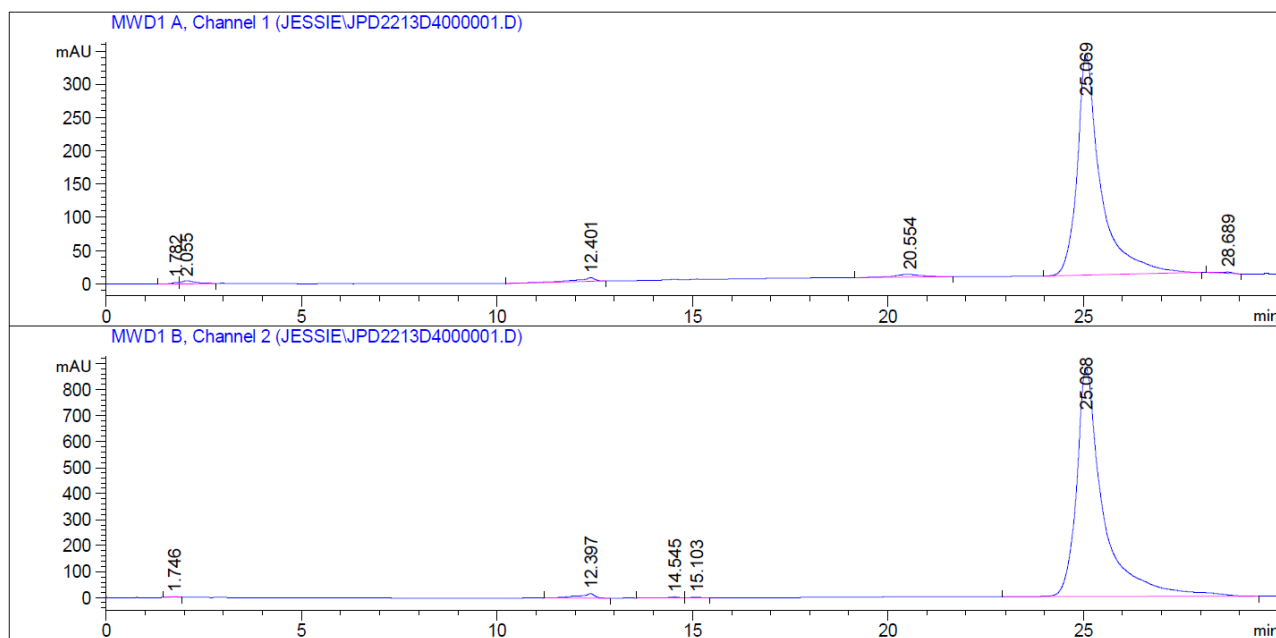
**Figure A2.15.** Analytical HPLC trace of purified HO-DDDD-OT4-AVAV-OH peptide (2). Traces monitoring 260 nm (top) and 420 nm (bottom). Method: Linear gradient of 10%-50% acetonitrile/buffer over 25 minutes, then linear gradient of 50%-10% over 5 minutes.



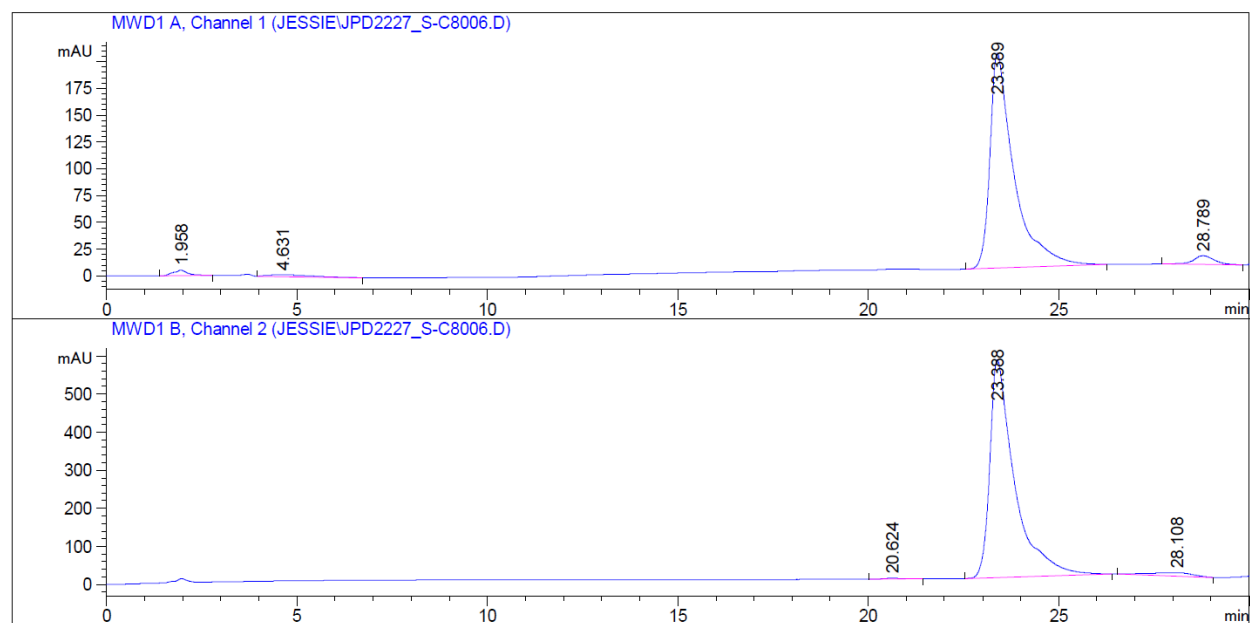
**Figure A2.16.** Analytical HPLC trace of purified HO-DDDD-VAVA-OT4-OH peptide (3). Traces monitoring 260 nm (top) and 420 nm (bottom). Method: Linear gradient of 10%-50% acetonitrile/buffer over 25 minutes, then linear gradient of 50%-10% over 5 minutes.



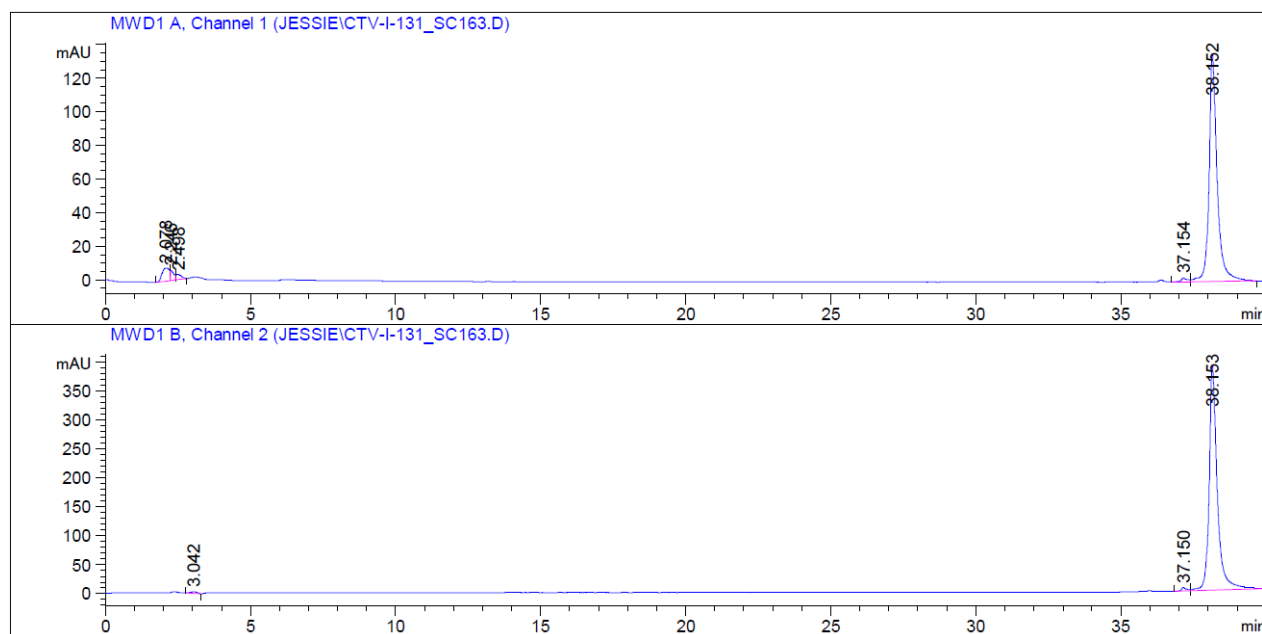
**Figure A2.17.** Analytical HPLC trace of purified HO-DDDD-OT4-AVAV-C8 peptide (4-C8). Traces monitoring 260 nm (top) and 420 nm (bottom). Method: Linear gradient of 20%-60% acetonitrile/buffer over 25 minutes, then linear gradient of 60%-20% over 5 minutes.



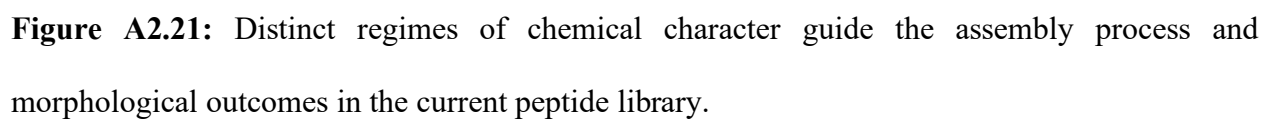
**Figure A2.18.** Analytical HPLC trace of purified HO-DDDD-OT4-AVAV-C16 peptide (4-C16). Traces monitoring 260 nm (top) and 420 nm (bottom). Method: Linear gradient of 30%-70% acetonitrile/buffer over 25 minutes, then linear gradient of 70%-30% over 5 minutes.



**Figure A2.19.** Analytical HPLC trace of purified HO-DDDD-VAVA-OT4-C8 peptide (5-C8).  
Traces monitoring 260 nm (top) and 420 nm (bottom). Method: Linear gradient of 20%-60%  
acetonitrile/buffer over 25 minutes, then linear gradient of 60%-20% over 5 minutes.



**Figure A2.20.** Analytical HPLC trace of purified HO-DDDD-VAVA-OT4-C16 peptide (5-C16).  
Traces monitoring 260 nm (top) and 420 nm (bottom). Method: Linear gradient of 30%-70%  
acetonitrile/buffer over 25 minutes, then linear gradient of 70%-30% over 5 minutes



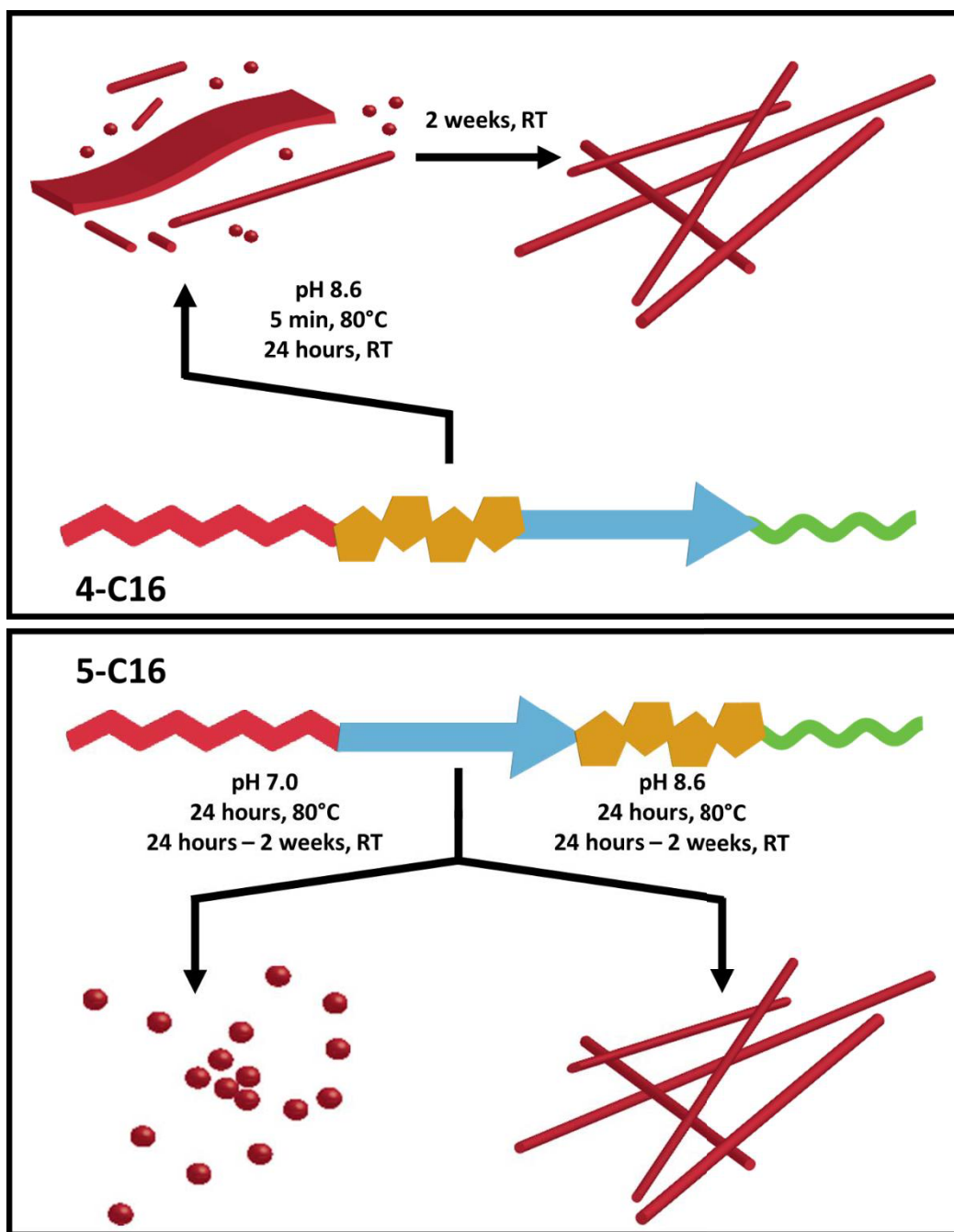


**Figure A2.22:** Assembly conditions and morphological outcomes for the 4-C16 and 5-C16 peptides.

## Chapter 3

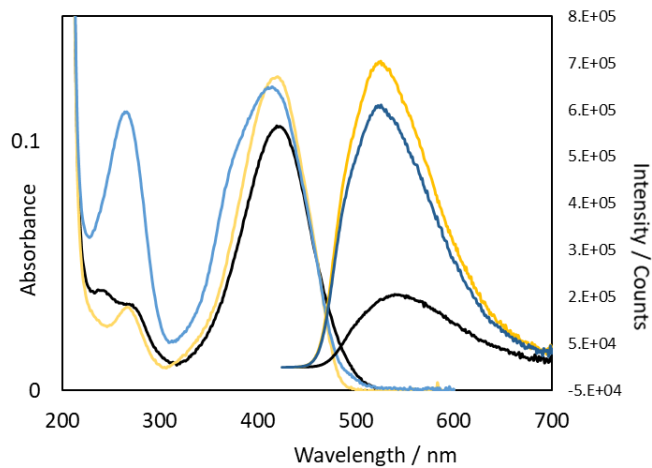


**Figure A3.1.** UV-vis absorbance (left) and PL (right) spectra for 1 (black), 2 (blue traces), and 3 (yellow traces) under basic conditions.

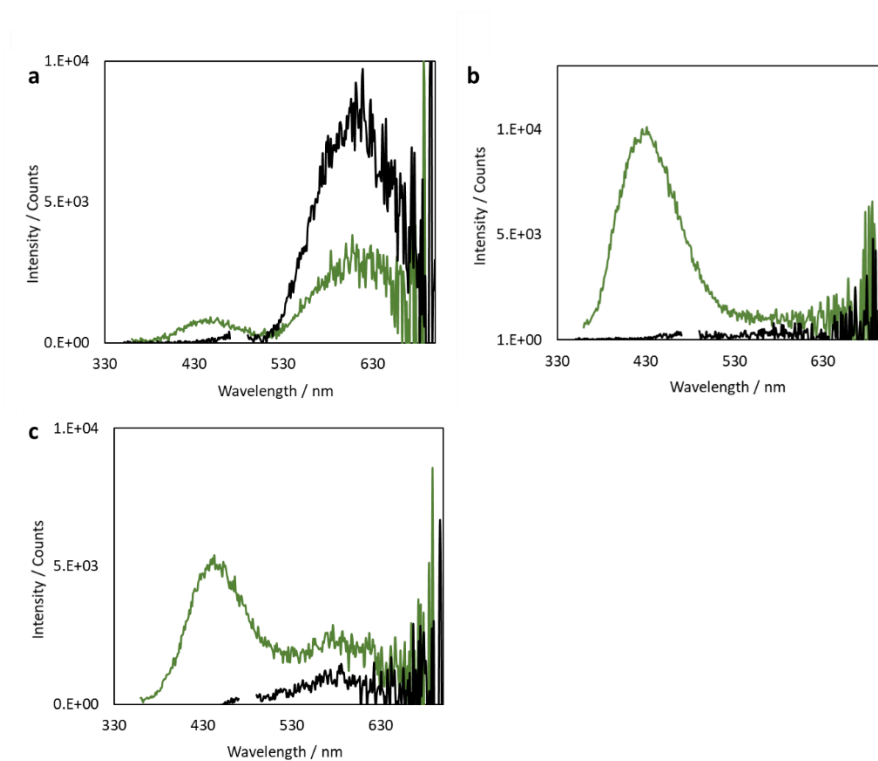


**Figure A3.2.** Emission spectra from a) 1 b) 2 and c) 3 when excited 350 nm (green traces) and 480 nm (black traces).



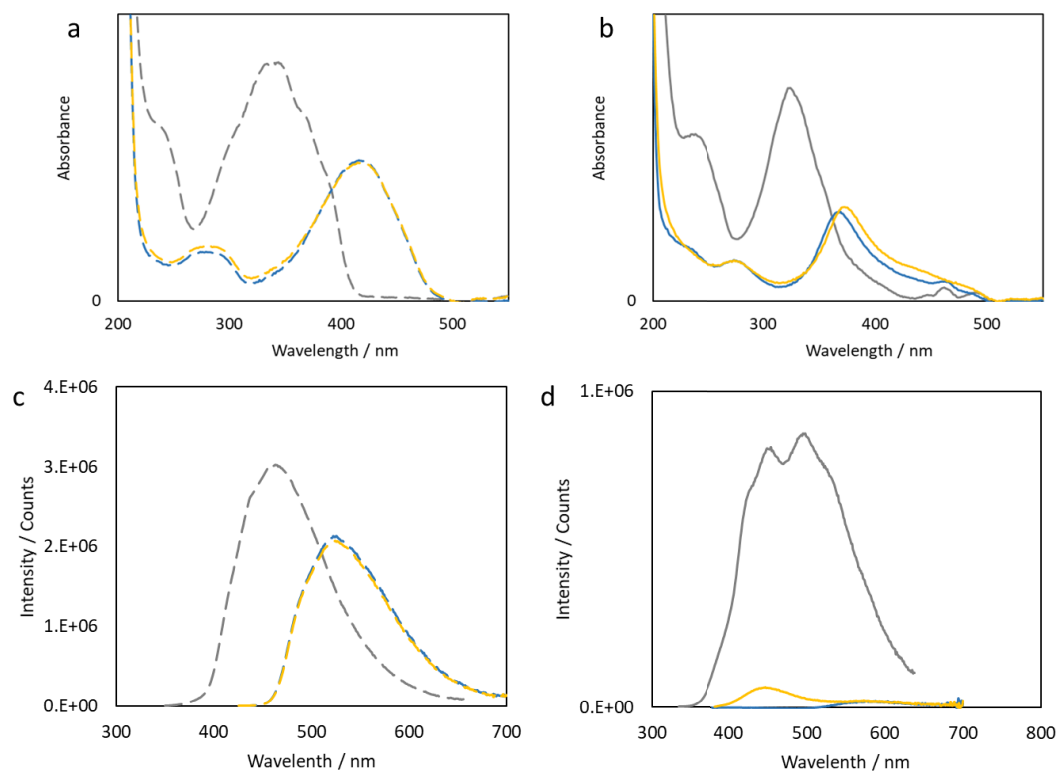


**Figure A3.3.** UV-vis absorbance (a,b) and PL (c,d) spectra for 2 (blue traces), 3 (yellow traces), and 4 (grey traces) under basic(a,c) and acidic (b,d) conditions.

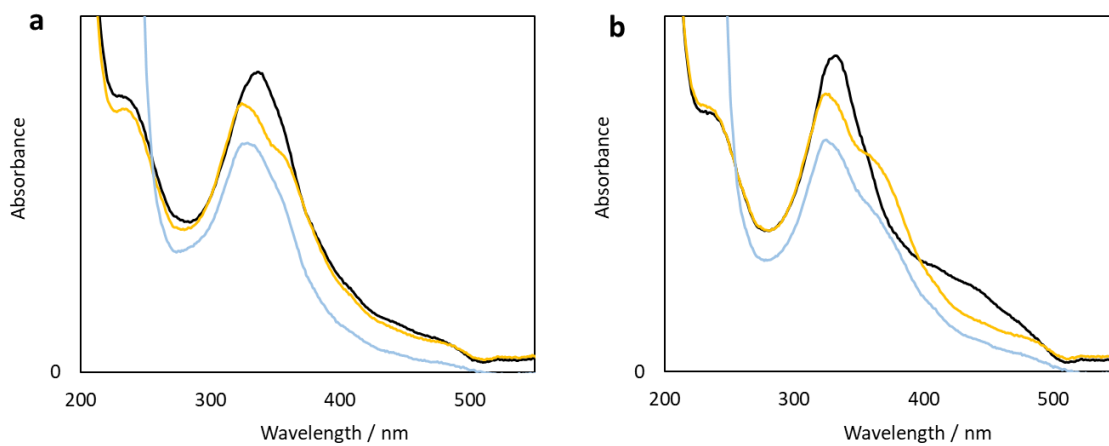
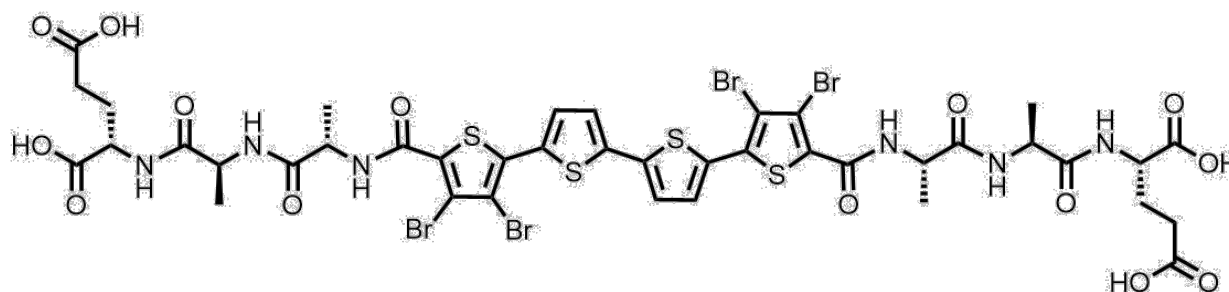
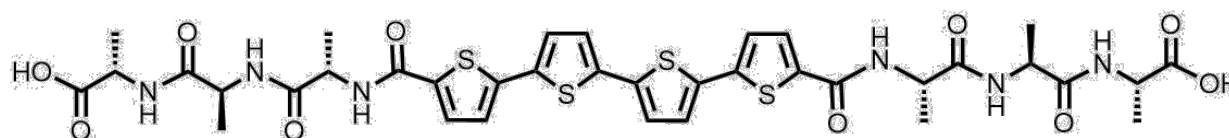


**Figure A3.4.** UV-vis absorbance profiles for 1:1 co-assemblies of a) **4** and **2** and b) **4** and **3** when assembled by HCl addition (black traces), when separately assembled and then mixed (yellow traces) and GdL hydrolysis (blue traces)

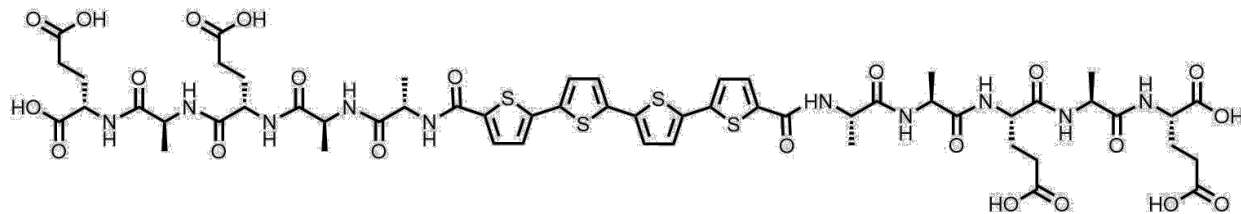


**EAA-OT4Br<sub>4</sub> (1):** Solid supported Wang-EAA-NH<sub>2</sub> peptide (0.2 mmol) was terminally Fmoc deprotected, capped with 3,4,5-tribromothiophene-2-carboxylic acid, and subjected to the standard Stille coupling procedure in the presence of 5,5'-bis- tributylstannyl-[2,2']-bithiophene (0.1 mmol, 0.07 g) and Pd(PPh<sub>3</sub>)<sub>4</sub> (0.008 mmol, 0.009 g). Following general cleavage, work-up, and HPLC purification, the peptide was obtained as a light orange powder (0.012 mmol, 6%). DATA UV-Vis (H<sub>2</sub>O)  $\lambda$ /nm (pH 10): 417. MS (ESI)  $m/z$  1275.17 (M-1H) (calc. 1275.82),  $m/z$  637.15 (M-2H)/2 (calc. 637.41),  $m/z$  1912.44 (3\*M-2)/2 (calc. 1912.75).

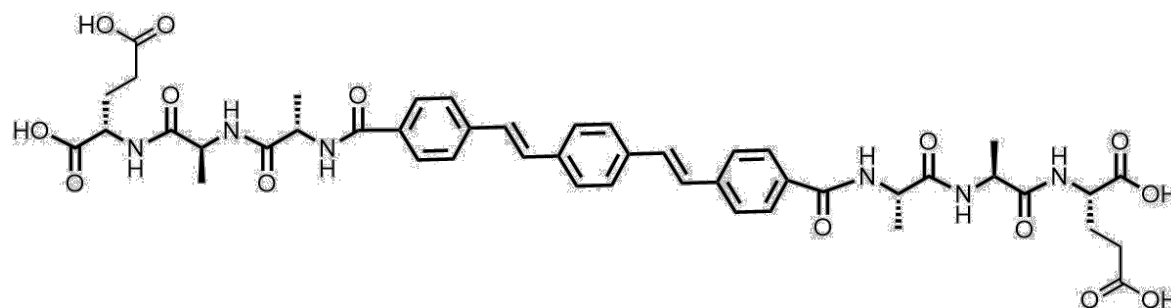


**AAA-OT4 (2):** Solid supported Wang-AAA-NH<sub>2</sub> peptide (0.2 mmol) was terminally Fmoc deprotected, capped with 5- bromothiophene-2-carboxylic acid, and subjected to the standard Stille coupling procedure in the presence of 5,5'-bis- tributylstannyl-[2,2']-bithiophene (0.1 mmol, 0.07 g) and Pd(PPh<sub>3</sub>)<sub>4</sub> (0.008 mmol, 0.009 g). Following general cleavage, work-up, and HPLC purification, the peptide was obtained as a light orange powder (0.023 mmol, 11.5%). DATA UV-Vis (H<sub>2</sub>O)  $\lambda$ /nm (pH 10): 418 nm. MS (ESI)  $m/z$  843.21 (M-1H) (calc. 843.99),  $m/z$  421.29 (M-

2H)/2 (calc. 421.50), m/z 1266.30 (3\*M-2)/2 (calc. 1266.49), 1688.21 (4\*M-2)/2 (calc. 1688.98).



**EAEAA-OT4 (3):** Solid supported Wang-EAEAA-NH<sub>2</sub> peptide (0.2 mmol) was terminally Fmoc deprotected, capped with 5- bromothiophene-2-carboxylic acid, and subjected to the standard Stille coupling procedure in the presence of 5,5'-bis- tributylstannyl-[2,2']-bithiophene (0.1 mmol, 0.07 g) and Pd(PPh<sub>3</sub>)<sub>4</sub> (0.008 mmol, 0.009 g). Following general cleavage, work-up, and HPLC purification, the peptide was obtained as a light orange powder (0.026 mmol, 13%). DATA UV-Vis (H<sub>2</sub>O) λ/nm (pH 10): 417 nm. MS (ESI) m/z 1360.31 (M-1H) (calc. 1360.45), m/z 679.70 (M-2H)/2 (calc. 679.23).



**EAA-OPV3 (4):** 0.022 g (0.06 mmol) of OPV3-diacid and 0.062 g (0.12 mmol) of PyBOP was dissolved in 10 mL of 2:1 NMP:DCM solution, after which 0.35 mL of DIPEA was gradually added then mixed for 1 min. This solution was added to solid supported Wang-EAA-NH<sub>2</sub> (0.2 mmol) peptide in a peptide chamber and mixed for 12 hours. The resin was drained and rinsed with coupling solvent. 0.014 g (0.04 mmol) of OPV3-diacid and 0.041 g (0.08 mmol) of PyBOP was dissolved in 10 mL of 2:1 NMP:DCM solution, after which 0.35 mL of DIPEA was gradually added then mixed for 1 min. This solution was added to the resin and mixed for another 12 hours.

The resin was drained and washed once with coupling solvent. A solution of 0.062 g (0.12mmol) of PyBOP was dissolved in 10 mL of 2:1 NMP:DCM solution, after which 0.35 mL of DIPEA was gradually added and mixed for 1 min. This solution was added to the peptide chamber and mixed for 12 hours. The peptide chamber was drained and washed 3 x NMP, 1 x MeOH, 3 x DCM. Following general cleavage, work-up, and HPLC purification, the peptide was obtained as a light-yellow powder (0.004 mmol, 2%). DATA UV-Vis (H<sub>2</sub>O)  $\lambda$ /nm (pH 10): 350 nm. MS (ESI) m/z 1328.2 (M-1H) (calc. 1238.4), m/z 663.7 (M-2H)/2 (calc. 663.7).

## ESI Mass Spectra:

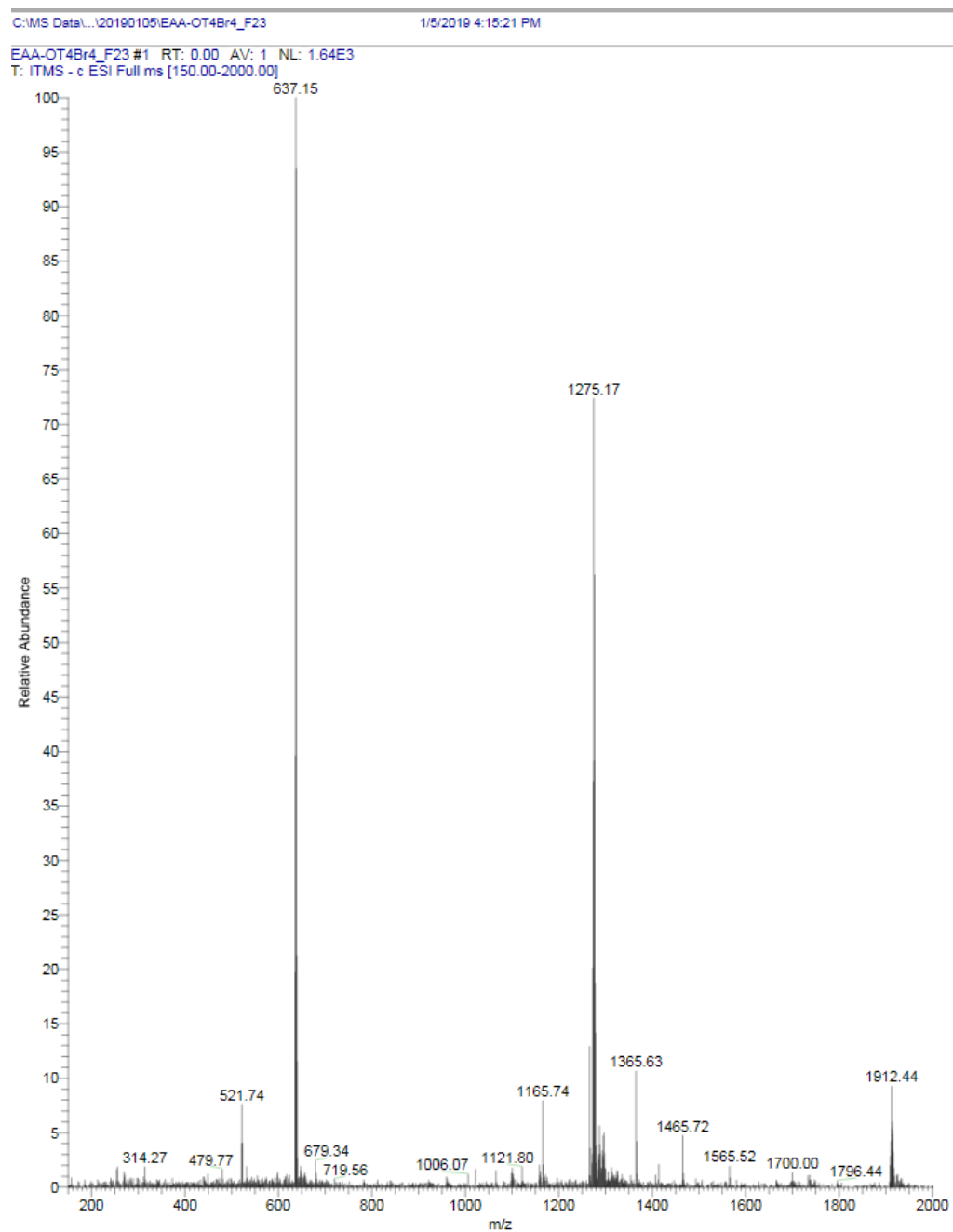


**Figure A3.5.** ESI spectrum of EAA-OT4Br<sub>4</sub> peptide (**1**). MS (ESI)  $m/z$  1275.17 (M-1H) (calc. 1275.82),  $m/z$  637.15 (M-2H)/2 (calc. 637.41),  $m/z$  1912.44 (3\*M-2)/2 (calc. 1912.75).

AAA-OT4\_f16 #1 RT: 0.00 AV: 1 NL: 8.43E3

T: ITMS - c ESI Full ms [150.00-2000.00]

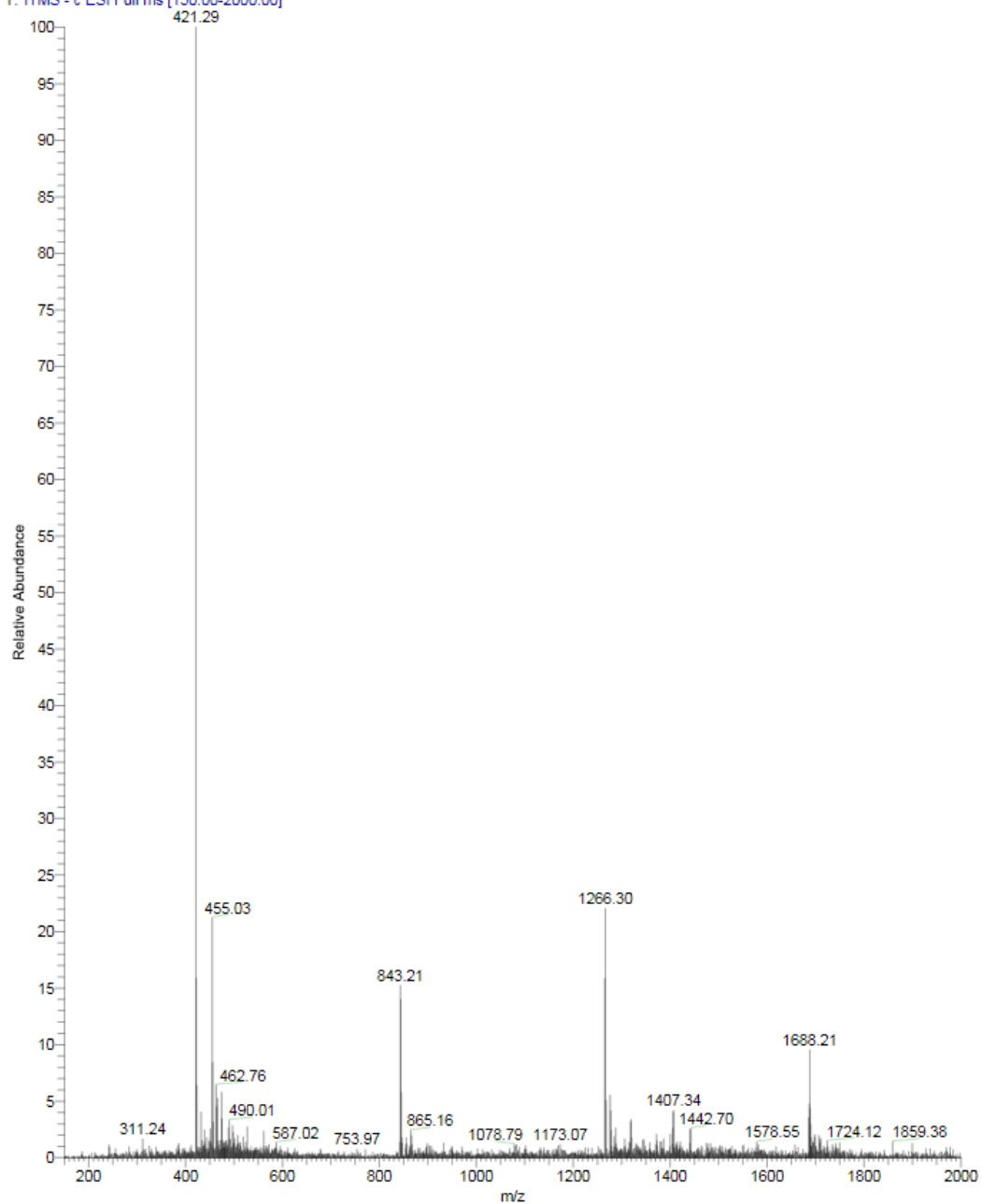


**Figure A3.6.** ESI spectrum of AAA-OT4 peptide (2). MS (ESI) m/z 843.21 (M-1H) (calc. 843.99), m/z 421.29 (M-2H)/2 (calc. 421.50), m/z 1266.30 (3\*M-2)/2 (calc. 1266.49), 1688.21 (4\*M-2)/2 (calc. 1688.98).

EAEEA-OT4\_F7 #1 RT: 0.00 AV: 1 NL: 6.18E3  
T: ITMS - c ESI Full ms [150.00-2000.00]

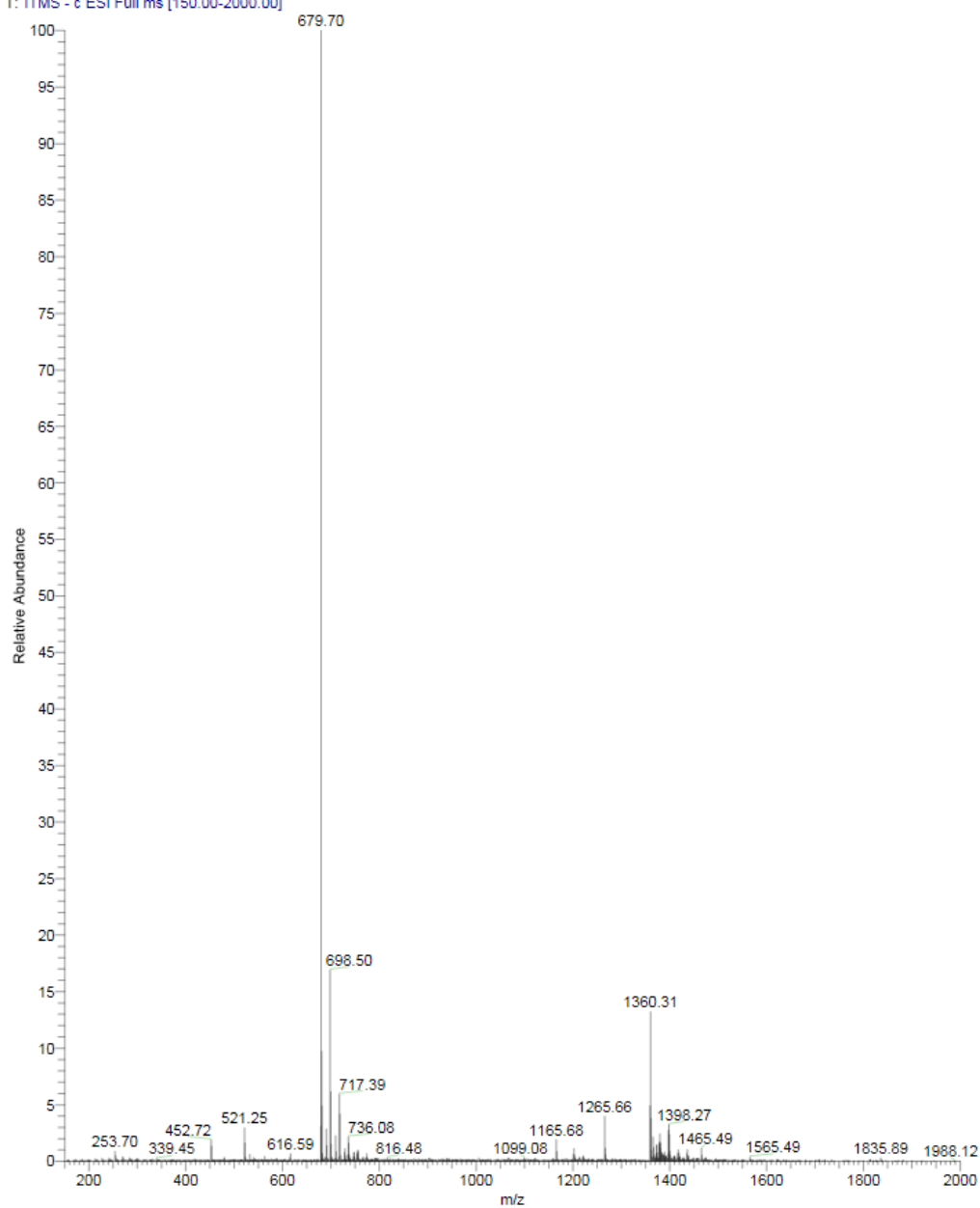


**Figure A3.7.** ESI spectrum of AAA-OT4 peptide (**3**). MS (ESI)  $m/z$  1360.31 (M-1H) (calc. 1360.45),  $m/z$  679.70 (M-2H)/2 (calc. 679.23).

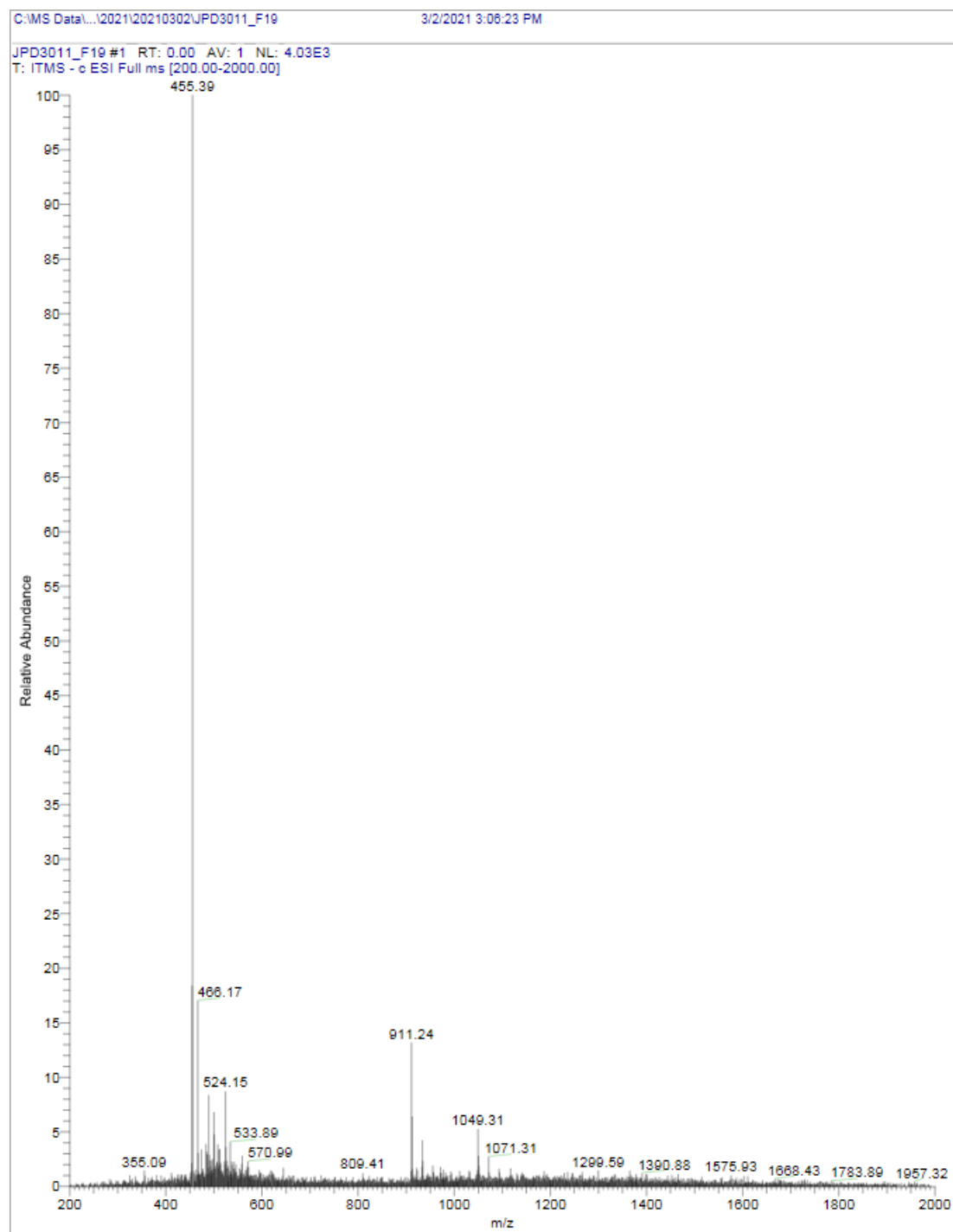


**Figure A3.8.** ESI spectrum of EAA-OPV3 peptide (**4**). MS (ESI)  $m/z$  911.24 (M-1H) (calc. 911.35),  $m/z$  455.39 (M-2H)/2 (calc. 455.18).



### HPLC Traces of Purified Peptides:

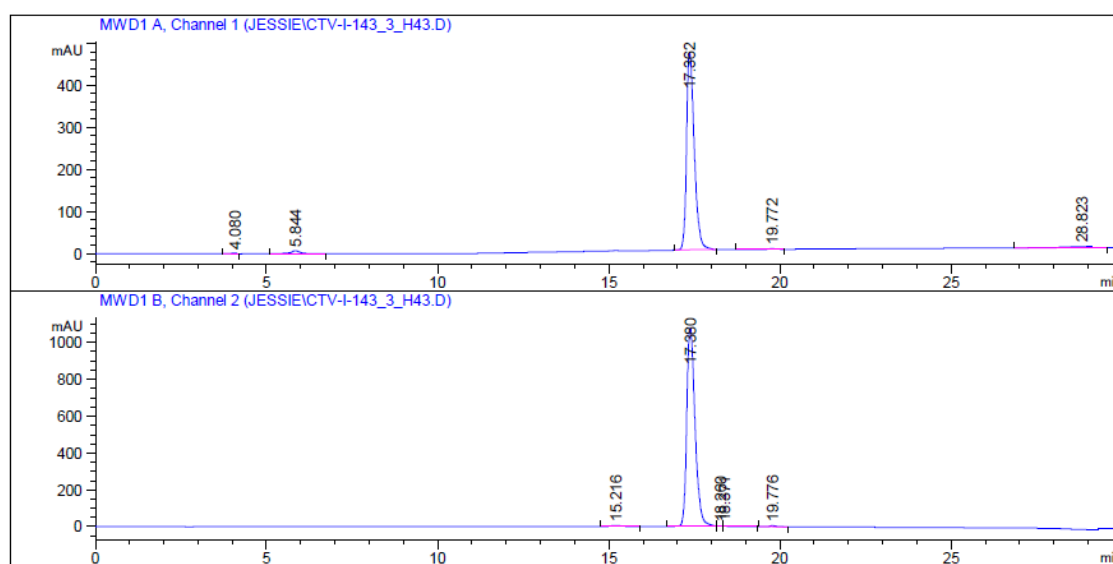


**Figure A3.9.** Analytical HPLC trace of purified EAA-OT4Br<sub>4</sub> peptide (**1**). Traces monitoring at 420 nm. Method: Linear gradient of 10%-50% acetonitrile/buffer over 25 minutes, then linear gradient of 50%-10% over 5 minutes.

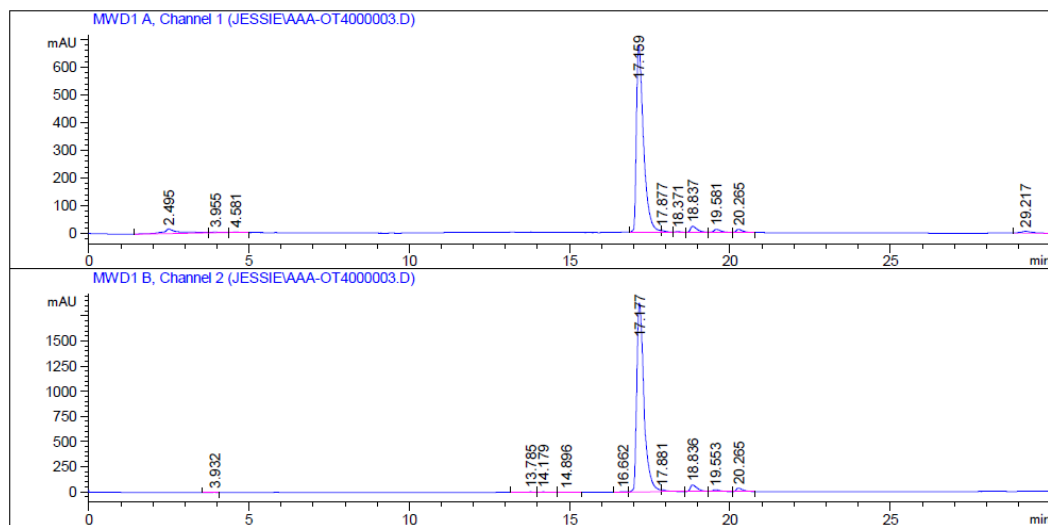


**Figure A3.10.** Analytical HPLC trace of purified AAA-OT<sub>4</sub> peptide (**2**). Traces monitoring 420 nm. Method: Linear gradient of 10%-50% acetonitrile/buffer over 25 minutes, then linear gradient of 50%-10% over 5 minutes.

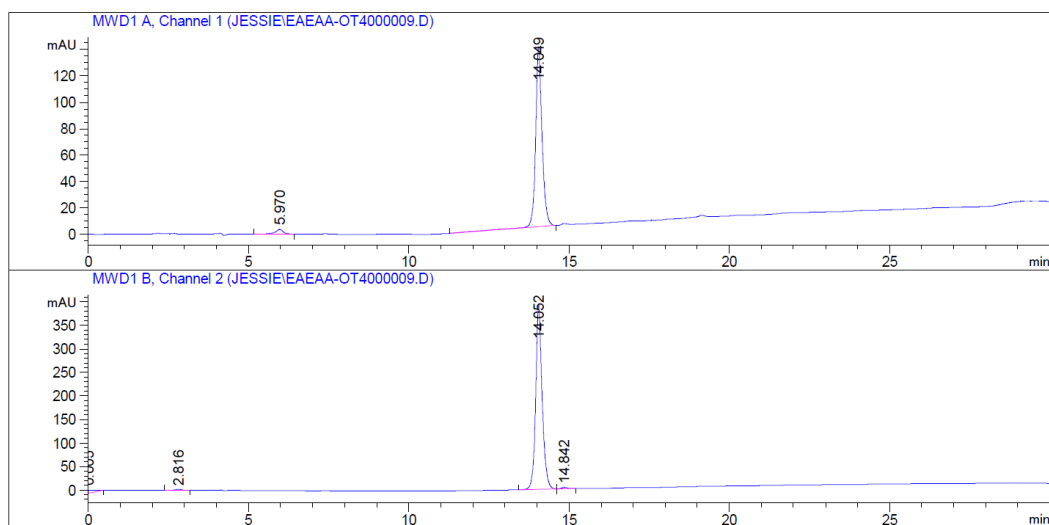


**Figure A3.11.** Analytical HPLC trace of purified EAEAA-OT4 peptide (**3**). Traces monitoring 420 nm. Method: Linear gradient of 10%-50% acetonitrile/buffer over 25 minutes, then linear gradient of 50%-10% over 5 minutes.

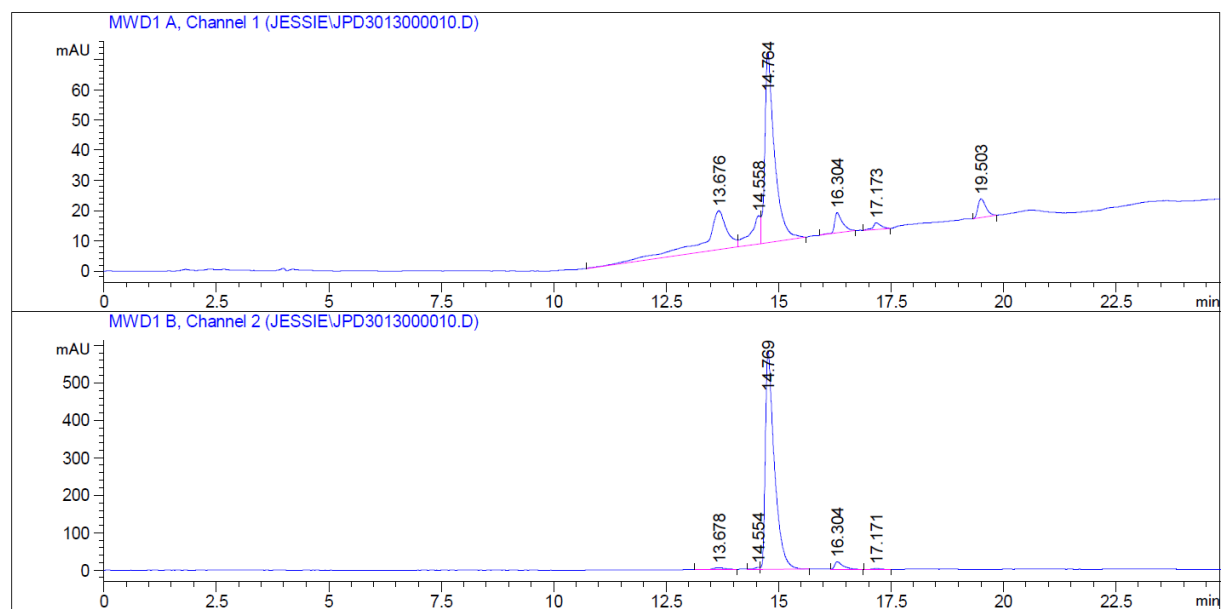


**Figure A3.12.** Analytical HPLC trace of purified EAA-OPV3 peptide (**4**). Traces monitoring 350 nm. Method: Linear gradient of 10%-50% acetonitrile/buffer over 25 minutes, then linear gradient of 50%-10% over 5 minutes.

## Chapter 4

### X-Ray Crystallography Experimental details and Report:

All reflection intensities were measured at 110(2) K using a SuperNova diffractometer (equipped with Atlas detector) with Cu  $K\alpha$  radiation ( $\lambda = 1.54178 \text{ \AA}$ ) under the program CrysAlisPro (Version CrysAlisPro 1.171.39.29c, Rigaku OD, 2017). The same program was used to refine the cell dimensions and for data reduction. The structure was solved with the program SHELXS-2018/3 (Sheldrick, 2018) and was refined on  $F^2$  with SHELXL-2018/3 (Sheldrick, 2018). Analytical numeric absorption correction using a multifaceted crystal model was applied using CrysAlisPro. The temperature of the data collection was controlled using the system Cryojet (manufactured by Oxford Instruments). The H atoms were placed at calculated positions (unless otherwise specified) using the instructions AFIX 13, AFIX 23 or AFIX 43 with isotropic displacement parameters having values 1.2 or 1.5  $U_{eq}$  of the attached C atoms. The H atom attached to O2 was found from difference Fourier map, and its coordinates were restrained pseudofreely using the DFIX instruction in order to keep the O–H bond distance within an acceptable range. The structure is mostly ordered.

The crystal contains a mixture of the fluorinated compound (one F and one H atoms attached to C7, major component) and the starting material (2 H atoms attached to C7, minor component). The occupancy factor for the major component (i.e., target compound) of the disorder refines to 0.736(6).

The absolute configuration has been established by anomalous-dispersion effects in diffraction measurements on the crystal, and the Flack and Hooft parameters refine to 0.00(7) and 0.01(6), respectively. The structure only contains the diastereomer with the R chiral center on C7.

**Table A4.1.** Experimental details of x-ray diffraction

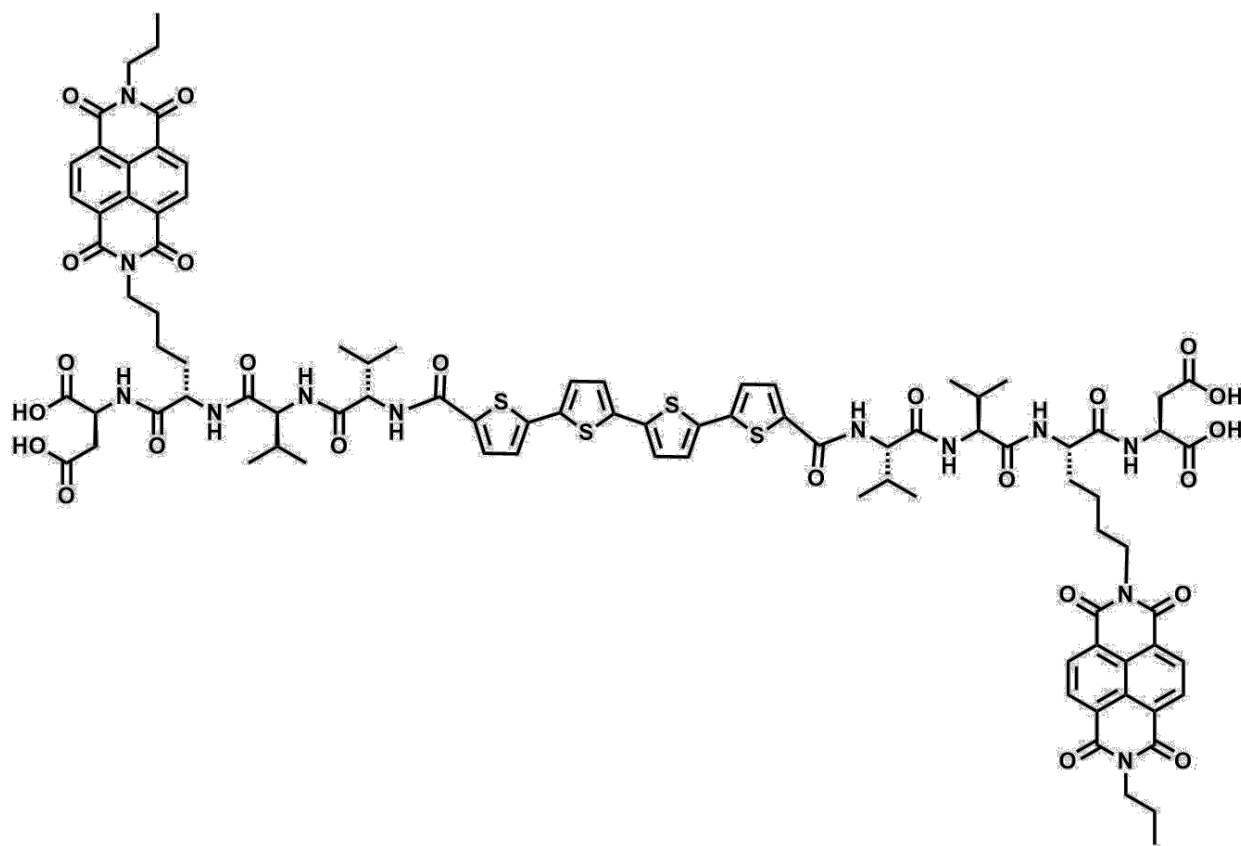
	xs2158a
Crystal data	
Chemical formula	C <sub>17</sub> H <sub>12.26</sub> F <sub>0.74</sub> NO <sub>4</sub>
$M_r$	308.50
Crystal system, space group	Monoclinic, $P2_1$
Temperature (K)	110
$a, b, c$ (Å)	9.70548 (18), 5.50361 (12), 13.0137 (3)
$\alpha$ (°)	92.9508 (17)
$V$ (Å <sup>3</sup> )	694.21 (3)
$Z$	2
Radiation type	Cu $K\alpha$
$\lambda$ (mm <sup>-1</sup> )	0.95
Crystal size (mm)	0.40 × 0.12 × 0.02
Data collection	
Diffractometer	SuperNova, Dual, Cu at zero, Atlas
Absorption	Analytical

correction	<i>CrysAlis PRO</i> 1.171.39.29c (Rigaku Oxford Diffraction, 2017) Analytical numeric absorption correction using a multifaceted crystal model based on expressions derived by R.C. Clark & J.S. Reid. (Clark, R. C. & Reid, J. S. (1995). <i>Acta Cryst.</i> A51, 887-897) Empirical absorption correction using spherical harmonics, implemented in SCALE3 ABSPACK scaling algorithm.
$T_{\min}, T_{\max}$	0.809, 0.980
No. of measured, independent and observed [ $I > 2\sigma(I)$ ] reflections	8757, 2693, 2618
$R_{\text{int}}$	0.023
$(\sin \theta / \lambda)_{\max}$ ( $\text{\AA}^{-1}$ )	0.616
Refinement	
$R[F^2 > 2\sigma(F^2)]$ , $wR(F^2)$ , $S$	0.027, 0.069, 1.06
No. of reflections	2693
No. of parameters	213
No. of restraints	2

H-atom treatment	H atoms treated by a mixture of independent and constrained refinement
$\square \rho_{\max}, \square \rho_{\min}$ (e $\text{\AA}^{-3}$ )	0.21, -0.14
Absolute structure	Flack x determined using 1134 quotients [(I+)-(I-)]/[(I+)+(I-)] (Parsons, Flack and Wagner, Acta Cryst. B69 (2013) 249-259).
Absolute structure parameter	0.00 (7)

Computer programs: *CrysAlis PRO* 1.171.39.29c (Rigaku OD, 2017), *SHELXS2018/3* (Sheldrick, 2018), *SHELXL2018/3* (Sheldrick, 2018), *SHELXTL* v6.10 (Sheldrick, 2008).

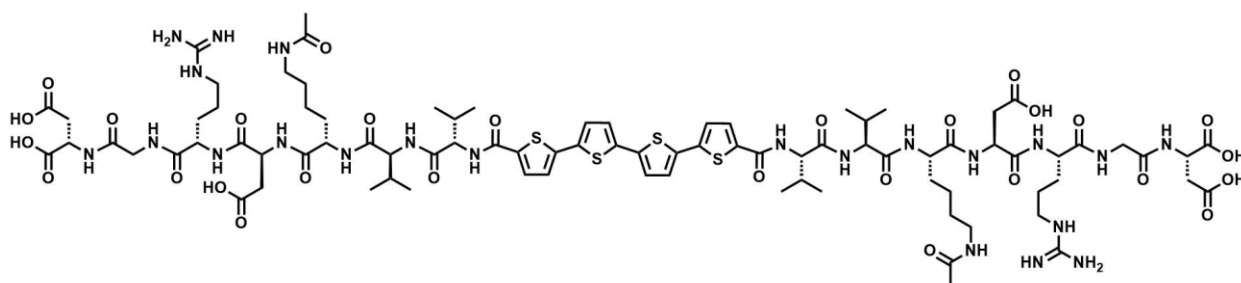
## Chapter 5



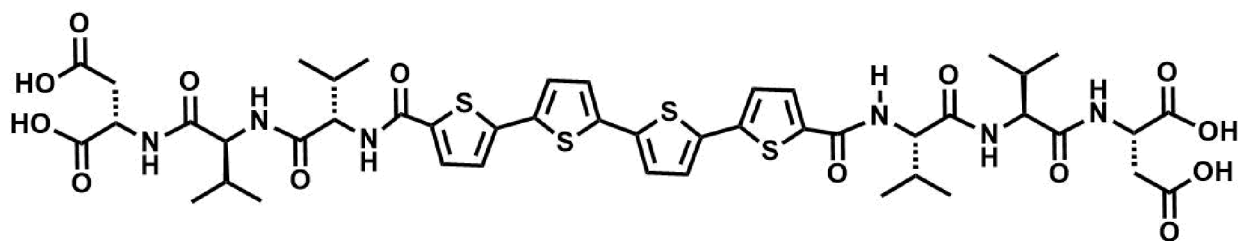
**DK(NDI)VV-OT4 (7):** Solid supported Wang-DK(Mtt)DVV-NH<sub>2</sub> peptide (0.2 mmol) was terminally Fmoc deprotected, capped with 5-bromothiophene-2-carboxylic acid, and subjected to the standard Stille coupling procedure in the presence of 5,5'-bis- tributylstannyl-[2,2']-bithiophene (0.1 mmol, 0.07 g) and Pd(PPh<sub>3</sub>)<sub>4</sub> (0.008 mmol, 0.009 g). Lysine Mtt protecting groups were removed and the resin washed. The resin bound free amine was subjected to imidation conditions with N-propyl-1,4,5,8-naphthalenetetracarboxylic. Following general cleavage, work-up, and HPLC purification, the peptide was obtained as a light orange powder (0.009 mmol, 4.5%).



DATA. UV-Vis (H<sub>2</sub>O)  $\lambda$ /nm (pH 10): 380 nm, 420 nm. MS (ESI)  $m/z$  1275.17 (M-1H) (calc. 1275.82),  $m/z$  637.15 (M-2H)/2 (calc. 637.41),  $m/z$  1912.44 (3\*M-2)/2 (calc. 1912.75).

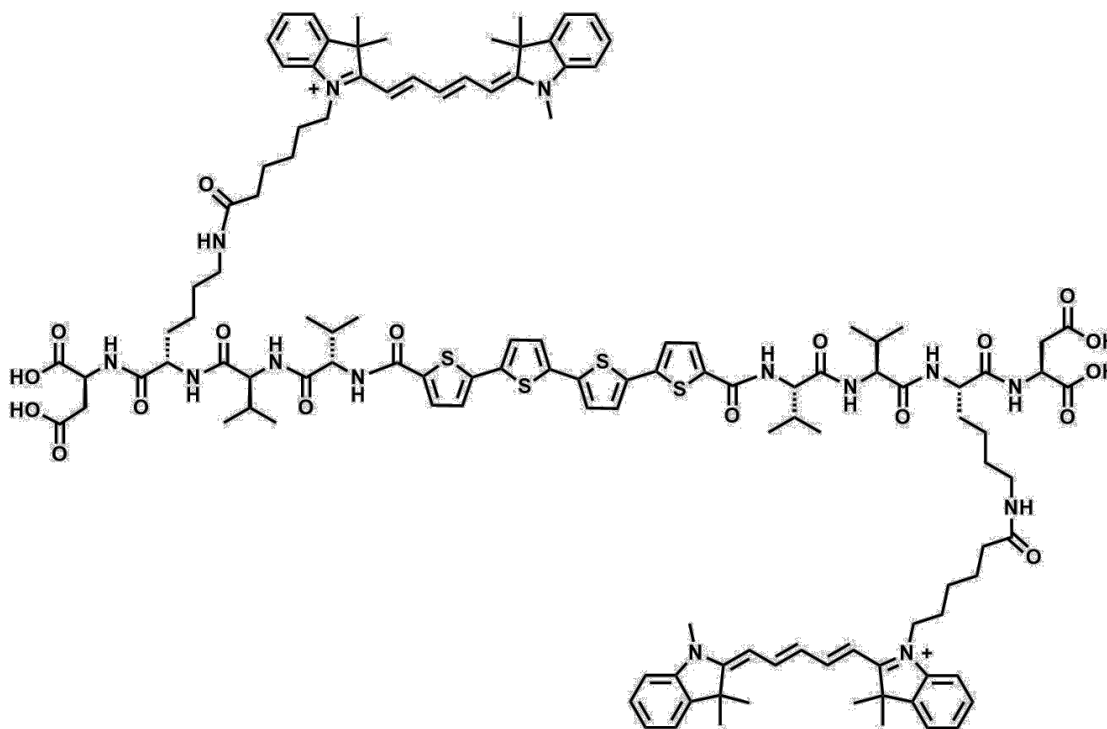


**DGRDK(Ac)VV-OT4 (8):** Solid supported Wang-DGRDK(Ac)VV-NH<sub>2</sub> peptide (0.2 mmol) was terminally Fmoc deprotected, capped with 5-bromothiophene-2-carboxylic acid, and subjected to the standard Stille coupling procedure in the presence of 5,5'-bis-tributylstannyl-[2,2']-bithiophene (0.1 mmol, 0.07 g) and Pd(PPh<sub>3</sub>)<sub>4</sub> (0.008 mmol, 0.009 g). Following general cleavage, work-up, and HPLC purification, the peptide was obtained as a light orange powder (0.007 mmol, 3.4%). DATA. UV-Vis (H<sub>2</sub>O)  $\lambda$ /nm (pH 10): 420 nm. MS (ESI)  $m/z$  1275.17 (M-1H) (calc. 1275.82),  $m/z$  637.15 (M-2H)/2 (calc. 637.41),  $m/z$  1912.44 (3\*M-2)/2 (calc. 1912.75).



**DVV-OT4 (10):** Solid supported Wang-DVV-NH<sub>2</sub> peptide (0.2 mmol) was terminally Fmoc deprotected, capped with 5-bromothiophene-2-carboxylic acid, and subjected to the standard Stille coupling procedure in the presence of 5,5'-bis-tributylstannyl-[2,2']-bithiophene (0.1 mmol, 0.07 g) and Pd(PPh<sub>3</sub>)<sub>4</sub> (0.008 mmol, 0.009 g). Following general cleavage, work-up, and HPLC purification, the peptide was obtained as a light orange powder (0.023 mmol, 11.5%). DATA. UV-

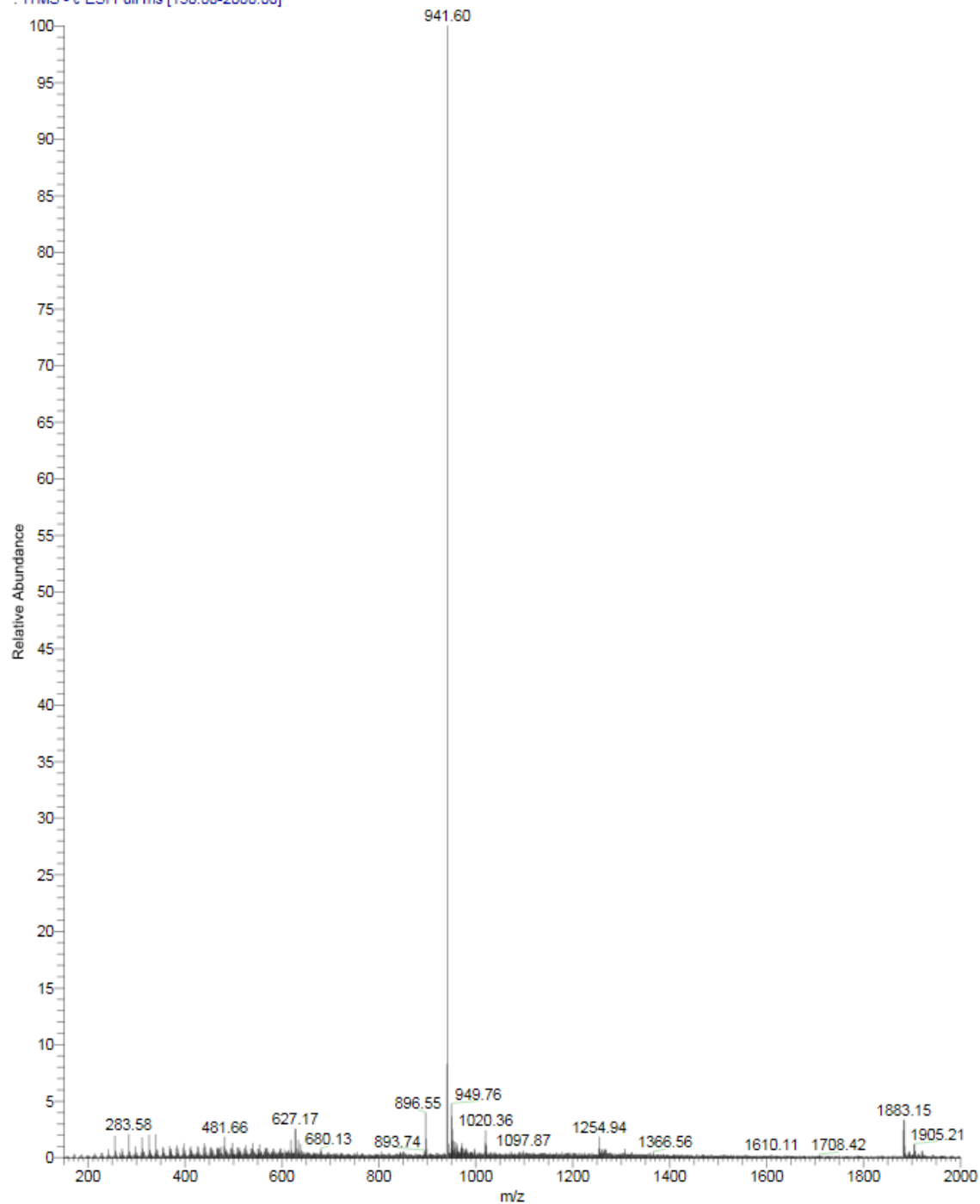
Vis (H<sub>2</sub>O)  $\lambda$ /nm (pH 10): 420 nm. MS (ESI) m/z 1275.17 (M-1H) (calc. 1275.82), m/z 637.15 (M-2H)/2 (calc. 637.41), m/z 1912.44 (3\*M-2)/2 (calc. 1912.75).



**DK(Cy5)VV-OT4 (11):** Solid supported Wang-DK(Mtt)VV-NH<sub>2</sub> peptide (0.1 mmol) was terminally Fmoc deprotected, capped with 5-bromothiophene-2-carboxylic acid, and subjected to the standard Stille coupling procedure in the presence of 5,5'-bis-tributylstannyl-[2,2']-bithiophene (0.05 mmol, 0.04 g) and Pd(PPh<sub>3</sub>)<sub>4</sub> (0.004 mmol, 0.005 g). Following general cleavage and work-up the free-amine peptide (0.008 mmol, 0.010g) was dissolved in 9 mL of 0.1M sodium bicarbonate. Cy5-NHS ester (0.007 mmol, 0.005g) was dissolved in 0.5 mL amine-free DMF. To this solution, 4.5 mL of the peptide solution was added and mixed for 4 hr. Following work-up the peptide was obtained as a green-blue powder (0.009 mmol, 9%). DATA. UV-Vis (H<sub>2</sub>O)  $\lambda$ /nm (pH 10): 427 nm, 624 nm. MS (ESI) m/z 1116.77 (M-2H)/2 (calc. 1116.02).

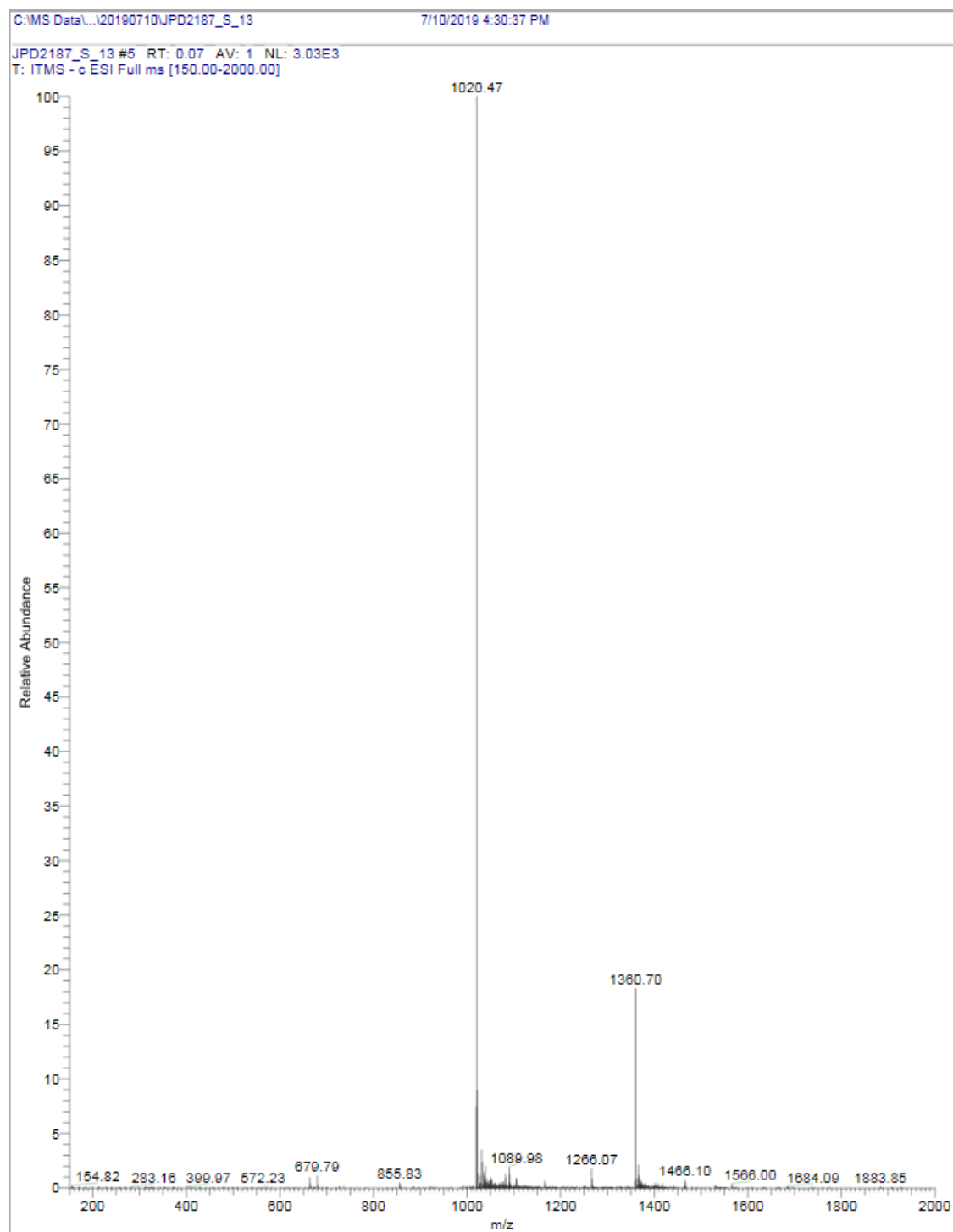
**ESI Mass Spectra:**

PD2189\_S\_52 #1 RT: 0.00 AV: 1 NL: 1.02E4  
ITMS - c ESI Full ms [150.00-2000.00]



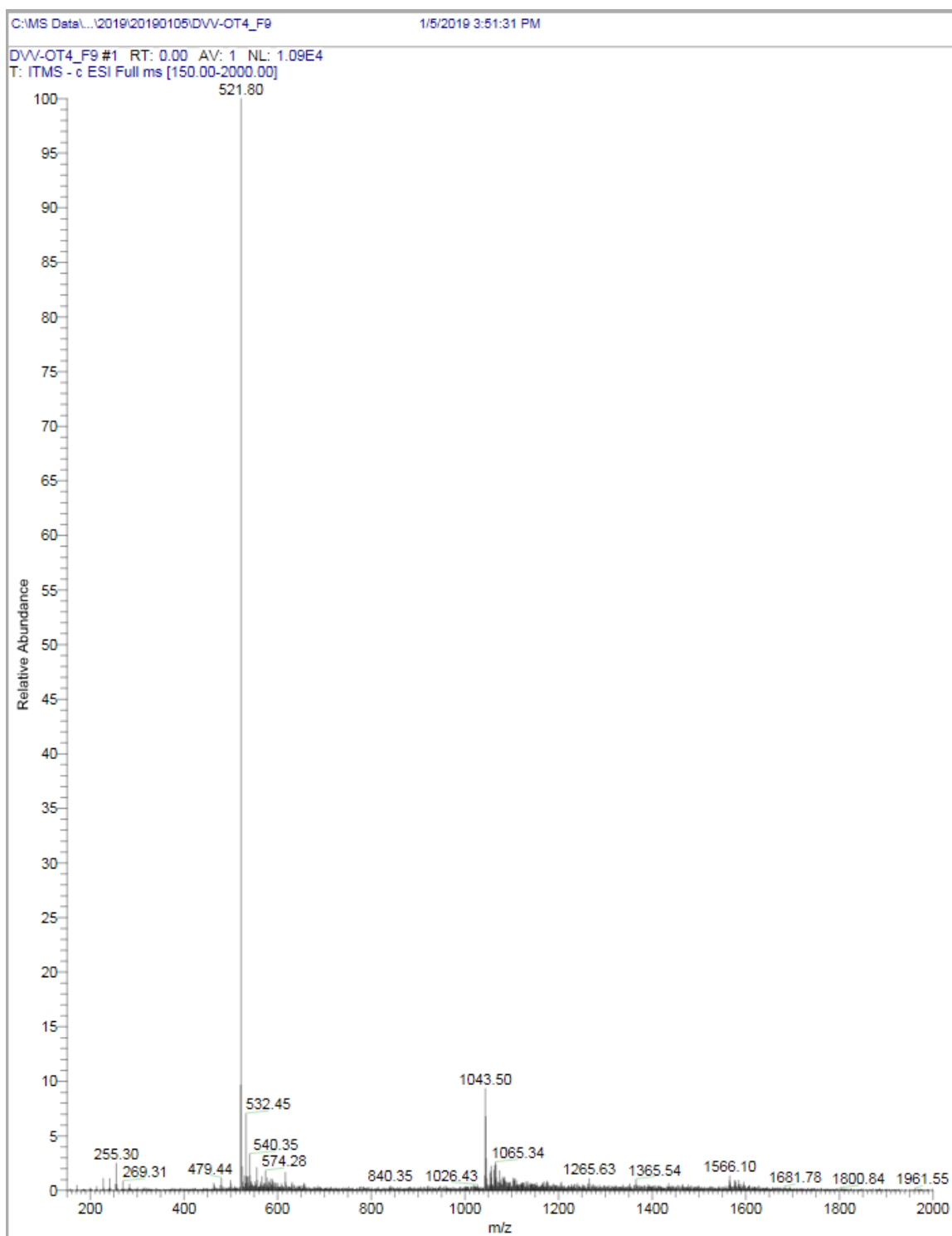
**Figure**

**Figure A5.3.** ESI spectrum of DK(NDI-n-Bu)VV-OT4 peptide (7). MS (ESI) m/z 1883.15 (M-1H) (calc. 1883.10), m/z 941.60 (M-2H)/2 (calc. 941.05).



**Figure**

**Figure A5.4.** ESI spectrum of DGRDK(Ac)VV-OT4 peptide (**8**). MS (ESI)  $m/z$  1020.47 ( $(M-2H)/2$  (calc. 1020.15),  $m/z$  1360.70 ( $(M*2-3H)/3$  (calc 1360.53).



**Figure**

**Figure A5.5.** ESI spectrum of DVV-OT4 peptide (**10**). MS (ESI)  $m/z$  1043.50 (M-H) (calc. 1043.27),  $m/z$  521.80 (M-2H)/2 (calc 521.14).

JPD-II-149\_semiCy5 #1 RT: 0.00 AV: 1 NL: 2.98E4  
T: ITMS + c ESI Full ms [150.00-2000.00]

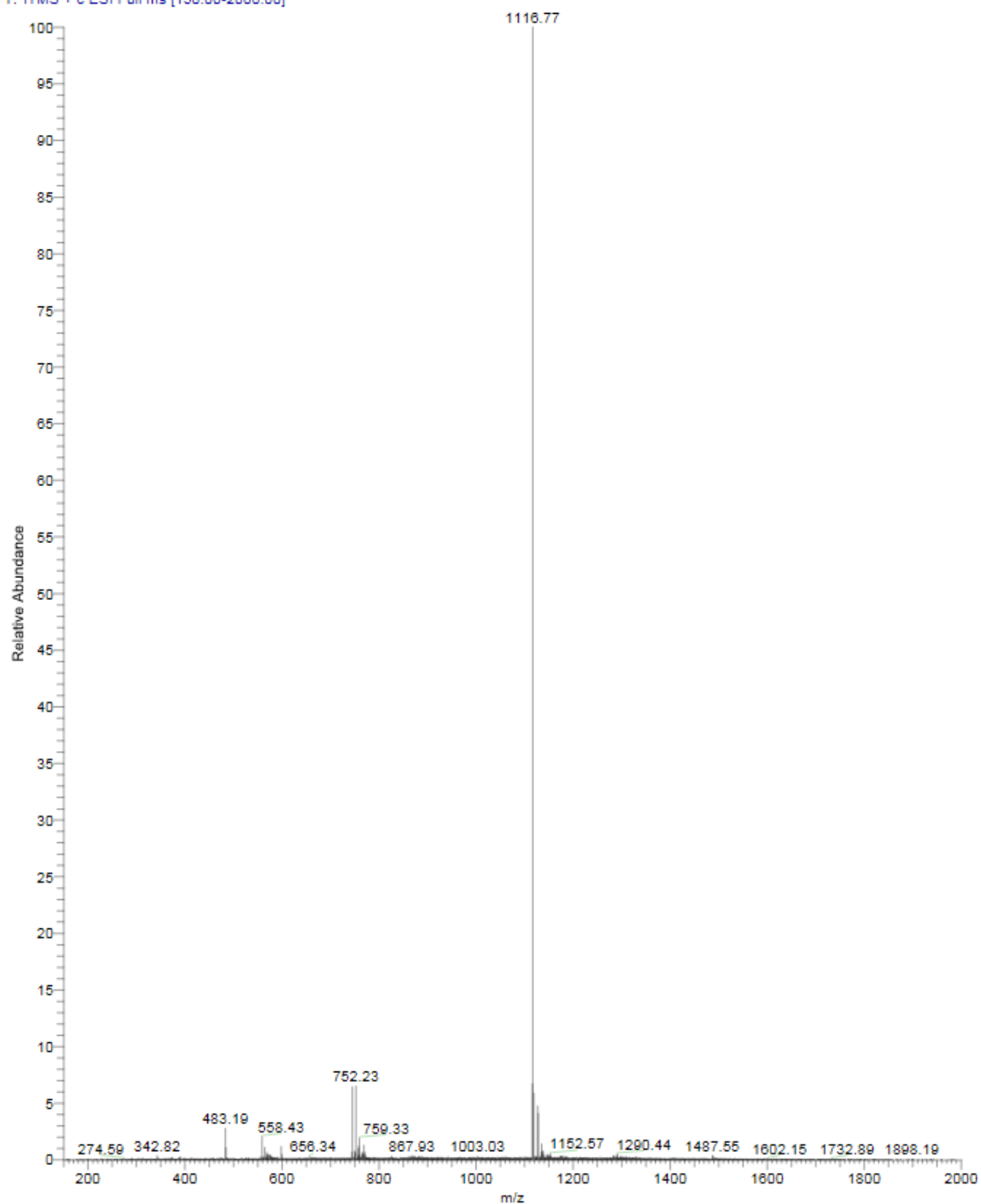


**Figure A5.6.** ESI spectrum of DK(Cy5)VV-OT4 peptide (**11**). MS (ESI)  $m/z$  1116.77 ( $M-2H$ )/2 (calc. 1116.02).

## HPLC Traces

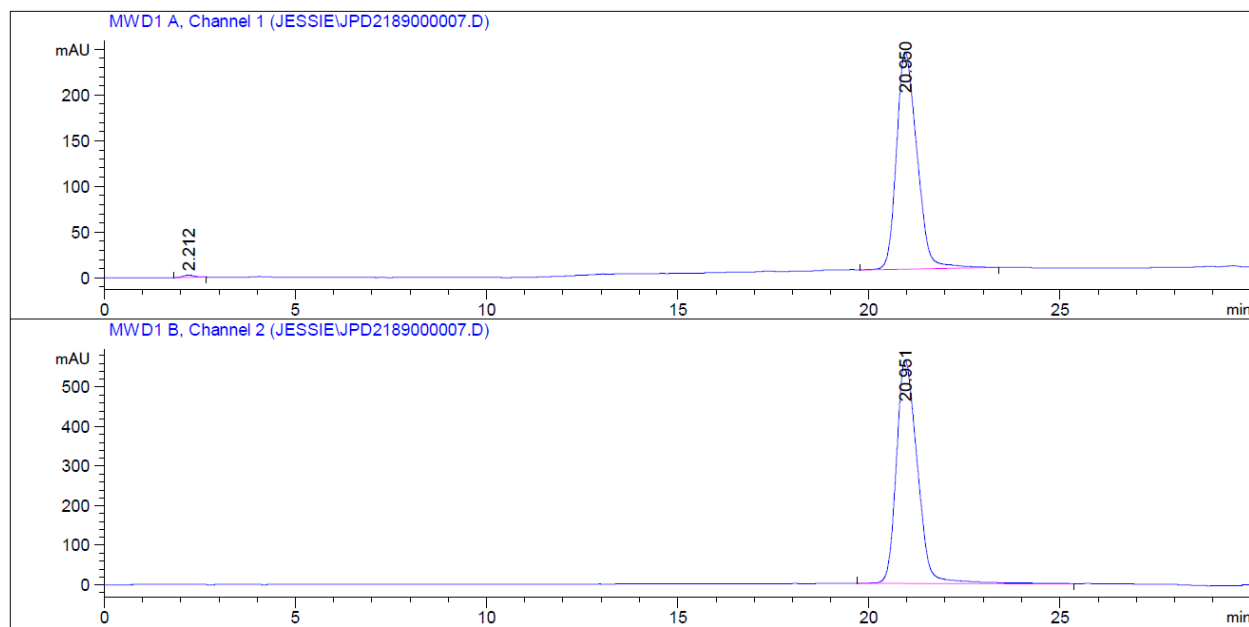


**Figure A5.9.** Analytical HPLC trace of purified DK(NDI-n-Bu)VV-OT4 peptide (**7**). Traces monitoring at 260 nm (top) and 430 nm (bottom). Method: Linear gradient of 10%-50% acetonitrile/buffer over 25 minutes, then linear gradient of 50%-10% over 5 minutes.

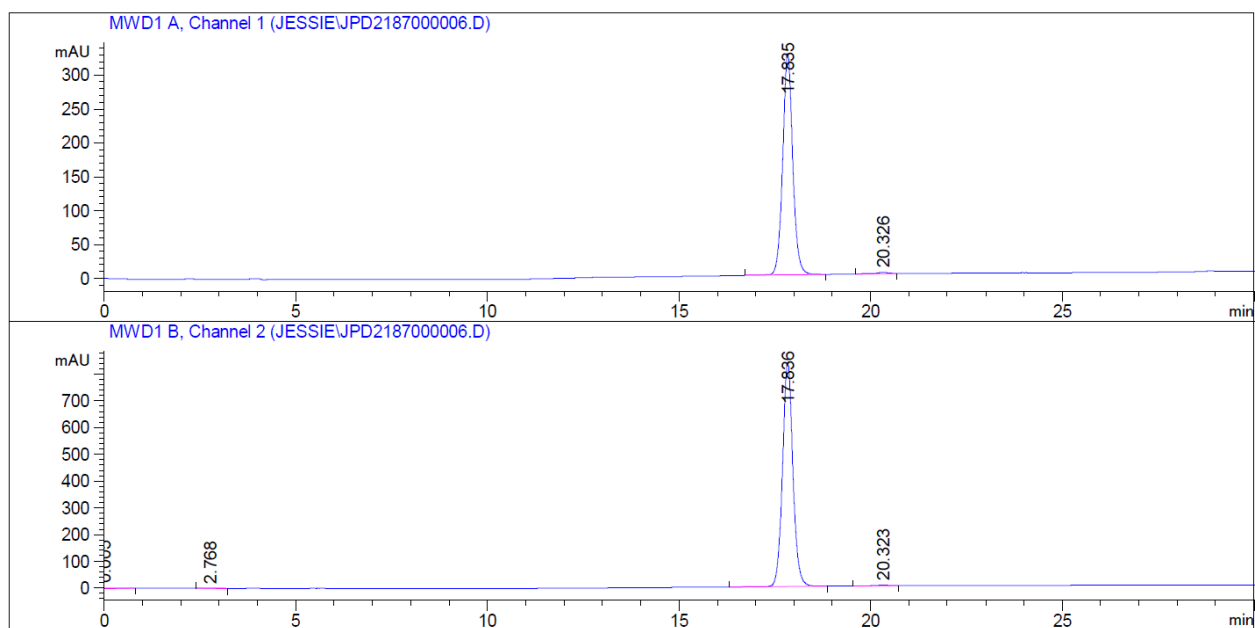


**Figure A5.10.** Analytical HPLC trace of purified DGRDK(Ac)VV-OT4 peptide (**9**). Traces monitoring at 260 nm (top) and 420 nm (bottom). Method: Linear gradient of 10%-50% acetonitrile/buffer over 25 minutes, then linear gradient of 50%-10% over 5 minutes.

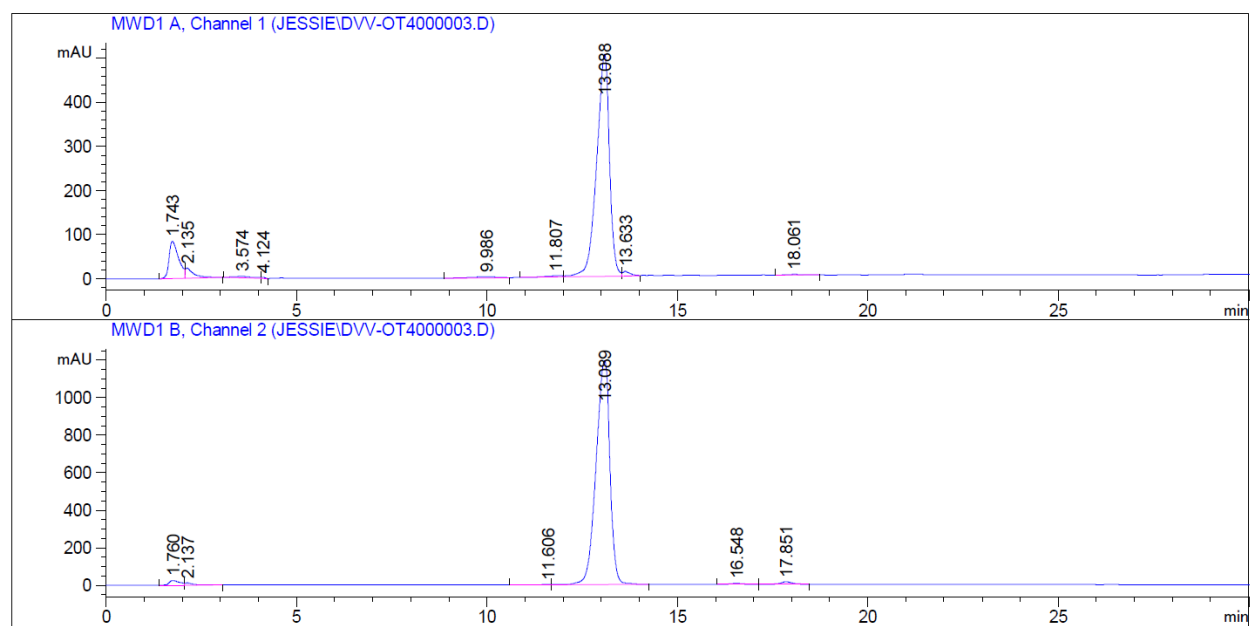




**Figure A5.11.** Analytical HPLC trace of purified DVV-OT4 peptide (**10**). Traces monitoring at 260 nm (top) and 420 nm (bottom). Method: Linear gradient of 10%-50% acetonitrile/buffer over 25 minutes, then linear gradient of 50%-10% over 5 minutes.

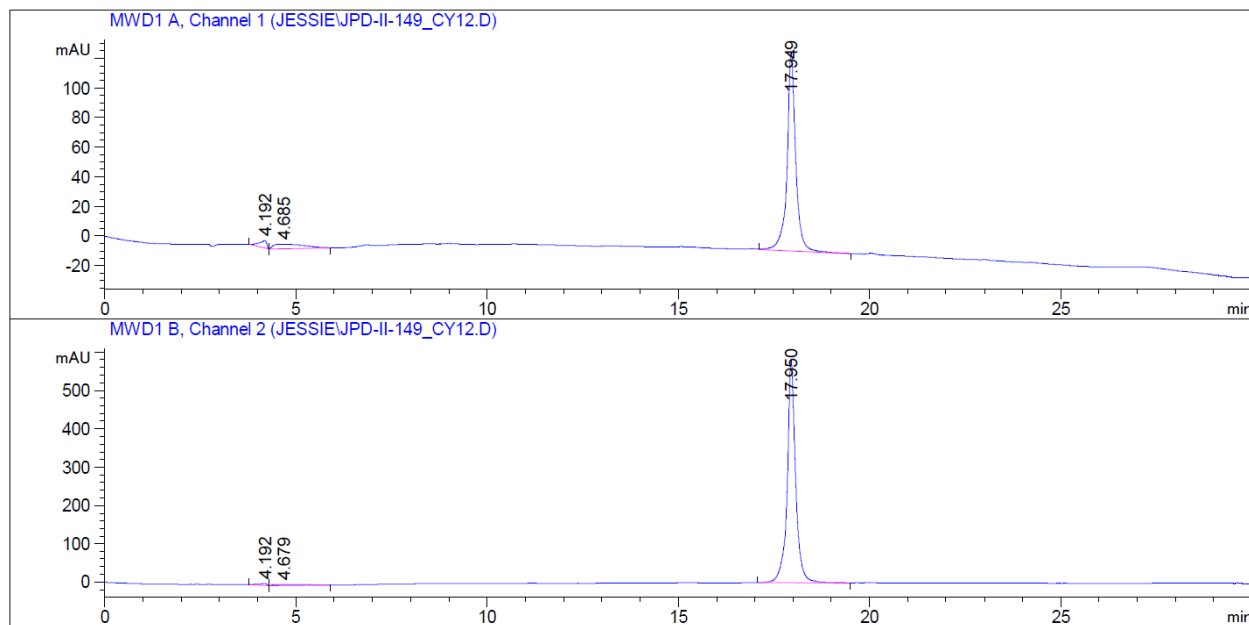


**Figure A5.11.** Analytical HPLC trace of purified DK(Cy5)VV-OT4 peptide (**11**). Traces monitoring at 426 nm (top) and 624 nm (bottom). Method: Linear gradient of 10%-50% acetonitrile/buffer over 25 minutes, then linear gradient of 50%-10% over 5 minutes.

# Jessie Perrin Dibble

313 W. 28<sup>th</sup> Street, Baltimore MD  
(707) 362-7526 | jessiedibble@gmail.com

---

## EDUCATION

- Ph.D. Candidate in Chemistry** June 2016-August 2021  
Johns Hopkins University, Baltimore, MD
- Certificate in advanced studies in Nanobiotechnology** June 2017-June 2021  
Johns Hopkins Institute for Nanobiotechnology, Baltimore, MD
- M.A. in Chemistry** June 2016- May2018  
Johns Hopkins University, Baltimore, MD
- B.S. in Chemistry** October 2010- August 2014  
University of California, Santa Cruz, Santa Cruz, CA

## RESEARCH AND PROFESSIONAL EXPERIENCE

- Graduate Research Assistant** June2016-Present  
Johns Hopkins University, Baltimore, MD  
Research Advisor: J.D. Tovar
- Designed and executed studies of constitutional isomerism, monomer design and assembly trigger in self-assembling  $\pi$ -conjugated peptides
  - Engineered creative strategies in peptide synthesis to build novel target compounds
  - Contributed to an interdisciplinary team of researchers to explore tissue engineering applications
  - Supervised the research of multiple undergraduates and junior graduate students
- Research Associate** March 2015- June 2016  
Gilead Sciences, Inc, Foster City, CA
- Performed routine release and stability testing for early phase clinical projects adhering to cGMP, Standard Operating Procedures, and following strict time constraints
  - Troubleshooted instrumentation to prevent delays in analytical testing
  - Conducted laboratory investigations to determine cause of suspect results
  - Organized, trended, and reported analytical data in Laboratory Information Management System (LIMS)
- Laboratory Analyst** September 2014 – March 2015  
Vanton Research Lab, LLC, Concord, CA
- Wrote and executed protocols for routine GMP analytical stability testing and managed data for commercial products
  - Developed HPLC analytical methods and maintained instrumentation
  - Conducted research and development projects toward proprietary sustained release formulation development

**Undergraduate Research Assistant**

September 2013 – September 2014

University of California, Santa Cruz, Santa Cruz, CA

Research Advisor: Dr. R. Scott Lokey

- Investigated passive membrane permeability in macrocyclic peptide library
- Designed and synthesized N-substituted glycine residues to increase chemical diversity in orally active macrocyclic drug candidates

**Undergraduate Research Assistant**

September 2012 – September 2013

University of California, Santa Cruz, Santa Cruz, CA

Research Advisor: Dr. Glenn Millhauser

- Examined copper-regulated enzymatic cleavage of prion protein

**HONORS AND AWARDS**

Sarah and Adolph Roseman Achievement Award, 2021

Phi Beta Kappa, 2014

Doug Drexler Chemistry Scholarship, 2013

**PRESENTATIONS AND PUBLICATIONS**

**J.P. Dibble**, J.D. Tovar (2020, June). A Tale of Three Hydrophobicities: Impact of Constitutional Isomerism on Nanostructure Evolution and Electronic Communication in  $\pi$ -Conjugated Peptides. Paper presented at the virtual Organic  $\pi$ -Electron Materials Meeting.

**J. P. Dibble**, C. Troyano-valls and J. D. Tovar, *Macromolecules*, 2020, **53**, 7263–7273.

A. J. McDonald, **J. P. Dibble**, E. G. B. Evans and G. L. Millhauser, *Journal of Biological Chemistry*, 2014, **289**, 803–813.

**TEACHING EXPERIENCE**

**Teaching Assistant**

Johns Hopkins University, Baltimore, MD

- Spectroscopic Methods of Organic Structure Determination, Spring 2018
- Intermediate Organic Chemistry Laboratory, Spring 2017
- Organic Chemistry, Fall 2016/2017

**UNIVERSITY SERVICE (Johns Hopkins University)**

ChemDNA Mentor Program: Graduate Student Mentor 2020

Graduate Representative Organization: General Counsel Representative 2017-2019